UNIVERSITÀ DEGLI STUDI DI PADOVA
Sede Amministrativa: Università degli Studi di Padova
Dipartimento di Fisica "G. Galilei"

SCUOLA DI DOTTORATO DI RICERCA IN: FISICA
CICLO XXI

Measurement of fission cross-section of actinides at n_TOF for advanced nuclear reactors

Direttore della Scuola:	Ch.mo Prof. Attilio Stella
Supervisore:	Ch.ma Prof.ssa Giovanna Montagnoli
Correlatori:	Dr. Nicola Colonna Dr. Pierfrancesco Mastinu

Dottorando: Marco Calviani

2 Febbraio 2009

A Claudio e Silvana

Contents

Appendices

Prefazione

Il lavoro oggetto della presente tesi ha riguardato la determinazione ad alta accuratezza della sezione d'urto per la reazione di fissione indotta da neutroni su vari isotopi - tutti radioattivi - di interesse per le tecnologie nucleari emergenti. Le misure erano precedentemente state effettuate presso la facility per tempi di volo di neutroni n_TOF, presso il CERN di Ginevra. In questo lavoro sono state in particolare analizzate le misure di fissione per il ^{233}U, il principale isotopo fissile alla base del ciclo di combustibile Th/U, e quelle sugli attinidi minori ^{241}Am, ^{243}Am e ^{245}Cm, le cui sezioni d'urto sono richieste per lo sviluppo di sistemi nuclear innovativi (ADS e reattori di IV Generazione) attualmente in fase di studio per la produzione di energia e per la trasmutazione delle scorie radioattive.

Le suddette reazioni sono state misurate con una camera a ionizzazione per frammenti di fissione (Fast Ionization Chamber), in combinazione con un sistema di acquisizione basato su Flash-ADC.

Il primo passo dell'analisi ha riguardato la ricostruzione dei segnali della camera di fissione, al fine di estrarre informazioni necessarie per la discriminazione dei frammenti di fissione dal background, nonché per la determinazione dell'energia dei neutroni, a partire dal loro tempo di volo.

Le sezioni d'urto di fissione per i vari isotopi sopra citati sono state determinate relativamente alla sezione d'urto della reazione $^{235}\mathrm{U}(n,f)$, considerata standard di misura in un vasto intervallo energetico. Al fine di minimizzare gli errori sistematici, tale reazione è stata misurata con lo stesso rivelatore, e contemporaneamente alle reazioni oggetto della tesi.

Una parte fondamentale del lavoro di tesi ha quindi riguardato l'analisi dei dati della reazione $^{235}\mathrm{U}(n,f)$, che ha permesso in primo luogo di studiare la risposta della camera a fissione, grazie anche all'utilizzo di dettagliate simulazioni effettuate con i più sofisticati codici Monte Carlo per il trasporto dei neutroni. L'analisi della reazione di fissione sul ^{235}U ha permesso inoltre la calibrazione energetica del fascio di neutroni, la determinazione del flusso neutronico incidente sul rivelatore ed una stima accurata del background.

Nella presente tesi sono presentati i risultati finali della sezione d'urto della reazione ^{233}U(n,f), nonché i risultati preliminari della sezione d'urto per le reazioni ^{241}Am(n,f), ^{243}Am(n,f) e ^{245}Cm(n,f). Le caratteristiche del fascio di neutroni di n_TOF hanno permesso di ottenere risultati in un vasto intervallo energetico, da circa 30 meV fino a 1 MeV, in una singola misura. Nel caso del ^{233}U(n,f), la sezione d'urto è stata determinata con una incertezza di circa il 3%, un valore prossimo a quello attualmente richiesto per lo sviluppo di sistemi nucleari innovativi. Al fine di raggiungere l'accuratezza richiesta, è stato necessario correggere i dati per effetti dipendenti dal bersaglio, legati all'efficienza del rivelatore. Inoltre sono state applicate correzioni dovute al dead-time, anch'esso dipendente dalla reazione studiata.

La tesi è organizzata come segue: nel Capitolo 1 sono presentate le motivazioni alla base della richiesta di sezioni d'urto accurate sulle sezioni di fissione per vari attinidi ed isotopi di interesse per il ciclo di combustibile Th/U. Le caratteristiche principali della facility n_TOF, in particolare quelle rilevanti per le misure di fissione, sono descritte nel Capitolo 2.

Il Capitolo 3 contiene la descrizione dettagliata dell'apparato sperimentale utilizzato per le misure di fissione oggetto del presente lavoro di tesi. È inoltre presentato lo studio della risposta del rivelatore, in particolare in termini di efficienza e attenuazione del fascio.

Nel Capitolo 4 è presentata la procedura di analisi seguita per la riduzione dei dati, a partire dalla ricostruzione dei segnali. Sono quindi presentati i risultati per le due reazioni tipicamente utilizzate come riferimento nelle misure di fissione, ^{235}U(n,f) e ^{238}U(n,f).

Il Capitolo 5 è dedicato alla determinazione della sezione d'urto per la reazione ^{233}U(n,f). In questo capitolo è descritta nel dettaglio la procedura seguita per la minimizzazione e sottrazione del background, nonché per la correzione degli effetti sperimentali, in particolare efficienza di rivelazione e dead-time. Le sezioni d'urto così ottenute, caratterizzate da una elevata accuratezza ($\sim$3%) nell'intero intervallo energetico (30 meV $\leq E_n \leq$ 1 MeV), sono quindi confrontate con i risultati di misure precedenti e con le sezioni d'urto tabulate delle principali librerie di dati valutati. Tale confronto indica la necessità di aggiornare le suddette librerie, al fine di rendere più attendibili i dati di sezioni d'urto necessari per la progettazione di sistemi nucleari innovativi basati sul ciclo del combustibile Th/U.

Il Capitolo 6 presenta i risultati, in qualche caso ancora preliminari, sulle sezioni d'urto di fissione per gli isotopi ^{241}Am, ^{243}Am e ^{245}Cm. In questo caso, l'elevatissimo background associato alla radioattività naturale dei campioni utilizzati, e la presenza di contaminazioni da altri isotopi, ha reso più complicata l'analisi dei dati, e più incerte le sezioni d'urto estratte. Per la reazione $^{243}\mathrm{Am}(n,f)$ è stato possibile ottenere sezioni d'urto accurate solo a partire da circa 350 keV. Negli altri due casi la sezione d'urto è stata determinata nell'intero intervallo energetico, da circa 30 meV fino ad 1 MeV. Tuttavia, non essendo stato possibile al momento stimare con buona precisione l'efficienza di rivelazione, per via dell'elevato background dovuto alla radioattività α, i dati ottenuti sono stati normalizzati a risultati di misure precedenti o alle sezioni d'urto tabulate in intervalli energetici opportunamente scelti. Per questo motivo, le sezioni d'urto fin qui ottenute sono ancora preliminari, e affetti da una incertezza superiore a quella richiesta per gli sviluppi di reattori di IV Generazione per la produzione di energia e per la trasmutazione delle scorie radioattive. Ciononostante, i risultati sugli attinidi minori presentati in questa tesi sono fra i migliori attualmente disponibili. È inoltre pensabile che un ulteriore raffinamento dell'analisi, ed eventualmente misure dedicate al problema della normalizzazione, permetteranno di migliorare l'accuratezza dei dati al livello richiesto dalle applicazioni nel campo dell'energia nucleare.

Preface

The subject of this thesis is the determination of high accuracy neutron-induced fission cross-sections of various isotopes - all of which radioactive - of interest for emerging nuclear technologies. The measurements had been performed at the CERN neutron time-of-flight facility n_TOF. In particular, in this work, fission cross-sections on ^{233}U, the main fissile isotope of the Th/U fuel cycle, and on the minor actinides ^{241}Am, ^{243}Am and ^{245}Cm, have been analyzed. Data on these isotopes are requested for the feasibility study of innovative nuclear systems (ADS and Generation IV reactors) currently being considered for energy production and radioactive waste transmutation.

The measurements have been performed with a high performance Fast Ionization Chamber (FIC), in conjunction with an innovative data acquisition system based on Flash-ADCs.

The first step in the analysis has been the reconstruction of the digitized signals, in order to extract the information required for the discrimination between fission fragments and the background, as well as for the determination of the neutron's energy from its time-of-flight.

Fission cross-sections for the various isotopes have been determined relative to the ^{235}U(n, f) reaction, which is considered a standard of measurement in a wide energy range. In order to minimize systematic uncertainties, this reaction has been measured with the same detector and at the same time of the reactions subject of this thesis.

A fundamental part of the thesis work has been the analysis of the ^{235}U(n, f) reaction, which has allowed to study the response of the fission chamber, thanks also to the use of detailed Monte Carlo simulations performed with state-of-the-art codes for neutron transport and interaction. Moreover, the analysis of the ^{235}U(n, f) reaction has allowed the energy calibration of the neutron beam, the determination of the incident neutron flux and an accurate estimate of the background.

In the present thesis the final results for the ^{233}U(n,f) cross-section are shown, as well as the preliminary results for the ^{241}Am(n,f), ^{243}Am(n,f) and ^{245}Cm(n,f) cross-sections. The characteristics of the n_TOF neutron beam have allowed to obtain results in a wide energy range, from about 30 meV to 1 MeV, in a single measurement. For the ^{233}U(n,f) case, the final uncertainties on the cross-section are slightly larger than 3%, a value required for the development of innovative nuclear systems. In order to reach such an accuracy, corrections for sample-dependent efficiencies, as well as for reaction-related dead-time effects, have been applied.

The thesis is organized as follows: Chapter 1 contains the motivations for the request of accurate fission cross-sections on actinides and on isotopes of interest for the Th/U fuel cycle. The main characteristics of the n_TOF facility, in particular those relevant to fission measurements, are presented in Chapter 2.

Chapter 3 contains a detailed description of the experimental apparatus used for the fission measurements. The study of the detector response, in particular in terms of detection efficiency and beam attenuation, is also presented.

In Chapter 4, the analysis procedure used for data reduction, starting from the signals reconstruction procedure, is presented. The results for the ^{235}U(n,f) and ^{238}U(n,f) reaction, typically used as reference for fission measurements, are presented and discussed.

Chapter 5 is dedicated to the determination of the ^{233}U(n,f) cross-section. In this chapter, the detailed procedures used for background minimization, subtraction and corrections of experimental effects (detection efficiency and dead-time), are described. The extracted cross-sections, characterized by a very high accuracy ($\sim$3%) in the entire energy range (from 30 meV to 1 MeV), are then compared with previous measurements and with cross-sections tabulated in evaluated data libraries. The comparison clearly shows the need to update the evaluations, in order to increase the reliability of the data required for the feasibility study and design of innovative nuclear systems based on the Th/U cycle.

Chapter 6 presents the results, in some cases still preliminary, of the ^{241}Am(n,f), ^{243}Am(n,f) and ^{245}Cm(n,f) reaction cross-sections. In this case, the very high background associated with the natural radioactivity of the samples and the contaminations from other isotopes, complicates the data analysis and results in an increased uncertainty on the extracted cross-sections. For the ^{243}Am(n,f) reaction it has been possible to obtain accurate cross-sections only above 350 keV. In the other two cases, on the contrary, cross-sections in the entire neutron energy range from 30 meV to 1 MeV, have been determined. Nevertheless, since it was not possible, in this work, to estimate with good accuracy the detection efficiency, due to the high background caused by the α radioactivity, the extracted cross-section has been normalized to the results of previous measurements or to tabulated cross-sections in conveniently chosen energy ranges. For this reason, the cross-sections obtained so far are still preliminary, and affected by an uncertainty higher than that required for the development of Generation IV reactors for energy production and nuclear waste transmutation. Nonetheless, the present results are among the best currently available. It is reasonable that additional refinements in the analysis procedures, and eventually measurements dedicated to the normalization problem, will allow to improve the accuracy of the data shown in this thesis, up to the point required by the applications in the field of nuclear energy.

Introduction

According to the International Atomic Energy Agency (IAEA) [1], at the beginning of 2009, 438 nuclear power plants are operating around the world, with a total net installed capacity of 371.569 GWe[1]; 5 are in long term shutdown and 44 are under construction, for a total net electrical capacity of 38 GWe, mainly in Eastern countries[2]; 34 of those are of the Pressurized Water Reactor (PWR) type, while the other ones share equally between Boiling Water Reactors (BWR), Fast Breeder Reactors (FBR), Light Water-cooled Graphite-moderated Reactors (LWGR) and Pressurized Heavy Water Reactors (PHWR) [1] (see § 1.1 for further description). During 2007 three new units (located in India, China and Romania), with a total net power of nearly 2 GWe, were connected to the grid.

The contribution of nuclear and other energy sources to the world primary energy and electricity supply in 2005 are shown in Fig. 1; nuclear energy contributes to the world electricity supply with about 16%, while it represents only a modest part of the total produced energy, due to the fact that this energy source is only used for electricity production, which constitutes only the 30% of the global energy needs. Clearly this is not the case everywhere: in France, for example, 39% of the total energy [2] and 78.1% of electricity [3] production comes from nuclear power.

Most of the world's energy is produced by combustion of fossil fuels, with a release of CO_2 and other pollutant gases - such as NOx or SOx - in the atmosphere. Such gases are considered among the main causes of the greenhouse effect, responsible for global warming and climate changes. Nuclear power is one of the possible options to mitigate this issue, mainly because it is already available on the market, it is essentially free from CO_2 emission during the energy production cycle (i.e. except in the milling phase) and it can be developed on a large scale. Moreover a further

---

[1] Gigawatt *electrical* is a term that refers to electric power, while Gigawatt *thermal* refers to the thermal power produced.

[2] With the most notable exception of Flamanville-3 reactor in France and Olkiluoto-3 in Finland, Europe.

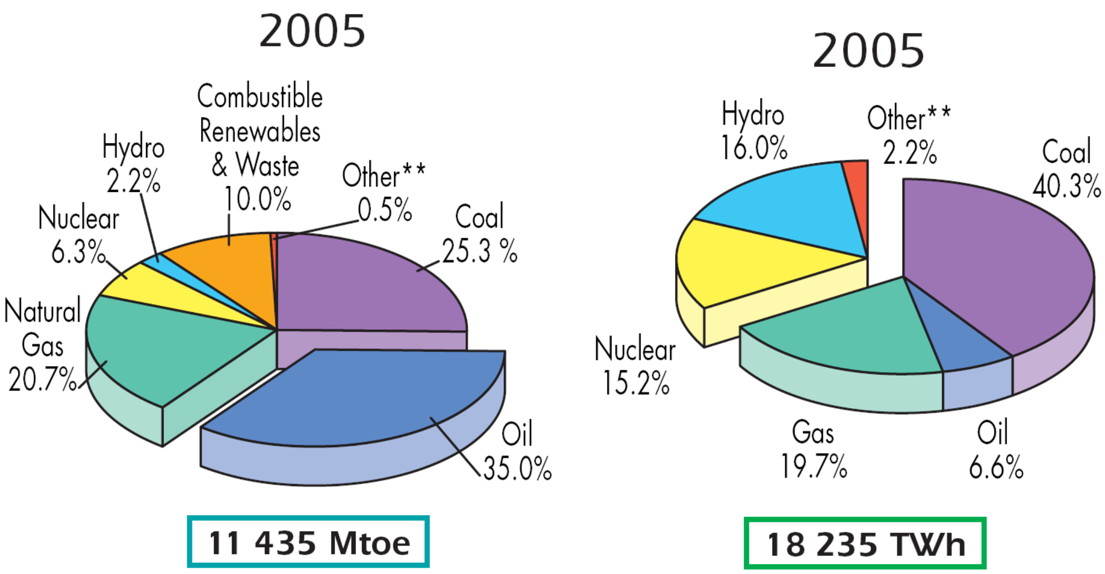

(a) Primary energy supply (b) Electricity supply

Figure 1 – Contribution of energy sources to the Total Primary Energy Supply (TPES) 1(a) and electricity supply 1(b) in 2005, as taken from International Energy Agency statistical data [4]. TPES are supplied as percentage of Million Ton Oil Equivalents (MTOE).

reduction in greenhouse emissions would be obtained if nuclear power plants could provide direct heat for home-heating and hydrogen generation [5].

According to Ref. [2], the present reserves of oil and gas allow, at present production rates, the use of those primary fuels for 41 and 64 years, respectively. This time span could be extended by an additional 50 yr taking also into account large reserves of coal, gas and oil in non-conventional forms. The main drawback of fossil fuels, however, are the production of CO_2 and other greenhouse agents and the increasing costs of the fuel, mostly related to the expanding energy demand, that cause a steady build up of energy generating costs.

Although renewable sources are gaining importance, their total share in the energy production is going to be, at least in the near future, marginal compared to other energy sources. Many hypothesis [2, 6] are envisaged, but all of them strictly depend on political choices and, as of now, can only be considered as projected estimations. The International Energy Agency (IEA) assumes that in 2030 - if all policies under discussion are going to be implemented - in OECD[3] European countries the contribution of renewables to the electricity generation will increase up to 22% [6]. It should be considered that renewable sources do not directly result in a reduction of CO_2 emission: in 2004 [6] - given a total contribution of renewable energy to the Total Primary Energy Supply (TPES) of 13.1%, 10.1% was produced

---

[3] Organization for Economic Co-operation and Development

with combustible renewables and renewable waste, while only 0.5% was CO_2-free, i.e. contribution from solar, geothermal, wind and tide power. The main problem of renewable energy production is the fact that they have a relatively low efficiency compared with nuclear and fossil sources and also a low specific energy (in the case of photovoltaic solar power plant, to obtain an annual energy production of 7 TWh, of the same order of a 1 GWe reactor, 26 km^2 would be needed [2]). Hydroelectric power resources have a significant share in existing renewable scenarios and also a good overall production potential, but their contribution in industrialized countries is very small; additionally hydroelectric plants have a significant impact, both from an environmental and social point of view. In the IEA "optimistic" scenario [6], it is foreseen that the electricity generated with this resource could increase only by a factor of two, mainly in developing countries, from a value of 2810 TWh to 4903 TWh, thus helping to reduce the use of fossil fuels.

Another issue of renewable sources is the link between their production possibilities and the base load electricity demand[4]: sun, wind, tides and waves cannot be controlled to directly provide either continuous base load power, or peak load power when it is needed[5], so requiring the use of other, controllable sources (the load factors[6] range between 10 and 25% for solar energy and between 15 and 45% for wind energy [7], while for coal and nuclear plant it is between 65 and 85%). A fuel backup solution would always be needed, to limit the impact of intermittent renewable energy generation, leading essentially to an increase in the cost of generated energy [8].

In conclusion, while fossil fuels are not capable of sustain the world's increasing energy demand, renewables (including hydropower) do not represent a full scale replacement, capable of substituting fossil fuels in the medium term. As a consequence, it is highly probable that nuclear power may play a major role in the future in industrialized and especially in developing countries, in which the demand of energy is growing at a higher rate. Clearly the issue of the fuel cycle is the most critical one in the context of social acceptance of nuclear energy, and it is of major concern if nuclear power is going to constitute a consistent part of the future electricity generation mix.

The main problems in the further development of nuclear energy programs around the world are essentially:

- The production of large quantities of waste. In particular the main issue regards

---

[4] A base load power plant is a generating station that provides a steady flow of power regardless of total power demanded by the electrical grid.

[5] Peak load plant generally run only when there is a high demand.

[6] The load factor of an energy producing system is the ratio between the net amount of electricity generated by a power plant and the net amount which it could have generated if it were operating at its net output capacity.

the production of long-lived radioactive isotopes. Although their volume is very limited, the associated radiotoxicity is a major long-term concern for the disposal of such waste (see § 1.1.2).

- The possible diversion of nuclear technology and especially the use of nuclear material for military and/or other purposes.
- Public concern regarding the risks associated with the operation of critical nuclear plants. These concerns have increased after the major accidents of Chernobyl (former Soviet Union) in 1986 and the core accident at Three Mile Island (USA) in 1979.

If nuclear energy is going to play a significant role in the world's energy future, these issues must be faced. In light of these concerns, the international community is now considering innovative nuclear systems for the future [5], with choices based on some important parameter such as waste minimization, sustainability, safety, economy and non-proliferation. Some of these systems also include the possibility of acting as transmuters of transuranic elements (mostly plutonium, americium, neptunium and curium isotopes) (see § 1.1.4). The optimization of these systems relies on advances in many different fields, among which new materials for fuels and fuel treatment and new development in the field of reactor and basic nuclear physics.

Connected with this last point, the role of basic nuclear data is essential and its contribution significant. The majority of nuclear data are available in evaluated libraries and in vast experimental databases, but most of them lack to date the needed accuracy, and are limited in energy range, while their validation represents still a significant problem [9, 10, 11, 12, 13].

Chapter 1

Nuclear energy and nuclear data

In this section, a brief introduction to nuclear power and to nuclear waste and fuel cycle issues will be given. Then, in the context of the new energy producing system, currently in the R&D phase, the role of nuclear data will be emphasized, in particular for the promising Th/U cycle and for transmutation of nuclear waste in advanced systems, such as ADS and Generation-IV critical reactors.

1.1 Nuclear reactors

The idea of a sustained neutron chain reaction came in the 30s as a consequence of the observation that a nuclear fission event produces two or more neutrons. In order to sustain a fission chain reaction, one or more of the neutron produced in the fission event must, on average, survive to produce another fission event. Such a chain reaction can be quantitatively described by the effective multiplication factor k_{eff}, defined as the ratio of the number of fissions in one generation divided by the number of fissions in the preceding generation. The critical condition - the steady state situation of a power producing reactor - is reached when $k_{eff} = 1$, that is when one neutron, in average, induces another fission, and the neutron population in the system is constant. The subcriticality ($k_{eff} < 1$) and criticality ($k_{eff} > 1$) condition are only used (for standard[1] reactor system) in transitories between steady states. Clearly k_{eff} is strongly affected by the composition of the fuel, that is by the relative number of nuclides of the different species that are present, by the neutron energy distribution and by the geometric configuration of the fuel and of the moderator.

In a simple picture this is expressed by the four-factor formula [14]:

$$k_{eff} \equiv \eta f \epsilon p P_{NL} \equiv k_{\infty} P_{NL}$$

---

[1] In § 1.1.5 it will be shown that the subcritical mode is a major advantage of ADS systems.

Here $\eta = \nu \frac{\sigma_f}{\sigma_f + \sigma_\gamma}$ is the number of fission neutrons per neutron absorbed in the fuel, f is the fraction of the absorbed neutrons which are absorbed in the fissile nuclides (called also thermal utilization factor), ϵ is the fast fission factor, p is the resonance escape probability (probability that a neutron is not captured during the slowing down process) and P_{NL} the non-leakage probability (defined as equal to 1 for an ideally infinite multiplication assembly). The isotope ^{235}U, present in natural uranium with a percentage of 0.7204%, is the only fissile isotope present in nature. Even if some reactor types can work with natural uranium fuel, enrichment[2] is usually used to achieve a higher fissile content (a bigger value of f) and thus increasing the multiplication constant (the most common enrichment for light water reactors is of the order of 2-3%). The most favorable region for fission is the thermal one: at 0.0253 eV the ratio between fission cross-section of ^{235}U and the capture cross-section of ^{238}U is $\simeq$200. It is possible to demonstrate that in this region a chain reaction can be sustained under proper condition of fuel composition and fuel geometry [16, 15, 14]. In the so-called thermal reactors (the most common type nowadays), the neutron energy is reduced from the MeV region, in which they are produced by fission events, to the thermal energy by the moderation process, i.e. elastic collisions with low-mass nuclei and inelastic collisions on uranium.

An important parameter in reactor physics is the ratio of the capture cross-section to the fission cross-section of a given isotope, since the most important neutron reactions that can occur in the reactor fuel are fission and capture. This ratio, commonly indicated by α, is defined as:

$$\alpha\left(E_n\right) = \frac{\sigma_\gamma\left(E_n\right)}{\sigma_f\left(E_n\right)}$$

The convolution of this parameter for all isotopes contained in the reactor fuel is a key parameter for assessing the neutron economy of a nuclear reactor core. Another important parameter is the conversion (or breeding) ratio, defined as the ratio between the rate of production of fissile nuclei to the rate of their destruction at any given time. The conversion ratio generally varies during reactor operation, so that the net conversion ratio must be calculated by integrating it over the operating life of the reactor. In the case of U-fuelled thermal reactor, the initial conversion ratio (that is before ^{239}Pu build up) is defined as:

$$C = \frac{N(^{238}\mathrm{U}(n,\gamma))}{N(^{235}\mathrm{U}(n,f)) + N(^{235}\mathrm{U}(n,\gamma))}$$

Here $N(^{238}\mathrm{U}(n,\gamma))$ is the number of capture events in ^{238}U producing ^{239}Pu, and $N(^{235}\mathrm{U}(n,\gamma))$+$N(^{235}\mathrm{U}(n,f))$ the number of absorption events in ^{235}U, "destroying" it

---

[2] Increase the concentration of ^{235}U over the natural value. See for example [15].

via (n, f) or (n, γ) reactions.

From a purely physical point of view, the main difference between various reactor types comes from the difference in the neutron energy distribution (that is the neutron spectrum), which determines differences in the reaction rates[3]. The first classification is between thermal reactors and fast reactors. Fast reactors rely on a chain reaction in which neutrons are not thermalized, and induce fission at relatively high energies; in the case of the U/Pu cycle, ^{239}Pu is the fissile fuel (both consumed and produced in the reactor) while ^{238}U is the fertile material. Due to inelastic collisions, a significant fraction of the neutron spectrum is in the energy range 1 keV - 1 MeV (thus justifying the importance of nuclear data in this energy region). In the upper part of the neutron energy spectrum, conditions for breeding are optimal due to the fact that neutron-induced fission of ^{239}Pu dominates ($\alpha \simeq$0.03), with a large cross-section of the order of 1 barn. Since η is close to 3 at 1 MeV, a breeding ratio greater than 1 (if desired) can be easily reached. A prominent example of an operating fast power reactor is the liquid-metal reactor (LMR) such as the 250 MWe reactor PHENIX and the now closed 1200 MWe SUPERPHENIX in France, both cooled with liquid sodium. It is worth noticing that the majority of fast reactors are fast breeder reactors (LMFBR - Liquid Metal Fast Breeder Reactor), since the breeding ratio is greater than 1 ($C \geq$1); as a consequence, more fissionable material is produced than consumed.

The neutron spectrum in a reactor is defined essentially by the moderator material, which very often is coincident with the coolant. The majority of electricity producing reactors use light water, either pressurized (PWR) or boiling (BWR). Currently operating Pressurized Water Reactors are generation II reactors that use ordinary water at high pressure (superheated water) both as coolant and neutron moderator; the primary coolant loop is kept under high pressure to prevent water from boiling when flowing in the reactor core. On the contrary, Boiling Water Reactors are characterized by two-phase mixed fluid flow (water and steam) in the upper part of the reactor core. Another widespread reactor is the pressurized heavy water reactor (PHWR) which uses D_2O as coolant[4]. The neutron spectrum in both designs is thermal, due to the good moderating properties of hydrogen. A gas can be used as a coolant for fast reactors, as well as for thermal ones, if a moderator such as graphite is employed. Of this type are the advanced gas reactors (AGR), cooled with CO_2 and the high-temperature gas cooled reactors (HTGR), cooled with He. More advanced reactor types, programmed for the 4th generation, are introduced in § 1.1.6 and are more thoroughly described in Ref. [5]

---

[3] Assuming an heterogeneous assembly, in which fuel, coolant and moderator (if present) are physically separated, which is the case for all present operating reactors.

[4] Commonly used in countries with no enrichment capability, since natural uranium can be used (see for example Ref. [16]).

1.1.1 Proliferation risks

Proliferation resistance and physical protection of facilities and materials used in the nuclear energy chain for electricity generation are a major concern for a sustainable exploitation of this energy source. Since the early 50s, the fear of diversion of civil nuclear material towards military use has always been present. This concern is a peculiar characteristics of nuclear energy and has motivated the implementation of measures to avoid that sensitive materials, such as enriched uranium and plutonium, or technologies, such as enrichment or reprocessing, developed for civilian purposes, could be diverted for military and/or terrorist use. Enhancing proliferation resistance and physical protection are essential goals for advanced nuclear energy systems. From a technical point of view, the abundance of plutonium in conventional nuclear waste (even if of reactor-grade purity [17]) could be a source of future nuclear weapons proliferation; additionally the presence of ^{243}Am could contribute to long term production of ^{239}Pu via α-decay and subsequent β-decay.

1.1.2 The issue of nuclear waste

The operation of nuclear reactors generates a significant amount of radioactive material, both as spent fuel or irradiated materials, that has to be handled and safely disposed (see Table 1.1). This is the major drawback of the currently operating nuclear energy systems. Generally speaking the definition of nuclear waste include all material that comes as radioactive residues produced during operation in all field of industry and medicine. The most dangerous waste are the spent fuel and reprocessed materials from commercial nuclear power reactors and plutonium-producing reactors. Waste from commercial reactors represents a critical issue, mainly because the production is continuous and the amount is large. Its composition depend on many factors, such as the fuel burn-up, the reactor type or the starting composition of the fresh fuel. Nuclear waste is normally divided into three classes[5]: high level waste (HLW), low level waste (LLW), and a separate category of transuranic waste (TRU). Among this last category, a special case is played by minor actinides (MA), i.e. neptunium, americium and curium isotopes. High-level waste are composed by highly radioactive fission and neutron-capture byproducts of the nuclear fuel cycle. They may be in the form of either spent fuel or liquid and solid products from the post-irradiation reprocessing of fuel, and the major component are long-lived fission fragments (LLFF). Low-level waste are composed by activated machine parts, structural materials and various protective clothings. TRU is waste that does not

---

[5] This is not always true, see for example Ref. [3].

qualify as a HLW but that contains more than 0.1μCi of long-lived ($t_{1/2}$ $\geq$20 yr) transuranic α-particle emitters per gram of material [15]. TRUs are responsible for most of the long-term radiotoxicity, due both to their abundance in the waste and their long half-lives; fission is the most effective way to eliminate this type of waste, preventing further production of actinides.

Table 1.1 – Material inventory of a 1 GWe PWR reactor at loading and at discharge (1 yr) assuming a burn-up value of 33 GWd/tHM (see text for the definition). Values taken from Ref. [2].

	Initial loading (mass in kg)	After discharge (mass in kg)
^{235}U	954	200
^{236}U		111
^{238}U	26328	25655
total U	27282	26047
^{239}Pu		156
total Pu		266
MAs[a]		20
^{90}Sr		13
^{137}Cs		30
LLFFs		63
total FFs		946
total mass	27282	27279

[a] The France yearly production of different minor actinides isotopes is as follows: 500 kg for ^{237}Np ($t_{1/2}$ $\simeq$2.1$\times$10^{6} yr), 250 kg for ^{241}Am ($t_{1/2}$ $\simeq$432 yr), 100 kg for ^{243}Am ($t_{1/2}$ $\simeq$7370 yr), 25 kg for ^{244}Cm ($t_{1/2}$ $\simeq$ 18.1 yr) and 1.5 kg for ^{245}Cm ($t_{1/2}$ $\simeq$8500 yr)

The radiotoxic inventory of a given radionuclide can be related to the Annual Limit of Intake (ALI), defined as the amount of radioactive material that an adult worker can absorb taken into the body by inhalation or ingestion in a year, without exceeding the annual dose [18]. This parameter is useful to define the so-called Potential Hazard Index of a given radionuclide, defined as the ratio of the amount of a given nuclide to its respective ALI value; figure 1.1 shows the potential hazard over 10^{7}yr of the HLW present in 1 ton of spent fuel from a PWR (burn-up of 33 GWd/tHM[6] with uranium and 99.5% of the plutonium recycle) and the level of radiological hazard of the 5 tonnes of natural uranium needed to produce 1 metric tonne of fresh fuel. For the first hundred years the activity is dominated by the short and medium-lived fission fragments, particularly ^{90}Sr and ^{137}Cs (assuming that

---

[6] The burn-up is defined as the amount of energy, usually expressed in terms of MWd, per unit mass of fuel, considering only heavy metal (HM: only U, Pu, etc, without the oxide and structural material of fuel rods and elements).

plutonium is essentially removed from the waste); these two isotopes and those of iodine are of particular concern. As an example, strontium behaves chemically like calcium and thus, if inhaled, is deposited in bone tissues, while iodine is concentrated in the thyroid gland, where it could induce tumors. Between 10^2 yr and 10^4 yr the main contribution comes from americium isotopes, while later the activity is dominated by ^{237}Np due to its longer lifetime and its production from the decay of ^{241}Am. As clearly seen, the potential hazard of LLFFs is orders of magnitude smaller than that of the MAs, but since confinement of these species is much more difficult to obtain, the high mobility of LLFFs in the biosphere increases their potential danger.

1.1.3 Th/U fuel cycle

In the course of the nuclear industry development, other fuel cycles in addition to the well exploited U/Pu cycle have been investigated.

In the thorium cycle shown in Fig. 1.2, the fissile element ^{233}U is produced starting from the fertile ^{232}Th isotope, similarly to the breeding process of the fertile ^{238}U to the fissile ^{239}Pu in fast breeder reactors or graphite moderated thermal reactors. The following reactions are at the basis of the Th/U fuel cycle:

$$^{232}\mathrm{Th}(n,\gamma)^{233}\mathrm{Th} \xrightarrow{\beta^-,\, t_{1/2}\sim 22\,\mathrm{m}} (^{233}\mathrm{Pa}) \xrightarrow{\beta^-,\, t_{1/2}\sim 27\,\mathrm{d}} (^{233}\mathrm{U}) \tag{1.1}$$

Thorium is 3 to 4 times more abundant than uranium in the earth crust and is widely distributed in nature as an easy mining resource in many countries. Unlike the case of the natural uranium, which contains $\sim$0.7% of the fissile ^{235}U isotope, natural thorium does not contain any fissile material and is constituted by the fertile ^{232}Th isotope only. For this reason, thorium and thorium-based fuel in the form of metal, oxide or carbide, has been used in conjunction with fissile ^{235}U or ^{239}Pu in nuclear research and power reactors for conversion of ^{232}Th to the fissile ^{233}U, thereby increasing the amount of available fissile resources. As will be shown later in the paragraph, ^{233}U is by far the best fissile isotope for thermal neutron spectrum and can be used for breeding in both thermal and fast reactors. During the developing years of nuclear energy, from the 1950s to the 1970s, there was considerable interest worldwide to develop the thorium fuel cycle, in order to increase the amount of fissile reserves, in addition to ^{235}U. This interest decreased in later years, due to the discovery of new uranium reserves and increased efficiency in the use of nuclear fuel. Nevertheless many different reactors have operated with the Th/U cycle: the most notable examples have been the Shippingport reactor is USA, the HTGR of Fort St.

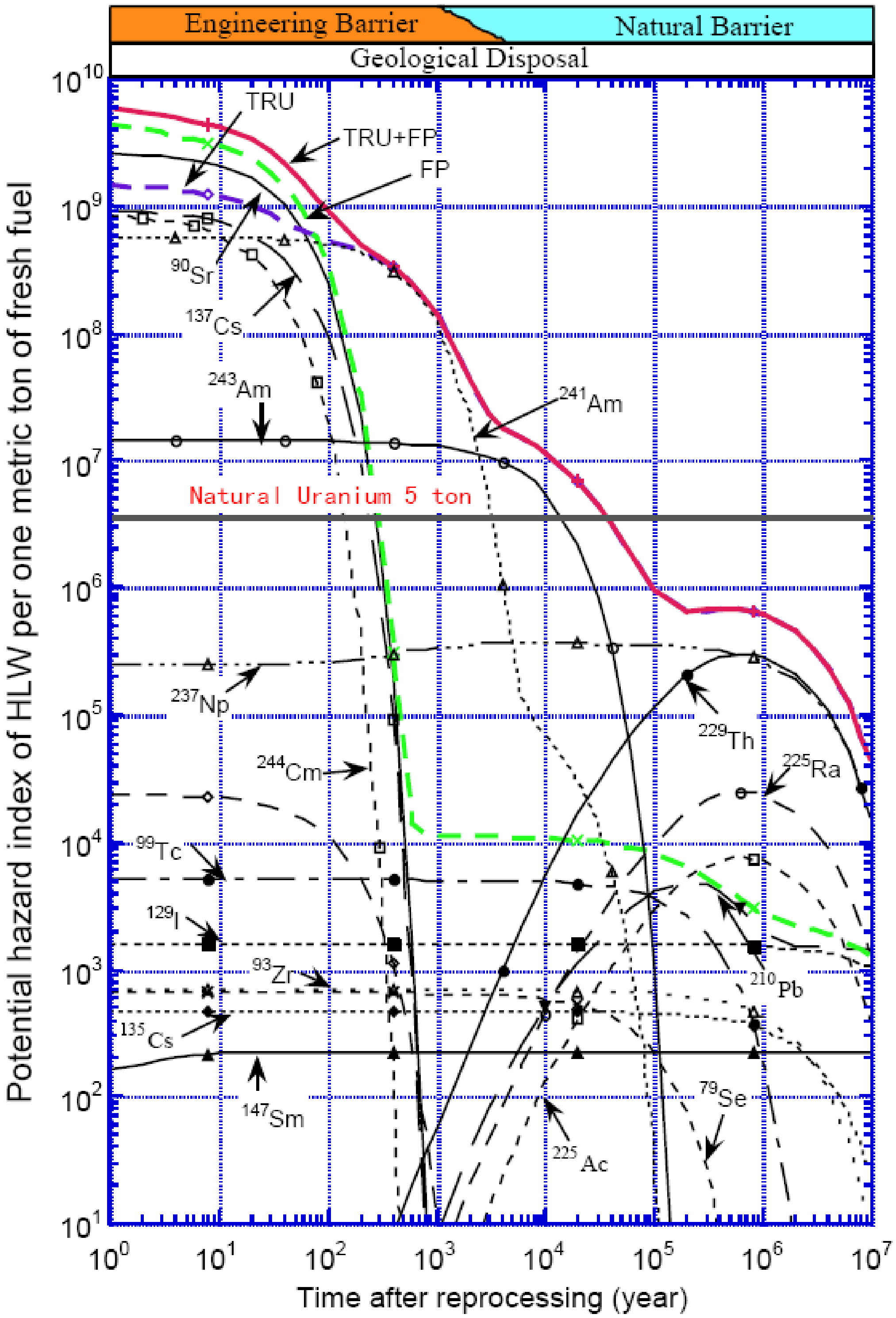

Figure 1.1 – Potential Hazard Index of the HLW from PWR spent fuel as a function of time. The mark at 1000 yr is the limit where engineering barriers could start to fail and one has to rely on natural barriers. Figure from Ref. [19].

Vrain. USA and[7] the THTR reactor in Germany [20]. Recently, a renewed interest in thorium-based fuels has arisen again in several developed countries due to the need to find new, proliferation resistant, longer fuel cycles, with higher burn-up and improved waste characteristics.

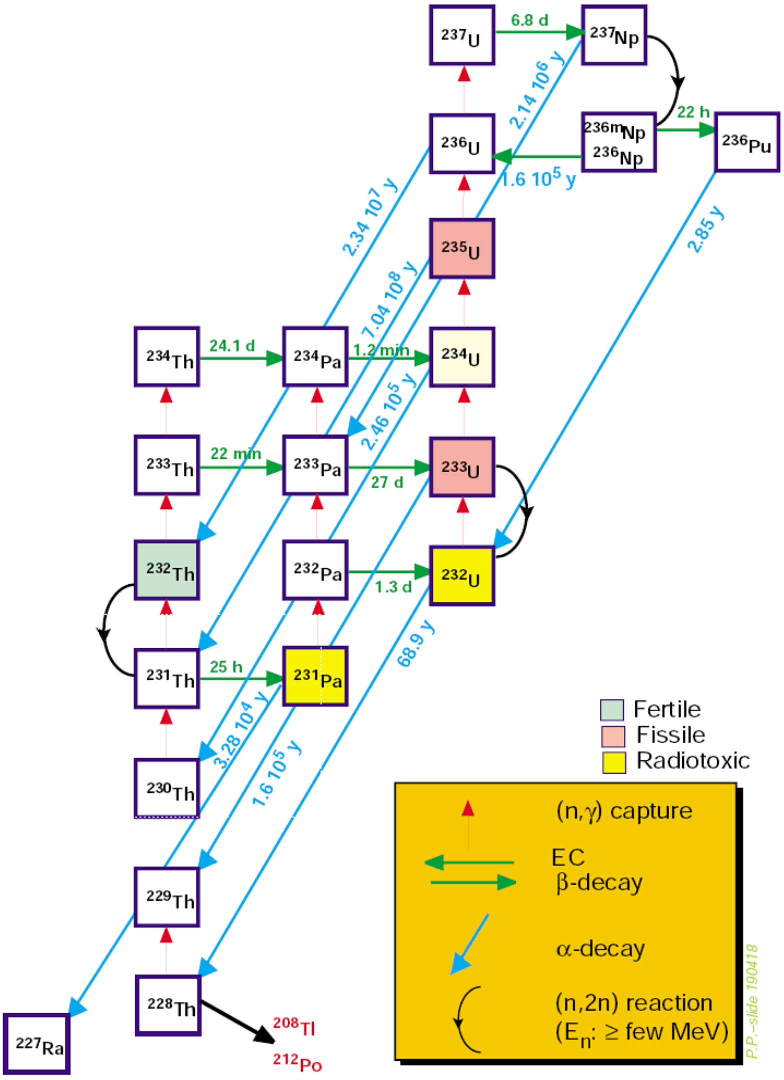

Figure 1.2 – Schematic view of the Th/U cycle with the various isotopes involved [21].

As far as the nuclear qualities of the material are concerned, ^{232}Th is a better fertile material than ^{238}U in thermal reactors because of the higher value of the thermal capture cross-section of ^{232}Th (7.4 b) as compared to ^{238}U (2.7 b). The conversion of ^{232}Th to ^{233}U is therefore more efficient than that of ^{238}U to ^{239}Pu for a thermal neutron spectrum. Another interesting aspect is related to the number of neutrons emitted per absorbed neutron (the η parameter described before). For the fissile

---

[7] India is nowadays using ThO_2 pellets in its PHWR reactors for neutron flux flattening of the initial core after start-up.

^{233}U isotope the value of η is above 2 over a wide neutron energy range, contrary to the ^{235}U and ^{239}Pu case. Thus the Th/U fuel cycle is less sensitive to the type of reactor, being it thermal or fast. The capture cross-section of ^{233}U is much smaller (46 b) than that of ^{235}U (101 b) and ^{239}Pu (271 b) for thermal neutrons, while the fission cross-section is similar for all three fissile isotopes (525 b, 577 b and 742 b for ^{233}U, ^{235}U and ^{239}Pu respectively). As a consequence, a smaller amount of higher mass material is produced in the Th/U fuel cycle with respect to the U/Pu cycle, for the same energy produced. Finally, the η parameter for ^{233}U is significantly higher than for ^{235}U (2.296 for ^{233}U as compared to 2.075 for ^{235}U), so that a larger fraction of neutrons is available for breeding.[8]

The Th/U fuel cycle could play also a role in reducing the amount of high level transuranic waste, since much smaller amounts of plutonium and long lived minor actinides are produced as compared to the U/Pu fuel cycle, therefore minimizing radiotoxicity and decay heat issues. Additionally the higher chemical and radiation stability of the ThO_2 with respect to the UO_2 allows[9] also the direct disposal of this kind of fuel in permanent repositories [20].

All these features make the Th/U fuel cycle appealing for energy production in many countries, especially those without uranium enrichment capabilities. Among them, India is particularly interested in this cycle, because of its large resources of thorium. A thorium (thermal) breeder reactor (ATBR) is in an advanced stage of design [22]: it is based on thin seed fuel rods (composed by PuO_2-ThO_2 MOX), with high plutonium content in order to produce large neutron fluxes able to breed fertile thorium material at a rate sufficient to compensate for the fissile depletion rate.

1.1.3.1 Proliferation resistance

Apart from international safeguards procedures, the most important barrier to proliferation should be definitively based on inherent passive properties of the fuel cycle itself; fuel cycles based on the Th/U cycle have intrinsic proliferation resistance due to the production of ^{232}U by means of inelastic $(n, 2n)$ reactions[10] on ^{232}Th, and by neutron capture on ^{230}Th (both reactions produce ^{231}Th, which then proceeds through the chain $^{231}\mathrm{Th} \xrightarrow{\beta} {}^{231}\mathrm{Pa} \xrightarrow{(n,\gamma)} {}^{232}\mathrm{Pa} \xrightarrow{\beta} {}^{232}\mathrm{U}$).

The half-life of ^{232}U is 68.9 yr and the daughter products have very short half lives; some, like ^{212}Bi and ^{208}Tl, emit strong gamma radiations, with energies of the

---

[8] This is not possible for ^{235}U-fueled reactors: since η =2.075, if breeding condition is required, 1 neutron should be necessary for sustaining the chain reaction, 1 for ^{239}Pu production, leaving for the absorption in the moderator and in reactor structure only 0.08 neutrons, a value clearly insufficient. Therefore a ^{235}U-fueled thermal breeder is not feasible.

[9] ThO_2 is relatively inert and does not oxidize like UO_2 does to U_3O_8 and UO_3.

[10] For neutron energies greater than 6 MeV due to the reaction threshold.

order of MeV, which makes very difficult the handling of the material for preparation of nuclear weapons. This is of advantage in burning weapon-grade or reactor-grade plutonium in fast reactors using once-through cycle and (Th-Pu)O_2 fuel as compared to a (U-Pu)O_2 one; in the thorium fuel matrix, indeed plutonium cannot be produced by breeding (due to the reduced mass of the U isotope) and it can only be burned as a fissile nucleus. Additionally the ^{232}U isotope is produced, therefore ensuring physical proliferation resistance due to the energetic gamma rays.

1.1.3.2 Problems of the Th/U cycle

Several challenges have to be faced before industrial exploitation of the thorium fuel cycle. Apart for the the mentioned presence of the short-lived ^{232}U, which complicates the post-irradiation reprocessing and treatment of the nuclear fuel, there are still some technological unsolved issues:

- in the conversion chain of fertile ^{232}Th to fissile ^{233}U, the isotope ^{233}Pa is formed in the intermediate step. This isotope has a longer half-life ($t_{1/2}$ $\simeq$26.96 d) as compared to ^{239}Np ($t_{1/2}$ $\simeq$2.35 d) which has the same role in the U/Pu cycle. Hence longer cooling times are required for completing the decay of ^{233}Pa to ^{233}U;

- although under intense study, the reprocessing technology has yet to be fully developed (see Ref. [23]);

- the experience accumulated over the years on the thorium fuel cycle is very limited as compared with the U/Pu one, and has to be enhanced before full-scale development of this technology.

- the presence of ^{232}U has to be minimized, for example by keeping the thorium breeding blanket in a reactor region where it is only exposed to a well moderated neutron flux. It is also necessary to minimize the concentration of ^{230}Th in natural thorium.

Regarding these points, a major issue is the lack of accurate nuclear data for the isotopes involved in the Th/U cycle: the experimental data is rather incomplete and mostly based on theoretical models and nuclear systematics [24]. It is worth noticing that the nuclear data related to the Th/U fuel cycle isotopes (^{230}Th, ^{232}Th, ^{231}Pa, ^{233}Pa, ^{232}U, ^{233}U, ^{234}U and ^{236}U) did not received sufficient attention in the past, since data requests were mostly for nuclei related to the U/Pu cycle. A large part of the available experimental data have been generated and evaluated in the early 70s and mid 80s and do not fullfill the current accuracy requirements; moreover (except in some cases) the quality of the data is poor and limited in energy in comparison to the comprehensive data produced for the U/Pu isotopes (see § 1.2.4). An effort is therefore necessary to collect the required data with sufficient accuracy. The present thesis is part of such effort.

1.1.4 Transmutation of nuclear waste

As previously mentioned the long-term hazard of nuclear waste comes from a limited number of radionuclides (less than 1% in weight, namely 300 kg/GWe/yr), with half-lives ranging from 10^2 yr to 10^5 yr. At present the only available option is the disposal of these radionuclides in geological repositories. However, the exposure of these isotopes to high fluxes of fast neutrons, produced by a nuclear reactor or by an accelerator (via spallation), could transmute them into nuclides with much shorter (or longer) half-life or to stable nuclei, so that the long-term radiotoxicity could be reduced by a large factor. Although the residual waste would still need to be placed in a geological repository, the problem of finding a suitable repository would be radically downsized (see Fig. 1.3) [25]. The nuclear reactions that can be exploited for waste disposal are essentially of two types:

Transmutation , in which a radioactive isotope is finally transformed into a stable one by means of neutron capture (n, γ) reactions. This method is suitable for LLFFs (such as ^{99}Tc and ^{129}I).

Incineration , in which neutron-induced fission reactions allows the reduction of transuranic elements. This method is physically always accompanied by neutron and energy emission. Some of the plutonium inventory, in France and Japan, is already industrially treated in this way, by using MOX-fuelled reactors.

The first step in the transmutation procedure is the separation of materials into different waste streams; this procedure is today well developed in countries like France and England, and it is used to retrieve plutonium for recycling in other reactors. This technology is adapted from the one that was used to extract plutonium for nuclear weapons.

After extraction, the radionuclides would be exposed to high neutron fluxes. A typical example of the transmutation process is made for ^{99}Tc, which has a very long half-life of $t_{1/2} \simeq 2.11 \times 10^5$ yr, and that can be destroyed by neutron capture. The resulting ^{100}Tc quickly ($t_{1/2} \simeq 16$ s) decays via β emission to the stable ^{100}Rb isotope. The removal of Rb isotopes is not critical, since further neutron capture lead to other stable Rb isotopes. Also ^{129}I ($t_{1/2} \simeq 15.7 \times 10^6$ yr) can be transmuted to stable Xe isotopes via a similar process.

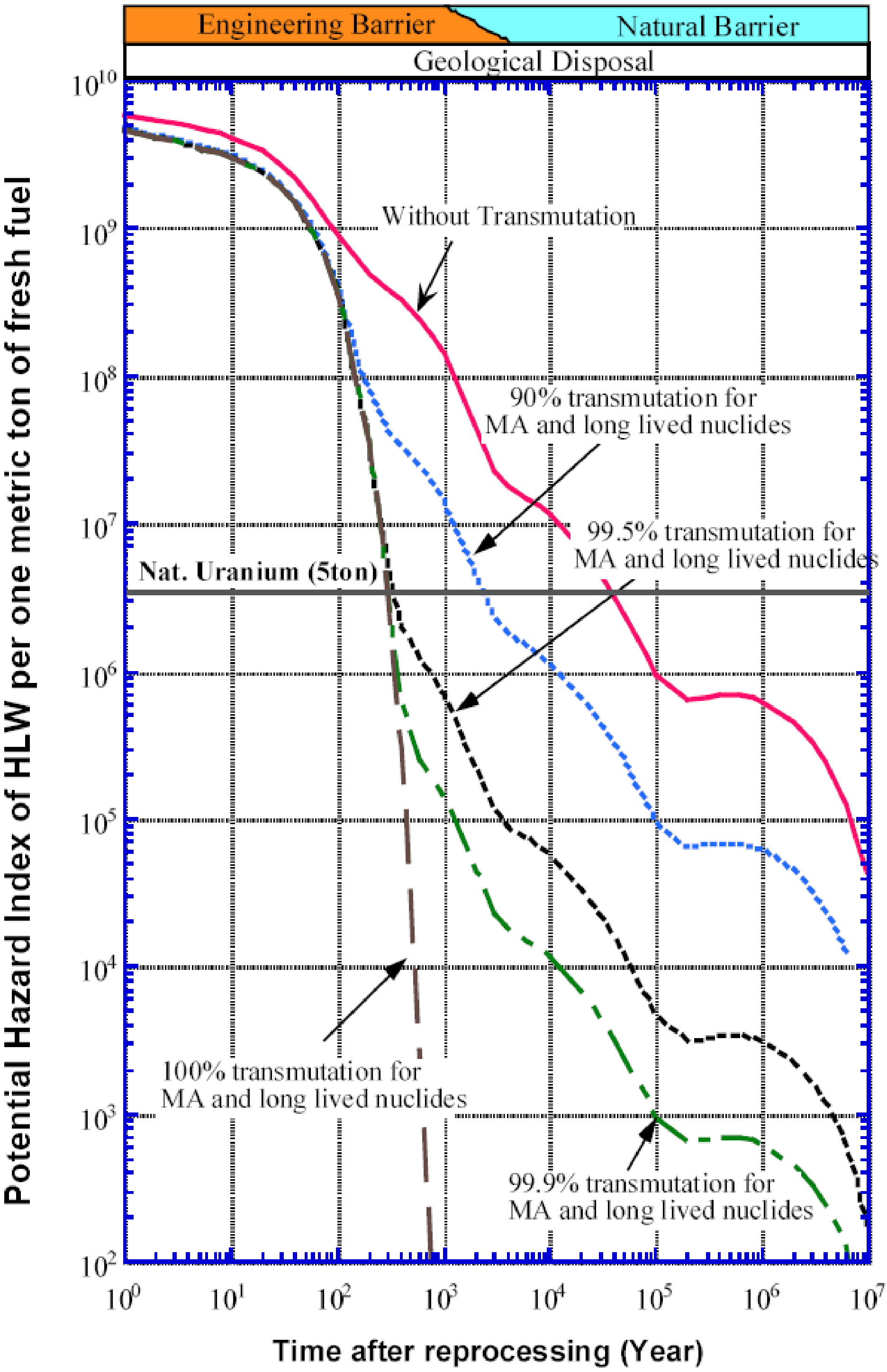

Figure 1.3 – Evolution of the Potential Hazard Index before and after transmutation of High Level Waste. Figure from Ref. [19].

A major advantage of separation and transmutation technologies could be the reduction of the actinide abundances: in this case the situation is more complex since there is competition between fission - which eliminates actinides - and capture, which transmutes them into heavier actinides. An example is the case of ^{239}Pu ($t_{1/2} \simeq$24110 yr), destroyed in neutron-induced fission or transformed to ^{240}Pu ($t_{1/2} \simeq$6564 yr) via neutron capture. The fission-to-capture ratio depends on the neutron energy spectrum, being generally higher for fast neutrons than for thermal ones.

Fig. 1.3 shows the evolution of the radiotoxicity of the nuclear waste for different scenarios of high level waste elimination. Without any waste transmutation, the radiotoxicity of MAs and LLFFs decreases to the level of natural radioactivity of 5 tons of uranium after $\simeq$40000 yr. If the level of MAs and LLFFs in the fuel is reduced to 90%, 99.5% and 99.9%, the radiotoxicity would decrease to the target level after, respectively, 2500 yr, 400 yr and 300 yr. Clearly the timescale of the necessary confinement and the requirements for their storage would be drastically reduced.

The question arises on the type of reactor or device that would be most suited for transmutation purposes. For plutonium, the stabilization of the inventory of the ^{239}Pu isotope, and even its slow decrease, should be possible with the existing nuclear energy systems (i.e. LWR) [2]. MAs show low fission cross-sections at thermal energies and also low fission-to-capture ratios for thermal neutrons (Fig. 1.4 shows the ratio as a function of the energy of the incident neutron). This has the

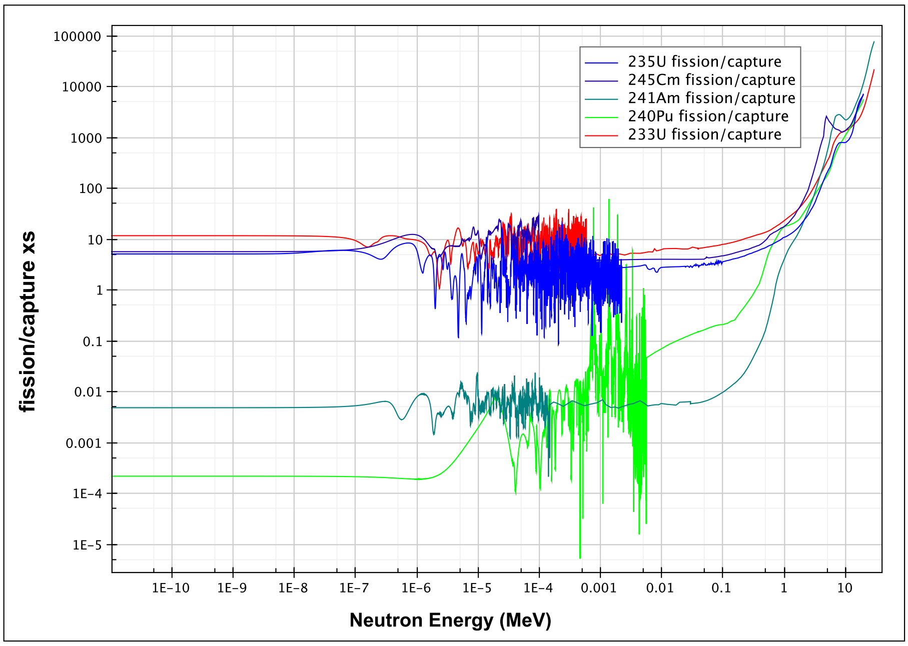

Figure 1.4 – Comparison of the ratio between the fission and capture cross-section for some isotopes considered in transmutation scenarios (^{240}Pu, ^{241}Am and ^{245}Cm). The ^{235}U and ^{233}U are taken as a reference fissile material.

consequence of degrading the neutron economy of the reactor and leads to a even larger buildup of TRUs (the most efficient plutonium thermal incinerators are, at the same time, efficient producers of minor actinides, as clearly seen from Table 1.2). Since the fission-to-capture ratio increases drastically for neutron energies above ∼100 keV for all actinides - including the fissile ones, the transmutation of MA requires necessarily fast reactors (see Table. 1.3).

Table 1.2 – Production of Pu and MAs in thermal reactors using different fuel cycles [2].

	Burn-up (GWd/ton)	Pu production (kg/8 TWh$_e$)	MA production (kg/8 TWh$_e$)
UOx open cycle	55	208	30.4
MOX[a] single recycle	55	-427.2	152
CORAIL[b] (7th cycle)	45	0	70.4
APA[c] (4th cycle)	90	-563.2	128

---

[a] Mixed OXide fuel, blend of oxides of plutonium and natural uranium, which behaves similarly to the low enriched uranium fuel (LEU) used in the light water reactors.

[b] UOx and PuOx rods are placed within the same fuel assembly.

[c] UOx and Pu are heterogeneously arranged on inert fuel matrices.

Table 1.3 – Neutron consumption (normalized to one fission event) in the incineration of selected actinides in the case of Light Water Reactors (LWR) and Fast Breeder Reactors (FBR) [10]. Negative values correspond to a net production of neutrons. The use of a fast spectrum allows in all cases to incinerate minor actinides (because of the neutron balance), whereas in a thermal reactor, the neutron surplus is not always sufficient [10, 2].

Nuclide	Thermal spectrum $\phi = 10^{14}$ n/cm^{2}s	Fast spectrum $\phi = 10^{15}$ n/cm^{2}s
^{237}Np	1.12	-0.59
^{240}Pu	0.44	-0.96
^{241}Am	1.12	-0.62
^{243}Am	0.82	-2.51
^{244}Cm	-0.15	-1.39
^{245}Cm	-1.48	-2.51

Fast reactors could be then used to close the fuel cycle, increasing the probability of reducing MAs by fission while minimizing their production (by capture). The problem of using MAs in fast systems resides essentially on safety, because in this type of nuclear systems, the reactor period - or equivalently the prompt neutron lifetime - tends to be shorter, since the fraction of delayed neutrons emitted after fission of MAs is lower than that of ^{235}U or ^{238}U (see for example Ref. [26]). This would further reduce the reactivity margin with significant implications for the safe operation of the system. Additionally, fuel containing TRUs hardly present negative feedbacks due to Doppler broadening in capture resonances[11], further degrading the safety parameters.

A solution for MAs incineration would be the implementation of subcritical accelerator-driven systems (ADS), i.e. with the direct use of high-energy, spallation neutrons for transmutation purposes.

1.1.5 Accelerator Driven Systems (ADS)

The concept of Accelerator Driven Systems (ADS) refers to a device obtained by combining a subcritical (i.e. non-self-sustained mode, with $k_{eff} < 1$) nuclear reactor core with a particle accelerator. Most of the proposals assume proton accelerators, delivering continuous-wave beams with an energy around 1 GeV. The accelerator could be either a linear accelerator (LINAC) or a cyclotron. In such a system the steady state operation defined by $k_{eff} = 1$ is obtained by producing neutrons with an external source, rather than through a self-sustaining chain reaction, as in conventional nuclear reactors. External neutrons are produced as the result of the nuclear cascades initiated by the protons inside a spallation target. A subcritical blanket of fissionable material is placed around the spallation target, so to produce energy (and additional neutrons). The dynamical behavior of the system is subject to the accelerator operation and the total thermal power is directly proportional to the proton current, giving an external control system for the kinetics of the sub-critical core. In the context of transmutation, the possibility to operate a reactor core at a neutron multiplication factor $k_{eff} < 1$ allows to obtain a higher degree of flexibility in core design and fuel management, and in particular allows transmuters to be designed as pure TRUs or MAs burners. From the safety point of view, the main advantage is that the criticality does not rely on delayed neutrons, thus allowing the safe operation of reactor cores with poor neutron economy, typical of pure MAs burners [9].

Of course these advantages has to be weighted by technological issues that have yet to be solved: for example, a very high reliability is required for the accelerator, which should be able to deliver steadily high beam current, while technical problems arise from the need of installing a target in the center of a reactor (containment issues). Moreover new transient events are expected from eventual beam trips or rapid current variations (an issue in particular with little or null negative feedbacks, typical of MAs cores). It is interesting to note that ADS may provide additional

---

[11] Since the fission cross-section depends on the relative velocity of the neutrons and uranium atoms, the thermal motions of the uranium nuclei in the fuel element lead to a Doppler effect [16].

neutrons which can be used to increase breeding, of ^{233}U and/or ^{239}Pu. In Ref. [2] it is shown that, by using a 20 mA accelerator, it is possible to obtain a ”parasitic” production of 100 kg/year of ^{233}U in addition to transmutation of 2.5 kg/yr/mA of LLFFs. The Energy Amplifier Demonstration Facility (EADF, Ref. [27]) is an example of an advanced design for a 80 MWth subcritical transmuter system, consisting of an annular core immersed in a lead-bismuth eutectic fluid used as primary coolant and as spallation target, with $ThPuO_2$ fuel mixed with MAs.

1.1.6 Gen-IV systems

In the last few years new impulse has been given to the development of critical systems for electricity production, more attractive than present reactors in terms of sustainability, economy, safety and proliferation resistance. The new systems are the so-called Generation-IV reactors (see Ref. [5] for a more detailed description of the term *generation*). The target date for the introduction of these systems is 2020-2040 and their development is coordinated by the so-called Gen-IV International Forum [5, 28]. The fuel cycles considered for these system should maximize the use of the uranium resources (therefore requiring higher fuel burn-up), and lead to a considerable reduction of MA and LLFF in the waste (some of the systems selected for further studies are fast reactors). More importantly, the new systems offer the possibility of transmutation of MAs with consequent reduction of their inventory. A detailed analysis of the new systems is contained in Ref. [5]. For some of these reactors, a basic requirement of the design is the reprocessing and recycling of fuel, which includes uranium, plutonium and all other actinides; the objective would be to have the spent fuel constituted only by LLFFs, with a major reduction of the final long-term radiotoxicity. Another objective of some Generation IV reactors is the possibility to produce hydrogen with thermochemical cycles at high temperature.

Since the design margins will have to be greatly reduced in order to maximize economy and fuel utilization (reaching higher burn-up would mean also to increase the amount of produced actinides in the fuel elements and to have a larger excess reactivity inventory), a relevant role is played by nuclear data (see § 1.2). Given the greater amount of MA in the fuel and due to the fact that some of the most promising systems have a fast spectrum, a major effort has to be devoted in collecting accurate data for several minor actinides in the energy region between $\sim$1 keV and 2-3 MeV.

1.2 Nuclear data and their role

The accurate knowledge of neutron cross-sections is of major relevance in the design and exploitation of critical and subcritical nuclear systems. In particular, the prediction of the behavior of the reactor cores depends strongly on capture and fission cross-section data. Parameters such as the multiplication factor k_{eff}, the Doppler and coolant void reactivity coefficient[12], the reactivity loss during irradiation and the nuclear density variation of isotopes due to transmutation strongly depend on the Nuclear Data (ND) used in calculations and projections. At present the international community has not yet recognized a single data library with recommended best neutron cross-sections values, and their accuracy and validation is still of major concern. It is worth noticing that accurate nuclear data are not only important for future reactors, but also for current ones. During the past years the average energy availability factor[13] of nuclear plants has steadily increased from the 73.9% in 1991 to 83.0% in 2006 [29]. The improved knowledge of nuclear data (namely cross-sections, neutron multiplicities, fission neutron spectra) has been essential in increasing this parameter, since it has permitted, for example, to relax some safety constraints on reactors operation, that were previously required to take into account uncertainties on several basic nuclear parameter.

1.2.1 Nuclear Data Libraries

Published experimental and theoretical results on neutron-nuclear reactions are collected by several collaborating nuclear data agencies worldwide. The experimental nuclear reaction databases, such as EXFOR (Experimental Nuclear Reaction Data) or CSISRS (Cross-Section Information Storage and Retrieval System) [30] store nuclear reaction data and their bibliographic information, as well as information about the measurements. The status (e.g., the source of the data), and history (e.g., date of last update) of the data set is also included. The vast amount of sometimes contradictory nuclear data must be evaluated before it can be used - for example - in reactor physics calculations. Such kind of evaluation consists in the interpretation and comparison of experimental data, validation against benchmark experiments, evaluation of statistical and systematic errors, check for internal consistency and uniformity with standard neutron cross-sections, etc. At the end of the process, ”preferred” values, obtained by appropriate averaging procedures, are derived. It should

---

[12] For the physical description of these parameters, see Ref. [16].

[13] The energy availability factor is defined as the ratio of available energy to theoretically possible energy output in the period under consideration and it characterizes the reliability of a plant in general, considering all complete and partial outages.

be stressed that an evaluated data set for a particular isotope needs to be as complete as possible, in particular for reactor applications. For example, a wide energy range should be covered. To this purpose, evaluators often combine experimentally measured cross-sections with predictions of nuclear model calculations (with codes such as EMPIRE [31] or TALYS [32]) in order to obtain a single complete data set. Due to the large number of variables involved in the evaluation procedure, including the arbitrary choice of experimental data and of the model parameters, several different large evaluated nuclear data files are compiled and maintained worldwide:

- Evaluated Nuclear Data File (ENDF/B), USA. The latest version (released in 2007) is ENDF/B-VII.0 [33].
- Joint Evaluated Fission and Fusion Library (JEFF), NEA[14] Countries. The current version is JEFF-3.1 (released in May 2005) [34].
- Japanese Evaluated Nuclear Data Library (JENDL). The current version (released in 2002) is JENDL-3.3 [35].
- Russian evaluated neutron data library (BROND - Library of Recommended Evaluated Neutron Data). The current version (released in 1992) is BROND-2.2 [36].

These nuclear reaction databases contain, under several different sublibraries, evaluated (recommended) cross-sections, spectra, angular distributions, fission product yields, thermal neutron scattering, photo-atomic and other data, with emphasis on neutron-induced reactions. All data are stored in the internationally adopted format (ENDF-6 [37], originally developed for the ENDF library but now adopted for all other libraries).

1.2.2 Simulation codes and relation with Nuclear Data

In the design of critical or subcritical systems both Monte Carlo and deterministic methods are used to calculate important parameters for reactor operation (some of them have been indicated at the beginning of the section).

The use of Monte Carlo codes have several advantages since, for example, the code can take into account as much information is experimentally available (for example, cross-sections could be provided point-wise and geometry of the system could be accurately implemented). However, a drawback is that it is very time-consuming to carry out full MC calculation and thus to reach statistical convergence.

---

[14] Nuclear Energy Agency

In order to reduce the processing time, deterministic code based on the solution of the the multi-group transport equation system, are used. This means that it is necessary to reduce the detailed structures in the cross-section, by averaging them over a set of energy regions called ”groups”. A module of the NJOY nuclear data processing system [38] carries out such averages from the data in the evaluated libraries, and it also generates multigroup ”matrices”, which describe the transfer of neutrons from one group to another. If the cross-sections are grouped the differences between different databases (see par. 1.2.1) are reduced due to within-group cancellation: therefore the lesser the group number, the smaller are the discrepancies, but also lower is the accuracy in the calculations, because a reduced amount of detail are present in the final nuclear data. Large discrepancies in the pointwise cross-sections can sometimes be due to a small difference in the energies of sharp resonances or to different evaluations of resonance valleys.

One of the principal tool to assess the effect of nuclear data uncertainties on the various parameter of a reactor system are the so-called sensitivities studies. They provide indications on uncertainties of particular variables relevant to reactor operation. The term ”sensitivity” (S) is defined as the derivative of a given integral parameter R (for example the reactivity coefficient) with respect to a particular nuclear data (for example the cross-section):

$$S_{a,b,c} = \frac{\partial R}{\partial \sigma_{a,b,c}} \frac{\sigma_{a,b,c}}{R} \tag{1.2}$$

Here, a,b and c are parameters that refers to the isotope type, cross-section type (e.g. fission, capture) and energy groups (see Ref. [12] for a thorough discussion). Different analytical expressions depending on which integral parameter has to be analyzed, are often conveniently used.

It is worth mentioning that the results of the sensitivity analysis does not depend only on the uncertainties on the cross-section data. For example, the effect of a given isotope on the calculated integral parameter may be larger relative to other ones, even if its cross-section is characterized by a small uncertainty, simply because of its abundance in the reactor fuel is larger.

A general comment on the role of evaluated data is necessary: even if the cross-sections of two evaluated databases agree with each other, it does not necessarily mean that the evaluated data are correct. In fact there could be a common systematic error, which could be revealed with further evaluation or validation, or with new measurements.

1.2.3 Data for MA in transmutation scenarios: the case of Am and Cm isotopes

The role of the accuracy of MA nuclear data becomes significant in the context of transmutation and of longer burn-up cores, not only for the analysis of reactor performances but also for the post-irradiation treatment of spent fuel. However, especially for higher mass actinides, the data in the current major evaluated libraries present large discrepancies [39], as clearly seen in Fig. 1.5.

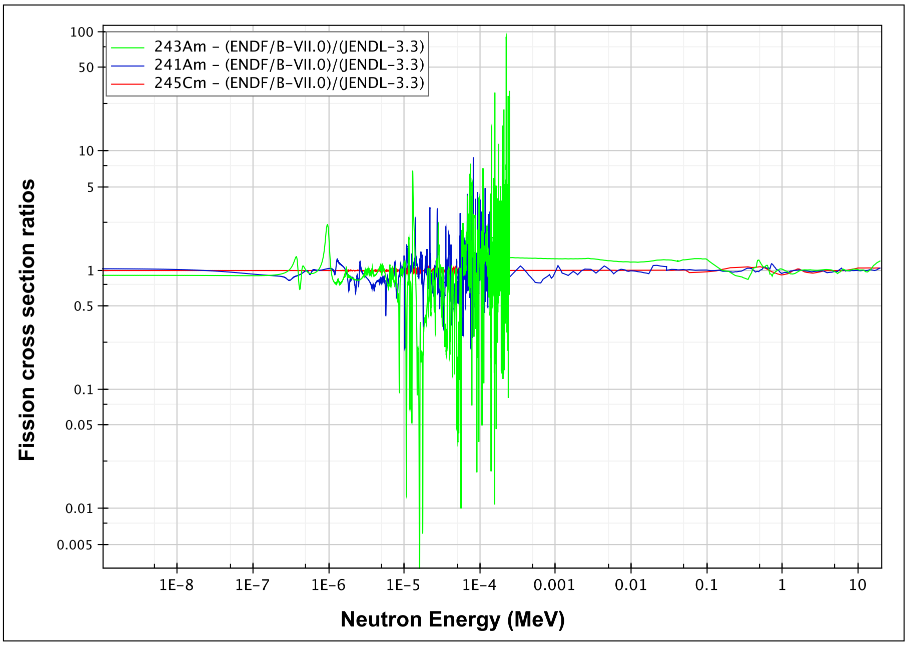

Figure 1.5 – Ratio of the evaluated fission cross-sections in the ENDF/B-VII.0 and JENDL-3.3 databases for ^{241}Am, ^{243}Am and ^{245}Cm. For ^{245}Cm(n, f) the two evaluations coincide up to 7 MeV, with ENDF/B-VII.0 cross-sections taken from JENDL-3.3 [40].

Sensitivity studies have been performed both for ADS, in which the core would be loaded with either large [12] or small [13] content of MA, and for innovative systems, in particular for selected Gen-IV reactors and extended burn-up light water reactors, in which the MAs are mixed to standard fuel components [11].

In the case of ADSs, it has been shown that the uncertainty on the multiplication factor is of the order of 3%, a value that is not acceptable since ADS would operate with a k_{eff} nearly 6% under criticality condition. The most relevant (accounting up to $\sim$2%) contribution comes from the uncertainty in the fission cross-section, especially in the energy range between 10 keV and 10 MeV. The isotopes for which the sensitivity is greater are essentially ^{237}Np, ^{241}Am, ^{243}Am and ^{244,245}Cm. Another major problem is the loss of reactivity[15] during a given irradiation cycle, due to nuclei that transform

---

[15] The reactivity of a chain reacting system is connected with the multiplication factor k_{eff} and

into more or less reactive ones following capture or inelastic scattering; also in this case the discrepancies due to the fission cross-section (especially of Am isotopes and ^{245}Cm) plays a major role [11]. As an example, current uncertainties in the fission and capture cross-section lead to an uncertainty of $\simeq$11% in the predicted abundance of ^{241}Am and ^{243}Am at the end of a single irradiation cycle, while the abundance of ^{245}Cm is affected by a $\sim$36% uncertainty related to its fission cross-section and by a 70% uncertainty related to its production via neutron capture by ^{244}Cm [12]. The knowledge of the spent fuel abundance variation of an isotope between the beginning of cycle and end of cycle is indicative of its transmutation potential.

Sensitivities studies indicate the required accuracies on the cross-section of specific isotopes, in particular energy groups, taking into account the required uncertainties on integral parameters. Some of the results obtained in Ref. [12] for ADS are shown in Table 1.4.

Table 1.4 – Required uncertainties on the cross-sections for some isotopes in the relevant energy interval, necessary to meet target accuracies on integral parameters. More details on the requests of new data can be found in Ref. [12]. In most cases, current uncertainties are significantly higher than required ones.

	$\sigma(n,f)$		$\sigma(n,\gamma)$	
^{237}Np	0.5-2.2 MeV	5-8%		
^{241}Am	0.5-6.0 MeV	4-6%	10 keV - 1.3 MeV	5-7%
^{243}Am	0.5-6.0 MeV	5-8%	25 keV - 1.3 MeV	5-10%
^{244}Cm	0.5-6.0 MeV	5-10%		
^{245}Cm	70-500 keV	10%		

Time evolution studies have indicated that the use of different libraries could lead to differences of up to 2 mA in the required proton beam current, in order to obtain the same value for the multiplication coefficient k_{eff} [13]. Clearly this would require the accelerator to be overdimensioned in order to be conservative with the required performances, with important consequences for ADS scenarios economy.

As far as critical systems are concerned, the requirements on the neutron data depend on the neutrons spectrum as well as on the degree of MAs loading in the fuel. In Ref. [11] different types of systems are studied. In all cases, however, the accuracy of the fission cross-section for the main fissile isotopes (such as ^{239}Pu, and other Pu isotopes) has to be drastically improved from 5% down to a maximum value of 1.5%. For fast reactor systems, such as the LFR[16], SFR[17] and EFR[18], new fission

---

defined as $\rho = \frac{k_{eff}-1}{k_{eff}}$

[16] Lead-cooled Fast Reactor

[17] Sodium-cooled Fast Reactor, acting as a transuranium burner with breeding ratio less than 1

[18] European Sodium-cooled Fast Reactor, similar to the SFR and based on PHENIX and SUPER-

cross-section data are needed for ^{245}Cm in the energy range from $\sim$30 eV up to 2 MeV, since this cross-section should be known with an uncertainty - of 10 to 15% - much smaller than currently available (40-50%) [11]. In the case of very long burn-up PWR cores, a significant improvement in the accuracy of ^{245}Cm(n, f) cross-section is necessary from the thermal region up to 25 eV. Studies show that, in this case, more accurate fission cross-section for ^{245}Cm could result in a much smaller uncertainty on the abundance of this isotope at the end of irradiation, from nearly 33% to about 5%.

1.2.4 Data for the Th/U fuel cycle: the role of ^{233}U

Nuclear data of relevance for the Th/U and Th/Pu fuel cycle are presently less reliable compared to the well established U/Pu cycle; the isotopes recommended by the IAEA as first priority for more accurate data are [41]: ^{230}Th, ^{232}Th, ^{231}Pa, ^{233}Pa, ^{232}U, ^{233}U, ^{234}U and ^{236}U (see Fig. 1.2) [21, 24, 20]. In some cases, measurements are difficult to perform due to the problem in acquiring samples of sufficient purity, or because of the high specific activity of the isotopes, such as, for example, ^{233}Pa and ^{232}U. Most of the data included in the new libraries were originally collected at the beginning of 1970s. In many cases the lack of neutron inelastic cross-section (no experimental data exist for $(n, 2n)$ and $(n, 3n)$ for ^{230}Th, ^{231}Pa, ^{233}Pa, ^{232}U and ^{234}U) results in discrepancies in the predicted reaction rates up to 30% in the case of subcritical systems both for thermal and for fast spectrum reactors [42]. As an example, in Ref. [42] it is shown that in the case of a fast system with ThUO$_2$ fuel, k_{eff} is predicted to change up to $\sim$1400 pcm (*per cent mil*, $10^{-5}\frac{\Delta k}{k}$) if different evaluated libraries of ^{233}U are chosen, whereas the maximum allowed value for critical reactors is of the order of $\pm$100 pcm for UO$_2$ fuels and $\pm$40 pcm for MOX fuels.

In an effort to improve the situation, in the new evaluation performed for the ENDF/B-VII.0 library, many of the results produced by the IAEA Co-ordinated Research Project (CRP) on "Evaluated Nuclear Data Files for the Thorium-Uranium Fuel Cycle" (INDL/Th-U) [43] have been included. This is particularly important in case where really old data was present (e.g. ^{231}Pa and ^{233}Pa). The adopted procedure is based on both resonance parameter re-analysis (with production of covariances matrices) and on theoretical analysis using the available experimental data and nuclear reaction code calculations (e.g. EMPIRE [31]). As a results of the IAEA Research Coordination Meeting Committee, a large improvement has been obtained with respect to the previous evaluations, with the production of the IAEA Evaluated Nuclear Data Library for the Th/U cycle [43].

Although a complete systematic assessment of the needed accuracy is missing

---

PHENIX FR technology, but with larger size with full recycling on MAs and breeding ratio 1.

in the case of the Th/U cycle, target uncertainties have been recommended for some isotopes, both for thermal spectrum and for fast (or ADS) spectrum. They are reported in Table 1.5 (see Ref. [41]). Generally speaking, since fission rate and the consequent produced energy are governed by the fission cross-section, a very high accuracy of 1% or better in the energy range of interest is required.

Table 1.5 – The table shows the required accuracy for selected isotopes of the Th/U cycle, in the case of both fast and thermal spectrum. Data from Ref. [41] and [44].

	$\sigma(n,f)$		$\sigma(n,\gamma)$	
	thermal	fast	thermal	fast
^{232}Th		5%	1%	1-2%
^{231}Pa[a]		20%	10%	10%
^{233}Pa[b]		20%	5%	3-10%
^{232}U[c]	10%	20%	10%	10%
^{233}U[d]	1%	1%	5%	3%
^{234}U[e]		3%	3%	5%
^{236}U	20%	5%		10%

---

[a] Relevant in the cycle because of its copious formation via $(n,2n)$ reaction on ^{232}Th and its α-decay radiotoxicity ($t_{1/2} \simeq 32750$ y).

[b] It plays an important role because is the intermediate isotope before ^{233}U formation (it has a longer half-life ($t_{1/2} \simeq 26.97$ d) with respect to ^{239}Np ($t_{1/2} \simeq 2.3$ d) that has a similar role in the breeding of the fissile ^{239}Pu).

[c] The knowledge of the concentration of this isotope is critical for fuel handling.

[d] Note that the fission cross-section of ^{235}U and ^{239}Pu (having its same role in the U/Pu cycle) has been measured in experiment with claimed accuracy of 2% to 3%.

[e] Produced by neutron capture on ^{233}U, is important because it allows the production of ^{235}U and reduce the reactivity deficiency in high burn-up thorium cores.

The status of the evaluated data for ^{233}U - which plays the very important role of the main fissile isotope for the Th/U fuel cycle - is presented in Fig. 1.6: except for the thermal region, easily accessible for measurements at reactors, there are significant discrepancies between different evaluated libraries, which in some energy regions may exceed 100%. Although these discrepancies are reduced when the pointwise cross-sections are processed into multi-group ones, they represent an obstacle towards the design of new systems based on the Th/U fuel cycle, especially for the correct evaluation of self-shielding effects.

Another important difference between libraries concern the upper limits for the resolved resonance region (RRR), as well as for the unresolved resonance region (URR). Current limits for the different libraries are listed in Table 1.6. It is evident that it is of particular relevance to obtain accurate data in the keV region, since the neutron energy spectrum of fast reactors (both Gen-IV and ADS) has a maximum in that range, as evident from the thick blue line in Fig 1.7, which represents the

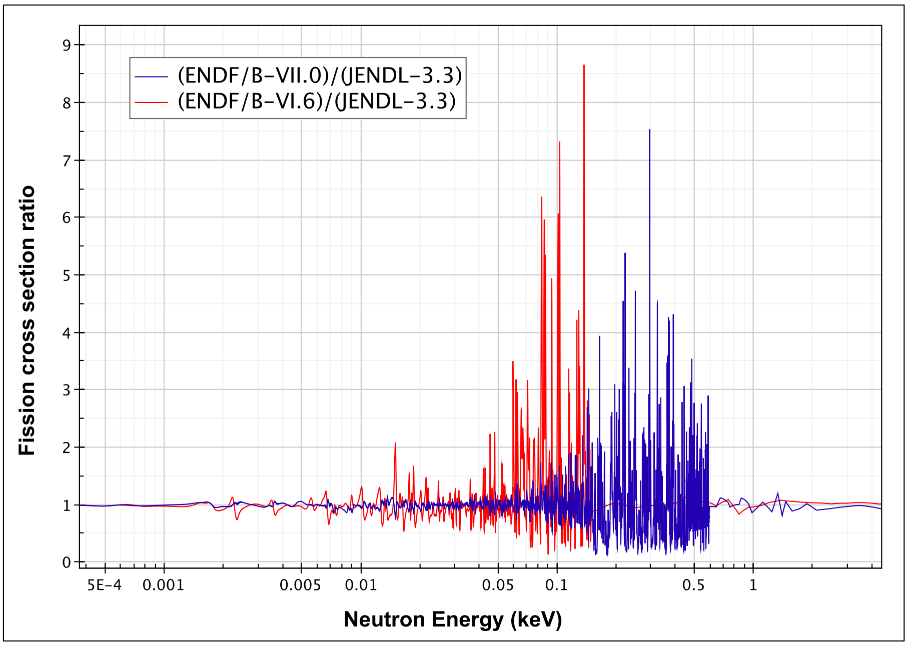

Figure 1.6 – Ratio between the fission cross-section of ^{233}U in ENDF/B-VII.0 and JENDL-3.3 (blue line) and between ENDF/B-VI.8 and JENDL-3.3 (red line). The JEFF-3.1 evaluation for this isotope is a replica of the JENDL-3.3 data.

spectrum of a Liquid Metal Fast Breeder reactor, together with a thermal one and selected fission cross-sections.

Table 1.6 – Upper limits in major evaluated data libraries for the Resolved Resonance Region (RRR) and Unresolved Resonance Region (URR) in the ^{233}U(n, f) cross-section.

	upper RRR	upper URR
ENDF/B-VII.0	600 eV	40 keV
ENDF/B-VI.8	60 eV	10 keV
JEFF-3.1	150 eV	30 keV
JENDL-3.3	150 eV	30 keV

As for the isotopes involved in the Th/U fuel cycle, a general remark on the inadequacy of present nuclear data can be made also for minor actinides and some long lived fission fragments. Some of the stringent requirements in the cross-section accuracy are very difficult to be met experimentally (such as the 1% uncertainty for fission of ^{233}U, or the 5% requirement for fission of ^{244}Cm), due in general to the short half-life of the isotopes and to difficulties in obtaining adequate samples (see Table 1.4).

It is thus clear that accurate new data can only be obtained after major improvements in the neutron beams or in the experimental techniques. To this aim, the neutron time-of-flight facility set in operation at CERN, represents, with its innovative characteristics together with high performance detection and data acquisition systems, a breakthrough in the field of neutron physics, which has and may continue to allow to finally collect long-needed nuclear data of interest for energy applications, as well as for other fields in fundamental and applied Nuclear Physics.

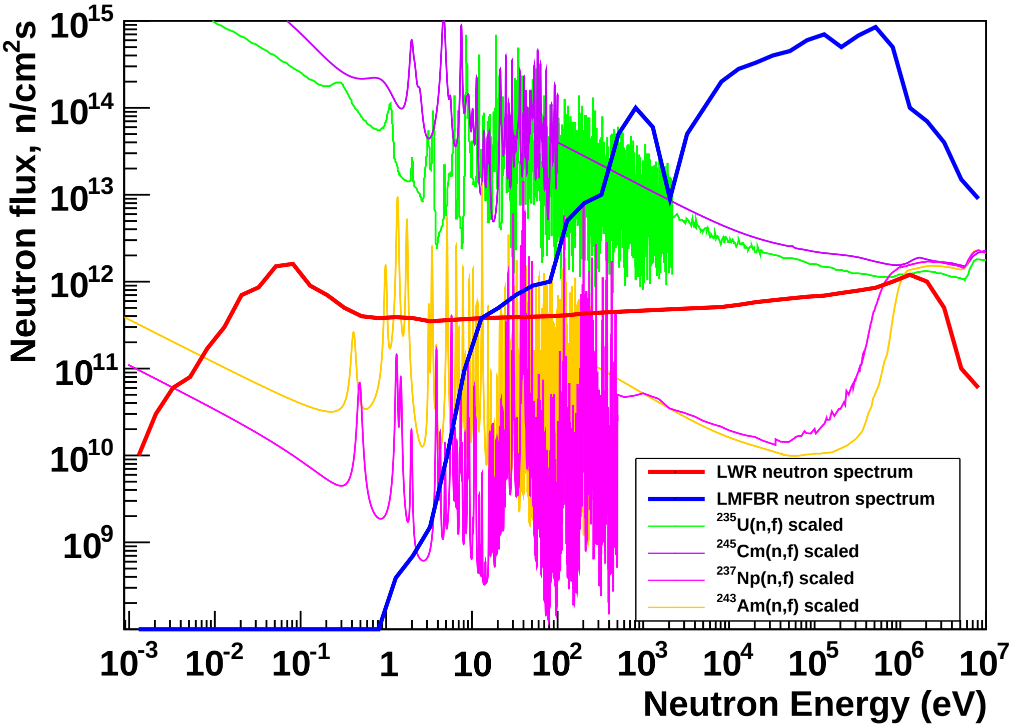

Figure 1.7 – Typical neutron spectrum of a thermal (Pressurized Water Reactor) and of a fast (Liquid Metal Fast Breeder Reactor or ADS-like) system. The fission cross-section of some actinides contained in the fuel is also shown in the figure by the thick curves.

Chapter 2

The n_TOF Facility

The need for new and accurate data on neutron-induced cross-sections has led an international collaboration to design and construct an innovative facility capable of delivering a neutron beam with high flux, white spectrum in a wide energy range, high resolution and low background. The n_TOF facility (neutron Time-Of-Flight), located at CERN (European Organization for Nuclear Research [45]) Switzerland, has been built with the aim of fullfilling these requirements. This chapter contains a description of the facility and of the main characteristics of the n_TOF neutron beam. After a brief introduction on the production method, the neutron flux, the energy resolution, the beam profile and the background in the experimental area are described. The precise knowledge of all these parameters is a fundamental pre-requisite in order to accurately determine neutron cross-sections for the field of nuclear energy, as well as for nuclear astrophysics and basic nuclear research.

2.1 Neutron production

Many white spectra neutron facilities are operating around the world, based on different production methods. At the CERN n_TOF facility, neutrons are produced via the spallation process of a high energy proton beam from the PS accelerator complex on a thick Pb target. The term ”spallation” refers to the physical processes taking place when high energy nucleons or light nuclei interact with a massive target, and involve many energy-dependent nuclear reaction mechanisms. Due to the high energy of the projectile (typically from a few hundreds MeV to a few GeV), several particles are ejected from the target nucleus, thus modifying the mass and the atomic number of all participants in the reactions. Fig. 2.1 pictorially shows the spallation reaction produced by 1 GeV protons in a matrix of heavy nuclei.

In a first approximation, the interaction can be divided in two stages [47]: in the

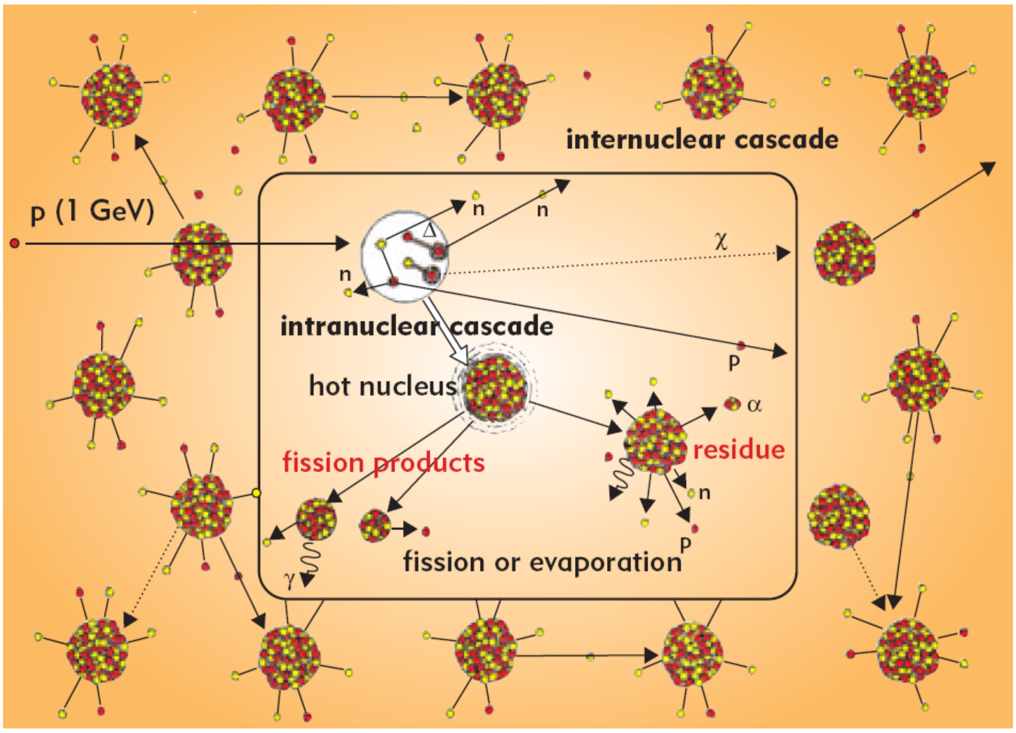

Figure 2.1 – Pictorial representation of the various processes contributing to the spallation mechanism, caused by a nucleon impinging on a heavy target [46].

first step, usually known as the Intra-Nuclear Cascade (INC), the incoming nucleon undergo incoherent scattering with nucleons of the target, thus depositing some fraction of its energy. This fast "knock-out" interaction leads to the emission of some of the nucleons of the target material, and to the excitation of the residual nucleus. The cross-section for this process is essentially the geometrical cross-section between the two participants. After a Pre-Compound Stage (which includes pre-equilibrium, multifragmentation and Fermi break-up processes), the deexcitation of the residual nucleus proceed essentially via evaporation (mostly of neutrons) and high energy fissions. At the end of the chain, low energy inelastic - (n, xn), (n, α), (n, γ) - and elastic reactions take place.

The number and energy of neutrons produced in a spallation mechanism mainly depend on the type and energy of the primary beam and on the target material. The effects of these two important characteristics are shown in Fig. 2.2, where the yield of spallation neutrons is shown as a function of the primary beam energy for different target materials. It is worth noticing that the number of produced neutrons per incident proton starts to saturate at 2 GeV. Heavier target materials, such as actinides, produce more neutrons; however, a severe drawback of actinides employed as spallation material is that they undergo fission, increasing the radioactivity of the spallation target itself.

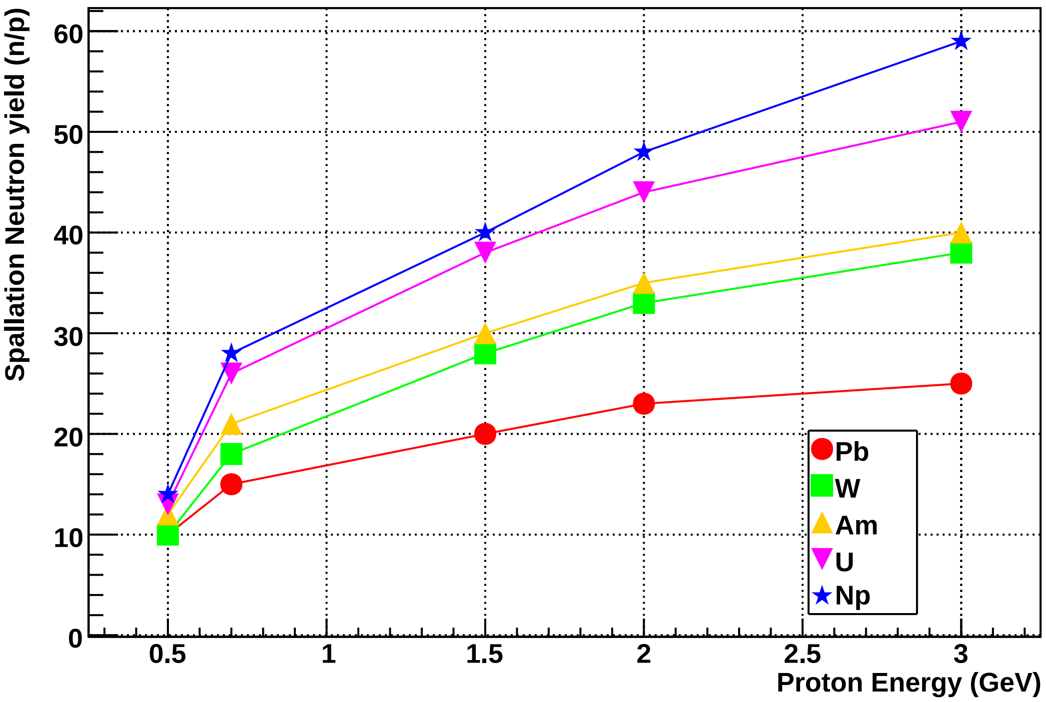

Figure 2.2 – Spallation neutron yield as a function of the incident proton energy for different materials. Data taken from [48].

Apart from spallation, several others nuclear reactions could be used to produce neutron beams. The characteristics of the most common accelerator-based neutron sources are presented in Table 2.1. The choice of spallation as production mechanism is natural if a high energy proton or deuteron beam is available, considering the large number of neutrons produced for each incident primary particle.

Table 2.1 – Description of various type of accelerator-based neutron sources, based on different nuclear reactions [48].

Reaction type	Incident particle and energies	Beam Current (part/s)	Neutron Yield (n/inc.part)	Target power (MW)	Deposited energy per n (MeV)	Emitted neutrons (n/s)
(e^-,γ), (γ,n)	e^- (60 MeV)	5×10^{15}	0.04	0.045	1500	2×10^{14}
$^3\mathrm{H}(d,n)^4\mathrm{He}$	d (300 keV)	6×10^{19}	10^{-5}-10^{-4}	0.3	10^4	10^{15}
fission	n, p		$\sim$1	$\sim$60	200	2×10^{18}
spallation[a]	p (1 GeV)	10^{15}	14	0.09	37	2×10^{16}
spallation[b]			30	0.4	55	4×10^{16}

---

[a] non-fissile

[b] fissile

2.1.1 The n_TOF spallation target and PS proton injection

The proton beam for the n_TOF facility is produced by the Proton Synchrotron (PS) of the CERN accelerators complex (see Fig. 2.3). The main characteristics of the PS, that is the high proton energy, the high current and the low repetition rate, are very convenient for a neutron time-of-flight facility, especially for the measurement of radioactive isotopes (as shown later in this work). The characteristics of the PS proton beam, in fact, led to the production of a pulsed neutron beam with very high instantaneous flux, and with an energy range up to hundreds of MeV. The PS beam was slightly optimized for the n_TOF facility, in particular by reducing the bunch length from the original 13 ns down to 7 ns (rms), with the aim of increasing the time resolution of the neutron beam.

Two modes of operation of the proton beam are typically provided for the n_TOF facility: a dedicated mode and a parasitic one. In the dedicated mode, bunches of $\simeq 7\times 10^{12}$ protons at a momentum of 20 GeV/c are delivered, while in the parasitic mode only $\simeq 4\times 10^{12}$protons/bunch are delivered, with a momentum of 24 GeV/c [49]. As shown in Fig. 2.2, due to saturation effects the different energy of the proton beam in the two cases does not significantly affect the neutron flux. The repetition rate of the proton accelerator is a more complex variable: the PS normally operates in a succession of machine states called "supercycles", in which several particle bunches can be accelerated and extracted for different users. The duration of the supercycle changes year by year, between 14.4 s and 19.2 s. Technically the PS could deliver proton bunches separated by 1.2 s, corresponding to a repetition rate of $\sim$0.8 Hz; however due to various constraints, i.e. sharing of the PS time with other experiments and technical limitations on the target temperature and on the radioactivity of the target area, at maximum 4 proton bunches in a supercycle can be delivered to the n_TOF spallation target, reducing the repetition rate down to 0.25 Hz.

The spallation target consists in a pure (99.99% [49]) Pb block of $80\times 80\times 60$ cm^3 size (Fig. 2.4(a) and 2.4(b)). These dimensions represent a compromise between the neutron intensity and the energy resolution of the neutron beam, which essentially depends on the moderation uncertainty $d\lambda$ (described in more details in § 2.2.1). The lead target is mounted on a stainless steel support (shown in Fig. 2.4(a)), which is an integral part of the target structure itself. The choice of Pb is dictated by many considerations, in particular the high atomic number, high density, the low cost and the possibility to easily machine it. Additionally, Pb is essentially transparent to neutrons with energy below $\sim$1 MeV, the region where the largest fraction of the n_TOF flux is located. Other materials, such as tungsten, have better properties in terms of neutron/proton ratio, melting point and thermal conductivity, but they are

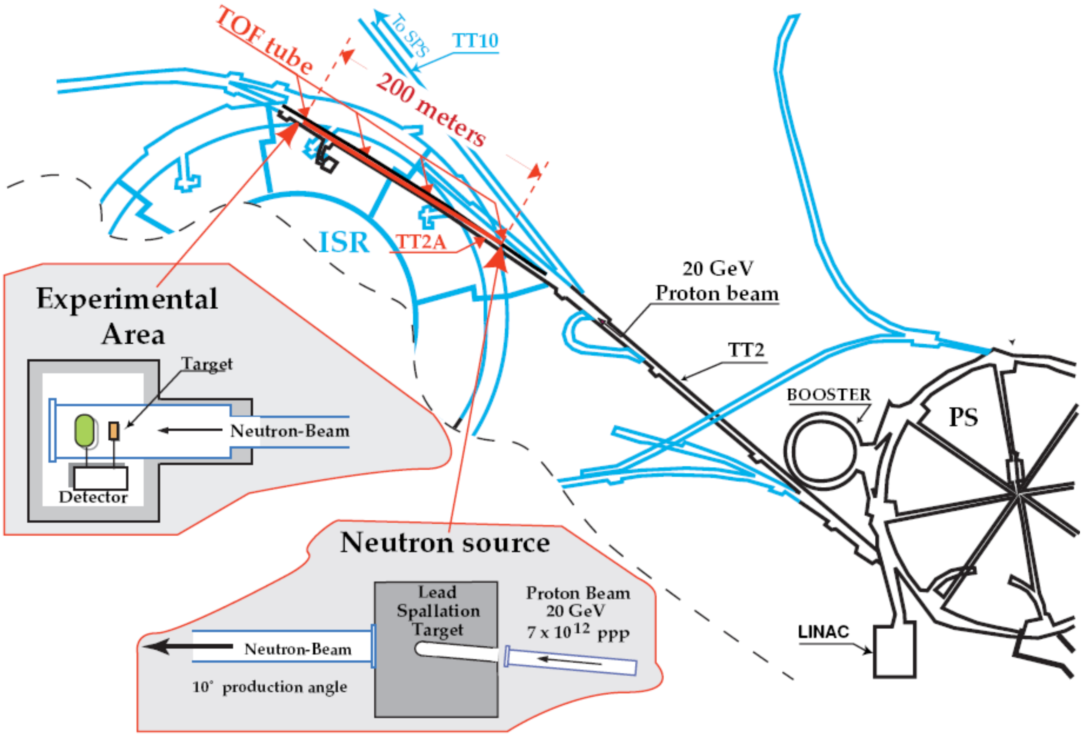

Figure 2.3 – Schematic layout of the n_TOF facility: the proton beam is extracted from the PS via the TT2 transfer line and hits the lead target. The experimental area is located at the end of the TOF tunnel (TT2A), 185 m from the primary target.

more expensive to build and present other engineering issues [50, 51, 52].

A large amount of secondary particles are produced by spallation of protons in the lead target, such as muons, protons and pions, preferentially emitted along the direction of the proton beam. In order to minimize the contamination of the neutron beam with primary protons and other high energy particles, the proton beam line has been designed so to form an angle of 10° relative to the TOF tunnel. Once emitted from the spallation target, neutrons propagate in a vacuum tube located in the existing TT2A tunnel, towards the experimental area positioned ∼185 m downstream from the target in the same tunnel (Fig. 2.3).

The Pb target is inserted in a pool containing demineralized water, circulating in a closed loop. The walls of the pool are in aluminum alloy (ISO Al-Si1-Mg-Mn 6082), so to reduce unnecessary activation. The water pool acts both as a coolant and as moderator of the neutron spectrum. Due to the large power dissipated by the incident proton beam in the Pb block, an efficient cooling system is required. With a water flow of 6 m/s at 30°C, the maximum asymptotic temperature at the center the target is predicted not to exceed 140°C (the melting point of Pb is 330°C), while the maximum theoretical temperature increase during one bunch is 34.5°C[1]. The water

---

[1] However after target inspection in 2007, it turned out that the water cooling was not sufficient at

(a) Lead target and its structure

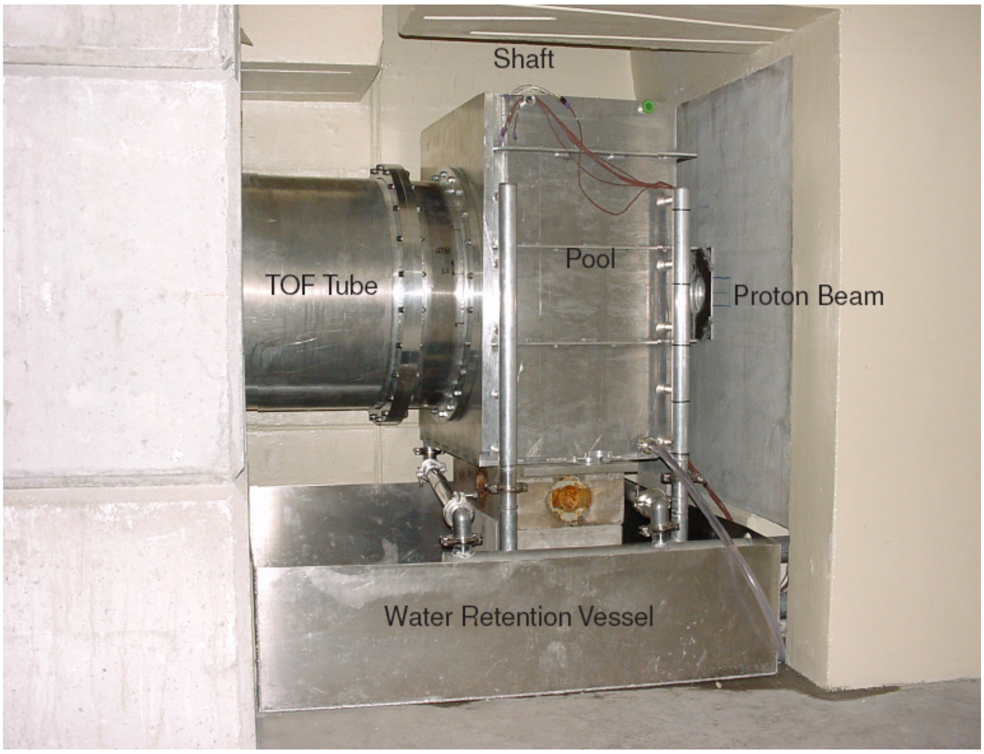

(b) Picture of the target in place at the nominal position

Figure 2.4 – Sketch of the lead target and a picture of the target zone.

layer all around the block is 3 cm thick except in the front face, where it is 5 cm for moderation purposes.

Due to the presence of hydrogen in the water layer, the neutron beam is produced with a wide energy spectrum spanning over various orders of magnitude, with an isolethargic distribution (flat distribution in the logarithm of energy).

The interface between the moderator water and the TOF vacuum tube is made by a single slab of aluminum 1.6 cm thick and 800 mm in diameter, reinforced by a grid 50 mm thick with sides of 100 mm in length. The characteristics of this single component are very important: on the one hand it must be solid enough to separate the water from the vacuum[2] while remain geometrically flat[3], in order to guarantee a constant water moderation of 5 cm. On the other hand it should be as light as possible to avoid neutron scattering and made of material with low absorption cross-section. Furthermore, it should be radiation resistant since the dose rate accumulated in one year of operation is of the order of 10^6 Gray [49, 54].

2.1.2 Neutron transport: the TOF vacuum tube and collimators

The time-of-flight tube, shown schematically in Fig. 2.5(a) and 2.5(b), starts immediately after the water-vacuum window and runs for a length of $\simeq$200 m [55]. It is divided in four different sectors connected by flanges and delimited by concrete and iron walls. The first part, closest to the target, has a diameter of 80 cm and is directly connected to the target tank. It is made of aluminum alloy, while all other sectors ones are made of stainless steel. The diameter of the tube is progressively reduced to 60 and 40 cm in correspondence of the collimators.

Three collimators are installed along the flight path to reduce the diameter of the neutron beam in the experimental area down to $\sim$2 cm for capture measurements and 8 cm for fission ones. A first reduction is placed at a distance of 70 m from the spallation target with a collimation system made by a 2 m thick Fe block. A second collimator, made by 1 m of Fe and 1 m of concrete, is placed at 136.7 m from the target, and has a diameter of 11 cm. The main purpose of this collimator is to minimize the divergence of the neutron beam in the experimental area. The shaping of the neutron beam profile is performed by the second collimator (Fig. 2.6), placed at $\simeq$178 m from the target, just before the experimental area. The structure of this collimator - composed by three parts - is more complex than the previous ones, mainly due to the need of minimizing the background in the experimental area. The first part consists

---

the hottest spots of the proton beam, such as at the proton impact point and at the face next to the neutron pipe. For this reason the cooling system was redesigned [53].

[2] Pressure difference of 1.2 bar.

[3] Maximum deflection allowed in the center <2 mm.

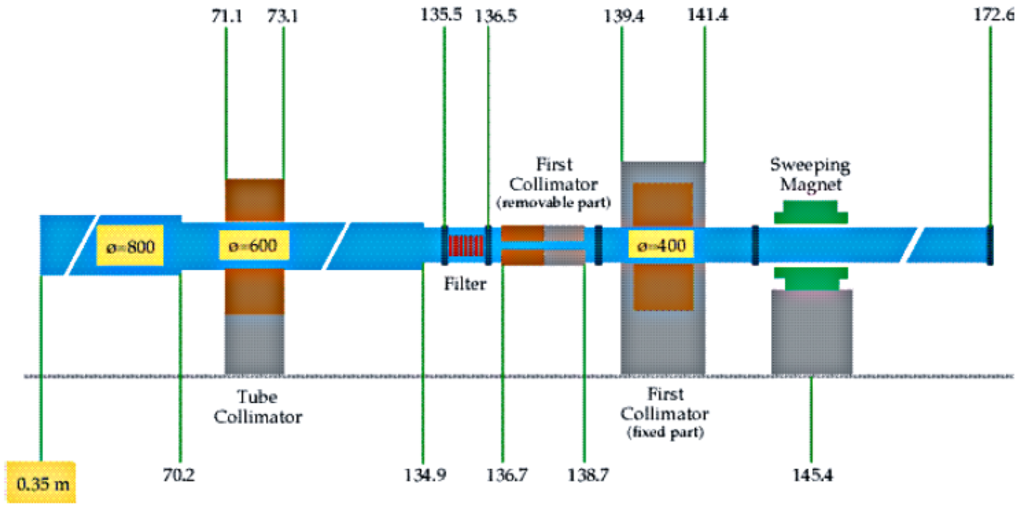

(a) n_TOF tube in the first 172 m

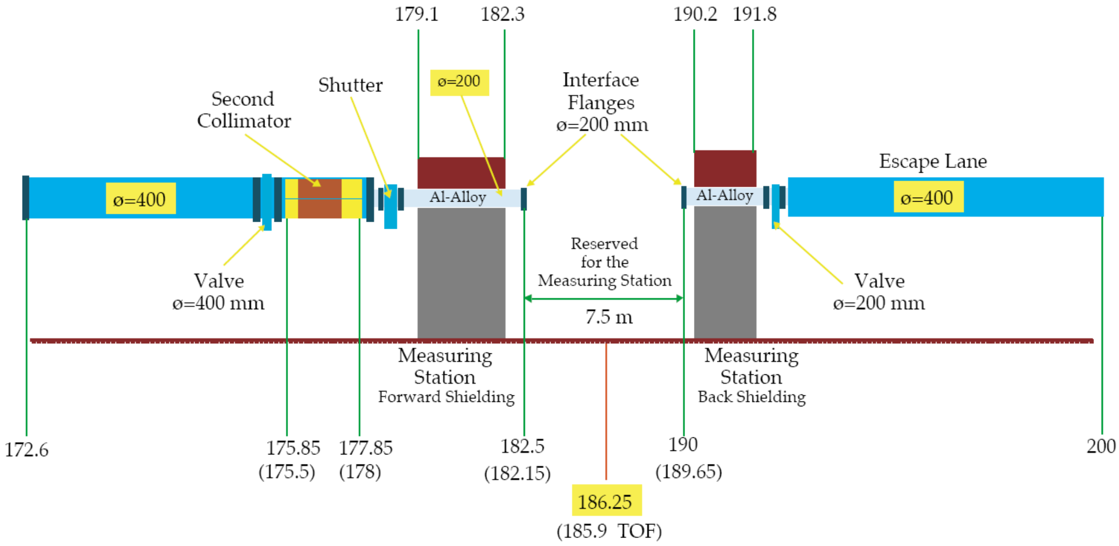

(b) n_TOF tube after 172 m

Figure 2.5 – Schematic drawing of the main elements of the n_TOF tube. Distances refer to the center of the Pb target. The section sketched in Fig. 2.5(a) includes shielding of concrete (grey) and iron (brown) as well as a sweeping magnet, a filter station, and the first collimator.

of 50 cm of borated polyethylene, with 5% concentration of ^{10}B. Due to the nuclear properties of the ^{10}B isotope, this part captures low energy neutrons, preventing them from being captured later on and produce γ-rays. The second part, 125 cm long, is made by Fe, whose aim is to moderate high energy neutrons, while the third part is made again of 75 cm of borated polyethylene for final moderation and capture of low energy neutrons produced in the Fe stage.

Figure 2.6 – Picture of the beam-shaping collimator located just before the experimental area.

Two different beam-shaping collimators can be used: in the case of capture cross-sections measurements, which require a small and well defined neutron beam, the inner aperture is 1.9 cm (diameter), while for fission cross-section measurements, in order to fully exploit a wider neutron beam on thin and larger samples[4], the inner diameter is 8 cm.

The experimental area, hosting the monitors and the detectors, is delimited by two concrete walls, at 182.3 m and at 190.2 m from the spallation target, respectively. After the measuring station, the neutron beam continues in a vacuum tube of 12 m length and 20 cm diameter, called the "escape lane". At the end of the tube, a polyethylene block moderates and blocks the neutrons, minimizing neutron backscattering to the experimental area. The device is equipped with BF_3 counters, to monitor the neutron

---

[4] As will be discusses later (see Chapter 3), thinner target deposits allow to increase the fission fragment detection efficiency, while larger area deposits permit to obtain a higher fission yield per neutron bunch.

beam position [49] (Fig. 2.7). During 2004 a fission ionization chamber with ^{235}U and ^{238}U samples has been added in this section of the TOF tube just after the concrete wall delimiting the experimental area, as an additional monitor of the neutron flux.

Figure 2.7 – Neutron escape lane area, with the polyethylene block placed at the end of the TOF tube [49].

Generally, the samples measured at n_TOF are placed in the vacuum tube crossing the experimental area, while detectors could be located both in open air or in vacuum. In the case of fission measurements, where sealed gas detectors have to be used, the vacuum is broken with kapton windows at the vacuum-air interfaces. It has been checked that this additional material does not produce significant attenuation nor background of the neutron beam.

In the TOF tube, since high vacuum is not necessary for neutrons, a pressure of $\simeq 10^{-1}$ mbar is maintained by several mechanical pumps located along the flight path.

2.1.3 Background minimization

Particular care has been taken at the n_TOF facility to minimize the background. This represents one of the most important parameters that characterize a neutron beam, since it directly affects the accuracy of the measured cross-sections and could introduce systematic effects in the results. In a time-of-flight facility it is not possible to identify and discriminate background from reaction events only on the basis of the time information. For this reason, all possible sources of spurious events have to be studied and minimized. Many sources of background usually coexists at a spallation source:

- Secondary charged particles produced by hadronic interactions in the spallation process or by decay of other particles (such components include π, K, μ and e^-);

- Neutrons scattered and reflected by the material along the flight path, such as the walls of the tunnel and the collimators, and ending in the experimental area;

- γ-rays produced in the spallation process or by secondary particles hitting the walls or the collimators.

In order to reduce these background components, several shielding blocks have been setup along the flight path of the time-of-flight tunnel. Most of the secondary particles produced in the spallation target are stopped on the large concrete and marble[5] shielding placed just after the Pb target (Fig.2.8(a)). Two concrete shielding walls of 2 and 3.2 m thick and a chicane, placed in the TOF tunnel just after the two collimators, are very efficient in suppressing the background (primarily neutrons and γ-rays produced by the collimators). A Fe wall of 3.2 m (Fig. 2.8(b)), located at nearly 150 m, further reduces the background by attenuating the muon component, which otherwise produces a neutron background in the experimental area, as a result of μ^- capture [56].

(a) Additional concrete shielding placed after the spallation target zone.

(b) View of the iron shielding placed after the sweeping magnet.

Figure 2.8 – Pictures of some of the shielding elements along the TOF tunnel [49].

---

[5] Marble has the advantage over concrete that it becomes less radioactive when irradiated with charged particles.

Finally, to suppress the secondary charged particles propagating along the vacuum tube toward the experimental area, a 2 m long dipole magnet (see Fig. 2.9), located at ∼145 m, is used. The magnetic field sweeps away these contaminating charged particles out of the beam tube, towards the side walls of the tunnel or on the iron shielding placed 10 m after the dipole. It has a magnetic rigidity of ≃1.0 T·m, so that particles with a maximum momenta of 10 GeV/c are deflected out of the neutron beam before reaching the experimental area [49].

In addition to the background described above, present in any case in all measurements, there are other background components associated with the sample, that may affect the determination of cross-sections. The sample-dependent background, especially important in capture measurements, is mainly caused by neutrons and γ-rays, scattered by the sample, that reach the detectors.

Figure 2.9 – The sweeping magnet on the n_TOF beam line [49].

2.2 n_TOF neutron beam characteristics

In a facility such as n_TOF, which has the objective of measuring neutron cross-sections with a high degree of accuracy in a wide energy range, it is very important to produce a neutron beam with a high flux, a wide energy spectrum, low background and good time resolution (which directly reflects in the neutron energy resolution). The most important factor that determine the characteristics of the neutron beam is the interplay between the spallation target and the (water) moderator. Extensive studies and simulations of the neutron production mechanism in the spallation target have been performed in order to obtain the optimal configuration of the target-moderator assembly, so to reach the best performance in terms of flux, energy spectrum and energy resolution of the neutron beam. Two codes have been used to this purpose: the intranuclear cascade code FLUKA [57] coupled with Energy Amplifier Monte Carlo code EA-MC [58, 59] and MCNPX [60]. This last code has been used only for flux comparison, while FLUKA/EA-MC have been employed extensively for the design of the facility and for predicting the characteristics of the neutron beam. In both codes, the detailed geometry of the lead spallation target and of the TOF tube is implemented. FLUKA is able to generate spallation neutrons (and all other secondary particles) and transport them from the production energy down to the cut-off energy of 19.6 MeV; at this point EA-MC comes to play and transport neutrons down to thermal energies using pointwise evaluated nuclear data tables.

2.2.1 Neutron flux

The neutron flux for various Pb target configurations with and without a water moderator layer of 5 cm is shown is Fig. 2.10. As expected, for pure Pb target without post-moderation the flux is mostly concentrated at high energy. On the contrary, using a hydrogen rich moderator, such as light water, an isolethargic behavior between $\sim$1 eV and 200 keV is achieved. The final configuration chosen for the spallation target ($80\times80\times60$ cm^3 block with 5 cm water layer) produces the flux distribution in red in Fig. 2.10, with a peak at low energy due to the moderation process and another one around $\simeq$1 MeV related to neutron evaporation from the spallation target. The simulation results presented in Fig. 2.11 show the neutron flux in the experimental area (in units of $dn/d\ln E$/cm^2/7×10^{12} protons). The two codes give similar results, especially in the energy range between 1 eV and few MeV. The discrepancy in the high energy part ($\geq$100 MeV) between FLUKA and MCNPX could be due to some difference in the physics models and nuclear data used by the two codes. MCNPX represents better the thermal part, since it includes a complete representation of the thermal neutron scattering by molecules and crystalline solids [60]. It has to be considered that a gravitational cut-off occurs for neutrons of kinetic energy lower than 0.02 eV [49], due to the geometry of the beam pipe.

The experimental measurement of the neutron flux performed with various detectors and techniques during the commissioning of the facility showed a disagreement between the predictions of the simulations and the experimental results of the order of 20%, particularly evident in the isolethargic region between $\sim$1 eV and 100 keV. It turned out, after a target investigation performed in 2006, that the actual moderator

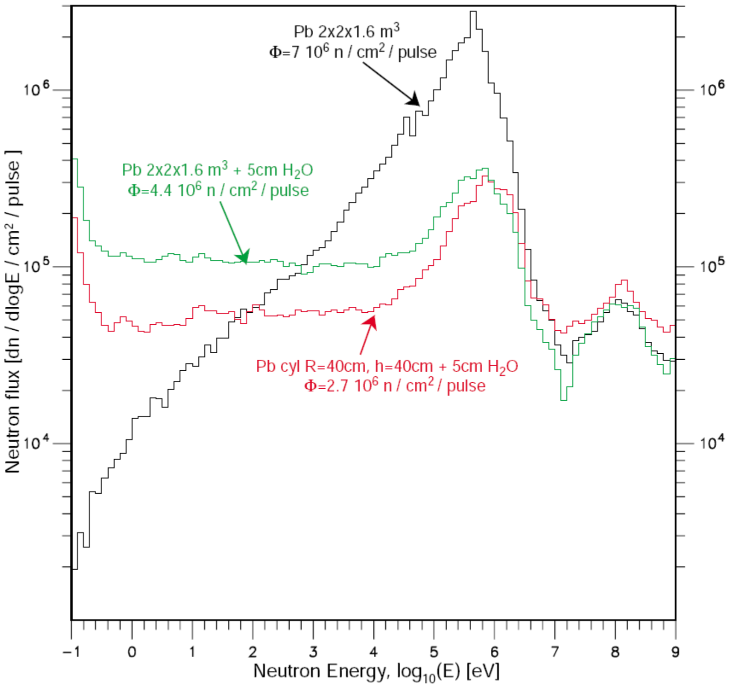

Figure 2.10 – Neutron energy distribution for different types of Pb target geometries and water moderator configurations. More details on the simulations can be found in Ref. [54].

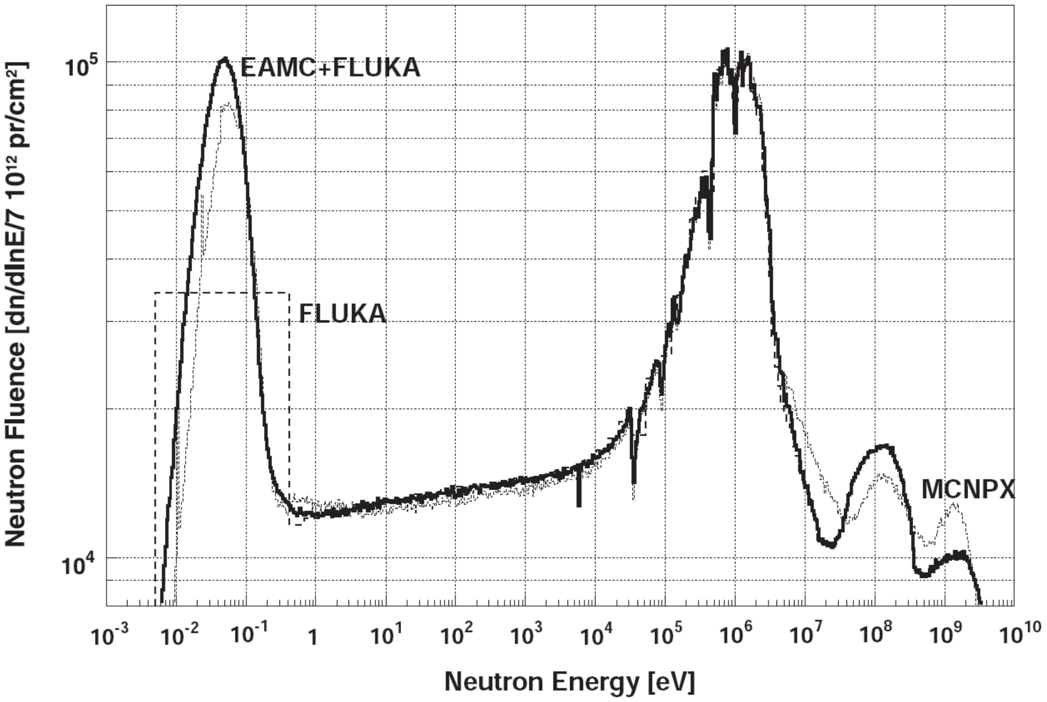

Figure 2.11 – Uncollimated neutron fluence at n_TOF, estimated from Monte Carlo simulations performed with different codes: FLUKA/EA-MC (continuous bold line), FLUKA alone (dashed line), recognizable by the single thermal group, and MCNPX (small dashed line) [55].

thickness in front of target was $\simeq$5.8 cm instead of the 5 cm chosen in the design. Simulation performed later on with the correct thickness showed a much better agreement with experimental results [61]. The dips present at $\simeq$30 keV, $\simeq$100 keV and $\simeq$200 keV are due to absorption in the aluminum window between the target and the TOF tube, while those at $\simeq$500 keV and $\sim$1 MeV are caused by the oxygen content in the moderator.

According to simulations, the number of produced neutrons per incident proton is on the order of 300; however only a fraction of this number, close to 25%, enters the TOF tube toward the experimental area. Since a supercycle contains at maximum 4 dedicated bunches of 7×10^{12} protons each, the total number of produced neutrons over a time interval of 14.4 s is $\simeq1.9\times10^{15}$. It is worth noticing that this number is orders of magnitude higher as compared to other existing facilities, and allows to use longer flight path. In fact, in the experimental area, located at 187.5 m from the Pb target, the uncollimated neutron flux is $\simeq6\times10^5$ neutrons/cm^2/pulse, a value comparable to that available at other facilities at a much shorter flight base. For the small diameter capture collimator the total fluence is of the order to 10^6 neutrons/pulse, while for the larger aperture collimator used in fission measurement the fluence is $\sim8\times10^6$ neutrons/pulse [49]. In Fig. 2.12(a) a comparison between the average flux at different facilities, namely GELINA at IRMM (Institute for Reference Materials and Measurements) in Geel, Belgium and the Manuel Lujan Neutron Scattering Center at Los Alamos National Laboratory, is presented. As mentioned, the n_TOF flux at 200 m is comparable to the one available at other facilities at shorter distances from the production target, with the consequence that the n_TOF neutron beam has a better energy resolution for the same neutron fluence. A more noticeable result is reported in Fig. 2.12(b). The n_TOF neutron flux is concentrated in bunches of $\sim$80 ms length (corresponding to the time-of-flight of thermal neutrons), separated by a minimum of 2.4 s (thanks to the low duty cycle of the PS accelerator complex), thus eliminating almost completely the problem of wrap-around between bunches, present in other time-of-flight facilities such as LANSCE. Furthermore the instantaneous neutron flux, i.e. the neutron flux per proton bunch, is extremely high, nearly three orders of magnitude higher than that of GELINA. This is one of the most important and innovative features of the n_TOF neutron beam, since it allows accurate measurement of radioactive samples, which would be very difficult to measure anywhere else. In fact, the natural radioactivity of the sample produces a background component that could strongly affect the measured cross-sections. A very high instantaneous neutron flux maximizes the signal-to-background ratio. The advantage of the n_TOF facility in this respect is evident.

Simulations and experimental measurements shows that the n_TOF neutron beam

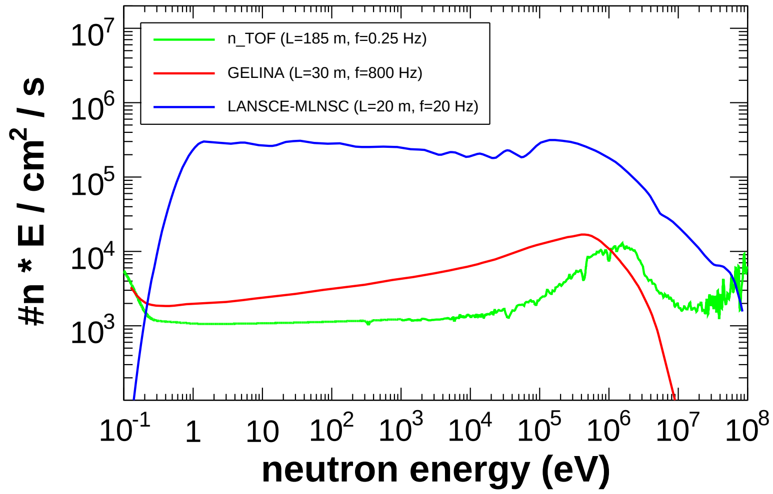

(a) Average neutron fluxes comparison (at different TOF length).

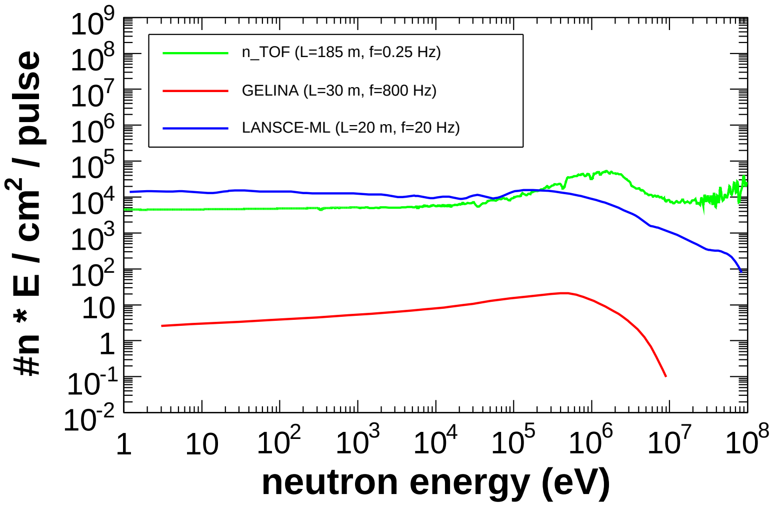

(b) Instantaneous neutron fluxes comparison (at different TOF length).

Figure 2.12 – Comparison between average and instantaneous neutron flux at _TOF, GELINA and LANL-MLNSC (Manuel Lujan Neutron Scattering Center). Figures courtesy of F. Gunsing.

profile can be approximated by a gaussian in two dimensions. However, due to the angular distribution of neutrons emitted from the Pb target (caused also by the 10° angle between the proton beam and the TOF tube), the size and shape of the beam depends on the neutron energy, with a beam profile progressively smaller with increasing neutron energy [62, 63].

2.2.2 TOF method and neutron beam energy resolution

The time-of-flight technique consists in the determination of the neutron kinetic energy via the measurement of the time difference between its production and its interaction. In the general relativistic case, the following time-energy relation is applied:

$$E_n = E_{tot} - m_n c^2 = m_n c^2 \left(\frac{1}{\sqrt{1-\beta^2} - 1} \right) \quad \text{with} \quad \beta = \frac{v_n}{c} = \frac{L}{cT} \tag{2.1}$$

where T is the time of flight of the neutron and L the flight path. In the non-relativistic case, that is for energies lower than $\simeq$100 keV, the classical expression can be used:

$$E_n = \frac{1}{2} m_n \left(\frac{L}{T} \right)^2 \approx \left(72.29826 \times \frac{L(m)}{T(\mu s)} \right)^2 \tag{2.2}$$

In general, at a time-of-flight facility, the energy resolution depends on the uncertainty in the determination of the neutron flight path and on the time resolution of the primary beam. In the case of n_TOF, mainly two factors enter into play: the moderation process both in the Pb spallation target and in the water, and the time resolution of the proton beam, with the last one important only at high energy, i.e. above 1 MeV. At low energy the most important contribution comes from the process of neutron slowing down in the spallation target and in the water moderator. Since the scattering cross-section in Pb is approximately constant below 10^4 eV, where the elastic scattering dominates, a correlation exists [64, 65] between the slowing-down time and the neutron energy inside of the Pb block ($E_n \propto \frac{1}{(t+t_0)^2}$, where t_0 is a experimentally fitted constant). It is therefore possible to introduce an effective neutron path λ inside the target, correlated with the velocity of the neutron v_n after the moderator, and t, the time elapsed since neutron creation (in our case since the arrival of the proton beam on target), so that:

$$\lambda = v_n \times t \tag{2.3}$$

The meaning of λ can be described in two ways. It can be considered that an amount equal to λ is added to the geometrical flight path length L, so that the total "apparent" flight path is equal to $\lambda + L$. Alternatively one can think of an imaginary neutrons source located in the outer face of the lead block at a distance, with respect to the real source, equal to $-\lambda$ along the TOF direction. Since, as predicted from the simulations in the case of the n_TOF spallation target, λ varies proportionally to $\sqrt{E_n}$, adding an offset t_0 on the measured time-of-flight is sufficient to account for the dependence of λ on the energy.

Due to the fact that moderation is a stochastic process, there is an intrinsic uncertainty associated with the moderation time, or, equivalently, an uncertainty in the "apparent" flight path, defined as $\Delta\lambda = v_n \times \Delta t$, where Δt is the uncertainty in the moderation time, for a given neutron energy. Fig. 2.13 shows $\Delta\lambda$ as a function of the neutron energy.

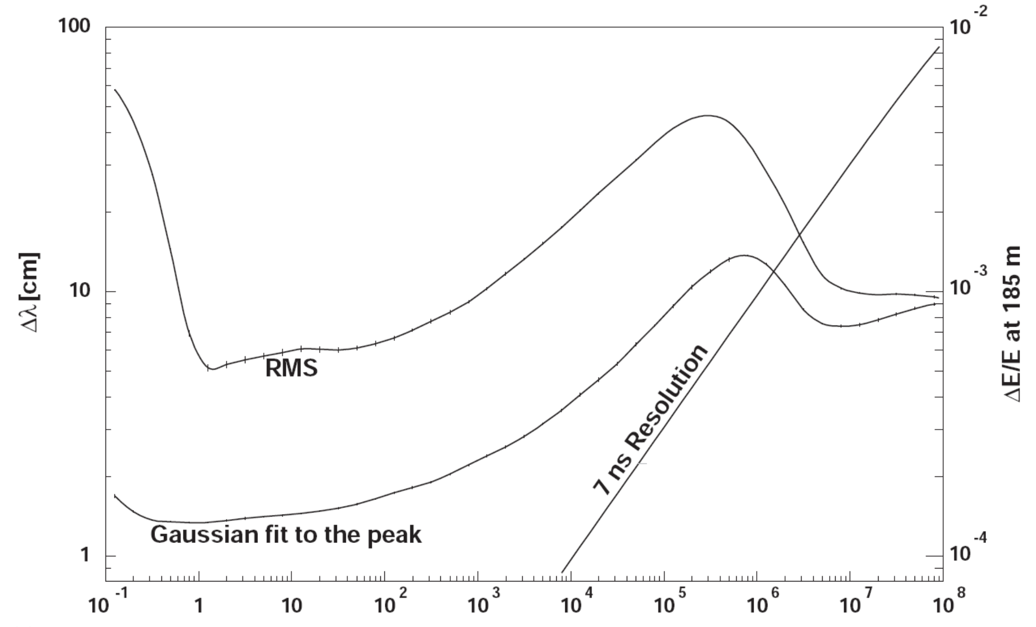

(b)

Figure 2.13 – Plot of the different components of the neutron beam resolution at 185 m, as a function of the neutron energy. Note that the 7 ns time resolution of the proton beam becomes dominant for neutron energies above few MeV [55, 49].

For all pulsed neutron facilities, the resolution function of the neutron beam at a given neutron energy E_n is defined as the time spread of neutrons with energy E_n coming out from the target-moderator assembly [66]. For convenience, the resolution function can be expressed in terms of the distance λ. In the classical approximation, it is defined by the following relation:

$$\Delta E_n = 2E_n \times \left[\left(\frac{\Delta L}{L} \right)^2 + \left(\frac{\Delta T}{72.29826L} \right)^2 E_n \right]^{1/2} \tag{2.4}$$

where ΔL is the uncertainty in the effective length of the flight path and ΔT is the uncertainty in the measured time-of-flight (typically dominated by the time resolution of the proton beam striking the target). Using the classical expression for the time-to-energy relation, Eq. 2.4 yields:

$$\frac{\Delta E_n}{E_n} = \frac{2}{L} \times \sqrt{(\Delta L^2 + (1.91313 \cdot 10^{-2})\, E_n\, \Delta T^2)} \tag{2.5}$$

where E_n, the energy at which the resolution is estimated, is measured in eV, L and ΔL in m, and ΔT in μs. Considering only the resolution of the target-moderator assembly and assuming only an uncertainty in the moderation length λ, it is possible to write the formula for the energy resolution as:

$$\frac{\Delta E_n}{E_n}|_{mod} = 2 \times \frac{\Delta\lambda}{\lambda + L} \tag{2.6}$$

As evident from Eq. 2.6, a higher resolution could be obtained increasing the flight path L (although at the expenses of the neutron flux). Another method commonly used relies on moderation in water, thanks to the optimal slowing down properties of hydrogen, that allow neutrons to reduce their speed without significantly increase in the moderation time. In Ref. [54] it is shown how the addition of 5 cm of water moderator produces a significant improvement in the neutron energy resolution with respect to a bare Pb block, from $\frac{\Delta E_n}{E_n}$ =5×10^{-3} at 1 keV for the bare Pb to $\sim1\times10^{-4}$ for the water moderated target.

The assumptions mentioned before are only valid for low neutron energies. As shown in Fig. 2.13, the resolution is dominated by the uncertainty on λ below 1 MeV, while beyond this value the time resolution of the proton bunch (7 ns) becomes predominant.

It is worth noticing that an energy resolution comparable to the n_TOF neutron beam can be obtained, choosing the appropriate flight path, also at other facilities. The main advantage of n_TOF is the combination of a good resolution with a reasonable flux at 200 m distance.

2.3 Background evaluation

The background is one of the most important characteristics that must be taken into account at a time-of-flight neutron facility, since it may strongly affect the accuracy of cross-section measurements.

At a time-of-flight facility, one of the most significant "background" contribution is related to the overlapping between contiguous neutron bunches; in this case slow neutrons belonging to one bunch can be misidentified as fast neutrons of the subsequent bunch. This is a serious issue in facilities with high repetition rate, such as ORELA at Oak Ridge and LANSCE at Los Alamos National Laboratory. However, at n_TOF, due to the low repetition rate of the PS, this type of background is practically absent. In fact, the minimum time separation between two proton bunches, 1.2 s, is much longer than the time-of-flight of the slowest neutrons of 0.025 eV energy, which corresponds to $\approx$85 ms.

Two types of background are present at n_TOF: the "facility" background, related to the configuration of the beam line and to the production method, and present only with the beam in the experimental area, and a sample-related background. The first one is an intrinsic "characteristic" of the facility and is independent of the single measurement being performed, while the second strictly depends on the sample being measured. Its consequences will be discussed in the following chapters, while describing the experimental apparatus and the results. The various background components act differently depending on the type of measurements and on the employed detector; in particular, neutron capture measurements are greatly affected by γ-ray background, while fission setups are very sensitive to neutron background, while relatively insensitive to γ-rays.

As far as the "facility" background is concerned, a further distinction can be made between "inside" and "outside" beam components. The biggest contribution to the in-beam component comes from highly energetic charged particles that are not deflected by the sweeping magnet and from γ-rays directly propagating from the spallation target. The result of both components is a "prompt" flash (also called γ-flash), arriving in the detector area $\simeq$600 ns after the proton beam impinges on the spallation target. The prompt flash is essential for a proper time of flight calibration, but its presence has the drawback that, if it is too strong, it could significantly increase the dead-time of detectors, making them blind to high energy neutrons. γ-rays are also present at later times since they are produced in neutron capture or inelastic reactions inside the lead target or in the water moderator tank; this component is mainly an issue in capture measurements, and does not constitute a significant background for fission measurements. Outside the neutron beam, the most significant contribution to the background comes from neutrons leaking through the concrete shielding walls toward the experimental area and from γ-rays and neutrons that, after being scattered on the beam pipe or on the walls of the time-of-flight tunnel, enter the detector station through the vacuum tube.

An additional background component originates from muons, produced after the interaction of the proton beam in the n_TOF target, which triggers neutrons production inside the experimental area, due to μ^- capture in the various materials and in the walls. The μ^- component is greatly reduced by the presence of a 3 m thick iron shielding wall located just after the sweeping magnet; Fig. 2.14 shows the effectiveness of this additional component in reducing the muon flux along the beam line [55, 49].

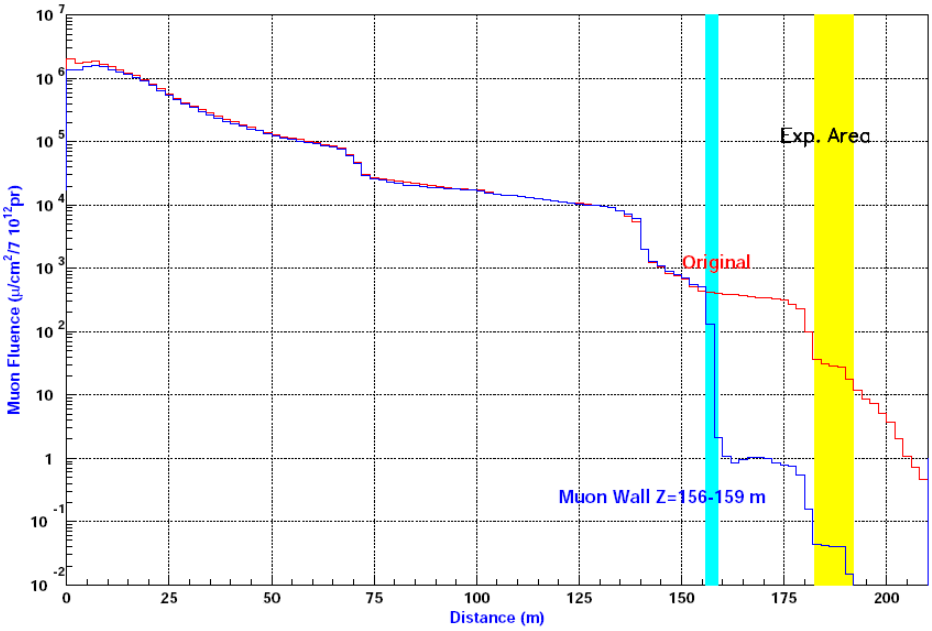

Figure 2.14 – Simulated muon fluence (n/cm^2) along the time-of-flight tunnel, for a proton bunch of $7{\times}10^{12}$ protons with and without an additional iron shielding at 160 m from the spallation target. The large reduction in the muon flux produced by the wall is evident [67].

Another source of neutron background comes from backscattering of neutrons in the experimental area after they have reached the end of the n_TOF beam pipe: since the mean free path of neutrons in air is 20 m, even few meters of air could introduce a background from backscattered neutrons at the level of a few percent. Simulations have shown that 8 m of vacuum line after the detector station and a concrete separation wall are enough to suppress such a background. The polyethylene box at the end of the tube further reduces this component.

As already pointed out in § 2.2.2, due to the large dimension of the spallation lead target, a fraction of the neutrons are emitted with a time-of-flight bigger than expected from their energy. These delayed neutrons will contribute to slightly modify the shape of neutron resonances. This contribution, which is typically included in the parametrized resolution function, can be taken into account when evaluating resonance parameters, by including it in the appropriate codes, such as SAMMY [68].

Charged particles and γ-rays are copiously produced in the spallation target. As already mentioned, the fluence of charged particles is strongly suppressed by the sweeping magnet located at 145 m from the spallation module. The simulated momentum distribution of the charged particles is reported in Fig. 2.15(a), together with that of neutrons. A significant fraction of muons have momentum above 2 GeV/c. These muons would certainly produce ionization signals, especially in gas detectors, but since they come as a ″prompt″ signal, in principle they don't affect the measurement of fission cross-section for energies below a few MeV.

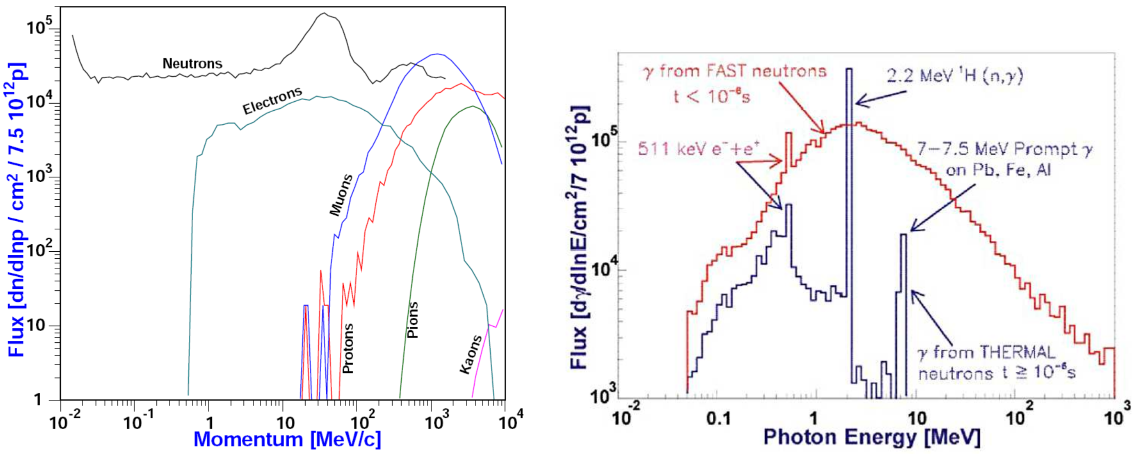

(a) Neutrons and charged particle energy distribution

(b) γ-ray flux and components

Figure 2.15 – 2.15(a): fluxes of neutrons and of secondary charged particles produced by the spallation process as a function of their momentum at the sweeping magnet location [67]. 2.15(b): photon energy distribution for the fast and thermal neutron component at 200 m from the spallation target.

The γ-ray background, mainly related to the in-beam photon component generated by the neutron capture by lead and H in the water moderator and due to annihilation processes, can be separated in two groups [49, 67]: a ″fast″ component direct consequence of the spallation process, arriving at times below 1 μs after the protons impinge onto the spallation block, and a ″slow″ component arriving at times between 1 μs up to 100 μs, mainly caused by thermal and epithermal neutron capture by various elements in the Pb block and water moderator. The ″fast″ component provides a mean for accurately calibrate the time of flight scale, while ″slow″ component, peaking at the time-of-flight corresponding to keV neutrons, is more that 1 order of magnitude lower than the neutron flux [49]. The energy spectrum of these photons (shown in Fig. 2.15(b)) shows that a large contribution comes from neutron capture on hydrogen, producing 2.2 MeV γ-rays, while a smaller fraction comes from capture on lead, aluminum of the target tank/windows and in the iron target support. This component does not practically affect fission cross-section measurements.

2.4 Comparison between different neutron facilities

In this section a comparison between different operating white spectrum neutron facilities for the cross-section measurement is proposed. In all cases the neutron energy is determined by the time-of-flight method. The main facilities here described are:

- Los Alamos Neutron Science Center (LANSCE), Los Alamos, USA. Three neutron beams are available: the Manual Lujan Neutron Scattering Center (MLNSC), the Weapons Neutron Research Center (WNR) and the Lead Slowing Down Spectrometer (LSDS). In all cases neutrons are produced by spallation of 800 MeV protons on tungsten targets. At the Lujan Center, cold thermal and epithermal neutrons in the meV-keV range are available, primarily for neutron scattering and nuclear science research. The WNR Facility is primarily used for basic and applied nuclear science. Neutrons are available with energy between 100 keV and 600 MeV, and are collimated to form beams for six flight paths viewing the neutron sources at different angles. The LSDS is used for measurements of neutron-induced reactions with neutron intensities over 1000 times greater than those in conventional beam-target experiments; neutrons in this case are produced by the pulsed 800 MeV proton beam striking a tungsten target in the center of 20 ton cube of pure lead. The usable neutron energy range starts from ≈1 eV and extends to more than 100 keV. Although the energy resolution at LSDS is bad (∼30%), it is possible to measure fission cross-sections on samples of 10 ng or less.

- ORELA: Oak Ridge Electron Linear Accelerator at Oak Ridge National Laboratory, USA. The neutron beam is produced with (γ, n) reactions from bremsstrahlung radiation generated by an electron beam on a tantalum radiator. Intense bursts of neutrons are produced with energies between 10^{-3} eV and 100 MeV. Pulse widths from 2 to 30 nanoseconds are available at repetition rates from 1-1000 pulses/second. Moderated or unmoderated neutrons can be produced, and the spectral shape of the neutron distribution can be tailored with movable filters. ORELA is primarily used to measure neutron cross-sections with high energy resolution in the resonance region for many isotopes.

- GELINA: Geel Electron-driven LINac Accelerator at the EU-JRC-IRMM institute in Geel, Belgium. Neutrons are produced by (γ, n) and (γ, f) reactions in a mercury-cooled depleted uranium target; the energy distribution of neutrons emitted by the target ranges from subthermal up to 20 MeV, with a peak between 1 and 2 MeV. In order to produce a spectrum with significant flux below

Table 2.2 – Partial comparison of n_TOF with other experimental facilities (data extracted from Ref. [69, 70, 71, 72]). The n_TOF facility is the only neutron source allowing to cover the whole energy range in a single measurement, thus minimizing errors related to the normalization procedure.

Facility	Energy (MeV)	Rep. rate (Hz)	E_n range	Δt (ns)	L (m)	P_{max} (kW)
MLNSC	800, p	20	~meV-~keV	125	7-50	80
WNR	800, p	1-100	100 keV-600 MeV	0.25	8-90	3.2
LSDS	800, p	1-100	1 eV-100 keV	0.25-125		0.8
ORELA	180, e	1-1000	1 meV-100 MeV	4-30	8-200	50
RPI	60, e	1-500	0.01 eV-2 keV 0.2-20 MeV	7-5000		2.7
GELINA	100, e	800	subthermal-20 MeV	1	10-400	
n_TOF	20 (GeV), p	0.25	thermal-500 MeV	7	185	6.2

100 keV, an hydrogen-rich moderator is added. Moderated or unmoderated neutron beams are shaped by means of collimators and their energy selected with the help of shadow bars and movable filters. Twelve neutrons flight paths are available from 10 m to 40 m, which allow a good choice of flux and resolution functions.

- RPI: Gaerttner Linear Accelerator at the Rensselaer Polytechnic Institute (RPI), United States, where, as in the previous case, neutron are generated via (γ, n) and (γ, f) reactions.
- n_TOF (neutron Time-Of-Flight) facility at CERN, Switzerland.

Several more facilities are available in the world, among which the GNEIS neutron time-of-flight spectrometer in Gatchina, St. Petersburg, Russia, while others are in the construction phase, like the JPARC complex in Japan.

Most of the facilities are flexible, especially for the choice of repetition rate and flight path. Additionally, in some cases (e.g. ORELA), moderated or unmoderated neutron spectrum can be provided, with the possibility to tailor the spectral shape of the neutron distribution with movable filters [73]. The neutron flux at the source and at the experimental location depends on the choice of the flight path length, filters, collimation systems, etc. Fig. 2.16 [69] shows the maximum source intensity of different facilities, and represents the potential average flux that can be obtained if no other limitations are present. Effects that come into play in limiting the useful flux include background, resolution, collimation systems, flight path length and bunch wrap-around.

It should be considered, however, that the average flux alone is not sufficient for a meaningful comparison of facility's performances, since the resolution has to be taken

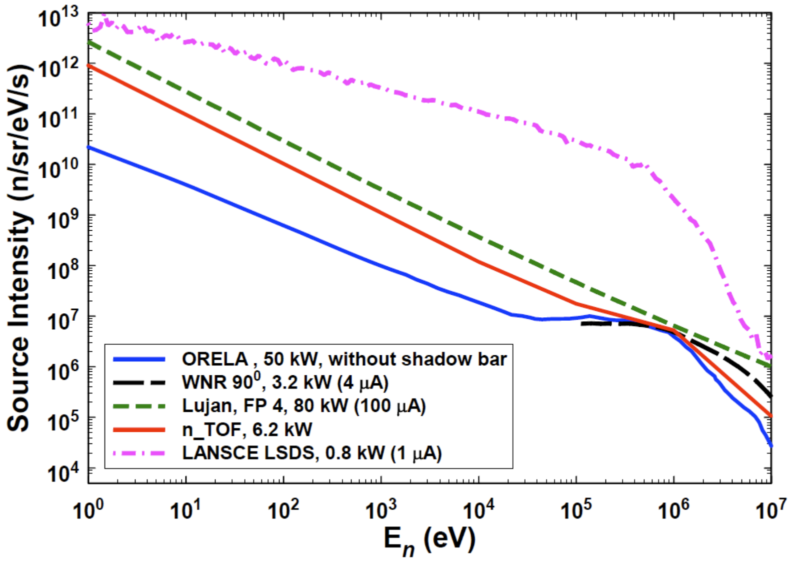

Figure 2.16 – Comparison of average neutron fluxes at the source position for different existing facilities. Plot taken from Ref. [69].

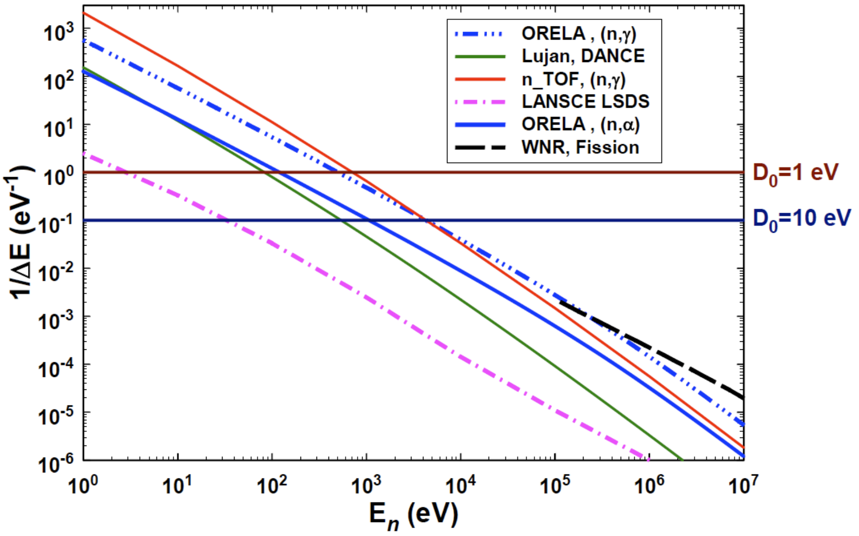

Figure 2.17 – The energy resolution of the neutron beams available for experiments in different facilities. For comparison the value of D_0 - the average level spacing of s-wave resonances - for the ^{241}Pu (∼1 eV) and for the ^{240}Pu (∼10 eV) isotopes is also shown. Plot taken from Ref. [69].

into account as well. Fig. 2.17 [69] shows the energy resolution of the experiments, expressed as $\frac{1}{\Delta E}$, with typical experimental conditions and calculated with Eq. 2.4. As expected, from Figs. 2.16 and 2.17 it can be seen that facilities with the highest average flux are characterized by the lowest resolution and viceversa. As already pointed out, however, the great advantage of the n_TOF facility is the very high value of the instantaneous flux, which gives unprecedented good signal/background ratio with respect to previous experimental facilities, in particular for the measurements of radioactive isotopes and low mass samples.

Chapter 3

The experimental fission setup

3.1 Neutron fission cross-section

The probability that a nuclear reaction takes place can be expressed in term of the cross-section (σ), which represents the reaction rate (r) produced by n neutrons travelling - with speed v_n - a distance dx (that is with a flux $\Phi = nv_n dx$) in a material with N nuclides per unit volume.

$$\sigma \equiv \frac{r}{nv_n N dx} = \frac{r}{\Phi N} \tag{3.1}$$

The dimension of σ is an area, which gives rise to the concept of σ as a cross-sectional area presented to the neutron by the target nucleus. The unit for the cross-section is historically given in multiple of 10^{-24} cm^2, referred to as *barn*[1] . The cross-section varies according to the type of the target nucleus, to the type of reaction involved and to the kinetic energy of the incident projectile.

Neutron cross-sections can show variations even of several orders of magnitude over an energy range of few eV; such variations are typically associated with resonances. The nature of the resonance structures observed at low incident neutron energies is related to the excitation of nuclear states in the compound nucleus (CN) formed by the neutron and by the target nucleus at excitation energies located above the binding energy of the last neutron (S_n), which is usually of the order of several MeVs. An excited level shows up as a resonance in the cross-section when the

---

[1] The unit was named by M. G. Holloway and C. P. Baker in December 1942. A value of 10^{-24} cm^2 was already being used as a unit for nuclear cross-section from the work in the Manhattan Project, but it had no name. Holloway and Baker considered and rejected the names ″bethe″ (disregarded due to similarity to the Greek letter β) and ″oppenheimer″ (too long), and finally arrived at ″barn″ because the size of 10^{-24} cm^2 ″for nuclear processes was really as big as barn″ [74].

excitation energy, defined as:

$$E^* = S_n + \frac{A}{A+1} E_n \tag{3.2}$$

(where E_n is the neutron kinetic energy), corresponds to an excited state of the CN (see Fig. 3.1). The corresponding life time of the CN is of the order of $\tau = \hbar/\Gamma \simeq 10^{-15}$ s (where Γ is the width of the resonance), which is several order of magnitude larger than the time needed by a neutron to cross the nucleus unperturbed. It is commonly assumed that the decay mode and the decay probabilities are independent from the formation of the CN (except for energy and angular momentum conservation). The decay probability is thus proportional to the ratio Γ_i/Γ, where Γ_i is the decay width through the i^{th} channel.

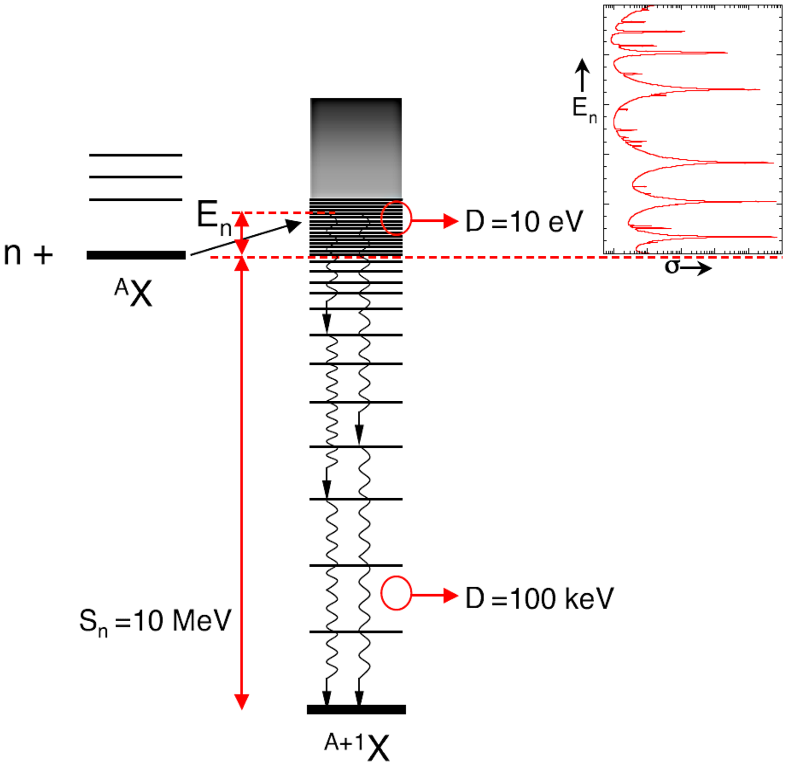

Figure 3.1 – Pictorial representation of the formation and decay of a compound nucleus, produced by neutron-induced reactions, with typical values of neutron separation energies and level spacings. The resonances observed in the reaction cross-section corresponds to the excitation of a given excited level above the neutron binding energy. Figure taken from [75].

Under the preceding assumptions, the cross-section for a given (n, i) channel is given by:

$$\sigma_{(n,i)} \equiv \sigma_i = \sigma_{CN}(E) \frac{\Gamma_i(E^*)}{\Gamma(E^*)} \tag{3.3}$$

where $\sigma_{CN}(E)$ is the cross-section for compound nucleus formation.

The fission cross-section, σ_f is a measure of the probability that a neutron impinging on a nucleus forms a CN which then decays through fission. Due to the pairing effect, the excitation energy of the CN formed by neutron absorption on an odd-A nucleus is generally higher than for an even-A nucleus. This leads odd-A nuclides to have a significantly larger cross-section that even-A nuclei, and more importantly, results in fissionable nucleus even at zero incident neutron kinetic energy, being the excited level above the fission barrier. A non fissionable nucleus, such as ^{234}U or ^{238}U, may still have a cross-section with resonances below the fission threshold, but its value is usually very small.

As an example, fission cross-section of ^{235}U and ^{238}U are reported in Fig. 3.2: it is evident the presence, for ^{235}U, of the resonance structure that corresponds to the population of excited states of the CN. It should be considered that all reactions that proceed through the formation of a given CN show resonances at the same energies, corresponding to the excitation of nuclear levels in the CN. Nevertheless the strengths and shapes of resonances are different, and related to the intrinsic width of the reaction channel.

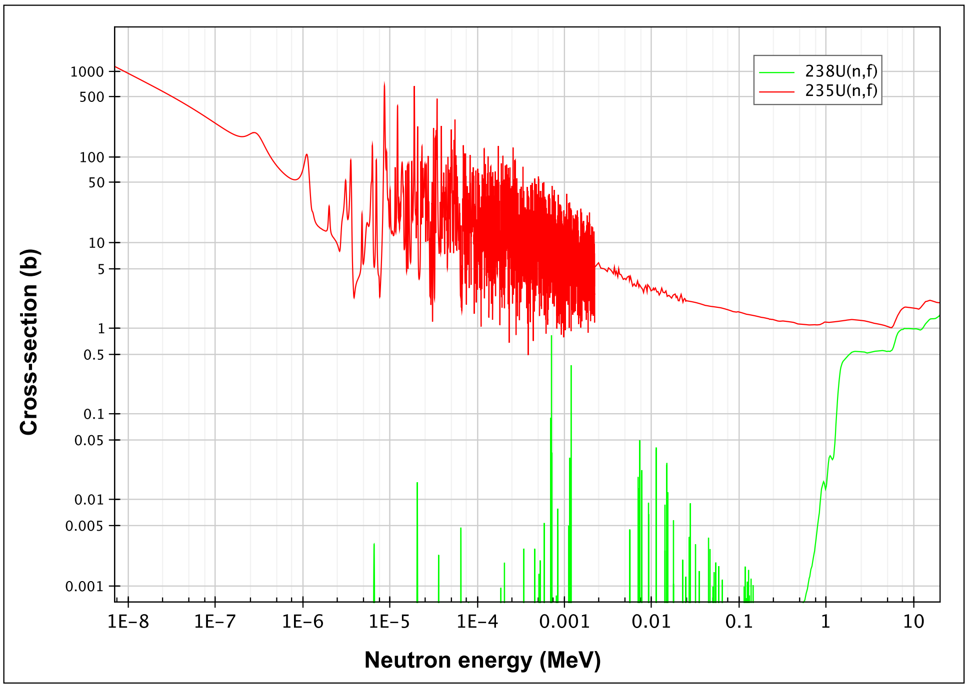

Figure 3.2 – Neutron-induced fission cross-section of ^{235}U (red line) and ^{238}U (green line). The fission threshold in the even-even isotope is evident. The cross-section for both isotopes are considered standard and used as reference in most fission measurements [76, 77].

In the case of a single isolated resonance, the shape of the absorption peak is described by the Breit-Wigner formula, which is the typical shape for any quantum-mechanical state with a finite lifetime. The cross-section for the general reaction $a + X \rightarrow b + Y$ (assuming it goes through a CN state), is given by [78, 79]:

$$\sigma_r(E) = \frac{\pi}{k^2} g \frac{\Gamma_{aX}\Gamma_{bY}}{(E_n - E_0)^2 + \Gamma^2/4} \tag{3.4}$$

where k is the wave number (connected with the momentum by $p = \hbar k$), E_n the kinetic energy of the incident neutron, E_0 the resonance energy, g the spin factor, Γ_{aX} the partial width for the entrance channel and Γ_{bY} the partial width for the exit channel. Γ^2 (with $\Gamma = \sum_i \Gamma_i$ sum of all partial widths) is related to the decay width of the resonant state and thus to its decay time.

For an isolated resonance with $l = 0$, in which the open channels are the elastic, capture and fission, the total cross-section according the Breit-Wigner formula is given by [75]:

$$\sigma_{tot}(E) = 4\pi R^{'2} + \frac{\pi}{k^2} g \left(\frac{4k\Gamma_n \left(E_n - E_0\right) R^{'} + \Gamma_n^2 + \Gamma_n\Gamma_\gamma + \Gamma_n\Gamma_f}{(E_n - E_0)^2 + \Gamma_{tot}^2/4} \right) \tag{3.5}$$

where Γ_n is the neutron width, Γ_γ the radiative width, Γ_f the fission width and g the statistical spin factor. The first term of the sum is the potential scattering cross-section $\sigma_p = 4\pi R^{'2}$, where $R^{'}$ is the effective nuclear radius.

In the context of reactor physics it is common to distinguish the neutron energetic domain into four regions, starting from 10^{-2} eV to 20 MeV (and above in the case of ADS), taking as a reference Fig. 3.2:

- *Thermal Region*: around a few tens of meV and generally below $E_n \leq$1 eV. For isotopes with mass from intermediate to heavy (25 $\lesssim$ A $\lesssim$ 92), the cross-section has a $1/\sqrt{E_n}$ behavior in this energy range. This region is of great importance for reactor physics where the moderated neutrons are in thermal equilibrium with the water, with a Maxwell-Boltzmann velocity distribution peaked at an equivalent kinetic energy $k_B T$. For an ambient temperature of nearly 300 K, this corresponds to 0.0253 eV or a velocity of 2200 m/s. The thermal cross-section at 0.0253 eV is a relevant quantity for reactor physics, and can be accurately measured in reactor experiments with only small amounts of material.

- *Resolved Resonance Region* (RRR): the cross-sections shows resonant structures due to the population of CN levels in the energy range 1 eV $\lesssim E_n \lesssim$10 keV for heavy nuclei and in the MeV region for light nuclei. The nuclear system is extremely complex and no nuclear model is capable of predicting the position and the properties of the excited states; the value of the cross-section can therefore be accessed only through measurements. The reaction cross-section is described in terms of resonance parameters, which are the properties of the excited states like energy, spin and parity.

- *Unresolved Resonance Region* (URR): for neutrons with energies above ≃50-100 keV, the number of accessible states of the CN is so large that their spacing is small compared to their width, so that the levels starts to overlap. A CN is still formed but it involves a continuum of overlapping states and the cross-section then varies smoothly with the neutron energy. In this case average values of the states can be predicted by nuclear models, so that the measured cross-section can be used to validate parameters of these models.

- *Fast domain*: for $E_n \geq$1 MeV many more decay channels open up: the "steps" in the fission cross-section visible above 1 MeV are due to the opening of the (n, xnf) channels (x =1 referring to the second-chance fission, x =2 third-chance fission etc...).

As an example, in Fig. 3.2 the neutron fission cross-section of ^{235}U is shown on an energy scale spanning over more than 8 decades (the plotted values are taken from a library). Resonances are clearly visible in the low energy part while a smooth cross-section is observed at higher energies (above 1 keV). The sudden transition between these two regions (that is from the RRR to the URR) is not physical but related to a different parametrization of the cross-sections, i.e. in the RRR by means of resonance parameters, while in the URR by means of interpolated points. Furthermore, the separation between the two regions is somewhat arbitrary, with different libraries adopting different limits between the RRR and URR.

At non-zero temperature, the width of the resonances is increased above the natural width of the levels by the thermal motions of the nuclei in the target (or - in the case of a reactor - in the fuel), which gives rise to the so-called Doppler broadening. The resulting resonance in the capture or fission cross-section is the convolution of the natural shape (described by Eq. 3.4) and the Doppler broadening shape function (which takes into account the averaging of the interaction cross-section over the thermal motion of the nucleus). Since the broadening increases with increasing temperature (in such a manner to preserve the area under the cross-section), the height of the resonances (that is the peak value of the cross-section) decreases, with a corresponding decrease of self-shielding effects [16]. This behavior has important consequences on reactor safety [14, 16], because an increase in the fuel temperature determines an increase in the effective capture or fission probability (the so-called negative-feedback Doppler temperature coefficient of reactivity). Self-shielding effects are important also in determining the burn-up efficiency of reactors, and therefore have to be carefully considered in the calculations of the reactor parameters. The effect of resonance self-shielding can be accounted for as long as accurate resonance parameters are given, as a function of the energy, for a specified nucleus and reaction. For this reason high resolution data are of great importance, since they allow to improve the accuracy of the resonance parameters already present in the libraries, as well as providing new parameters in cases never measured before.

3.2 Time-Of-Flight determination

As discussed in § 2.2.2, the time-of-flight method consists in the determination of the neutron energy using the time difference between its production and the detection of a reaction product. Schematically - in the case of the n_TOF facility - the method is shown in Fig. 3.3 representing, as a function of time, the sequence of signals for each proton pulse.

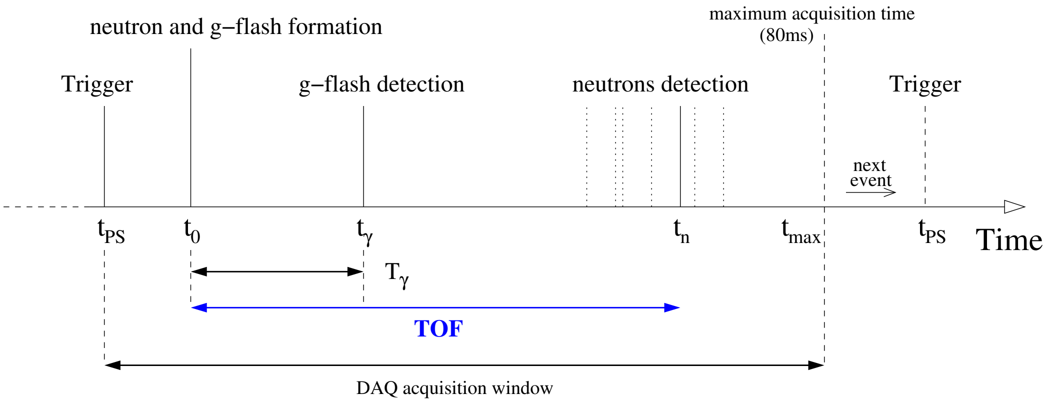

Figure 3.3 – Schematic representation of the different time signals that enter in the determination of the neutron time-of-flight at n_TOF (for each proton bunch).

When the proton beam impinges on the spallation block, at instant t_{PS}, a trigger signal is sent to the n_TOF Data Acquisition System, starting the acquisition window. The neutrons, created at time t_0 in the lead target, cover the flight path L and are detected at instant t_n. The neutron time-of-flight is thus determined by the difference $T = t_n - t_0$. While t_n is accurately measured by the detectors in the experimental area, it is not possible to know precisely the neutron creation time. In order to circumvent this inconvenience it is possible to determine the physical time origin by using the so called "prompt flash". This is the signal generated by photons and highly energetic charged particles, produced together with the neutrons inside the spallation target. The flash is detected in the experimental area, at a distance L from the spallation target, at time t_γ; thus, since the "prompt flash" is travelling at the speed of light, the neutrons creation time t_0 is given by $t_0 = t_\gamma - \frac{L}{c}$. The neutron's time-of-flight (TOF) is then given by:

$$TOF = t_n - t_\gamma + \frac{L}{c} \tag{3.6}$$

It is important to remark that, due to the low duty cycle of the PS accelerator, there is no superposition between the slowest neutrons of a pulse and the fastest ones of the following bunch.

3.3 The n_TOF Data Acquisition

Due to the specific experimental conditions present at the n_TOF facility, namely the high instantaneous neutron flux, a critical element of the setup is the data acquisition and processing system. In fact, in the presence of high count rates - which is a direct consequence of the intense neutron flux - the density of signals in the detectors is very high. Therefore, a high probability of signal pile-up exists. In such experimental context the use of standard Data Acquisition Systems (DAQ) would be inadequate, since they would be affected by a large dead-time. Additionally, pile-up events would not be identified and reconstructed, with the consequence of large systematic uncertainties on the final cross-section data.

According to these requirements, the n_TOF DAQ has been designed based on Flash Analogue to Digital Converters (flash-ADCs or FADC). Their main benefit is the possibility to sample and record the full analogue waveform of the detector signals for each neutron pulse, which can be later processed off-line in order to extract the required informations, such as time of flight, amplitude, charge, baseline and others characteristics of the signal. The use of FADCs allows to keep under control systematic uncertainties associated with the detectors performances, during the off-line analysis. A schematic view of the n_TOF DAQ is shown in Fig. 3.4 and 3.5.

The FADC modules used at n_TOF are the DC240 and DC270 Acqiris Digitizers [81]. The DC270 modules have four data inputs and one trigger input, a maximum sampling rate of 1 GHz (1 sample every 1 ns) and a bandwidth of 250 MHz. The DC240 modules have only two inputs plus an external trigger, but with a sampling rate of 2 GHz maximum (1 sample every 0.5 ns) and a bandwidth of 500 MHz. Both modules have 8 bits resolution. Once the acquisition has been triggered by an external signal, the input data are stored in an onboard buffer of the FADC (one for each channel) with a maximum size of 8 MB (DC270) or 16 MB (DC240). The data stored by the digitizer in its memory buffer contains the full sequence of signals produced within the single neutron bunch. For this reason it is normally referred to as a FADC "movie". For the acquisition of the FIC detector, the DC270 modules are used, with a

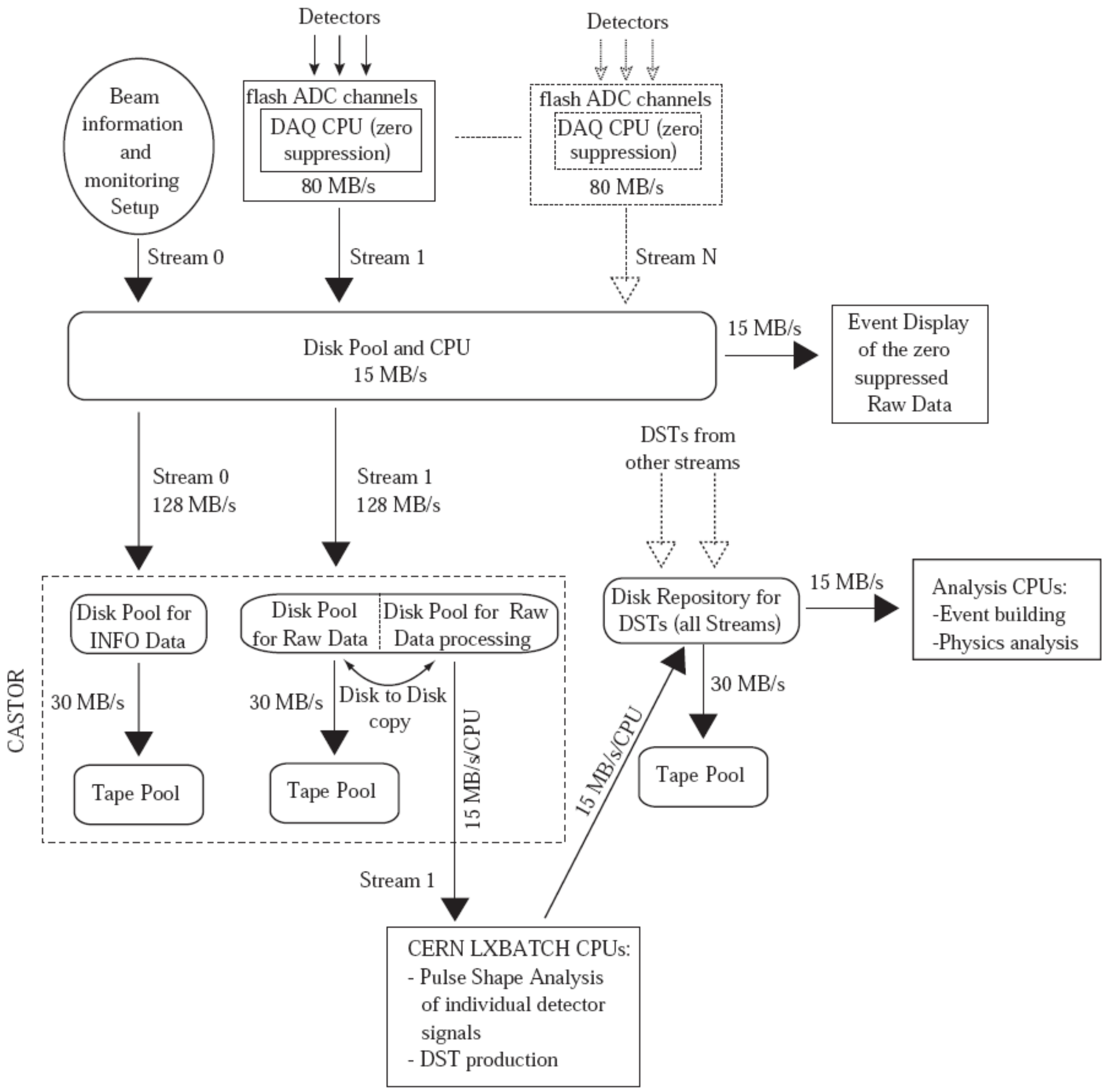

Figure 3.4 – Scheme of the data flow scheme from detectors signals to tape (for temporary and long term storage) and to data processing. Figure from Ref. [80].

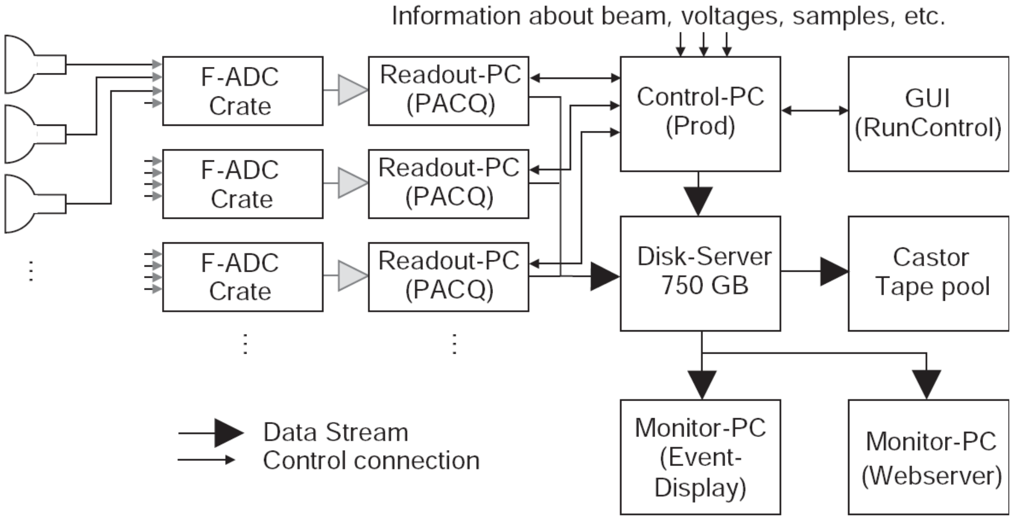

Figure 3.5 – Schematic view of the n_TOF data acquisition system, taken from Ref. [80]. The detector's signals are digitized by FADCs up to 80 ms (depending on the sampling rate). Data are then transferred to readout PCs, which compress and transfer them to the Disk Server using Gigabit links. From the CERN Central Data Recording the raw data are finally stored on to CERN's tape pool CASTOR. A quasi-online monitoring of events is performed by analyzing data temporarily stored on the Disk Server.

sampling rate of 100 MHz; at this rate the buffer is filled after $\simeq$80 ms following the trigger, which, taken into account the n_TOF flight path, roughly corresponds to a neutron energy of $\sim$30 meV.

In order to reduce the large amount of data to be recorded on disk for a single neutron pulse, a software-based zero suppression algorithm is applied to the raw data before they are transferred to disk. The method is in principle simple, since only signals above a predefined threshold are considered valid and stored; in addition a fixed number of samples are recorded preceding the time the signals cross the threshold (pre-sample interval), and after it goes again below it (post-sample interval). They can be used to extract important informations on the baseline value and on the noise. All other data present in the movie are discarded. Therefore, for every neutron bunch, the data copied to memory is constituted by the pre-sample data, followed by the above threshold valid data, and then by the post-sample informations. If a new signal arrives during the post-sample interval of a preceding signal, the post-sample interval is reset to the new value and valid data are recorded until the value falls back again under the set threshold. The speed of this operation is mainly limited by the number of readout PCs and by the FADC readout time, which in turn is limited by the PCI bandwith of 80-100 MB/s. The compression due to the zero-suppression operation mainly depends on experimental conditions (sample-related) and by the detectors, ranging between a factor 2 and 1000.

The group of signals corresponding to one detector for each neutron bunch are buffered and data belonging to 4 or 8 FADC (physically connected to one readout-PC) are grouped into a data stream. Each stream is saved - for each neutron bunch - on a file located in a local temporary disk pool. When the size of this file reaches 2 GB (adopted to minimize occasional data loss, while keeping a reasonably small number of files), all data are transferred, via Gigabit ethernet connection, to the CERN central storage system CASTOR (CERN Advanced STORage system) [82] through CERN Central Data Recording software (CDR) [83]. Once there, the files are independently migrated to tape for long term storage, from where they can be retrieved later on for offline analysis.

During acquisition, a semi-automatic analysis of the raw data is performed for all detectors. Specific algorithms for each detector type are applied for signal reconstruction. As a results of this analysis, Data Summary Tapes (DSTs) are produced, containing all interesting physical parameters, such as time, energy, baseline value and root mean square and others [80]; these DSTs are written and stored on tape at the same time as the raw data. The FIC detectors used for the present work, however, have not been integrated in this analysis scheme, with only raw data written on disk. The simple algorithm developed with the aim of extracting physical information will be described in a subsequent section (§ 3.5.2).

A continuous detector acquisition period is called *run*, which may be subdivided in different data files, called *segments*. In the case of fission FIC data, each run could last up to several hours and could contain different number of segments.

3.4 The Fast Ionization Chamber

The fission measurement at n_TOF are carried out with two distinct apparata, both based on the direct detection of fission fragments produced in fission reactions. The first setup is based on Parallel Plate Avalanche Counters (PPAC) [49] while the second, the detector used in this work, is constituted by a Fast Ionization Chamber (FIC), described thoroughly in Ref. [84]. The detector has been developed in the context of a collaboration between the Joint Institute of Nuclear Research (JINR), Dubna (Russian Federation), the Institute of Physics and Power Engineering (IPPE), Obninsk (Russian Federation), the Emerging Energy Technologies (EET) group of CERN and INFN. The chambers have been designed and built in order to meet the following guidelines:

- to allow the mounting of samples in vacuum and simplify the installation of radioactive targets inside the chamber itself;

- to minimize the material in and around the neutron beam and in particular to reduce the thickness of the electrodes, windows and sample backing and to employ material composition that minimizes neutron interactions;
- to obtain a fast charge collection time in order to allow reliable operation at the very high instantaneous counting rates presently available at the n_TOF facility;

In the following sections, the design and performances of the FIC detector will be described.

3.4.1 Principle of operation

The measurement of energy deposited in gas by fission fragments (FF) produced in thin deposits of fissile material is one of the standard techniques for measurement of neutron-induced fission cross-sections, as well as for neutron flux measurements. The volume sensitive to ionizing particles is in physical contact with the fissile deposit, so that the solid angle coverage is very close to 2π. Due to the peculiarities (multiplicity and kinematics) of the fission process, the number of detected FFs is therefore equal to the total number of fission reactions. Fission ionization chambers operate in the ionization regime, in which the signal is strictly related to the charge produced by ionization in the gas. This happens when the electric field between electrodes is sufficiently high to collect all the charges produced by the ionization and low enough to prevent the production of secondary pairs (a multiplication phenomenon that occurs in proportional chambers, such as PPACs). Since the charge state of FFs decreases with decreasing velocity, their specific energy loss (dE/dx) decreases as they slow down in the medium, a behavior opposite to that of lighter particles, like α particles or protons, for which the energy loss becomes most significant at the end of the range. Provided that an appropriate distance between electrode is chosen and that the ionization chamber is operated at a suitable gas pressure (so that light particles are not stopped in the gas), the signals produced by FFs are larger that those produced by any other competing reaction. A simple amplitude threshold, which corresponds to a deposited energy threshold, is therefore typically sufficient to discriminate fission events from signals related to the natural radioactivity of the samples, in particular α-particle decay.

In the case of highly radioactive isotopes, such as ^{241}Am and ^{245}Cm, the superposition of signals generated by two or more α-particles becomes possible. Such a pile-up may simulate a FF signal or in general a particle that has lost a greater amount of energy. In order to reduce the pile-up effect, a reduced sample mass must be used, as well as using a fast detector (the effect of pile-up is strongly dependent on the time response of the chamber, related to the drift time of an electron in the gap between the electrodes). In the present measurement, a charge collection time of 50 ns, corresponding to an electron drift velocity of 12 cm/μs in the 0.5 cm gap between the electrodes, and the absence of a Frisch grid[2], makes the FIC detector very fast, and therefore suitable for measurements of very highly radioactive isotopes.

3.4.2 The mechanical design

Two fission chambers were built with similar designs, both of which complying with the safety rules at CERN for handling radioactive sources. The first type of detector, for which two almost equal copies were made, called FIC0 and FIC1, was designed for measurement of highly α-active isotopes, while a second type, called FIC2, was used only as neutron flux monitor. This last detector was operated only with ^{235}U and ^{238}U, which are both fission standard. The two chambers of the first type, FIC0 and FIC1, shown in Fig. 3.6, were loaded with various samples, some of which with activities of the order of hundreds of MBq. For this reason the chambers had to be certified as a sealed source, as requested by the radioprotection department at CERN. Targets of ^{235}U and ^{238}U were also included in both chambers, for normalization purposes.

Each of the FIC chambers is constituted by a stack of cells, mounted one after the other along the direction of the neutron beam. A basic cell is made by three aluminum electrodes: the central one, 100 μm in thickness, is plated on both sides with a fissile isotope, while the external ones, 15 μm in thickness, are used to define the electric field in the gas-filled region. Since the ionization chamber is not operated in proportional mode a gas flow can be avoided, thus eliminating the need of a complex gas distribution system and of the safety infrastructure required in a radioactive environment. The FIC0 and FIC2 chambers have been assembled and loaded with samples at CERN while FIC1 has been assembled and filled with gas in a dedicated laboratory suitably equipped for handling unsealed radioactive sources (a Class-A laboratory, also called "hot lab"). The absence of the gas recirculation system is of great advantage in the case of very radioactive species, such as ^{245}Cm, since the detector can be considered as a sealed source. This fact facilitates the transfer from the hot lab to the experimental area and the handling inside the experimental area. Fig. 3.7 shows two photos of the FIC1 chamber taken during assembly.

---

[2] Used in some ionization chambers to remove the dependence of the pulse amplitude on the position of interaction. It is placed between the two electrode of the chambers and it is constituted by a grid maintained at an intermediate potential between the two electrodes and made to be as transparent as possible to electrons.

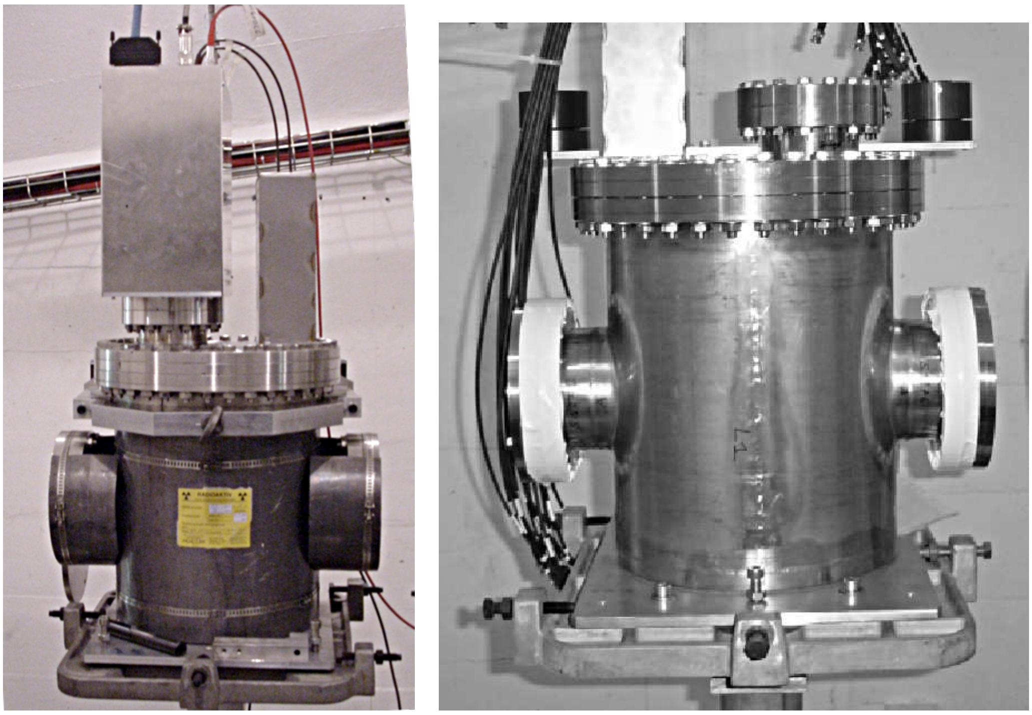

(a) FIC0 chamber, which contains ^{235}U, ^{236}U and ^{238}U samples.

(b) FIC1 chamber, which contains ^{233}U, ^{235}U, ^{238}U, ^{241}Am, ^{243}Am and ^{245}Cm samples.

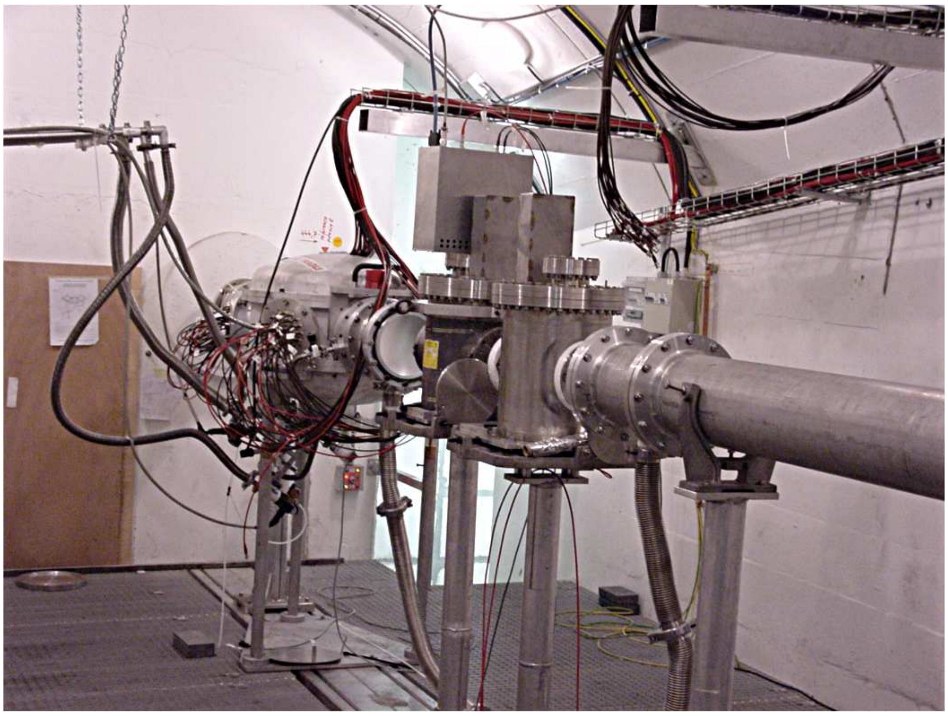

(c) Global view of the experimental area during fission measurements. From left to right (direction of the incoming neutron beam): PPAC chamber, FIC0 and then FIC1.

Figure 3.6 – Photos of FIC0 and FIC1 detectors mounted in the experimental area.

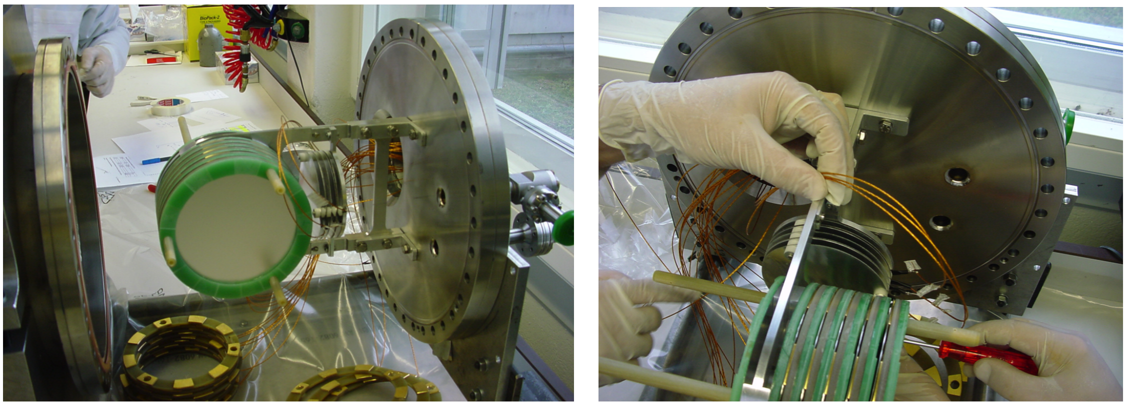

(a) (b)

Figure 3.7 – Photos of the inside of the FIC1 chamber, taken during assembly.

3.4.2.1 Chambers for very radioactive isotopes (FIC0 and FIC1)

As already pointed out, the n_TOF FIC fission detector was designed following the requirements of the ISO2919 standard as ISO/04/43323, normally defined as "sealed source for a general source application". Since CERN is not qualified for the construction of sealed radioactive sources, and it does not have the proper infrastructure for the tests required by the ISO standard, the FIC1 chamber was assembled and sealed in a Class-A laboratory at Paul Scherrer Institut (PSI) in Villigen, Switzerland. After the radioactive samples were mounted, the vessel was sealed, put under vacuum and filled with gas mixture at 720 mbar. A certification for the use of this detector in CERN experimental areas was then obtained. In table 3.1 the main operation parameters are reported for the case of FIC0 and FIC1 detectors.

Table 3.1 – Main parameters of the Fast Ionization Chambers used for measurements with highly radioactive samples.

Gas composition	Ar (90%) + CF_4 (10%)
Gas pressure	720 mbar
Gas flow	not needed
Electric field	600 V/cm
Gap between electrodes	5 mm (FIC1,FIC2), 20 mm (FIC0)
Electrode diameter	12 cm
Sample diameter	8 cm (FIC0,FIC1), 5 cm (FIC2)
Samples	^{233,235,236}U, ^{241,243}Am, ^{245}Cm
Sample thickness	4-450μg/cm^2
Backing thickness	100μm (Al)
Sample uniformity	5-10%

A total of 16 samples can be mounted in the detector perpendicular to the neutron beam, allowing the possibility to simultaneously measure all samples together. An additional chamber with a ^{235}U sample is mounted outside (parallel) to the neutron beam, in order to provide a measurement of the neutron background, in particular the one related to neutron scattering from the detector windows and electrodes. The length of the detector along the neutron beam is approximately 50 cm. In Fig. 3.8 the mechanical layout of the chamber is shown.

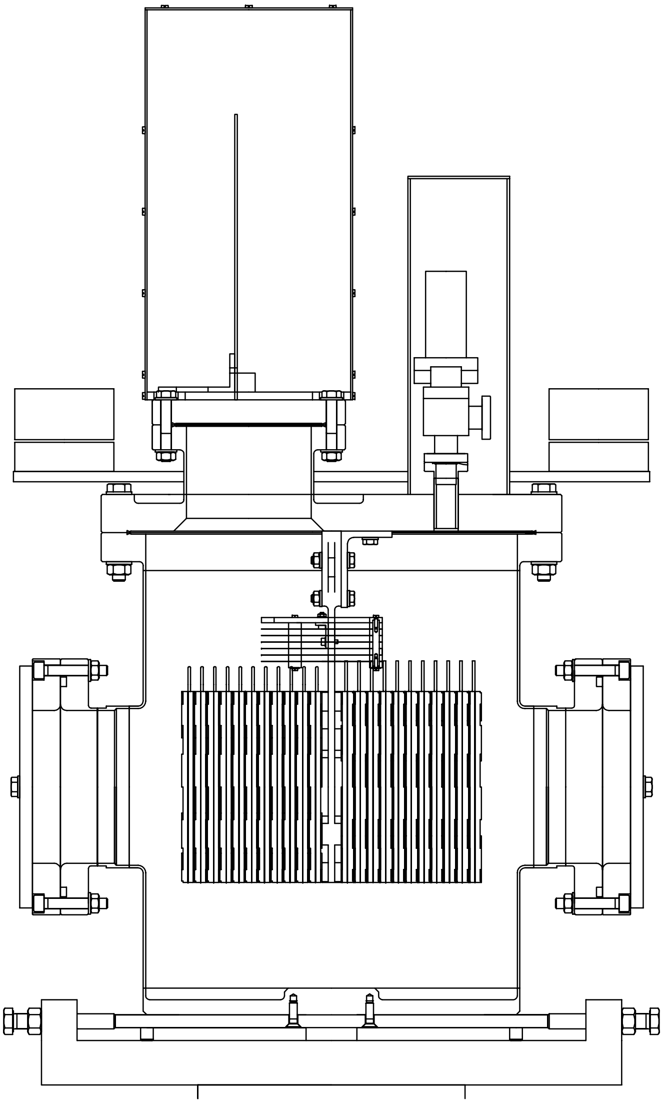

Figure 3.8 – Schematic view of the FIC1 chamber. The beam is coming from left to right in the picture. The design for FIC0 is similar except for the gap width between anode and cathode of 20 mm (instead of 5 mm of FIC1) 3.1.

In order to avoid the spill of contaminated gas into the atmosphere, all welded parts have been certified by X-ray imaging and the chamber is operated below atmospheric pressure at all times. Since the chamber have been sealed before being transported into the experimental area, the alignment of the samples relative to the neutron beam have been performed into two separate steps: during mounting of the samples, they have been aligned inside the detector body with their position determined relative to external reference points on the detector chassis. After the chambers have been sealed and transported to the measuring station, the external reference points have been then used for the alignment of the whole detector relative to the beam direction.

3.4.2.2 Chamber for neutron flux monitoring (FIC2)

FIC2 is a specially designed chamber, with the same detector parameters of FIC0 and FIC1, except for the smaller sample diameter (5 cm instead of 8 cm) and for the fact that high vacuum techniques have not been used. Furthermore, since there was no need for special arrangement for sealed sources, special care has been devoted in the minimization of materials along the neutron flight path; for this reason, the vessel containing the gas and the samples is mounted inside a structure which is directly coupled to the n_TOF vacuum tube. All metal parts are made of an aluminum alloy and the windows between the gas-vacuum interface are made of a 125 μm thick kapton foil. Since this detector is used as a flux monitor, it has been mounted outside the experimental area, in the so-called "escape lane", where it is operated continuously, both in fission and capture runs. The mechanical layout and a picture of the chamber is shown in Fig. 3.9.

3.4.3 Sample preparation and description

As already pointed out, the chamber hosts various fissile/fertile samples. The U samples, i.e. ^{233,235,238}U, were all in the chemical form of triuranium octaoxide (U_3O_8), while ^{241,243}Am are in the form of dioxide (AmO_2), as ^{245}Cm (CmO_2). The mass and thickness of the deposit for each sample is reported in Table 3.2. All samples have been prepared at the IPPE (Institute of Physics and Power Engineering, Obninsk, Russia) by means of the painting technique [85, 86, 87]. The samples consist of fissionable materials in the form of a thin oxide coating, with thicknesses ranging between 1 μg/cm^2 and 0.5 mg/cm^2, deposited on a metal substrate. The oxide coatings may be applied to the substrate by a variety of different techniques such as vacuum evaporation, electrodeposition, sputtering and painting [87]. This last method is very efficient when compared with other methods for producing actinide fission foils since as much as 90% of the fissionable material can be deposited on the

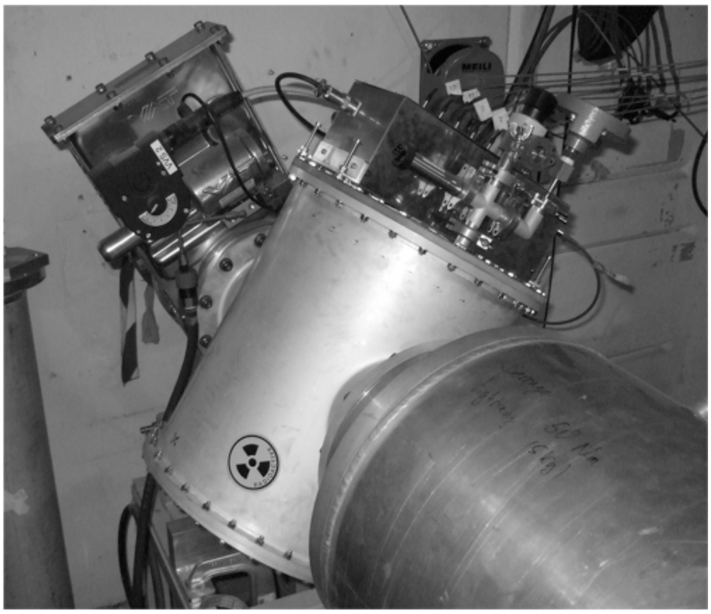

(a) Picture of the FIC2 chamber in its position in the escape lane. The direct coupling with the vacuum tube is visible.

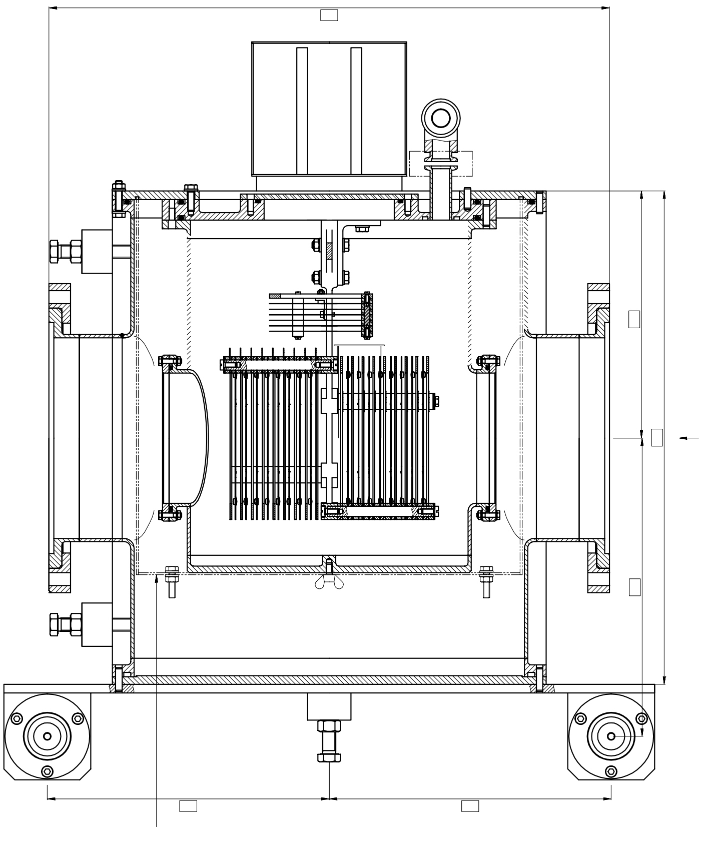

(b) Schematic view of the FIC2 chamber, with target plates orthogonal to the beam direction and background ones parallel to it.

Figure 3.9 – Photo (upper panel) and schematic view (bottom panel) of the FIC2 detector used as a neutron flux monitor.

substrate, a feature of great importance when only small amounts of rare high purity isotopes are available. Additionally, minimal equipment is needed to produce fission samples, resulting in reduction of production costs by a factor of ten with respect to other techniques.

Apart for the sample mass, another important aspect in the measurements of fission cross-sections is the purity of the fissile deposit, and the precise knowledge of the eventually present impurities. For the samples used at n_TOF and discussed in this thesis, the amount of contaminations was determined by means of α-spectrometry, performed with silicon detectors. Fig. 3.10 shows the spectra measured for some of the samples, used to estimate their composition.

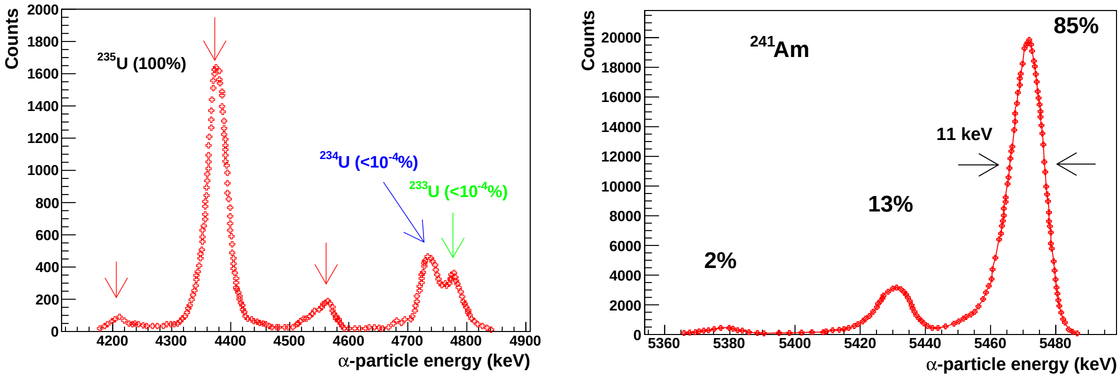

(a) ^{235}U α spectrum (b) ^{241}Am α spectrum

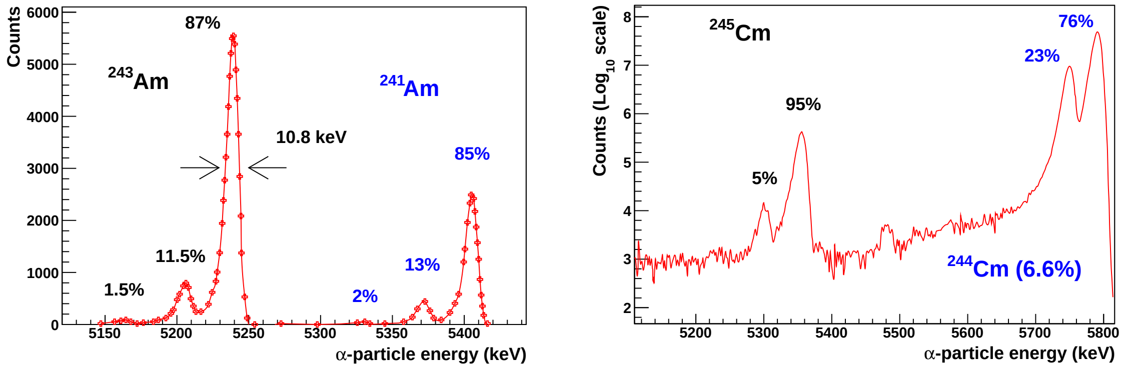

(c) ^{243}Am α spectrum (d) ^{245}Cm α spectrum

Figure 3.10 – The α spectrum of the various samples used in the fission cross-section measurements at n_TOF. The contamination in each of the sample is reported. Data from [88].

For the production of actinide samples by painting technique, an organic solution of an actinide nitrate is brushed on a backing surface. After the paint solution has dried on the substrate, the foil is placed in a oven and heated at a temperature of about 750 K. Organic compounds are burned off and a layer of up to 100 μg/cm^2 remains on the backing. By repeating this procedure several times, the areal density is increased to the needed value. Substrates made of beryllium, aluminum, nickel and copper have been successfully used in the past. Beryllium has the advantage of having a very high melting point, which permits the substrates to be baked at very high temperature, ensuring a better conversion of the nitrate to oxide. However beryllium is an hazardous material to handle and it is very brittle. On the contrary aluminum substrates are much easier to handle: the disadvantage is the low melting point of aluminum (933 K), which limits the maximum bakeout temperature to approximately 750 K. By means of the painting technique it is possible to apply multiple layers of fissionable material to the substrate. This involves repetitive painting and backing, and can produce areal densities of up to 2000 μg/cm^2 of fissionable material. As reported in [85] a coating with a total thickness of 400 μg/cm^2 could require about 40 individual layers. Repeated painting of the substrate using low concentration painting solutions also improves the uniformity of the coating thickness. The variation in uniformity of the coating can be generally kept well below 10%. Painting produces coatings which adhere much better to the aluminum backing than the ones made by simple evaporation of the solutions. Additionally, tests have been made with ^{240}Pu samples of very high α-activity ($\geq$ 0.4 GBq, similar to the case of the present ^{245}Cm sample), which shows that the adherence has not changed 1 year after target preparation.

3.5 The signal reconstruction and analysis tools

3.5.1 Raw data processing

Since the FIC chambers were not fully included in the n_TOF data acquisition system, in the sense that DSTs were not produced with the standard method described in § 3.3, the first step of the analysis required the processing of the full raw data recorded on CASTOR. DSTs that contain basic information on the signals, extracted by the analysis routine, have thus to be produced before performing basic data analysis. The total amount of processed raw data for FICs analysis (summed for all three chambers) is on the order of ~5 TB.

An example of the raw data, recorded during the measurement, is shown in figures 3.11 and 3.12. The data are from FIC1 and FIC2, respectively, and refer to the ^{235}U(n, f) reaction. The γ-flash and subsequent fission fragment signals are easily recognized, as well as the zero suppression effect, that eliminates signals that do not cross a predefined amplitude threshold (see § 3.3).

The digitized waveform of a typical signal produced by a fission fragment is shown in Fig. 3.13. As expected from the operational characteristics of the chamber

Table 3.2 – List of samples used in the FIC1 chamber for the measurement of fission cross-sections. All samples were built by depositing the material on the electrodes by means of the painting technique (see text, sect. 3.4.3). The diameter of the target deposit is 8 cm.

Sample	Chemical Form	Mass (mg)	Areal density (atoms/b)	Uncertainty (%)	DAQ channel
^{235}U	U_3O_8	15.2	7.75×10^{-7}	1.4	12
		16.6	8.46×10^{-7}	1.3	
^{233}U		8.04	4.13×10^{-7}	1.2	13
		7.45	3.83×10^{-7}	1.2	
		7.49	3.85×10^{-7}	1.3	16
		7.86	4.04×10^{-7}	1.1	
^{238}U		12.8	6.44×10^{-7}	1.4	11
		12.4	6.24×10^{-7}	1.4	
		13.4	6.74×10^{-7}	1.2	10
		13.7	6.90×10^{-7}	1.4	
^{245}Cm	CmO_2	0.367	1.79×10^{-8}	1.3	14
		0.538	2.63×10^{-8}	1.2	
		0.407	1.99×10^{-8}	1.3	15
		0.399	1.95×10^{-8}	1.3	
^{243}Am	AmO_2	0.556	2.741×10^{-8}	1.2	7
		0.585	2.884×10^{-8}	1.3	
		0.613	3.022×10^{-8}	1.3	5
		0.631	3.111×10^{-8}	1.3	
		0.537	2.648×10^{-8}	1.2	4
		0.558	2.751×10^{-8}	1.2	
		0.595	2.933×10^{-8}	1.3	8
		0.710	3.500×10^{-8}	1.2	
^{241}Am		0.234	1.163×10^{-8}	1.1	6
		0.230	1.143×10^{-8}	1.2	
		0.280	1.392×10^{-8}	1.2	3
		0.279	1.387×10^{-8}	1.2	
		0.304	1.511×10^{-8}	1.2	1
		0.336	1.670×10^{-8}	1.2	
		0.321	1.596×10^{-8}	1.2	2
		0.277	1.377×10^{-8}	1.2	

Table 3.3 – List of samples used in the FIC2 chamber for the measurement of fission cross-sections. The diameter of the target deposit in this chamber is 5 cm. The uncertainty on the mass of the ^{238}U sample is not known with very high precision.

Sample	Chemical Form	Mass (mg)	Areal density (atoms/b)	Uncertainty (%)	DAQ channel
^{235}U	U_3O_8	6.47	8.44×10^{-7}	1.1	3
		6.32	8.25×10^{-7}	1.1	
^{238}U		20	2.6×10^{-6}	5?	7

Table 3.4 – List of samples used in the FIC0 chamber for the measurement of fission cross-sections. The diameter of the target deposit used in this chamber is 8 cm.

Sample	Chemical Form	Mass (mg)	Areal density (atoms/b)	Uncertainty (%)	DAQ channel
^{235}U	U_3O_8	18.9	9.63×10^{-7}	1.1	3
		16.7	8.51×10^{-7}	1.1	
^{236}U		5.25	2.66×10^{-7}	1.4	2
		4.95	2.51×10^{-7}	1.4	
		5.82	2.95×10^{-7}	1.3	1
		5.33	2.70×10^{-7}	1.4	

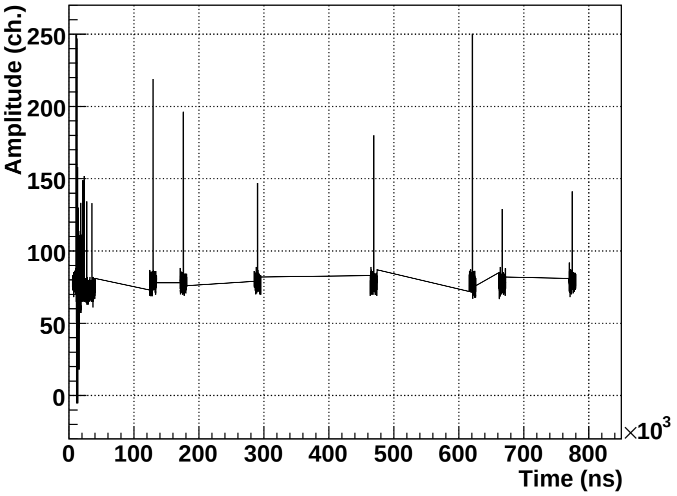

(a) Selection of a ″movie″ of a given neutron bunch up to 0.8 ms (only 1/100 of the total recorded time window).

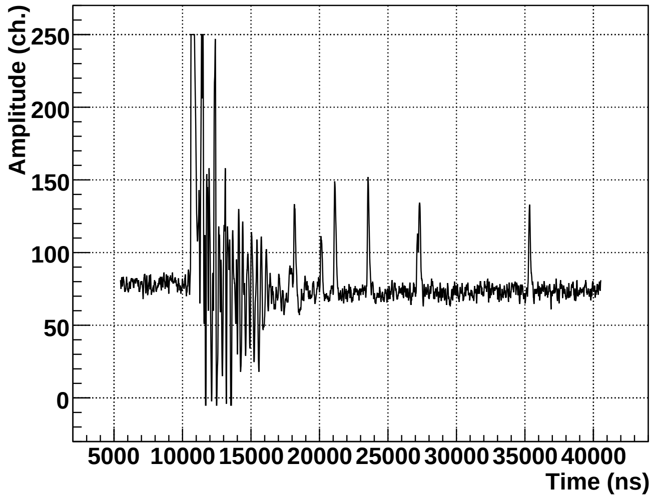

(b) Zoom in the prompt flash region: shortly after the end of the electronic noise, starting from ~18μs, the first FF signals are present.

Figure 3.11 – Raw data for a single neutron bunch in FIC1 for a ^{235}U sample.

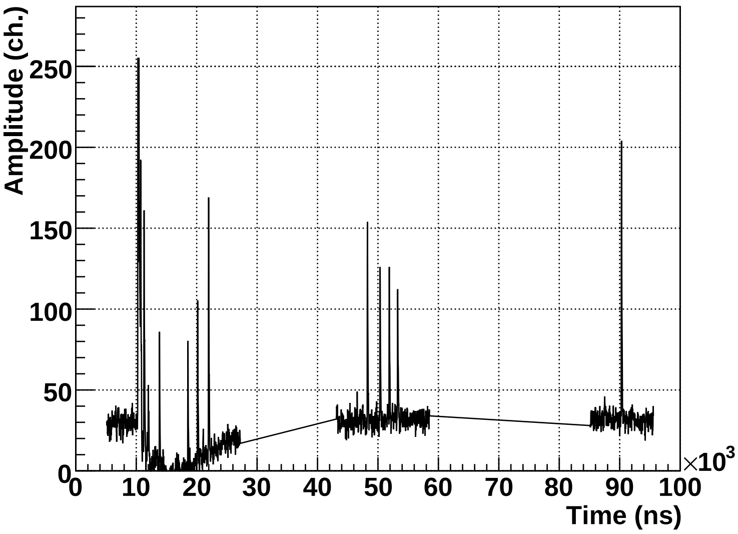

Figure 3.12 – Raw data for a single neutron bunch in FIC2 (for the large collimator setup) for a ^{235}U sample.

and of the front-end electronics, the signal shows a risetime of approximately 40 ns and a decay time of 120 ns.

The electronic oscillation present after the prompt flash, and visible in Fig. 3.11(b), constitute a serious problem for the identification of FF produced by high energy neutrons, since they are superimposed on those large oscillation. In order to get rid of the contribution of these non-interesting signals, only signals produced ~5.4 μs after the prompt flash have been accepted for the DST production and analysis. It is worth noticing that the effect of γ-flash depends on the beam intensity. The oscillations are therefore smaller for parasitic beams, which have half the proton intensity of dedicated ones. Furthermore, the raw data from FIC2 (the chamber located in the escape lane, several meters after FIC1) show smaller oscillations, as evident in Fig. 3.12, due to a compensation technique that was used for this chamber, and that will be described in a later section. A significant undershooting of the baseline is instead present, which has to be taken into account in the analysis routine.

3.5.1.1 Saturation effect

As previously mentioned, the n_TOF digitizers have a low resolution of 8 bits (corresponding to a digitized signals amplitude between 0 and 256). On the contrary, the range of deposited energy for α-particles and fission fragments is quite large, from few MeVs up to ~100 MeV. Since it is important to clearly discriminate between α-particles and fission fragments, it is preferable to have a greater sensibility for low released energy. For this reason, a high amplification gain was used in the fission

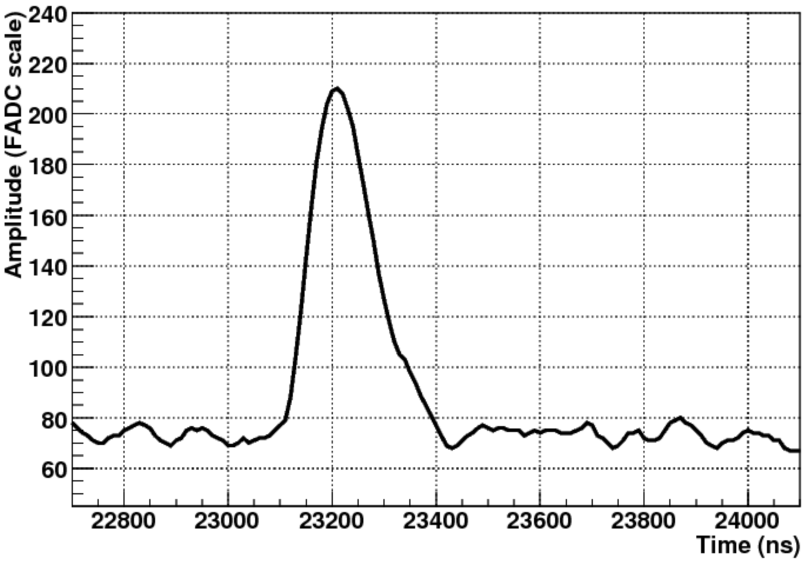

Figure 3.13 – Typical FIC signal of a fission fragment, digitized with a 100 MS/s Flash Analog-to-Digital Converter.

measurements at n_TOF. Fission fragments that release a large amount of energy therefore saturate the dynamic range of the FADC, with a saturation peak observed around channel 256. For saturated signals, the clipping of the peak in the signal prevents from recovering the exact value of the amplitude and of the corresponding time-of-flight. However since usually the saturation plateau lasts at maximum 50-60 ns, the error in the TOF is of 0.5% at maximum in the MeV neutron energy range, where, due to the absence of neutron resonances, precise evaluation of the energy is not required. At low energies, the indetermination in neutron energy is much smaller and will therefore be neglected.

3.5.2 Peaks finding procedure

After the FIC data are retrieved from the Central Data Storage of CERN, a signal reconstruction procedure, operating on the LXPLUS public linux machines[3] at CERN and running within the LXBATCH cluster infrastructure with LSF[4] jobs, is applied. The routine allows to determine the signal amplitude, its area and its time flag[5]. Two different approaches can be used for this purpose: a detailed pulse shape analysis, typically used in the data reduction at n_TOF, or a simpler solution, adopted in this

---

[3] The PLUS service (Public Login User Service) is the interactive logon service to Linux for all CERN users. The cluster LXPLUS consists of public machines provided by the IT Department for interactive work.

[4] *Load Sharing Facility* is a job scheduler software suite, used to execute batch jobs on networked Unix systems.

[5] It's the time recorded by the FADC, so its physical meaning is not the "real" time of flight, which has to be evaluated with Eq. 3.6.

case, which consists in a C++ routine developed using ROOT [89] libraries. The routine is based on the advanced Spectra Processing Function class TSpectrum. In order to determine the baseline, i.e. the low frequency component of the digitized waveform, the routine uses the Sensitive Non-Iterative Peak-clipping algorithm described in Ref. [90, 91]. In this way, variations of the baseline, such as the one evident in Fig. 3.12 after the prompt γ-flash, are correctly taken into account. The baseline, as a function of time, is then subtracted from the original data. The TSpectrum class is also able, on the basis of the method described in Ref. [92] and extended in Ref. [93], to automatically identify peaks present in a continuous spectrum, by means of an algorithm based on the analysis of the smoothed second derivative of the signal. Two parameters are needed as input in the peak searching routine: the width of the signals and an amplitude threshold. In the present analysis, the values of these parameters were determined by looking at individual signals and at pre and post signal interval. Once a peak has been identified, the time information, the baseline-subtracted amplitude, the integral of the signal and the original baseline value are stored in a ROOT binary file for subsequent analysis. Furthermore, for each proton bunch, the time of the prompt signal is also recorded, together with the intensity of the proton bunch impinging on the spallation target, used for relative normalization purposes. After the DSTs are produced in the LXBATCH system, they are automatically copied via remote `ssh` session to a local server, where further data reduction takes place using on a local cluster system running LSF.

The analysis here discussed has been performed up to $\simeq$1 MeV neutron energy, due to the presence of large γ-flash oscillations. Above $\sim$1 MeV a software compensation technique allows to overcome the effect of the oscillations. The technique is based on the observation that the prompt γ-flash of two contiguous electrodes has the same shape. Data up to 500 MeV may be recovered in this way (although they are not the subject of the present thesis) [94].

A pictorial scheme of the whole analysis procedure is represented in figure 3.14. For the reconstruction of the events, ad-hoc routines have been written in order to access the produced DSTs, extract informations, select "good" events and, after application of appropriate cuts and normalization constants, extract fission yield or cross-section. In order to accomplish this steps, the ROOT object-oriented framework has been used, with C++ routines specifically developed to this purpose.

3.5.3 Prompt flash identification

As previously described, the prompt flash (PF or γ-flash) is due to photons and relativistic charged particles that are produced in the spallation process in the lead

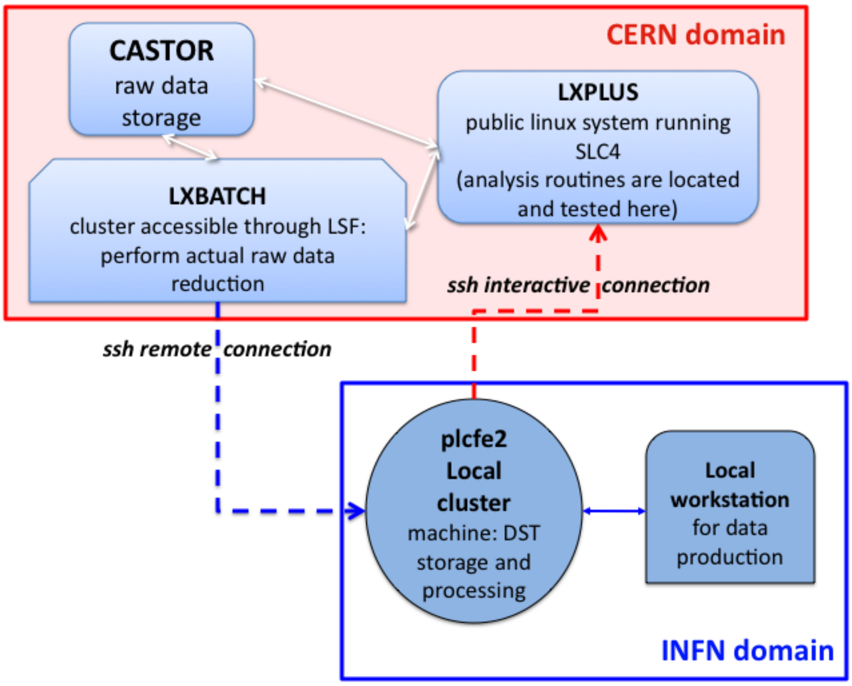

Figure 3.14 – Flow chart of data processing of FICs raw data.

target and reach the experimental area before the neutron beam. Since the FIC detectors are sensitive to charged particles, the PF produce a large signal inside the chamber. It is the first signal correlated with the proton pulse used as trigger, and it is present in every detector. Since the time interval required to cross all ionization chambers is less that 1 ns, it can be considered as a common start for all detectors.

In the case of FIC0 and FIC1, the prompt flash is unmistakably recognized by the fact that, as shown in Fig.3.15, the signal saturates, and remains saturated for more than 100 ns. This allows to easily set conditions for the determination of the time of the γ-flash (see Appendix C).

The main advantage of the prompt flash signal is the fact that it can be used as an absolute time reference for each neutron pulse and for all detectors, thus allowing to deduce the physical TOF for each fission reaction. An event-by-event analysis of the prompt flash signal is necessary, due to the fact that the PF timing is different for dedicated and parasitic bunches (for reasons related to the PS trigger). This effect is shown in Fig. 3.16(a) for a single run in the case of the FIC1 chamber, with the correlation between the proton beam intensity and time of prompt flash in Fig.3.16(b); a correct event-by-event identification of the position of the prompt flash is thus mandatory in order to precisely determine the correct value of the neutron's time-of-flight.

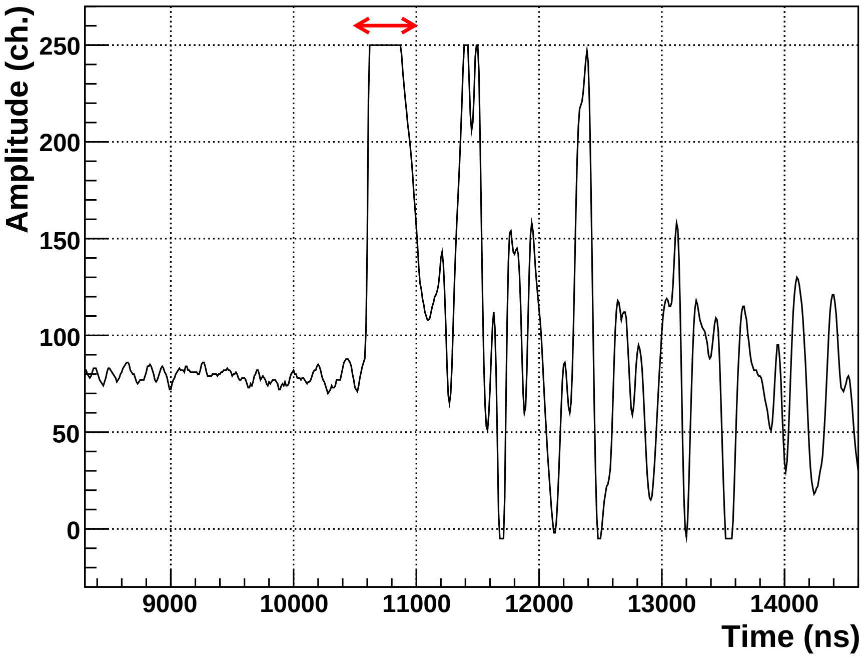

Figure 3.15 – Raw data representing the prompt-flash, recorded in one of the FIC1 electrodes. The saturation peak used to precisely determine the time position of the signals is indicated by the red arrow. The implications of the oscillations related to the γ-flash are discussed in the text.

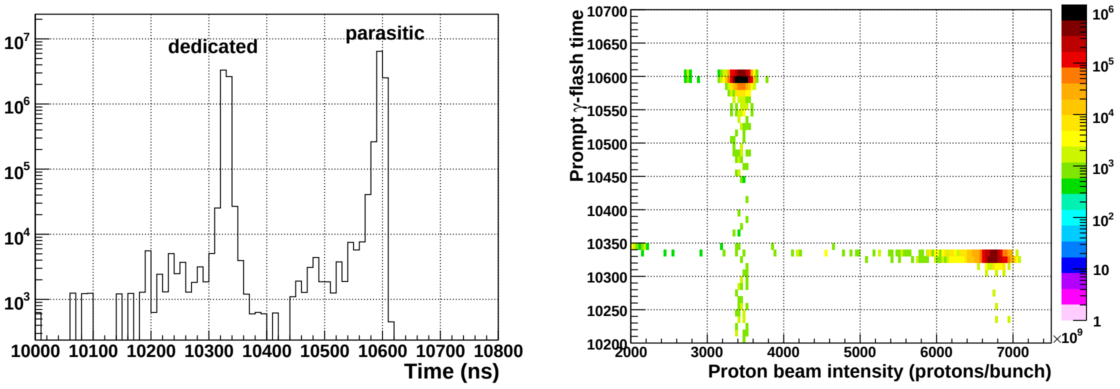

(a) Distribution of the prompt γ-flash time position.

(b) Correlation between the nominal proton bunch intensity and the prompt γ-flash time position.

Figure 3.16 – 3.16(a): time distribution of the γ-flash in the FIC1 detector. The dedicated (TOF) and parasitic (EASTC) pulses, are characterized by a different timing, thus making mandatory an event-by-event identification for a correct calibration of the neutron time-of-flight. The correlation between the proton beam intensity and γ-flash timing is evident in the right panel (Fig. 3.16(b)).

3.6 Detector simulations

The accurate determination of the fission cross-section requires a precise knowledge of the detector performances, in particular its efficiency. The response of the FIC detector has been investigated by realistic Monte Carlo simulations, with a detailed implementation of the geometry of each ionization chamber, the sample deposit and the gas composition and pressure. One of the main objectives of these simulations is the determination of the total efficiency of the detector as as function of the amplitude threshold. A schematic drawing of the chamber, used in the simulations, is shown in Fig. 3.17.

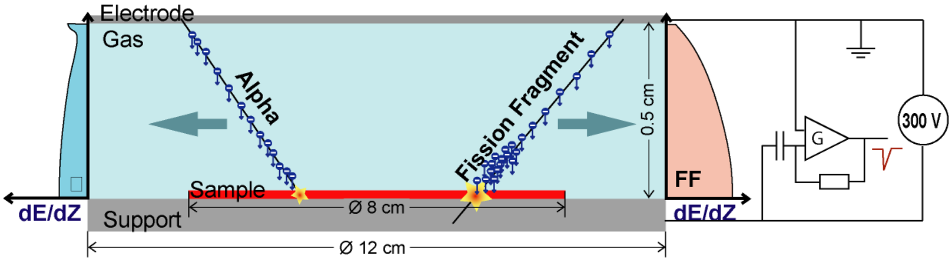

Figure 3.17 – Schematic representation of the behavior of a fission ionization chamber. The different energy loss of α-particles and fission fragment in the gas region is also shown in the figure.

In order to get a more precise estimate of the efficiency correction factor, detailed simulations of the energy deposited by the fission fragments in the sample deposit and in the gas have been performed. To this end the FLUKA Monte Carlo code [57] has been used, with modified source routines in which realistic fission fragment energy and mass distributions were included. FLUKA is a fully integrated particle physics Monte Carlo simulation package which has also been extensively used in the context of the n_TOF Collaboration for simulation of the neutron transport and for background evaluation. Within the FLUKA code, the ionization energy losses are implemented according to models [95].

The energy deposition of fission fragments and α-particles was simulated for particles emitted isotropically from the U_3O_8 deposit (or from CmO_2 and AmO_2 in the case of curium and americium isotopes). The mass and energy distribution of the fission fragments has been generated according to the systematics reported in [96], and shown in figure 3.18. Fragments are emitted with an isotropic angular distribution, since up to 1 MeV neutron energy the effect of linear momentum transfer that could affect the forward/backwards distribution, is negligible. The energy deposition of fission fragments inside the detector is calculated within FLUKA from their initial energy down to a low threshold value. A limit of 1 keV in the particle transport has been set in the simulation.

3.6.1 Efficiency evaluation

As shown later, since the cross-sections for all measured samples are extracted relative to a reference sample of ^{235}U, one does not need in principle to correct for the detector efficiency, provided that the same experimental and analysis conditions apply to both the sample and reference measurement. This is mostly true in the present case, since the reference sample was measured simultaneously with the same detector, and the same analysis procedure and thresholds have been applied for the different samples. However, as shown in table. 3.2, the thickness of the fissile deposits is different for different targets. This implies that the fraction of fission fragments exiting from the deposit is not the same for all samples under consideration. If precise evaluation of the fission cross-section is required, this effect has to be taken into account into the analysis. As an example, the thickness of the ^{235}U sample is almost double than that of ^{233}U. Therefore a larger fraction of fission fragments are absorbed in the ^{235}U deposit, or exit the deposit with lower energy. Since the discrimination is essentially performed via an amplitude threshold for both isotopes, this effect leads to a different efficiency for the various isotopes, since the shape of the respective energy loss distribution is different.

A validation of the simulations has been performed using the ^{235}U sample: in this case, since the α-activity of the sample is very low, we expect the shape of the simulated and of the experimental energy distribution to be very similar (except in the low amplitude region, where a cut is introduced in the analysis routine on the amplitudes to reject electronic noise). In Fig. 3.19 the results of the simulations (with a 7% energy resolution applied to the simulated energy loss) are compared with the experimental results. The good agreement observed provides confidence on the reliability of the simulations.

As will be shown in following chapters, the effect of the efficiency correction is significant and, if not considered, it would introduce a systematic uncertainty affecting the final results of the cross-sections.

Figure 3.20 shows the distribution of the energy deposited in the gas volume for the ^{233}U and ^{235}U cases. When applying the same threshold used in the analysis of the experimental data, the obtained efficiencies are 97.6% and 94.9% for the ^{233}U and ^{235}U samples, respectively. Therefore a correction factor of $\approx$3% has to be considered for the efficiency (see Chapter 5).

Additional simulations have been performed in order to understand the reason for the peculiar shape of the energy loss inside the gas region, in particular to explain the

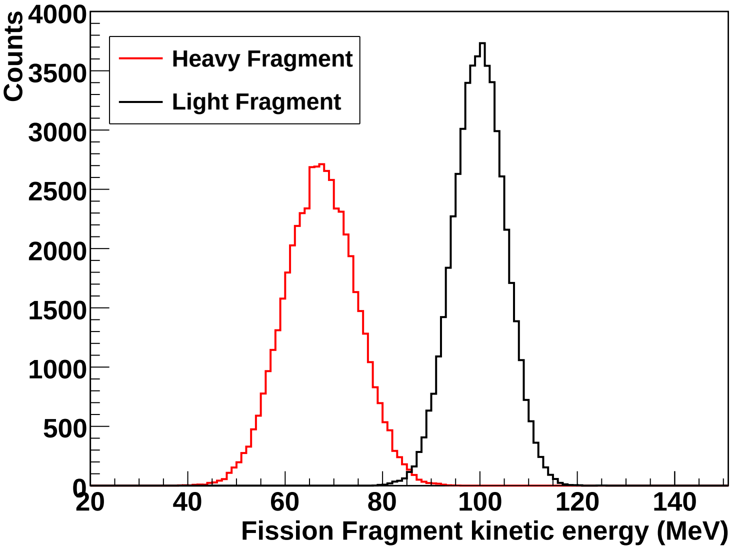

(a) Energy distribution of fission fragments.

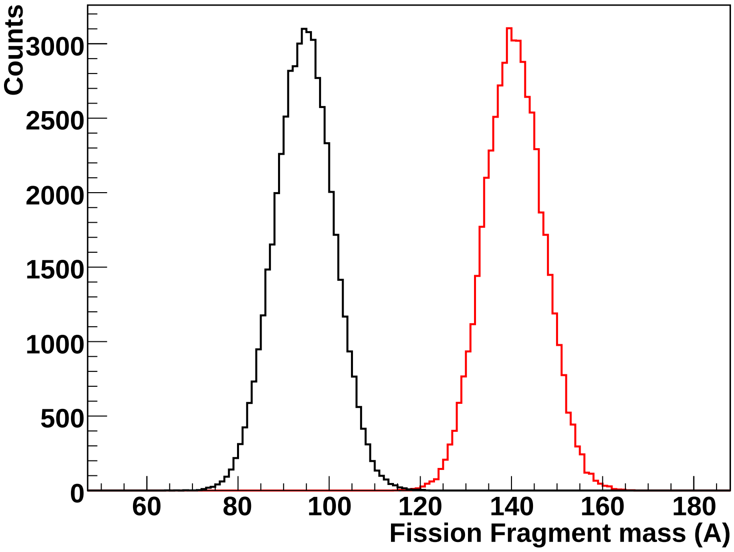

(b) Mass distribution of fission fragments.

Figure 3.18 – Energy and mass distributions of fission fragments used in the simulation of the detector's response. The energy distribution have been smoothed by a gaussian function.

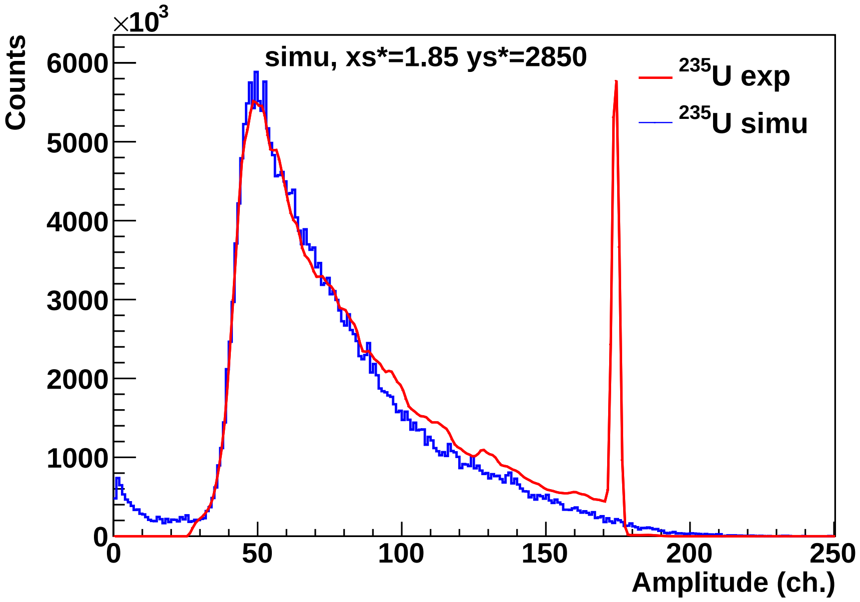

Figure 3.19 – The measured pulse height distribution of signals recorded in FIC1 for the ^{235}U sample is compared with the simulated energy loss distribution in the gas region. In the simulations, fission fragments are emitted isotropically from the ^{235}U deposit. The results of the simulations have been conveniently rescaled on the x and y axis so to match the experimental results.

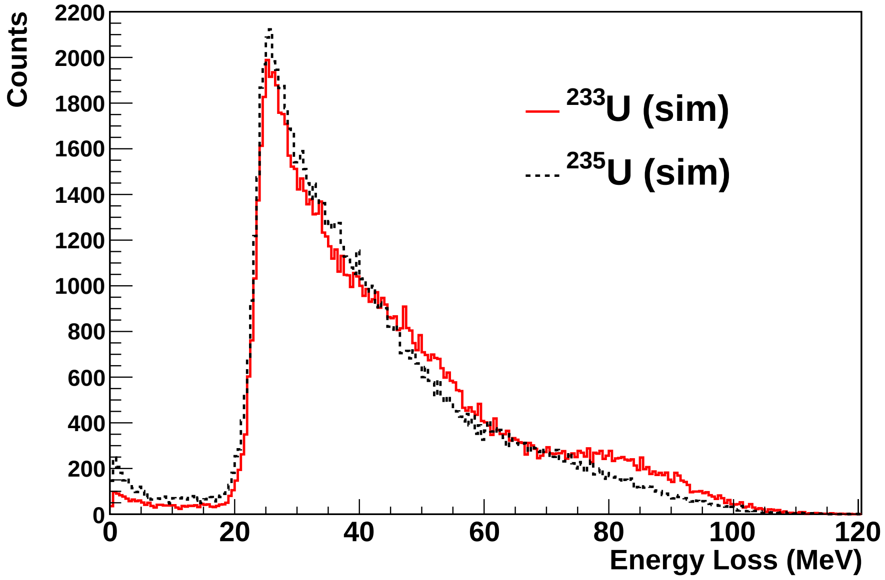

Figure 3.20 – Simulated energy loss distribution inside the gas region for fission fragments emitted by the ^{235}U sample (black dashed line) and by the ^{233}U sample (red line).

absence of the double peak expected in the energy distribution of fission fragments [97]. In particular, we have investigated the effect of the particles emission angle and the gas effective thickness (i.e. the electrode gap width and gas pressure) on the energy loss of FF.

3.6.1.1 Emission angle

A significant fraction of the fission fragments emitted at small angles with respect to the plane of the sample are expected to lose a larger fraction of their energy inside the deposit. As a consequence, the energy released in the gas depends on the emission angle between the FFs and the plane of the deposit.

To study this dependence, Monte Carlo simulations of FFs interaction in the chamber have been performed, selecting the emission angle of fission fragments. Figure 3.21 shows the results. The angle θ is defined as the angle between the particle (FF) direction and the direction of the neutron beam. Fragments emitted at large angles (red line), corresponding to small angles with respect to the deposit plane, lose most of their energy in the sample, since they cross an "effective" thickness of the fissile deposit much greater than the nominal one; their residual energy is such that they are completely absorbed in the active region, in large part releasing a very small amount of energy. As the emission angle increases, the fragments release in the gas at least 15 MeV, while the maximum released energy decrease (the effective thickness is reduced). In the case of mostly forward directed particles ($\theta \in$(0°-26°)),

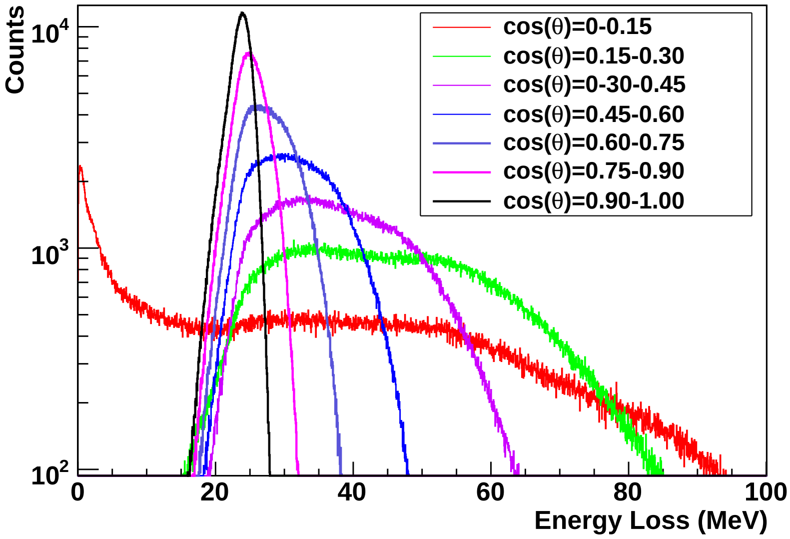

Figure 3.21 – Simulated energy loss distribution of fission fragments as a function of the angle between the emission direction and the orthogonal to the deposit's axis (i.e. the direction of the neutron beam).

the released energy is constituted by a narrow peak centered at approximately ∼22 MeV, since FFs lose just a small fraction of their total energy in the gas, being emitted from the samples with a relatively high energy. They stop completely, however, in the Al electrode, without punching through in the other chamber (see Appendix A).

3.6.1.2 Effect of the gas pressure and electrode gap

The peculiar shape of the released energy distribution has been also investigated by simulating the effect of the pressure inside the FIC chamber and observing the effect on the energy loss distribution of fission fragments. Due to safety requirements (i.e. possibility of spill of contaminated gas in the experimental area), the chamber is operated below atmospheric pressure at 720 mbar. The resulting gas density of 1.439×10^{-3} g/cm^3 is such that the fission fragments release only a small amount of energy in the gas, while stopping completely only in the 15 μm aluminum electrode that delimites the gas cell. The behavior changes if the gas pressure is increased. This is shown in Fig. 3.22, where the simulated energy loss of fission fragment inside the chamber is plotted as a function of the gas pressure, for FF isotropically emitted over 2π.

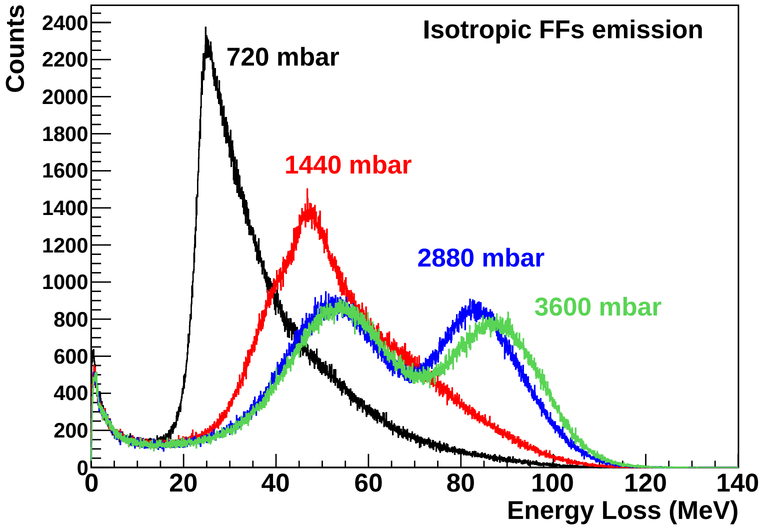

Figure 3.22 – Simulated energy loss distribution of fission fragments for different gas pressures. 720 mbar is the pressure actually for all FIC chambers at n_TOF.

While at 720 mbar the released energy peaks around 25 MeV, at higher pressure, or, equivalently, for a bigger thickness of the gas region, the peak of the distribution shifts to the right, since FF lose progressively a larger fraction of their energy in the gas cell. For a gas pressure ∼4 times the nominal one (2880 mbar) the energy distribution shows both peaks of the FF original kinetic energy distribution. This case corresponds to a gap between electrodes of ∼20 mm. This is the configuration used for the electrodes distance in FIC0. Although the simulations were not optimized, a reasonable agreement with the behavior of the experimental amplitude distribution is observed, as evident in Fig. 3.23, showing both fission fragment peaks.

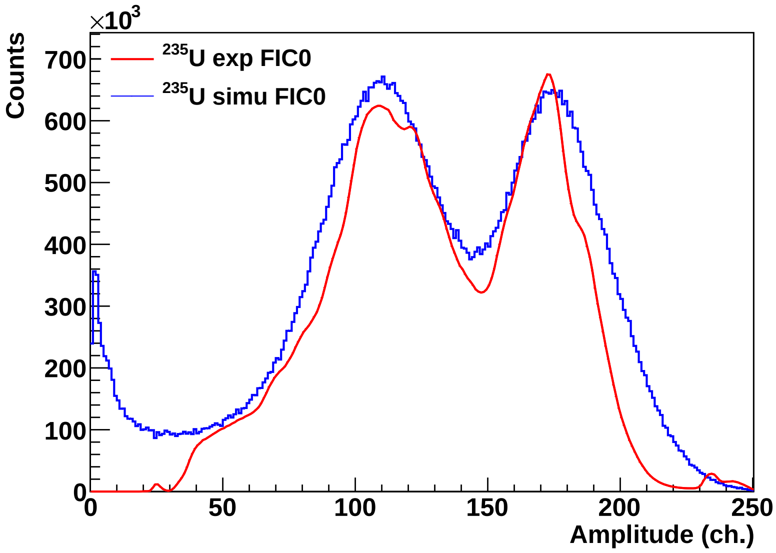

Figure 3.23 – Comparison between the simulated energy loss and experimental pulse height distribution in the case of the FIC0 chamber for a ^{235}U sample.

3.6.2 Flux attenuation

Since several samples are measured simultaneously, it is important to estimate the neutron flux at the different sample positions in order to take into account the appropriate attenuation of the incident neutron flux, in particular through the Al electrodes of the chamber. With this aim the general purpose Monte Carlo radiation transport code MCNPX [60] has been used. Fig. 3.24 shows the transmitted flux through the chamber considering all materials in the beam, that is for each section the two 15 μm aluminum anodes and the 100 μm aluminum cathode with the sample material deposited on both sides. The attenuation factor, defined as the ratio between the neutron flux impinging on two consecutive cells, integrated over the whole energy range of the n_TOF beam, is of the order of a few per thousands, with a total attenuation in the detector of less that 1%. For most practical application this effects can be neglected. As shown in Fig. 3.24, the increase in the attenuation factor for the higher energy region (above 10 keV) is due to the fact that the total neutron cross-section on the ^{27}Al isotope in that region is higher, due to the presence of strong resonances in the tens of keV region).

The effect of the aluminum windows can also be seen from Fig. 3.25, where the

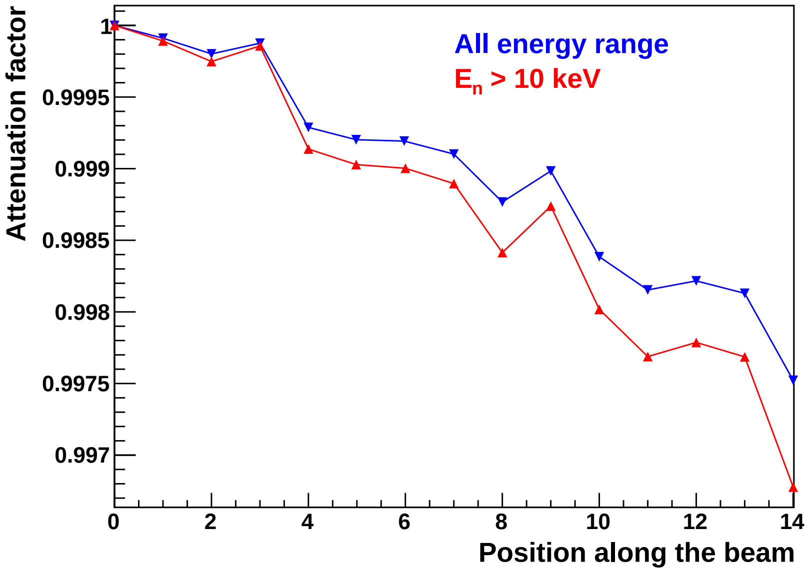

Figure 3.24 – Attenuation of the neutron beam through the cells of FIC1 detector. The y axis represents the fraction of the flux at various positions, relative to the flux incident on the first cell. The red line refers to the attenuation factor for neutron energies above 10 keV.

ratio between the flux impinging on the first and last cell is plotted as a function of neutron energy. The influence of the resonances in the Al cross-section is here very clear.

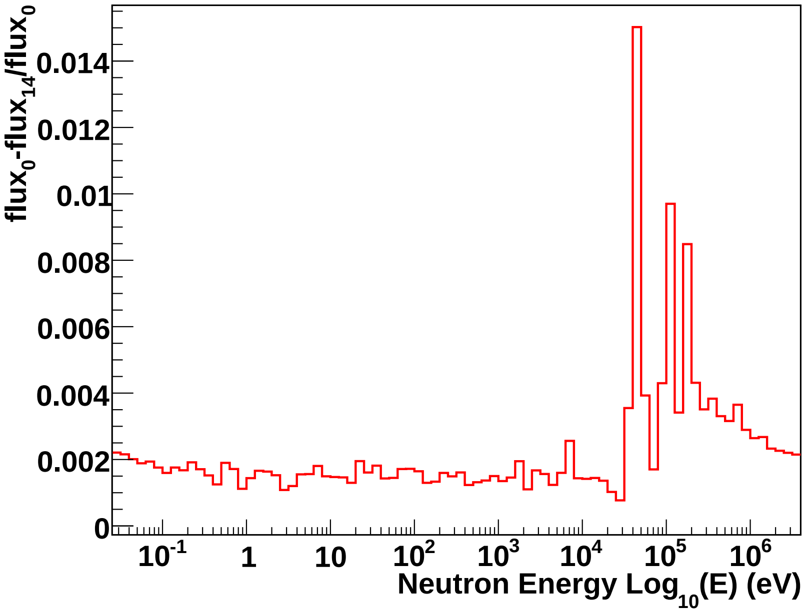

Figure 3.25 – Ratio between the flux incident of the first ($flux_0$) and last ($flux_{14}$) cell of the FIC1 detector. The effect of the resonance in the Al cross-section is evident in the region above 30 keV.

Chapter 4

Analysis of the ^{235}U(n, f) reaction

A first, fundamental step, in the analysis of the neutron-induced fission cross-section of ^{233}U and of minor actinides is the analysis of the fission data collected simultaneously on ^{235}U. This reaction, in fact, is considered a standard of measurement for fission cross-section, and for this reason is used as reference for all other reactions object of this thesis.

This chapter describes the procedures followed in the analysis of the ^{235}U(n, f) reaction, and presents the results together with a comparison with the internationally adopted cross-sections from evaluated libraries and from experiments.

4.1 Analysis procedures

4.1.1 Amplitude selection

As previously described, a routine based on ROOT libraries is applied to the signals in order to extract informations on the time-of-flight, baseline, amplitude and total area of recorded signals above a given threshold. In this first step, a very small value is used for the threshold, in order to avoid rejecting also fission fragments that deposit a small energy in the detector. Figure 4.1 shows the experimental amplitude distribution for the ^{235}U sample, in the range between thermal and 1 MeV neutron energy. The corresponding distribution measured without neutron beam is shown by the dashed line. The electronic noise and α-particle background, even if essentially negligible, are visible below channel $\simeq$25. The fission fragment amplitude distribution is, in this case, well separated from the region corresponding to the α-particle background[1]. A simple amplitude threshold is therefore sufficient to discriminate fission fragments from electronic and α-particle background. The peak

---

[1] In the next chapters it will be shown that the discrimination becomes increasingly difficult as the radioactivity of the sample increases.

observed near FADC channel 180 is due to the saturation effect already discussed in § 3.5.1.1.

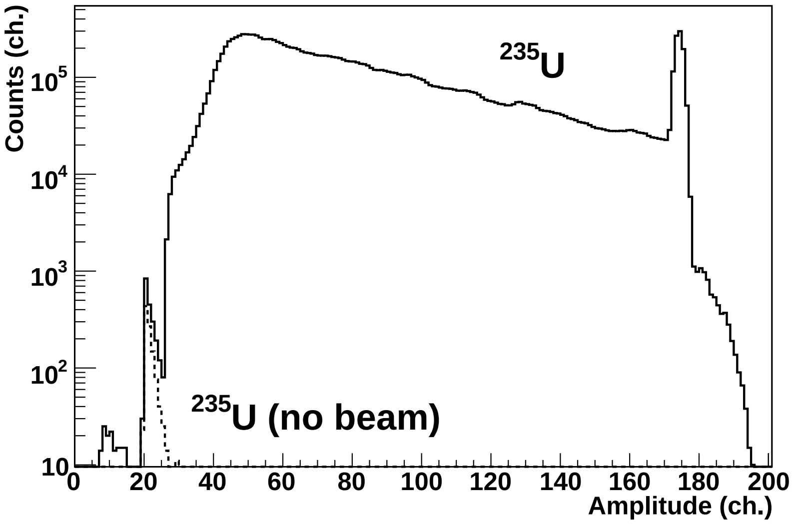

Figure 4.1 – Measured amplitude distribution of signals for neutron-induced fission of ^{235}U. The dashed line correspond to runs without the neutron beam and illustrate the effect of electronic noise and α-particle background.

Fig. 4.2 shows the correlation between the amplitude distribution of the ^{235}U sample in FIC1 as a function of the run number for the fission campaign. A good stability of the behavior of the chamber (in terms of gain and noise) is observed. This behavior is similar for all the other electrodes of FIC0, FIC1 and FIC2 and allows the use of a fixed threshold in the analysis for the whole fission campaign, which lasted over 3 months of data taking.

4.1.2 Energy Calibration

The neutron energy calibration was performed, according to Ref. [98], using Eq. 2.2, reported here for convenience:

$$E_n = \left(72.29826 \times \frac{L(m)}{T(\mu s)}\right)^2$$

The effective flight base L was determined by minimizing the χ^2 between the energy of the ^{235}U(n,f) resonances measured at n_TOF, and the tabulated ones, up to an energy of 600 eV (which is the limit of the Resolved Resonance Region in ENDF/B-VII.0). The energy of the resonances was determined with an R-matrix resonance analysis performed with the SAMMY code [68], which includes corrections for the Doppler broadening, multiple scattering and for the n_TOF resolution function. The

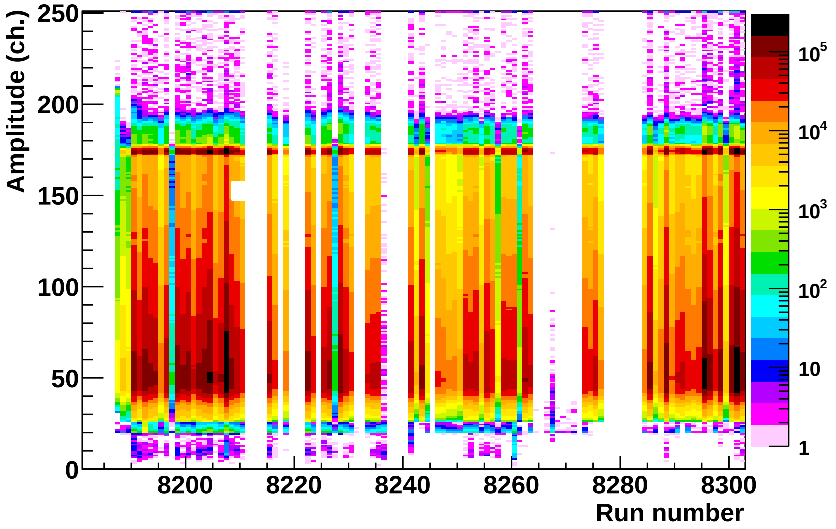

Figure 4.2 – Amplitude distribution of signals in the ^{235}U(n, f) reaction as a function of the run number. The behavior is similar for all the other electrodes of FIC0, FIC1 and FIC2. The saturation peak is evident around channel $\sim$170.

extracted flight-path is 186.95±0.05 m, a value which takes into account the geometrical distance of the experimental apparatus from the surface of the Pb spallation target, as well as the average moderation distance inside the target itself. The additional term in the neutron time-of-flight, suggested in Ref. [98] to account for the moderation process, was also included in the calibration. Fig. 4.3 shows the relative ratio between the experimentally determined resonance energies at n_TOF and those from the ENDF/B-VII.0 evaluated library. As expected, a very good agreement is found between the two, with most resonances within 0.1% from the tabulated energy, thus demonstrating the accuracy of the energy calibration.

4.1.3 Dead-Time correction

The accurate determination of fission cross-sections requires corrections of all possible experimental effects. Among them, one of the most important is typically the dead-time and pile-up of the detector-electronics-acquisition setup. In principle, an acquisition system based on Flash ADCs, like the one used at n_TOF, should not be affected by dead-time, while pile-up effects are minimized, since overlapping signals can still be identified and analyzed separately. However, an effect similar to electronic dead-time is introduced in the analysis by the signal reconstruction routine, which is not able to recognize two different signals when their separation in time is small. A detailed analysis of the dead-time in the present data is not straightforward, since it depends on the relative amplitude of the signals.

However it was verified that, for typical fission signals, the dead-time introduced

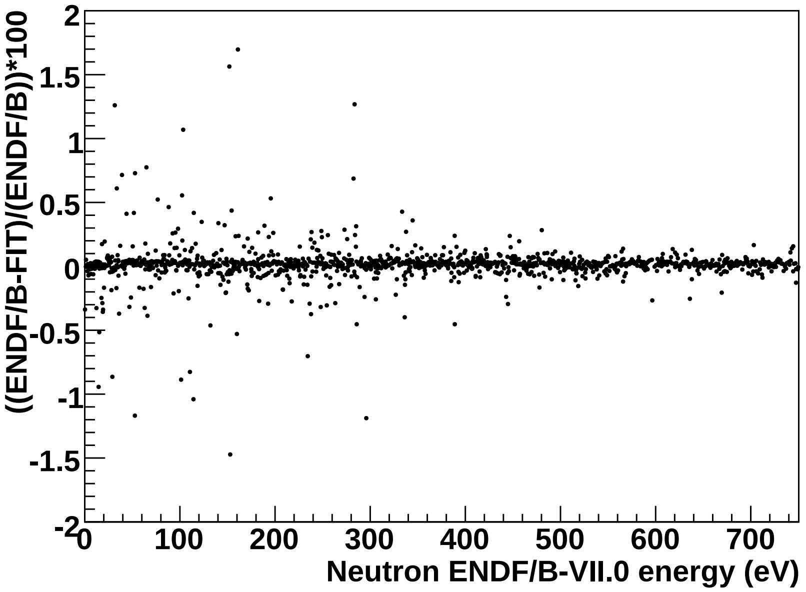

Figure 4.3 – Ratio between the resonance energy determined at n_TOF and the one from ENDF/B-VII.0 evaluated database. For most resonances the differences between experimental and tabulated energies are within 0.1%.

by the reconstruction routine is - on average - around 220 ns (see Fig. 4.4). Although small, some correction has to be applied for the loss of events due to such a dead-time. For this purpose, the non-paralyzable model was assumed. The correction was calculated by means of Eq. 4.1, [99]

$$C_r^R = \frac{C_r^m}{1 - C_r^m \times \Delta t} \tag{4.1}$$

In this expression C_r^R is the true count-rate, C_r^m is the measured count-rate and Δt is the dead-time. In order to apply this correction, the instantaneous count-rate (as a function of neutron energy) has to be determined. To this purpose, an histogram of the counts vs. neutron energy per neutron bunch is constructed. Starting from the energy bins of width ΔE, it is possible to calculate the corresponding bin width in time-of-flight (ΔT) using Eq. 2.2. Denoting C the number of counts in each energy bin, the instantaneous measured counting rate in the bin is then calculated as $C_r^m = \frac{C}{\Delta T}$. It is important to stress here that the instantaneous count-rate has to be estimated separately for each sample and, especially, for dedicated and parasitic proton beams, which are different by a factor of two in terms of neutron flux (and therefore in fission count-rate).

The dead-time correction factor, expressed as $\frac{C_r^R}{C_r^m}$, is shown in Fig. 4.5 for the ^{235}U sample for the dedicated and parasitic mode. Below 100 keV, the correction is found to be negligible for parasitic beam, while it goes up to 2% for the strongest

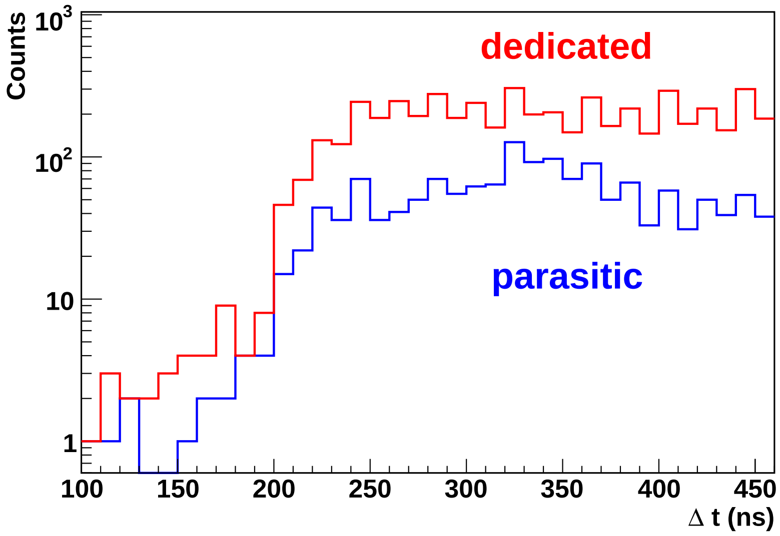

Figure 4.4 – Histogram of the time differences between two consecutive signals. The dead-time of ≃220 ns, introduced by the reconstruction routine, is evident in the figure.

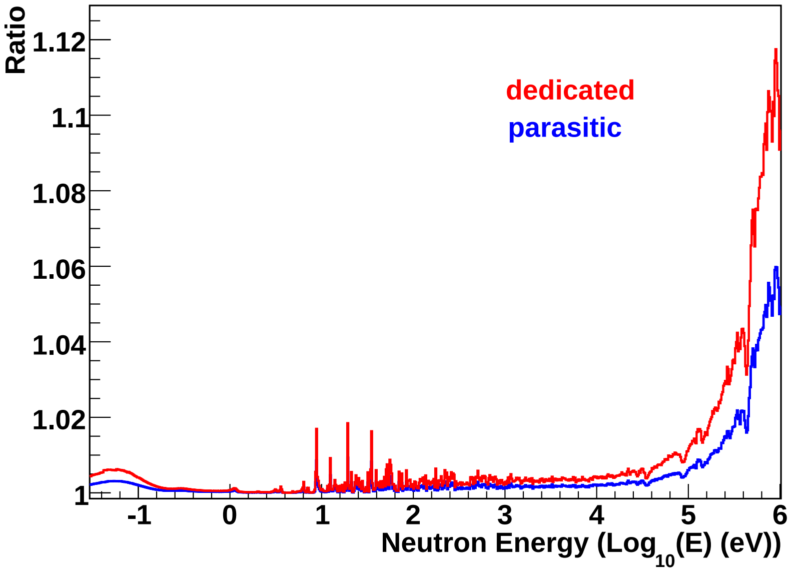

Figure 4.5 – Ratio between the count-rate corrected for dead-time, and the measured one in the ^{235}U(n, f) reaction. The effect of dead-time is different for dedicated and parasitic beams, due to different proton intensities.

resonances in dedicated beams. However it becomes important above 300 keV, reaching approximately 6% at 1 MeV for parasitic beams and ∼10% for dedicated ones. The effect of dead-time is therefore important and has to be taken into account in order to extract high accuracy cross-section data.

4.2 n_TOF neutron flux

As mentioned in Chapter 2, the fission measurements at n_TOF are performed with a final collimator of the neutron beam that has a larger aperture with respect to the capture campaign (∅=8 cm as compared with ∅=1.9 cm). While several measurements have been made in the past in order to determine the neutron flux with the small-aperture collimator, no previous measurements exist for the flux corresponding to the large-aperture collimator. Nevertheless in the fission campaign the neutron flux can be determined by means of the ^{235}U sample, which is a cross-section standard at thermal energy and from 0.15 eV to 200 MeV [76]. Since the ^{235}U sample is mounted in the same chamber as all other samples, a very accurate estimate of the neutron flux impinging on the ^{233}U and MA samples can be obtained this way.

The neutron flux $\Phi(E_n)$ enters in the determination of the cross-section for the isotopes under study, according to the following expression:

$$\sigma(E_n) = \frac{C_{^A\mathrm{X}}(E_n)}{N_{^A\mathrm{X}} \times \Phi(E_n) \times \varepsilon} \tag{4.2}$$

Here C$_{^A\mathrm{X}}$ is the total number of counts recorded for the isotope ^{A}X under investigation, for a given neutron energy, and normalized to the nominal n_TOF bunch of 7×10^{12} protons[2], $N_{^A\mathrm{X}}$ is the total number of atoms per barn of the ^{A}X samples, $\Phi(E_n)$ is the neutron flux per proton bunch impinging on the detector, and ε the total efficiency, which may vary with the isotope under consideration, due to the effect of the amplitude threshold used in the event selection. Eq. 4.2 is valid on the assumption that the absorption of the neutron flux in the samples and in the electrodes is negligible. As shown in Chapter 3, this assumption has been verified for the present experimental setup by means of Monte Carlo simulations performed with the MCNPX code [60], which indicated that the attenuation in the Al electrodes and windows are of the order of a few per thousand with the exception of few selected very narrow regions in the keV neutron energy range.

The neutron flux $\Phi(E_n)$ is determined from the analysis of the ^{235}U(n, f) data

---

[2] Although not necessary, the normalization of both the counts and the flux to the nominal proton bunch (obtained by dividing the number of protons by 7×10^{12}), is a convenient way to proceed if different runs are used for different isotopes.

collected simultaneously to all other isotopes with the same detector, according to the following expression, derived from Eq. 4.2:

$$\varepsilon \times \Phi(E_n) = \frac{C_{^{235}\mathrm{U}}(E_n)}{N_A \times \sigma^{eval}_{^{235}\mathrm{U}}(E_n)} \tag{4.3}$$

Here, $\sigma^{eval}_{^{235}\mathrm{U}}(E_n)$ represents the evaluated cross-section used as reference, which, in the present work, was extracted from the ENDF/B-VII evaluated database [33].

Fig. 4.6 shows the counts as a function of neutron energy between 1 and 10 eV, measured for the ^{235}U(n, f) reaction, for a threshold at channel 40 in the amplitude distribution (for background rejection), and after applying the dead-time corrections. The line in the figure shows the predictions based on the tabulated cross-section from the ENDF-B/VII.0 database. For comparison with the experimental data, the evaluated cross-section has been scaled by an arbitrary factor so to match the first resonance (a fixed scaling factor corresponds to assuming a flat neutron flux distribution, almost true in the energy range of the figure). Typically, a very good agreement is observed for most resonances. However, some differences can be observed in restricted energy regions, mostly in correspondence of valleys between resonances. In those cases, differences of up to 20% can be seen. Such discrepancies propagate to the extracted neutron flux and, as a consequence, affect the measured cross-section of all the other isotopes under investigation.

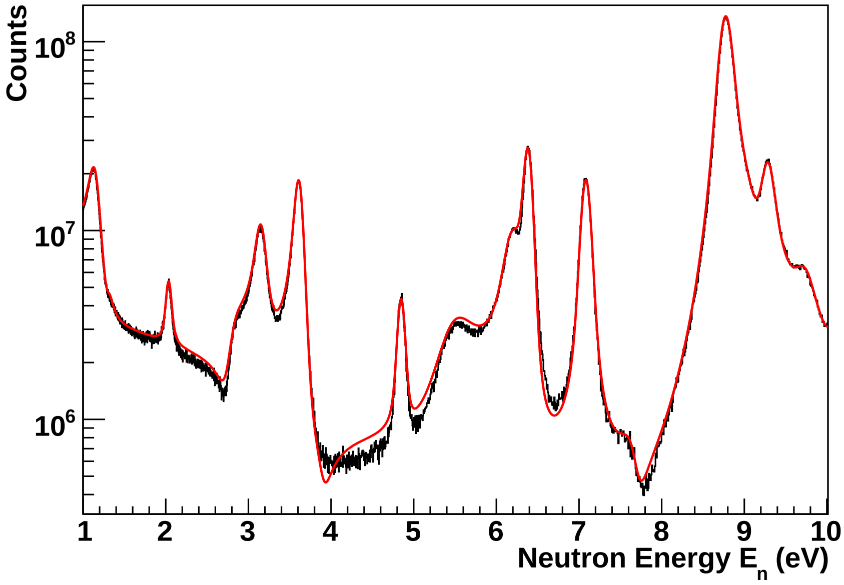

Figure 4.6 – Measured fission yield for ^{235}U in the neutron energy region from 1 eV to 10 eV (black line), compared to the ENDF/B-VII.0 evaluated data (red line). The two data sets are normalized relative to each other at the first ^{235}U(n, f) resonance.

Figure 4.7 shows the neutron flux extracted via Eq. 4.3 (black histogram). The artificial structures between 1 eV and ~200 eV are the direct consequence of the observed discrepancy between experimental data and evaluated cross-section mentioned above (and seen in Fig. 4.6). To avoid these effects, the energy dependence of the neutron flux in this limited energy region was adopted from the so-called "capture flux" [100], shown in Fig. 4.8, measured with the small-aperture collimator used during the n_TOF capture program. Detailed data on this flux are available from measurements performed with the ^{6}Li(n, α)T reaction-based monitor [101] and with a ^{235}U loaded parallel plate fission ionization chamber from the Physikalisch-Technische Bundesanstalt, Braunschweig [55]. The red curve in Fig. 4.7 shows the adopted flux in the region from 0.16 eV to 245 eV, obtained by normalizing the "capture flux" to the one extracted via Eq. 4.3 between 0.16 eV and 1 eV. The various dips in the neutron flux correspond to absorption from O and Al resonances, either in the water moderator or in the entrance window of the neutron TOF tube. The neutron flux shown in Fig. 4.7 has been used to determine the fission cross-sections for ^{233}U and MAs, from thermal to 10 keV.

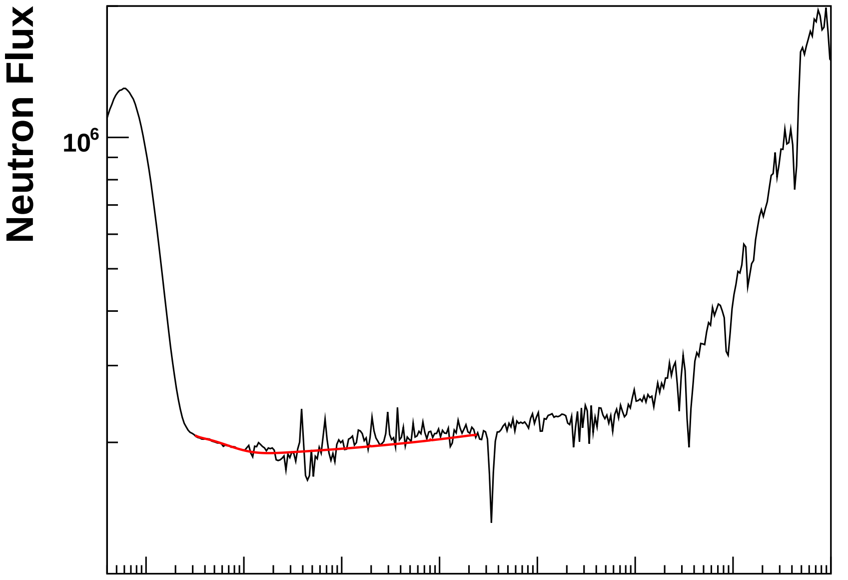

Figure 4.7 – Isolethargic neutron flux distribution (expressed as $dn/d\ln E$ per 7×10^{12} protons) distribution for the fission collimator, measured with the FIC detector via the ^{235}U(n, f) reaction (black histogram). The flux refers to the large aperture collimator (8 cm diameter), used in the fission measurements. The red line indicates the flux used in the present analysis between 0.16 eV and 245 eV, which was obtained as described in the text.

The right-hand side of Eq. 4.3 gives the neutron flux convoluted with the detection efficiency of the fission chamber. However, since this is close to 100% (as shown later),

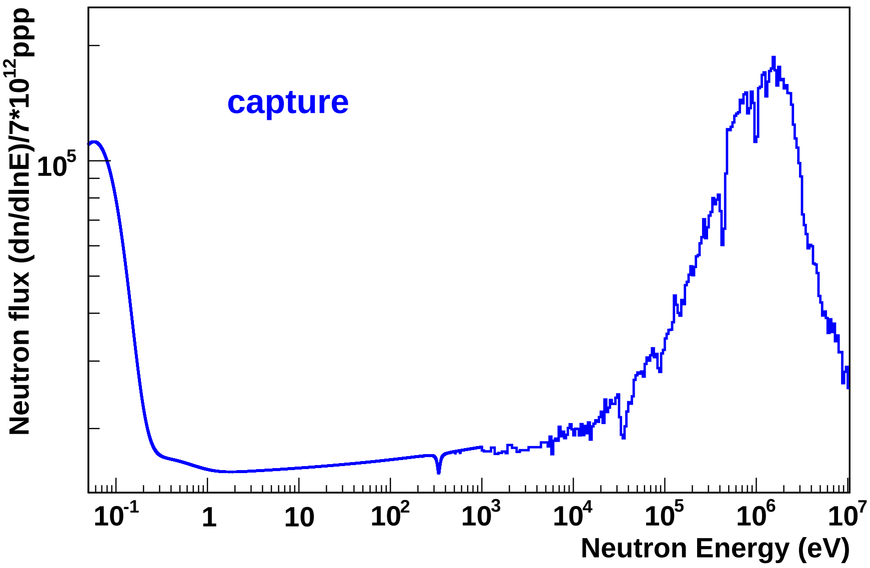

Figure 4.8 – n_TOF flux measured with the silicon monitor (SiMON) [101] and with the PTB fission chamber [55] (below 1 eV and above 1 keV) with the small aperture (1.8 cm diameter) "capture" collimator.

the result in Figure 4.7 represent, within a few percent, the neutron flux available for the fission measurements[3].

Above ≃10 keV, i.e. in the energy region in which the ^{235}U(n, f) cross-section is a smooth function of the neutron energy, the cross-section can be determined directly from the ratio between the number of events measured for the isotope under consideration and the ones measured for ^{235}U, using the evaluated fission cross-section of ^{235}U from ENDF/B-VII.0,

$$\sigma_{^A\mathrm{X}}(E_n) = \frac{C_{^{235}\mathrm{U}}(E_n)}{C_{^A\mathrm{X}}(E_n)} \times CF \times \sigma^{eval}_{^{235}\mathrm{U}}(E_n) \tag{4.4}$$

In the expression, the correction factor CF includes the ratio between the number of atoms per barn of the ^{A}X and ^{235}U samples, as well as the efficiency and dead-time corrections described later on. Since the evaluated cross-section above 600 keV becomes a smooth function of the neutron energy, the use of Eq. (4.4) provides a more direct measurement of the ^{A}X(n, f) cross-section, minimizing in particular the systematic uncertainties related to the extraction of the neutron flux.

The effects of possible target non-uniformities are negligible in the case of fission measurement, because the neutron beam profile is slightly larger than the sample diameter and almost flat in the region of the sample, as shown in Fig. 4.9, where the

---

[3] This is true in the assumption that the neutron flux is fully intercepted by the 8 cm samples. Simulations have shown that the tail of the neutron beam falls outside the sample, for an estimated fraction of ≃20% of neutrons lost.

simulated neutron beam profile in fission runs is plotted for different neutron energy ranges.

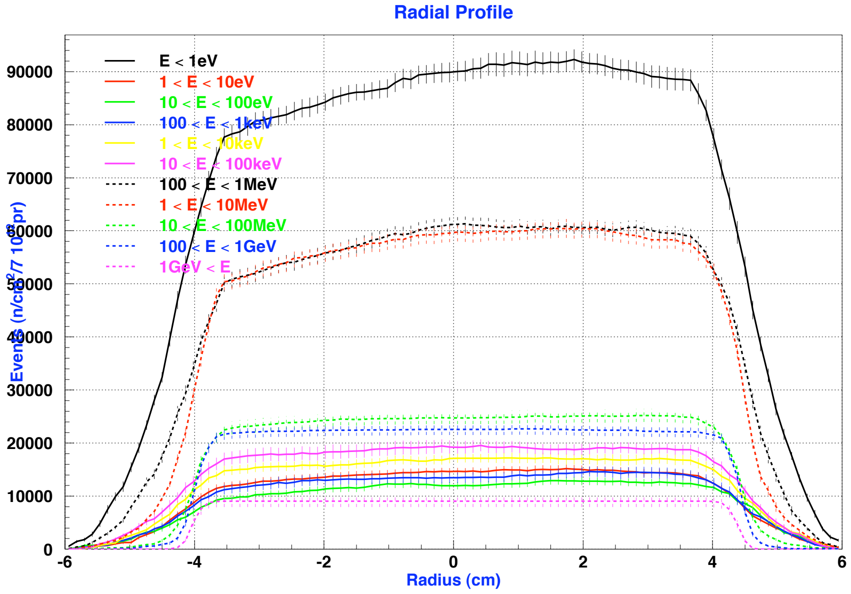

Figure 4.9 – FLUKA simulation of the neutron beam profile for the fission collimator [102]. The plot shows the number of neutrons/cm^2/10^7 protons as a function of the distance from the beam central axis, for different neutron energy regions.

4.3 ^{235}U(n, f) cross-section

In order to better understand the origin of the structures in the flux extracted from the ^{235}U sample, shown in Fig. 4.7, the ^{235}U(n, f) cross-section has been extracted using the independently determined "capture" flux in the whole energy range, normalized to the fission one in the energy region between 0.16 eV and 1 eV. This analysis is important also to extract further informations on the cross-section of ^{235}U by comparing the n_TOF results with previous data. As a reminder, a threshold on the signal amplitude at channel 40 was applied in the analysis, and corrections for the dead-time and detection efficiency have been applied.

An overall view of the extracted fission cross-section for the ^{235}U sample can be observed in Fig. 4.10 in the whole energy range from 0.03 eV up to 1 MeV, with a 2000 bin/decade binning. For a more meaningful comparison, the data have been renormalized to the 0.12 eV resonance of ENDF/B-VII.0.

Figs. 4.11, 4.12 and 4.13 report some examples of the ^{235}U(n, f) cross-section for selected energies in the resolved resonance region. A comparison with previous experimental results extracted from the EXFOR database is also shown [30] (with

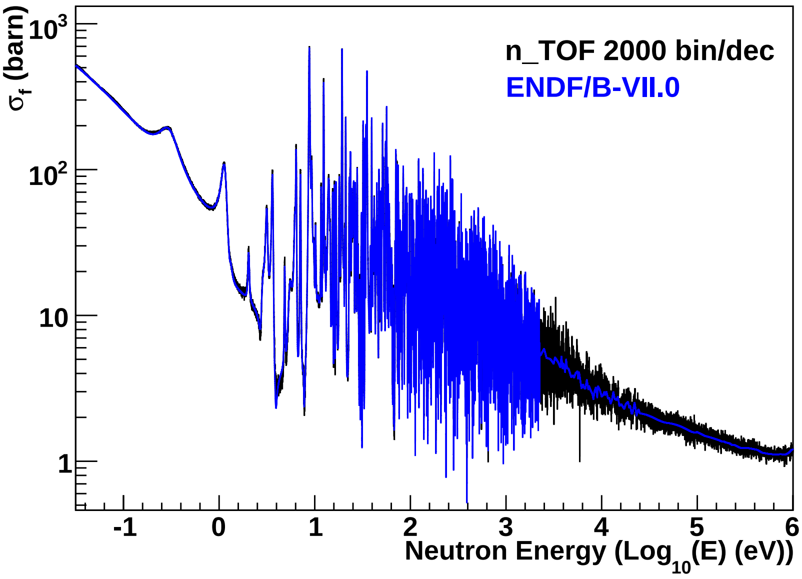

Figure 4.10 – The measured and evaluated ^{235}U(n, f) cross-section from near thermal up to 1 MeV neutron energy. The n_TOF data are normalized to the 0.12 eV resonance of ENDF/B-VII.0.

data from refs. [103, 104, 105, 106, 107, 108, 109, 110, 111, 112, 113, 114]). Particular interest has been devoted to the valleys between resonances, since in those regions the background is expected to have a greater effect. As already mentioned, the dips between the resonances in the n_TOF ^{235}U(n, f) data appear in some cases to be deeper than in the evaluations (similar behavior is observed up to 20 keV for all three databases ENDF/B-VII.0, JEFF-3.1 and JENDL-3.3). A comparison with previous experimental results in the EXFOR database, shows a large spread of results in correspondence of the dips, of the order of 200-300%, with very large fluctuations within each data set. The present results, confirmed by the data taken at n_TOF with the PPAC detector, using the coincidence method [115, 116], confirm the low ambient background of the n_TOF facility. Presumably, some previous data may be affected by a larger background, which fills the valleys between resonances, where the cross-section is very low. The comparison also shows that some previous data present discrepancies in the resonance energy, shifted with respect to most of the data and to evaluations (e.g. Wagemans *et al.* [109] and Van Shi Di *et al.* [112]).

From these arguments, it can be concluded that the artificial peaks in the flux (extracted from ^{235}U(n, f) data with Eq. 4.3) result from the discrepancies between n_TOF data and evaluated libraries in the valley between resonances These differences could be most probably be attributed to an incorrect value in the libraries, due to the large spread of previous measurements and to possible errors in the determination of some resonance doublets.

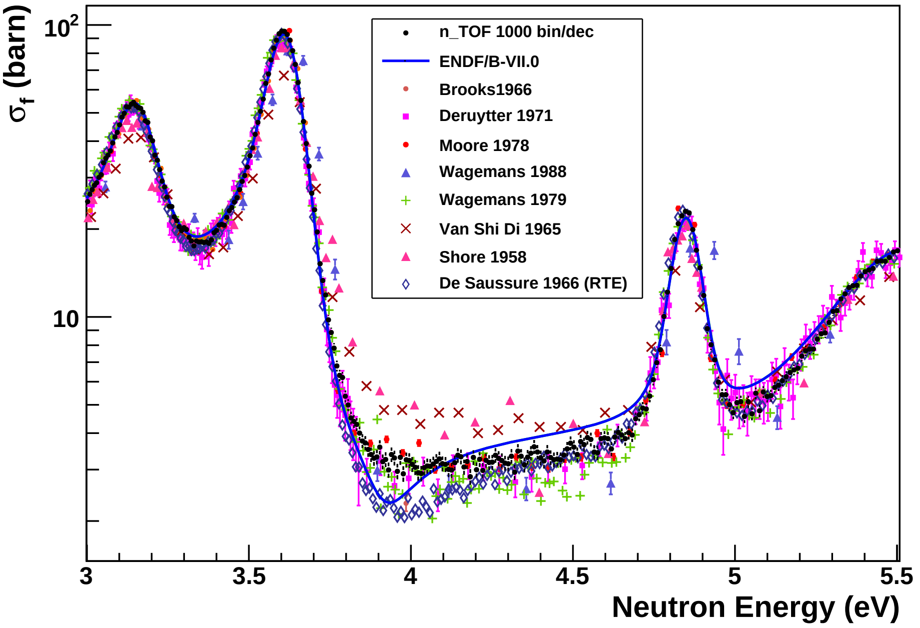

Figure 4.11 – The ^{235}U(n, f) cross-section measured at n_TOF in the energy range from 3 eV to 5.5 eV, compared to previous experimental data.

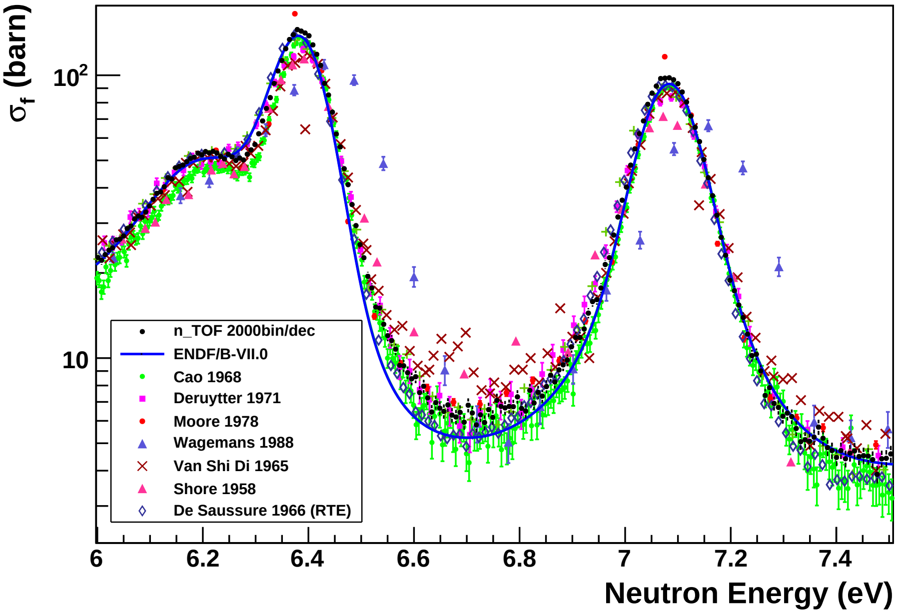

Figure 4.12 – The n_TOF ^{235}U(n, f) cross-section in the energy range from 6 eV to 7.5 eV, compared to previous results.

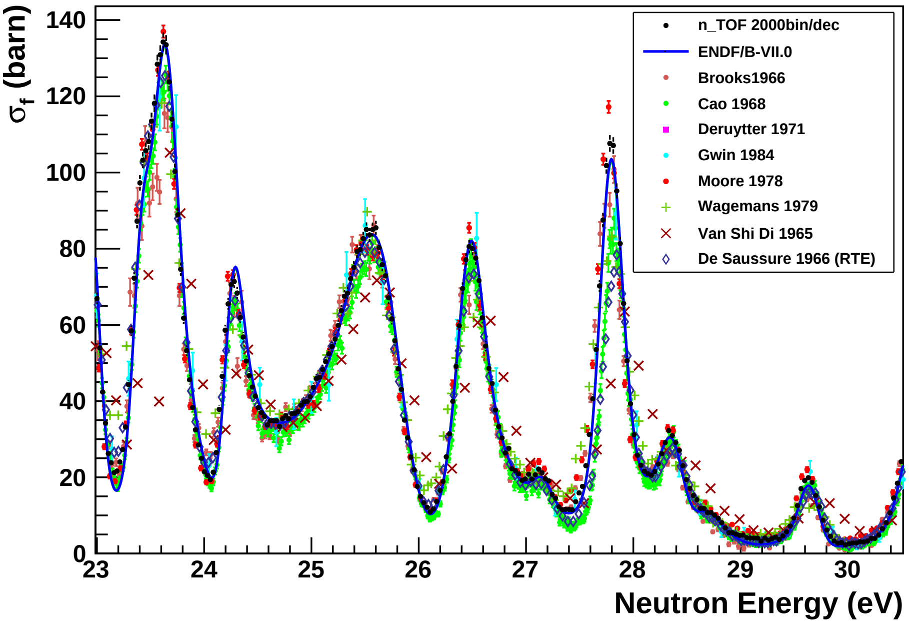

Figure 4.13 – The ^{235}U(n, f) cross-section measured at n_TOF in the energy range from 23 eV to 30.5 eV, compared with previous experimental results.

The statistical errors are included in the data shown in the pictures. Since these cross-sections are of interest only to investigate the reason for the presence of peaks in the fission flux, no further error analysis is presented in this section. This will be thoroughly discussed in the following chapters, when presenting the results of the fission cross-section of the ^{233}U and MAs isotopes.

4.4 ^{238}U/^{235}U (n, f) cross-section ratio

As previously pointed out, the ^{235}U(n, f) cross-section is a standard at 0.0253 eV and from 0.15 eV to 200 MeV [76], while the ^{238}U(n, f) cross-section is a standard from 2 MeV to 200 MeV [77]. The measurement of the ^{238}U/^{235}U fission cross-section ratio is particularly important since it can be used by evaluators to test nuclear reaction codes, which are used to predict fission cross-sections and to compile nuclear data evaluations.

At present, this ratio is known with an accuracy of $\simeq$5%, and relatively new data [117] have hinted that the ratio may be systematically lower than previously known. It was possible, at n_TOF, to measure the ^{238}U/^{235}U (n, f) cross-section ratio, since both samples were mounted in the same chamber. Considering that ^{238}U is a threshold isotope, the cross-section starts to be significant only in the MeV region.

As shown in previous sections however, it is not straightforward to extract fission cross-sections above 1 MeV with the FIC1 detector, due to the presence of a large

γ-flash oscillation in the raw data. For this reason, it was decided to use the FIC2 chamber mounted in the escape lane, in which a compensation technique was employed to suppress the γ-flash. Since FIC2 has been used for measurements with the small (capture) as well as large (fission) collimator, two data groups can be analyzed. However, in the fission configuration a residual electronic noise near the γ-flash hinders the possibility to reach 1 GeV neutron energy, while providing reliable results up to the 300 MeV neutron energy. On the contrary, in the capture configuration, where the noise associated with γ-flash is much smaller, the reduced statistics is the main problem.

A description of the samples installed in FIC2 and used in the measurements analyzed in this section is given in Table 3.3.

4.4.1 ^{235}U(n, f) and ^{238}U(n, f) with FIC2 (fission configuration)

As previously mentioned, the FIC2 detector is less sensitive to problems caused by the γ-flash, due to the compensation technique used in the measurement. This technique is based on the fact that the shape of the γ-flash signal is similar for contiguous electrodes: therefore, by electronically subtracting the output of two consecutive electrodes, one of them without sample, it is possible to obtain clear fission fragments signals. However the identification of signals for neutron energies above $\simeq$20 MeV neutron energy is still difficult for two reasons. A significant undershooting of the baseline is present, especially for dedicated bunches. Although this is mostly taken into account by the reconstruction routine, it could happen, as shown in Fig. 4.14, that the baseline becomes negative. In this case, the amplitude distribution of the signals is distorted and the threshold is not anymore well under control. The second effect is due to the fact that a residual γ-flash tail remains, on top of which fluctuations due to electronic noise may simulate a fission fragment signal, that cannot be easily distinguished from a real event. This effect tends to be more important when signals are close to the γ-flash, as can be seen in Fig. 4.15, where two example of raw data are shown together with the neutron energy corresponding to the observed fission fragment peaks.

The negative baseline and residual γ-flash problems affect the reconstructed amplitude of the signals, making more difficult to distinguish fission fragments from the electronic noise. This is evident in Figs. 4.16, 4.17 and 4.18. The first plot shows the correlation between the signal's amplitudes and the neutron energy in the whole energy range for the ^{235}U sample; at about 10 MeV, low amplitude signals starts to appear, with increasing amplitude as the neutron energy increases. They were identified as due to the noise overimposed in the tail of the γ-flash. Using a

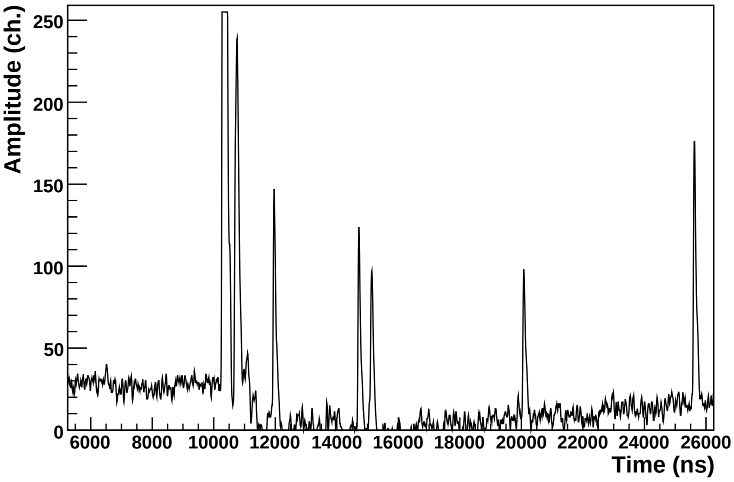

Figure 4.14 – Raw data from FIC2-fission showing the undershooting effect present after the prompt γ-flash signal. Contrary to FIC1, no electronic oscillations are present in this case.

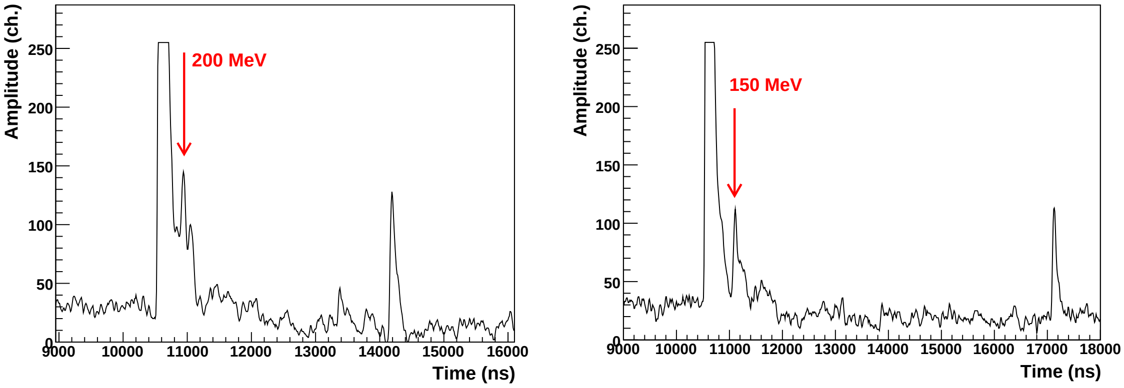

(a) FIC2-fission, ^{235}U sample.

(b) FIC2-fission, ^{238}U sample.

Figure 4.15 – Raw data from FIC2-fission, showing the signals after the prompt flash. The neutron energy corresponding to the peak on the tail of the γ-flash are also indicated in the figure.

simple amplitude threshold would include such noise in the fission cross-section. It is thus necessary to apply a graphical cut to separate real signals from noise. The cuts have to be different for dedicated and parasitic bunches, since the shape of the prompt flash (and thus of the subsequent tail) is significantly different in the two cases. Additionally, the γ-flash peak, observed in the figures as a spot close to 1 GeV neutron energy at an amplitude close to 230, has to be excluded from the analysis.

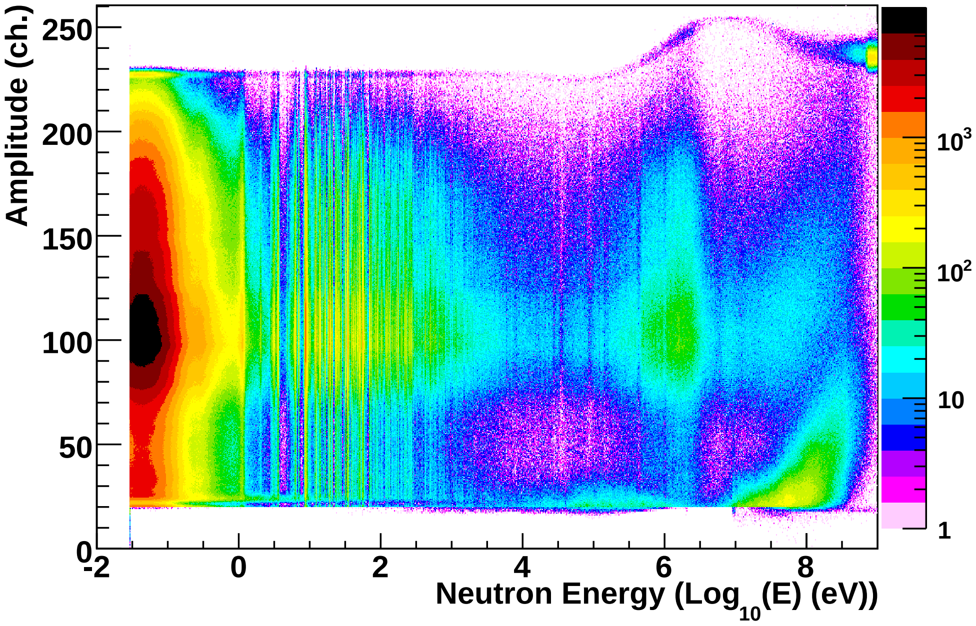

Figure 4.16 – Correlation between the signal's amplitudes and the corresponding neutron energy for the ^{235}U sample, measured with FIC2-fission in dedicated events.

The ratio of the neutron-induced fission cross-sections for ^{235}U and ^{238}U does not depend on the shape and value of the neutron flux, if the two samples are measured simultaneously and in the same experimental setup. The only corrections that have to be applied to both the ^{235}U and ^{238}U date are the dead-time and the detection efficiency, which are different for the two samples.

Figs. 4.19, 4.20 and 4.21 shows the ^{238}U/^{235}U fission cross-section ratio compared with the ENDF/B-VII.0 evaluation, and with the data from Shcherbakov *et al.* [117] and Lisowski *et al.* [118]. These are the only two experimental results that cover a wide energy range. An additional measurement, from Behrens *et al.* [119], up to $\sim$30 MeV, is essentially in agreement with Shcherbakov's results. Also shown in Fig. 4.19 are some preliminary results extracted from FIC1 data [94], although only up to 10 MeV (due to the presence of a strong γ-flash oscillation). Since the samples in the FIC1 chamber have a smaller mass uncertainty (Table 3.3 for FIC2 and Table 3.2 for FIC1 samples), this ratio data have been used as an overall renormalization of FIC2-fission results in the threshold region around 1 MeV.

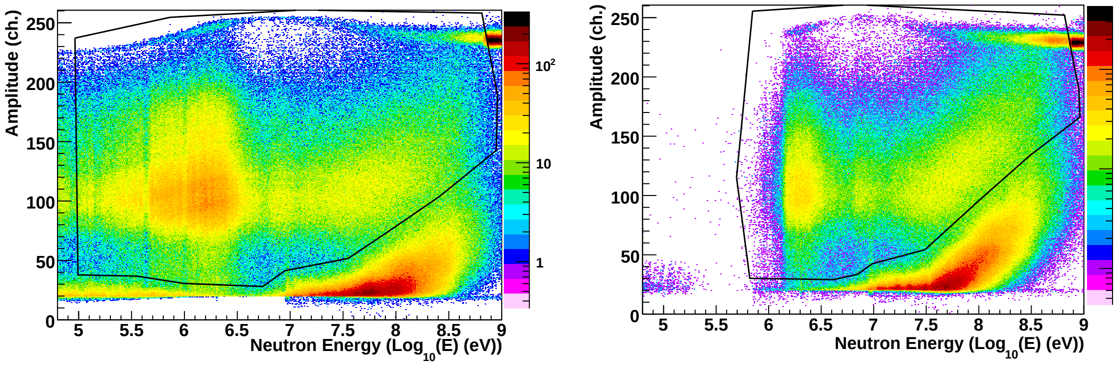

(a) Amplitude/energy correlation for ^{235}U sample of FIC2 in dedicated (TOF) bunches.

(b) Amplitude/energy correlation for ^{238}U sample of FIC2 in dedicated (TOF) bunches.

Figure 4.17 – Correlation between the signal's amplitudes and the corresponding neutron energy (above 100 keV), measured for the ^{235}U and ^{238}U samples in the FIC2 detector, for dedicated proton bunches. The graphical cut used to reject electronic noise is also shown in the figure.

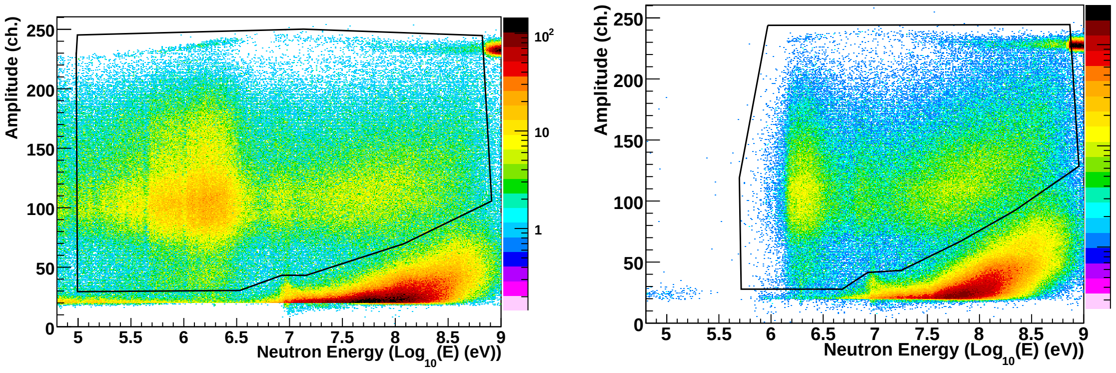

(a) Amplitude/energy correlation for ^{235}U sample of FIC2 in parasitic (EASTC) bunches.

(b) Amplitude/energy correlation for ^{238}U sample of FIC2 in parasitic (EASTC) bunches.

Figure 4.18 – Same as Fig. 4.17, but for parasitic proton bunches. Note that the amount of noise present at high energy is less than in the dedicated bunches, making the selection of fission fragments easier.

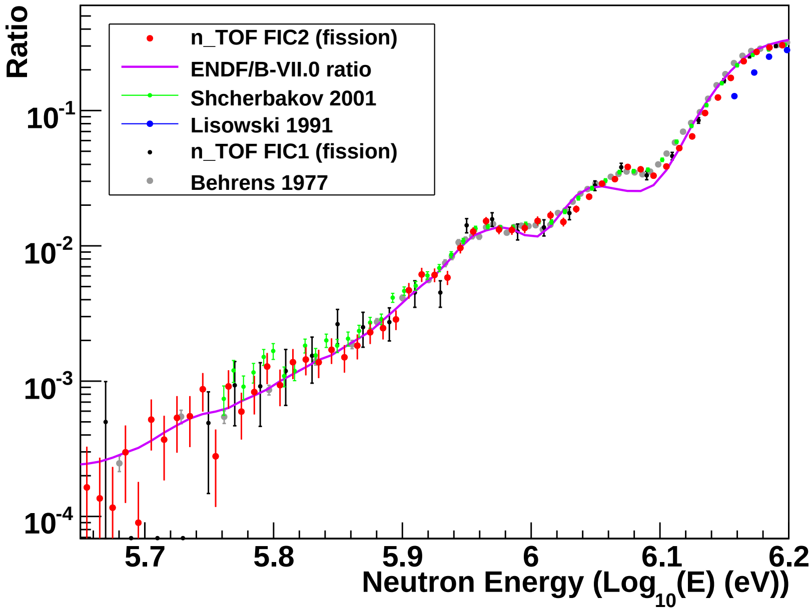

Figure 4.19 – Ratio of the fission cross-sections of ^{238}U and ^{235}U, measured at n_TOF with both FIC1 and FIC2 detectors. The figure shows also a comparison with previous experimental results, taken from the EXFOR database (Shcherbakov *et al.* [117], Lisowski *et al.* [118] and Behrens *et al.* [119]) and with the ratio given by ENDF/B-VII.0 [33] in the energy range between 460 keV and 1.6 MeV. Error bars show purely statistical uncertainties.

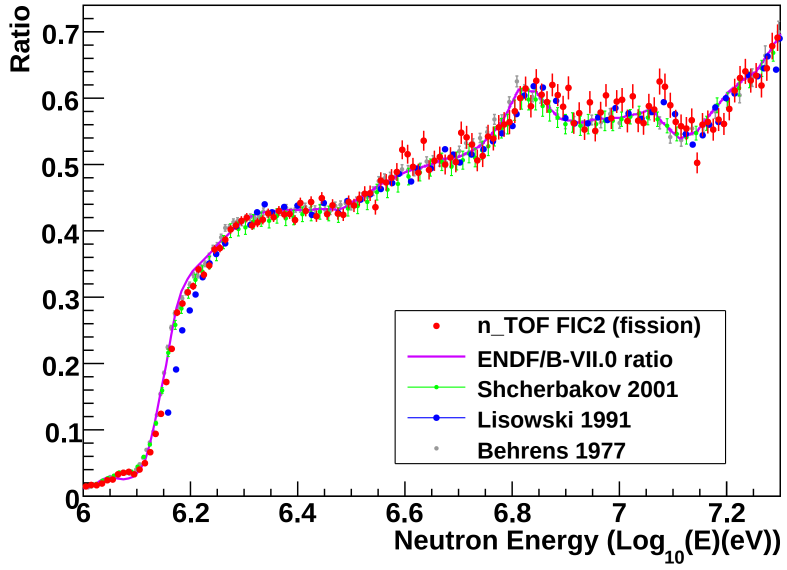

Figure 4.20 – ^{238}U/^{235}U fission cross-section ratio measured at n_TOF in the energy range between 1 MeV and 20 MeV, compared with EXFOR data and ENDF/B-VII.0 evaluation. Error bars show purely statistical errors.

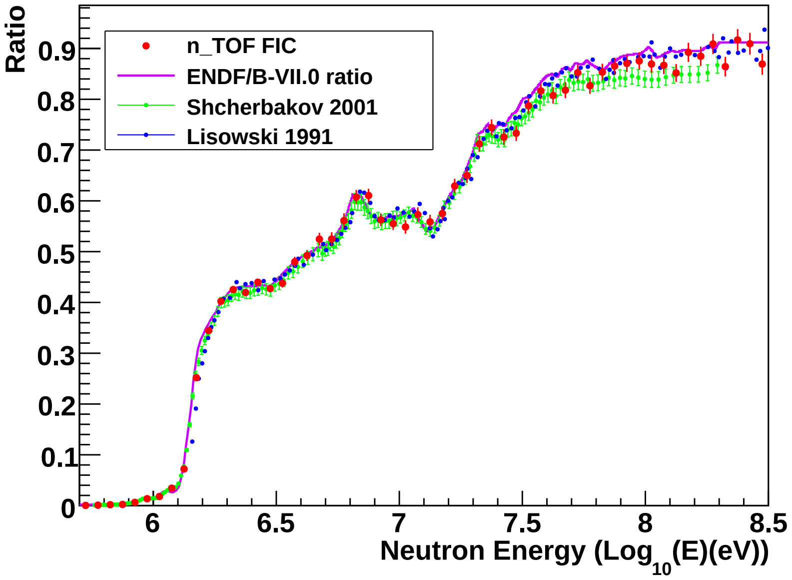

Figure 4.21 – Fission cross-section ratio of ^{238}U and ^{235}U, measured at n_TOF in the whole energy region between the threshold (~1 MeV) and 300 MeV. The present results are compared with data from Shcherbakov *et al.*, Lisowski *et al.* and with evaluated cross-section in ENDF/B-VII.0. Error bars show purely statistical errors.

In the threshold region, n_TOF data confirm Shcherbakov's results, especially around the two subthreshold peaks at about 900 keV and 1.2 MeV, where the tabulated cross-section from the ENDF/B-VII.0 library differs from experimental data, and between ~1.4 MeV and 1.75 MeV where Lisowski's data are significantly lower.

Good agreement with evaluated as well as with experimental results is found from the threshold up to 20 MeV, where anyway the discrepancies between evaluated and experimental results are not particularly significant, being well within experimental errors.

On the contrary, the region between 20 MeV and 1 GeV is crucial, since only two measurement exists and they differ by nearly 5% at the highest energies (E_n ≥100 MeV), while the 2% discrepancy at lower energies can be considered, with good approximation, within the systematic errors of each measurement. Recent results by Nolte *et al.* [120, 121] although with rather large uncertainties, support the data of Lisowski *et al.*. Fig. 4.21 shows the n_TOF results in comparison with other data: the systematic uncertainties are of the order of 2% for the region up to 20 MeV due essentially to the mass uncertainty and normalization, while from 20 MeV up to 300 MeV this value is increased up to 4% due to the dead-time correction factor and due to a graphical cut imposed in the analysis. The present data are closer to Lisowski's data (and ENDF/B-VII.0 evaluated cross-section) and seems to rule out the smaller value for the ratio proposed by Shcherbakov *et al.*. A more careful analysis is however needed to drawn a final conclusion on this point.

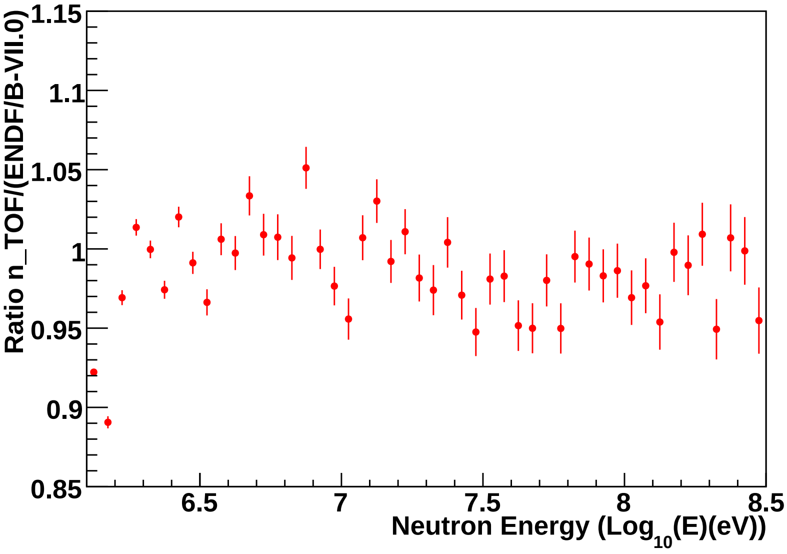

Figure 4.22 – Divergence of the n_TOF data on the ^{238}U/^{235}U cross-section ratio from the one based on the ENDF/B-VII.0 library. Error bars show purely statistical uncertainties.

4.4.2 ^{235}U(n, f) and ^{238}U(n, f) with FIC2 (capture configuration)

In the case of the fission measurements performed with the FIC2 detector and the small aperture collimator (the so-called FIC2-capture setup), the prompt flash does not pose particular problems, since the smaller aperture of the collimator results in a significant reduction of the flux of high energy γ-rays and relativistic particles impinging on the detector. In principle it is therefore possible, with this setup, to extract fission cross-section ratios up to 1 GeV. The possibility to extend the energy range of the fission data is demonstrated by Fig. 4.23, which shows the count-rate distribution for the ^{235}U sample measured with the FIC2-capture setup, from 0.03 eV up to 1 GeV neutron energy.

However, two problems affect the results obtained with the FIC2-capture setup: a worse energy calibration and low statistics. Contrary to the measurements with the FIC2-fission setup and FIC1 (both performed with the large aperture collimator), in the FIC2-capture data it was not always possible to clearly identify the signal of the γ-flash, since this is small and seldomly saturates. This causes a problem in the time calibration of the data. A solution to this problem consisted in using a fixed value of the time reference for all neutron bunches, instead of the one extracted from the analysis of the γ-flash on a bunch-by-bunch basis. The value of t_γ used in the analysis was determined from the distribution of the time of the first signal

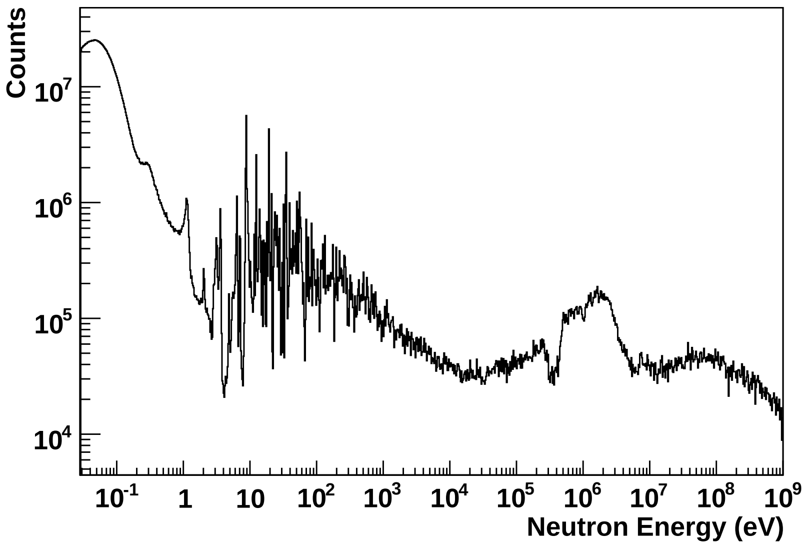

Figure 4.23 – Raw data of ^{235}U(n, f) collected with FIC2, used as a monitor of the neutron flux.

(above threshold) for each neutron bunch. The position of the first peak in the distribution was assumed as reference for the time calibration. Clearly, the error in the time calibration is higher than in the standard analysis, with an estimated uncertainty of up to 300 ns. Such a problem, however, does not significantly affects the determination of the cross-section, since a very high energy resolution is not required in the region above $\approx$1 MeV, where resonances are not present and the cross-section is a smooth function of the energy. For the 192 m flight path, the energy resolution associated with the 300 ns uncertainty in the time calibration is of the order of 2% at 1 MeV, 8% at 10 MeV and 35% at 100 MeV.

Fig. 4.24 shows the ^{238}U/^{235}U fission cross-section ratio compared with the data from Shcherbakov *et al.* [117] and Lisowski *et al.* [118], from the threshold up to $\simeq$1 GeV. From the figure it is clear that the main problem in these data is the low statistics. It should be considered, in fact, that the use of a small aperture collimator results in a neutron flux 15 times lower than available with the large aperture collimator. Although data with the FIC2-capture setup were collected in approximately the same time as the fission measurements, the resulting statistics is therefore more than 10 times smaller. For this reason, although the mean value of the cross-section is approximately consistent with Lisowski and Shcherbakov - the quality of the data is not sufficient to be able to distinguish again between the two experimental results, being the statistical errors too big to draw a meaningful conclusion.

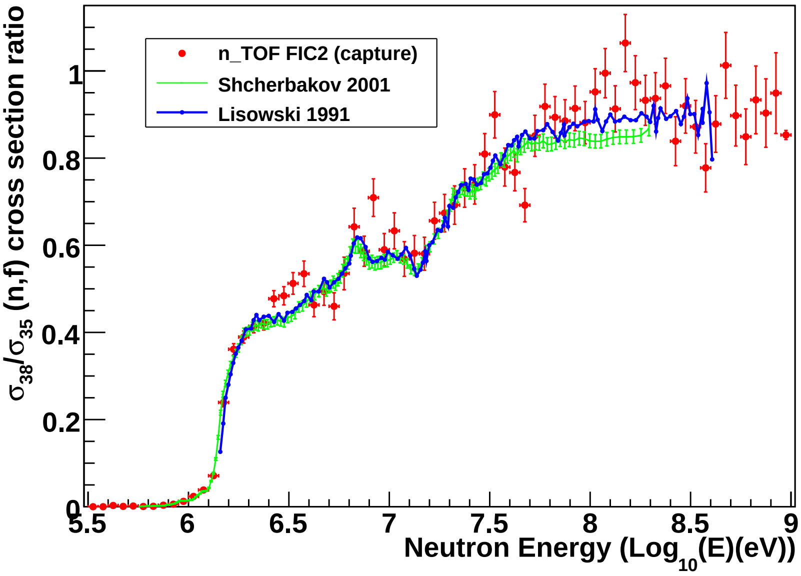

Figure 4.24 – ^{238}U/^{235}U (n, f) cross-section ratio up to 1 GeV from FIC2 samples in capture configuration. The present results are compared with the data from Shcherbakov *et al.* [117] and Lisowski *et al.* [118]. The fluctuations in the data are too high to allow a meaningful conclusion.

Chapter 5

^{233}U(n, f) cross-section

This chapter reports the cross-section of the ^{233}U(n, f) reaction measured at n_TOF with the FIC chamber, in the energy region from ≈30 meV to 1 MeV. For sake of simplicity, in the text we will refer to the low energy limit of 30 meV as "thermal". The first part is devoted to the description of the analysis procedure, while in the second one the uncertainties that affect the experimental results are discussed. Finally, experimental results are compared with previous measurements and with evaluated cross-sections from major libraries.

5.1 Analysis procedure

In the present measurements, four ^{233}U and two ^{235}U samples were used (Table 5.1). The samples were prepared as thin U_3O_8 layers by means of the painting technique [85, 86, 87], described in Chapter 3. While the total mass of the two isotopes is approximately equal, the ^{233}U layers are thinner than those of ^{235}U, to compensate for the higher fission cross-section of ^{233}U. In this way, similar count-rates were obtained for each electrode, thus reducing the systematic uncertainties related to the dead-time corrections. The samples were made of pure uranium deposited on an Al backing. The enrichments of the ^{233}U and ^{235}U samples were 99.9% and 100%. An analysis of contaminations in the sample, performed by means of α-spectroscopy revealed that ^{233}U and ^{234}U impurities in the ^{235}U sample were less than 10^{-4}.

As for the ^{235}U data discussed in the previous chapter, fission fragments are discriminated from noise and α-particle background by means of a threshold on the amplitude distribution of the reconstructed signals. Figure 5.1 shows the amplitude distribution measured for the ^{235}U (dashed) and ^{233}U (solid) samples, in the range between thermal and 1 MeV neutron energy. A higher α-decay background is present in the case of the ^{233}U sample, as expected due to the shorter half-life. Nevertheless,

Table 5.1 – Samples used in the ^{233}U(n, f) measurement. The mass reported in the table is that of the U isotope only (not of the compound).

Sample	Chemical form	Mass (mg)	Areal density (10^{-7} atoms/b)	Uncertainty (%)
^{235}U	U_3O_8	15.2	7.75	1.4
^{235}U	U_3O_8	16.6	8.46	1.3
^{233}U	U_3O_8	8.04	4.13	1.2
^{233}U	U_3O_8	7.45	3.83	1.2
^{233}U	U_3O_8	7.49	3.85	1.3
^{233}U	U_3O_8	7.86	4.04	1.1

the fission fragment distribution is still well separated from the region corresponding to the α-particle background. Therefore, in this case as well, a simple amplitude threshold is sufficient to discriminate fission fragments from electronic and α-particle background.

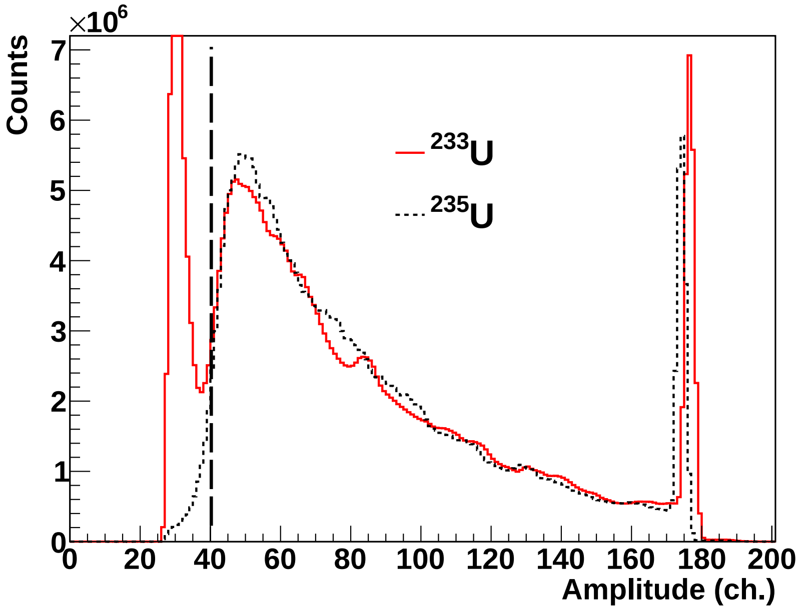

Figure 5.1 – Pulse height spectra for the ^{233}U sample (solid red line) and for the ^{235}U reference sample.

For a consistent normalization between the ^{233}U and the reference ^{235}U sample, the same threshold is applied on the signal amplitude. The threshold, shown in the figure by the line at channel 40, allowed to reject most of the background, while losing only a very small fraction of the fission fragment distribution. A check of the residual background has been performed by analyzing runs without the neutron beam, and its contribution has been found to be negligible even at low energy - less than 0.5% - as already apparent in the amplitude distribution of Fig. 5.2.

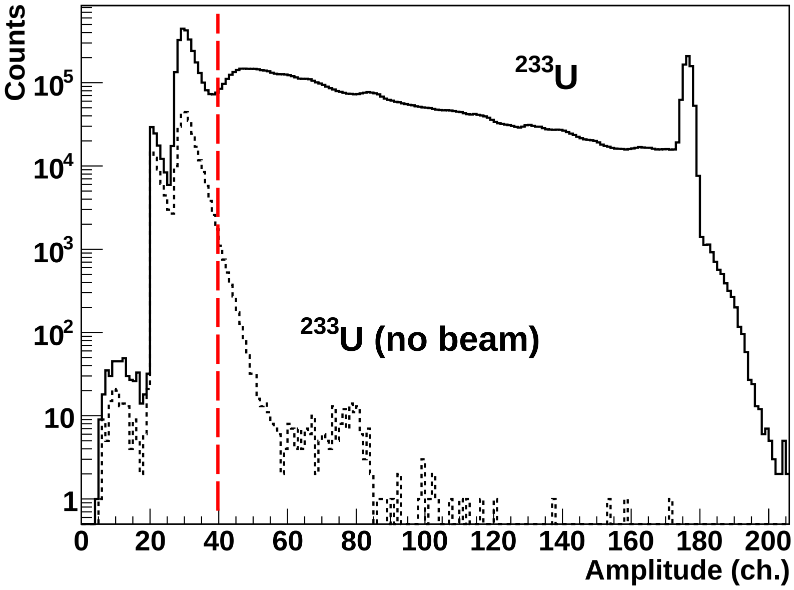

Figure 5.2 – Measured amplitude distribution of signals for neutron-induced fission of ^{233}U. The dashed histogram corresponds to runs without the neutron beam and illustrate the effect of electronic noise and α-particle background. The line at FADC channel 40 represents the amplitude threshold used in the analysis to discriminate fission fragments from α-particles background and electronic noise.

The different thicknesses of the fissile deposits for the ^{235}U and ^{233}U makes necessary to correct for the detection efficiency, since a different fraction of fission fragments exit the two samples and are detected above threshold. To this end, simulations of the detector response were performed with the FLUKA code [57]. Figure 5.3 shows the simulated distribution of the energy deposited in the gas volume for the ^{233}U and ^{235}U cases. The efficiencies calculated by applying the same threshold used in the analysis of experimental data are 97.6% and 94.9% for the ^{233}U and ^{235}U samples, respectively. Therefore a 3% correction factor related to the detection efficiency has been considered in the data analysis.

The dead-time correction factor calculated with Eq. 4.1, for a software dead-time of about 220 ns, is shown in fig 5.4. The correction is found to be negligible at low energy for both parasitic and dedicated beams, being below 1% even for the strongest resonances in dedicated beams. However, as in the ^{235}U case, it becomes significant above 300 keV, reaching approximately 5% at 1 MeV for parasitic beams and up to 9% for dedicated beams. Since the correction values in the ^{235}U case - used as a reference sample - are close to 6% and 10%, for parasitic and dedicated beam, respectively, the dead-time contribution to the final cross-section is 1% at maximum[1].

---

[1] Due to the lower count rate of the ^{233}U samples, the overall ^{233}U(n, f) dead-time effect is slightly less significant than that for the ^{235}U samples.

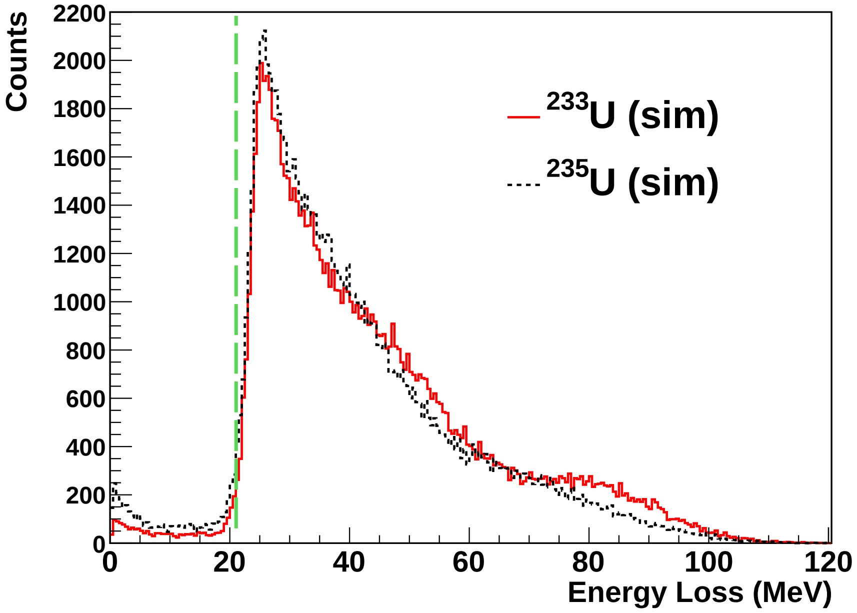

Figure 5.3 – Simulated energy loss of fission fragments in the gas cell, for the ^{235}U (red line) and ^{233}U (black line) samples. The green line corresponds to the thresholds used in the analysis of experimental data.

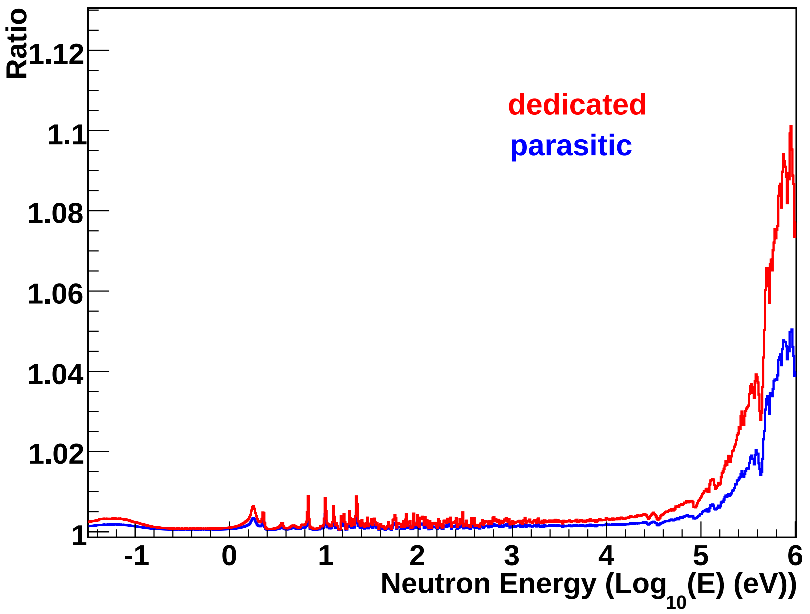

Figure 5.4 – Ratio between the count-rate before and after dead-time corrections, for the ^{233}U sample, both for dedicated and parasitic proton bunches. The figure can be directly compared with Fig. 4.5, the analogous one for ^{235}U.

The ^{233}U(n, f) cross-section is extracted according to the following expression:

$$\sigma(E_n) = \frac{C_{33}(E_n)}{N_{33} \times \Phi(E_n) \times \varepsilon} \tag{5.1}$$

where C_{33} is the number of counts summed over all ^{233}U samples at a given neutron energy E_n, normalized to the nominal n_TOF bunch of $7{\times}10^{12}$ protons. N_{33} is the total number of atoms per barn of the four ^{233}U samples, $\Phi(E_n)$ the neutron flux per proton bunch impinging on the detector (described in section 4.2). Finally, ε is the detection efficiency, which varies with the threshold used in the event selection. The formula is valid on the assumption that the absorption of the neutron flux in the samples and in the electrodes is negligible; the validity of this assumption has been confirmed by the simulations discussed in § 3.6.

5.2 Uncertainty analysis

While the accurate determination of the systematic uncertainties requires a detailed analysis of the full covariance matrix, we discuss here the main sources of uncertainty and their relevance, with the aim of providing a first, conservative assessment of the accuracy of the present results.

The statistical errors in the resonance region are generally smaller than 1% per data point, except in the valleys between resonances where the low value of the cross-section results in a higher value of the uncertainty. In the keV region, the energy bins are chosen in order to meet the requirement of a statistical uncertainty below 1%. The systematic uncertainties of the measurement are summarized in Table 5.2. The uncertainty on the total mass of the ^{233}U samples, which was determined by means of α-spectrometry, is 1.2%, whereas the mass of the ^{235}U sample is given with an uncertainty of 1.35%. These values result in an overall contribution of 1.8% due to the mass uncertainties. The effect of possible target non-uniformities are negligible, since the neutron beam profile is larger than the sample diameter and almost flat in the region of the sample, as seen in Fig. 4.9.

In the Unresolved Resonance Region (E_n $\geq$1 keV), where the ratio method is used (according to Eq. 4.4), the uncertainty on the normalization procedure is related only to the uncertainty on the tabulated fission cross-section of ^{235}U, which is typically 1% (or lower). A slightly larger uncertainty has to be considered for the low energy region (E_n $\leq$1 keV) due to the use of a more complicated procedure, described in § 4.2, for extracting the neutron flux. In this case, the uncertainty, estimated from the combination of the ^{235}U(n, f) data with the known n_TOF neutron flux distribution,

Table 5.2 – Systematic uncertainties (in %) of the present results on the ^{233}U(n, f) cross-section.

Component	Uncertainty (%)
Sample mass	1.8
Normalization to ^{235}U(n, f)	1.0 ($\geq$1 keV), 2.0 ($\leq$1 keV)
Pulse height threshold	1.5
Dead-time correction	1.0
Total	2.7% ($\geq$1 keV), 3.3% ($\leq$1 keV)

is of the order of 2%.

Another important uncertainty is related to the detection efficiency, which depends essentially on the adopted pulse height threshold. Similar thresholds were chosen in the off-line analysis for the ^{233}U and ^{235}U samples, corresponding to the half-maximum of the fission fragment amplitude distribution. The threshold could be defined within ± 1 channel in the experimental pulse height spectrum, thanks to the small contribution of the α-background. From FLUKA simulations of the detector response it was estimated that the corresponding variation in the efficiency is of the order of 1.5%.

The dead-time corrections, which had to be considered for neutron energies above 300 keV, reach values of 10% and 9% at 1 MeV for the ^{235}U and ^{233}U samples, respectively. Since most of the dead-time corrections cancels out in the cross-section ratio, the uncertainty in the correction factor is always a less than 1%.

The uncertainties related to neutron beam attenuation in the samples and in the Al electrodes are of the order of a few per thousand and, therefore, negligible. However, at the energies of the strongest resonances in the Al cross-section, the attenuation can reach a level of 4%, with a corresponding uncertainty of $\sim$0.5%. The uncertainty due to the divergence of the neutron beam can be neglected in view of the close spacing of the samples (1 cm).

Effects related to the angular anisotropy in the fission fragment distribution have not been included in the present data analysis, because they are small below 1 MeV [122, 123], and because of the almost complete angular coverage that characterizes the fission chamber used in the measurement. It has been estimated that their contribution is below 1%, so that the related uncertainty is of that order.

In summary, the present fission cross-sections of ^{233}U in the keV region is affected by a systematic uncertainties of 2.7% (see Table 5.2). Including the statistical errors, an overall uncertainty of 2.9% is obtained. In the energy region up to 1 keV, on the contrary, a systematic uncertainty of 3.3% has to be assigned.

5.3 Results

In this paragraph, the ^{233}U(n, f) cross-section, extracted from n_TOF measurements, is compared with previous experimental data and with cross-section extracted from evaluated libraries. The most significant conclusions from this new measurement are reported.

Figure 5.5 shows a global view of the ^{233}U(n, f) cross-section measured at n_TOF from near thermal ($\sim$30 meV) to 1 MeV neutron energy. It is important to stress that the data here shown are not normalized to any previous result, as in some previous data, but rely purely on the ^{235}U(n, f) cross-section, which is a standard for fission measurements. A further noteworthy aspect is that, for the first time, the whole energy range from thermal to 1 MeV is covered in a single measurement, thus minimizing possible systematic uncertainties related, for example, to the absolute normalization of the cross-section.

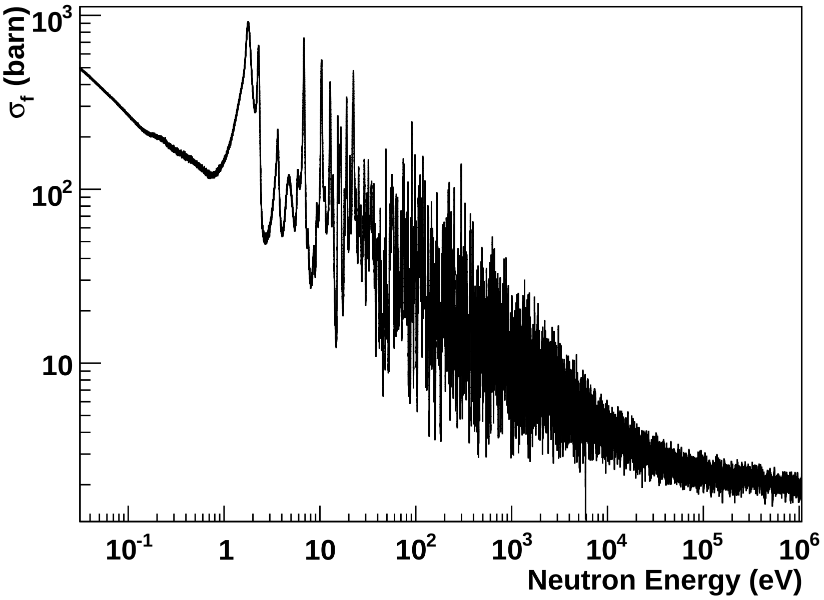

Figure 5.5 – Overall view of the extracted ^{233}U(n, f) cross-section in the whole energy range from thermal up to 1 MeV. The results are plotted with a binning of 5000 bin/decade. In this figure the cross-section is extracted using Eq. 5.1 in the whole energy region.

5.3.1 Comparison with evaluated libraries

A comparison between n_TOF data and evaluated cross-sections has been performed, considering the latest databases: ENDF/B-VII.0, JEFF-3.1 and JENDL-3.3. The last two libraries contain essentially the same evaluated cross-sections below

6.75 MeV [124], i.e. in the region of interest for this work. In some specific energy regions, also the ENDF/B-VI.8 library has been considered.

An important difference between evaluated libraries is the limit of the so-called Resolved Resonance Region (RRR), i.e. the region in which resonances, or resonance-like structures, as still clearly identified. In particular, while in the relatively new ENDF/B-VII.0 evaluated database the RRR extends up to 600 eV, in JEFF-3.1 this limit is still at 150 eV, probably because the high resolution fission and transmission data collected at the ORELA facility in Oak Ridge in 2000 [125, 126] have not been included. In the case of the previous ENDF/B-VI.8 library, this limit is even below at 60 eV.

Fig. 5.6 shows the velocity-averaged n_TOF ^{233}U fission cross-section in the energy region between 0.08 eV and 0.7 eV, together with the evaluated cross-sections from the different libraries. JEFF-3.1 reproduces correctly the behavior of the cross-section in the interval between 0.35 eV and 0.6 eV, while ENDF/B-VII.0 and ENDF/B-VI.8 miss completely the broad structures observed in the present data.

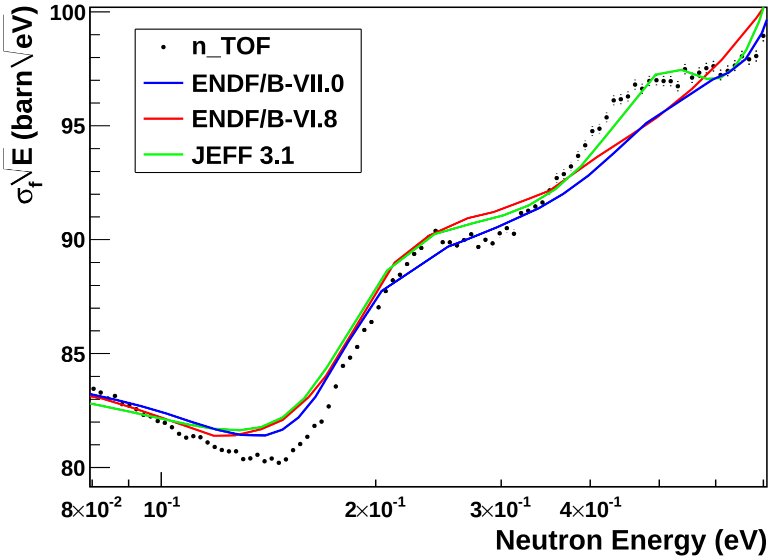

Figure 5.6 – The ^{233}U(n, f) cross-section measured at n_TOF in the low energy region between 80 meV and 0.7 eV.

The results for the first two resonances of the ^{233}U(n, f) cross-section, at about 1.785 eV and 2.3 eV, are shown in Fig. 5.7. JEFF-3.1 is in almost perfect agreement with the n_TOF data both in terms of the energy of the resonances and absolute value of the cross-section. On the contrary the new ENDF/B-VII.0 library only the energy of the resonance at 2.3 eV is correct.

Apart from the first two resonances, the resonance energies in the ENDF/B-VII.0 library are different by less than 0.1% compared to the present data, all the way up

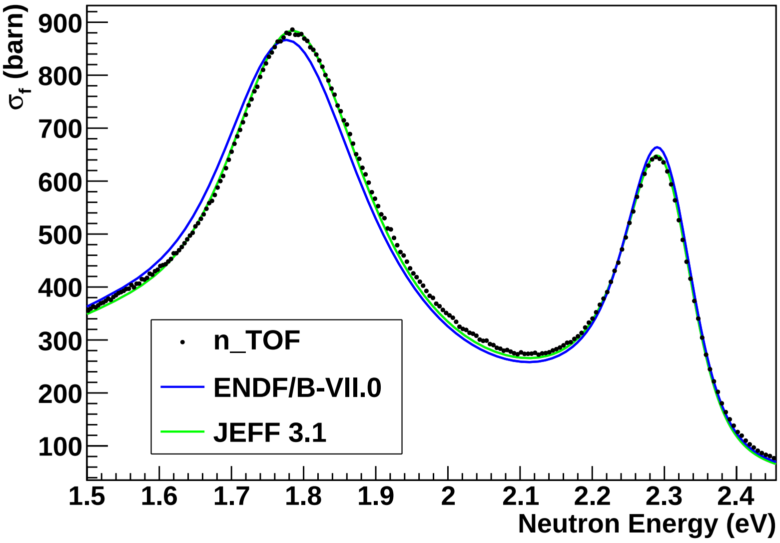

Figure 5.7 – n_TOF experimental ^{233}U(n, f) cross-section for the first two resonances as compared with different databases of evaluated cross-sections. A better agreement is observed for these two resonances with JEFF-3.1, while ENDF/B-VII.0 does not reproduce the energy of the first resonance nor the strength of the second one.

to 600 eV. On the contrary, JEFF-3.1 (or equivalently JENDL-3.3) shows a very good agreement with n_TOF data only up to about 65 eV; above this limit - up to the RRR limit of 150 eV - a systematic disagreement of about 0.5% is present. This last effect could be seen in Fig. 5.8 and 5.9, where the n_TOF data are shown together with evaluated libraries in different energy ranges.

Figs. 5.9 and 5.10 show n_TOF data in the energy region corresponding to the limit of the RRR for JEFF-3.1 (150 eV) and ENDF/B-VII.0 (600 eV), respectively. The possibility provided by the n_TOF data to extend the RRR above the current limits is evident in Fig. 5.11, where resonance structures are still visible in the interval between 600 eV and 1 keV in the n_TOF data, contrary to the evaluated cross-sections.

The n_TOF results at higher neutron energy, i.e. between a few keV and 1 MeV, are shown in Fig. 5.12. In this region, the fission cross-section is extracted with the method of the ratio, discussed in § 4.2, using the following expression (reported again for convenience):

$$\sigma_{33}(E_n) = \frac{C_{33}(E_n)}{C_{35}(E_n)} \times CF \times \sigma_{35}^{eval}(E_n) \tag{5.2}$$

The correction factor CF includes the ratio between the number of atoms/barn in the ^{233}U and in the ^{235}U samples, as well as the efficiency and dead-time corrections already described.

In the keV energy region, some difference is observed between different evaluated

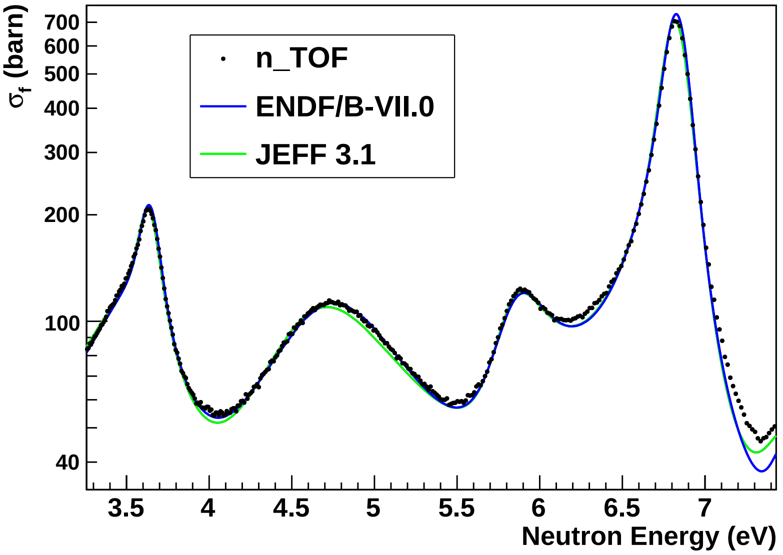

Figure 5.8 – Present results for the ^{233}U(n, f) cross-section in the energy region between 3.5 eV and 7.5 eV. In this case a good agreement is observed with ENDF/B-VII.0.

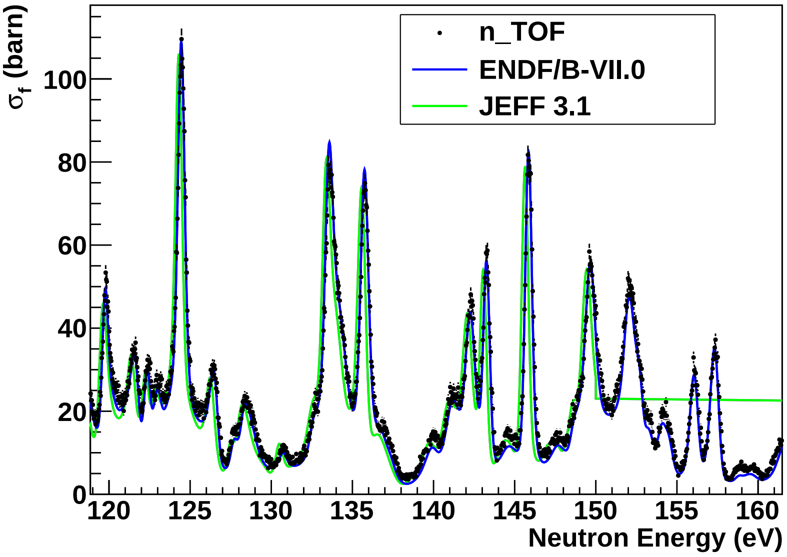

Figure 5.9 – The ^{233}U(n, f) cross-section measured at n_TOF, compared with evaluated data, in the region between 120 eV and 160 eV. ENDF/B-VII.0 agrees very well with the n_TOF results, while JEFF-3.1 (and JENDL-3.3) are slightly shifted in energy (by ∼0.2%). The limit of the JEFF-3.1 Resolved Resonance Region is currently at 150 eV.

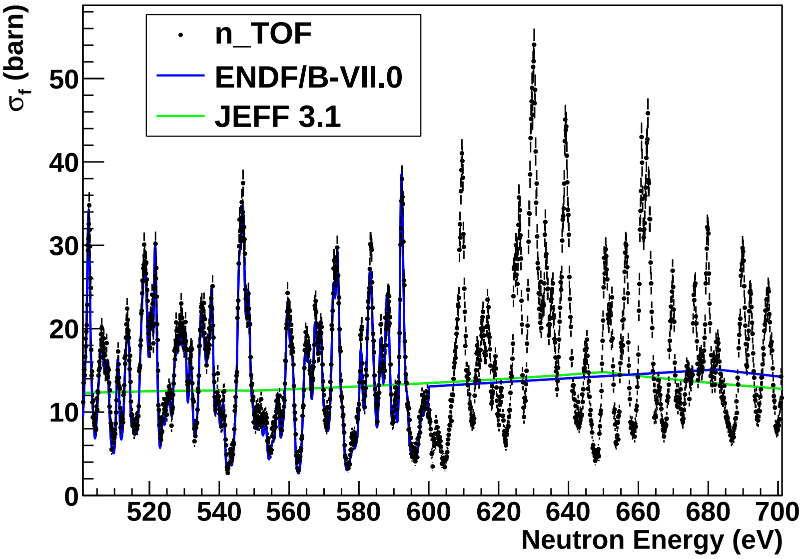

Figure 5.10 – Measured cross-section for the ^{233}U(n, f) reaction, compared with evaluated data in the region between 500 eV and 700 eV. The upper limit of the ENDF/B-VII.0 RRR is located at 600 eV. The high resolution of the n_TOF data may allows to extend the resonance analysis above the present limits in the libraries of evaluated cross-sections.

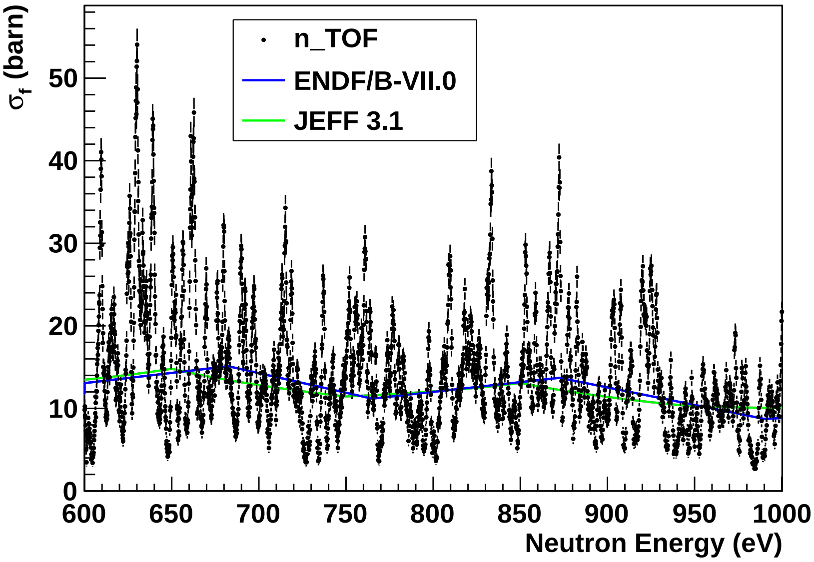

Figure 5.11 – n_TOF results for the ^{233}U(n, f) reaction in the region between 600 eV and 1 keV. For comparison, the cross-section in the evaluated libraries is also shown.

libraries, most probably due to the different choices made by evaluators, in particular on the weight attributed to the different experimental data sets. It is interesting to note that the ENDF/B-VII.0 cross-section differs from a previous version of the database, ENDF/B-VI.8, also shown in Fig. 5.12. New experimental data have been in fact considered, and a comparison with critical benchmark has been performed [127]. According to the n_TOF results, however, the new version of the ENDF/B library underestimates the cross-section up to 100 keV neutron energy, more than the previous version. If a correction had to be applied in the new version, it should have gone in the opposite direction. The shortcoming of the new ENDF/B-VII.0 version is an important conclusion of the present work, and suggest that a revision of the evaluated libraries is necessary.

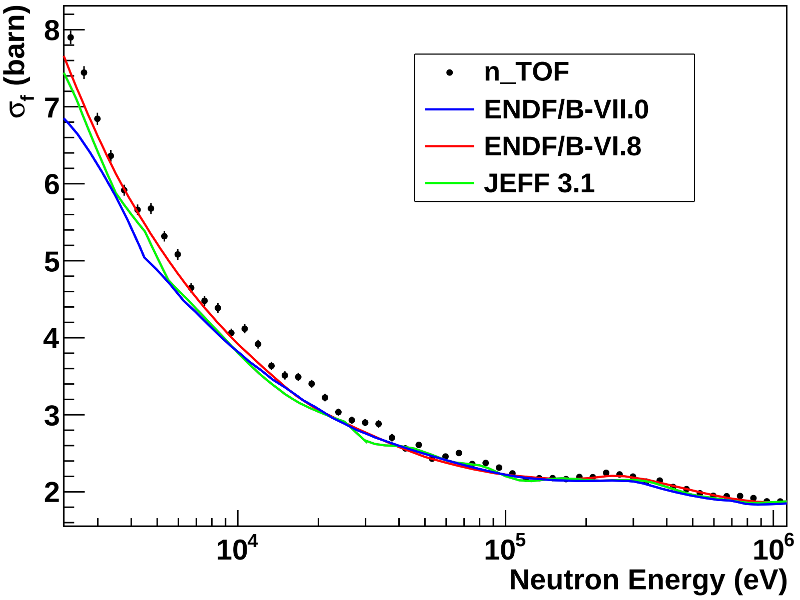

Figure 5.12 – The ^{233}U(n, f) data of this work are compared with evaluated cross-sections in the URR from 2 keV to 1 MeV.

5.3.2 Comparison with previous measurements

Some interesting considerations can be drawn from a comparison of the n_TOF results with previous data available in different energy regions. For reference, the evaluated data from ENDF/B-VII.0 will be shown together with the experimental data.

Fig. 5.13 shows the low ($\leq$0.1 eV) neutron energy part of the n_TOF results compared to previous data and evaluated libraries: a tendency to obtain a flat distribution of $\sigma_f(E_n)\sqrt{E_n}$ is observed close to the thermal region, as expected in the case of a pure $1/v$ behavior of the cross-section. By performing an extrapolation with a linear fit in the neutron energy range from ∼33 meV to 40 meV, it is possible to obtain a value for the fission cross-section at thermal (0.0253 eV) neutron energy, which has been very accurately determined in several previous measurements. The value obtained from the n_TOF results is 536.9±0.2 barn, slightly higher than 1% compared to the ENDF/B-VII.0 value of 530.70 barn. A good agreement for the thermal cross-section provides a high confidence on the accuracy of the n_TOF data. Good agreement is also observed with the data of Wagemans [128], which were normalized to the thermal cross-section value of 531.14 barn (±0.25%).

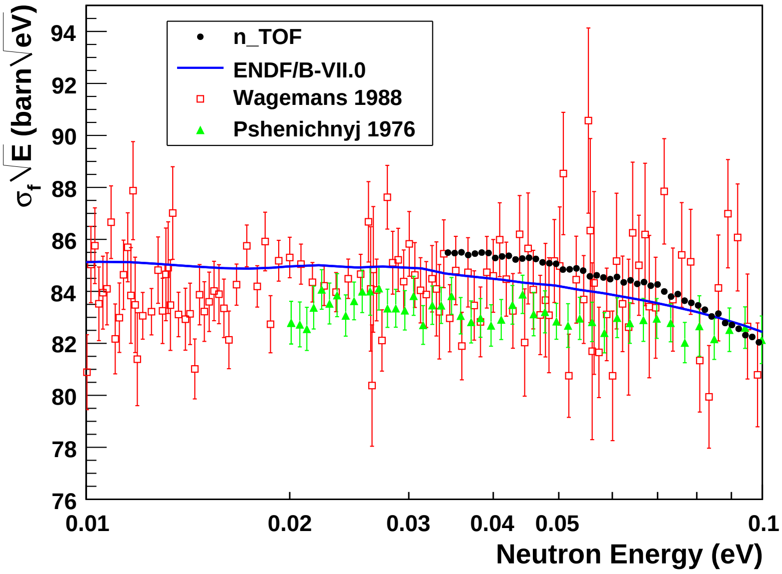

Figure 5.13 – Velocity-weighted fission cross-section from 10 meV to 100 meV. The present results (black symbols) are compared with previous measurements, in particular with the data of Wagemans [128], which extends down to 2 meV, and with the cross-sections from the ENDF/B-VII.0 library (blue curve).

Figure 5.14 shows the n_TOF results (in black) compared with the evaluated cross-section and with the most recent measurements reported in EXFOR in the energy range from 70 meV to 700 meV [128, 129, 130, 131]. Contrary to previous data, n_TOF cross-sections are affected by very small statistical errors. A reasonable agreement is observed in general with previous measurements. The structures observed around 200 and 300 meV can be most probably attributed to low-lying broad resonances. These resonances are present in the ENDF/B-VII.0 library, although they do not correctly reproduce the data. It should be noticed that these structures have never been clearly observed in previous experimental data on fission cross-section (although they have been observed in total cross-section measurements, es. [132]).

Figures 5.15 and 5.16 show the comparison for selected resonances in two different energy regions. In general, previous data show sizable discrepancies between them-

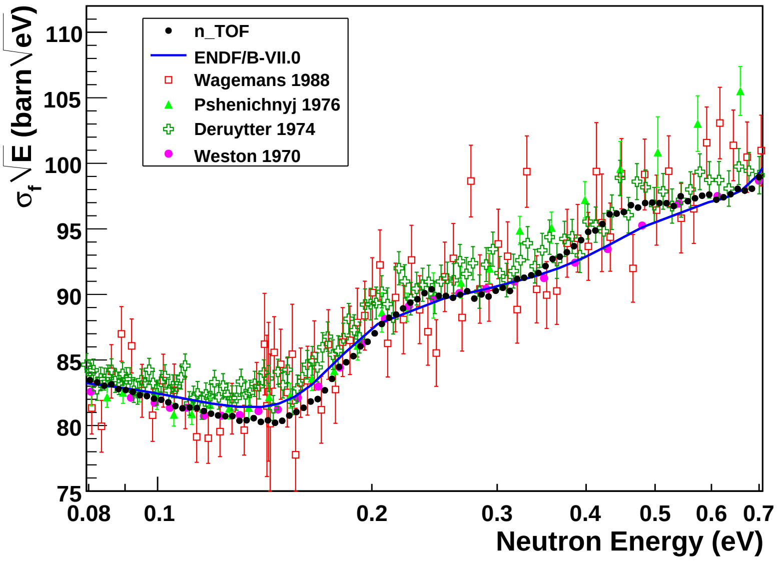

Figure 5.14 – Velocity-weighted fission cross-section from 80 meV to 0.7 eV. The n_TOF results (black symbols) are compared with previous measurements and with ENDF/B-VII.0 database (blue curve). The two resonances at 0.25 and 0.45 eV, present in the evaluation, are clearly observed in the n_TOF results.

selves, both in terms of resonance strength and energy. For the first two resonances of the ^{233}U(n, f) cross-section, in the eV region, the n_TOF cross-section are 10% higher than the most recent data from Guber *et al.*[2] [125], while a good agreement is observed with the libraries, in particular with JEFF-3.1. On the contrary, around 90 eV, n_TOF data confirm the results of Guber, with a small difference observed only for the resonance energy. A striking agreement is observed in this region with the ENDF/B-VII.0 database, while discrepancies exist with other data sets [133, 134, 135].

As already pointed out, the high resolution in neutron energy that characterizes the n_TOF facility allows to extend the limit of the resolved resonance region. This is evident in Figure 5.17, where the n_TOF data show well resolved resonance structures above 600 eV. Combined with Guber's data, the only previous measurement that show a comparable resolution, the new results from n_TOF allow to achieve a more accurate determination of the resonance parameters and to extend the resonance region beyond the present limits, which would result in a more accurate calculation of self-shielding effects in reactors based on the Th/U fuel cycle.

The n_TOF results in the unresolved resonance region from 3 keV up to 40 keV are shown in Fig. 5.18, and from few tens of keV to 1 MeV in Fig. 5.19. The results from previous measurements are also shown for comparison. It is important to notice that some of the previous data are reported only as the ratio between the ^{233}U(n, f)

---

[2] However these results have not been probably corrected for the self-shielding, which is significant in their measurement since they used a thick ^{233}U sample, $\sim$2 g.

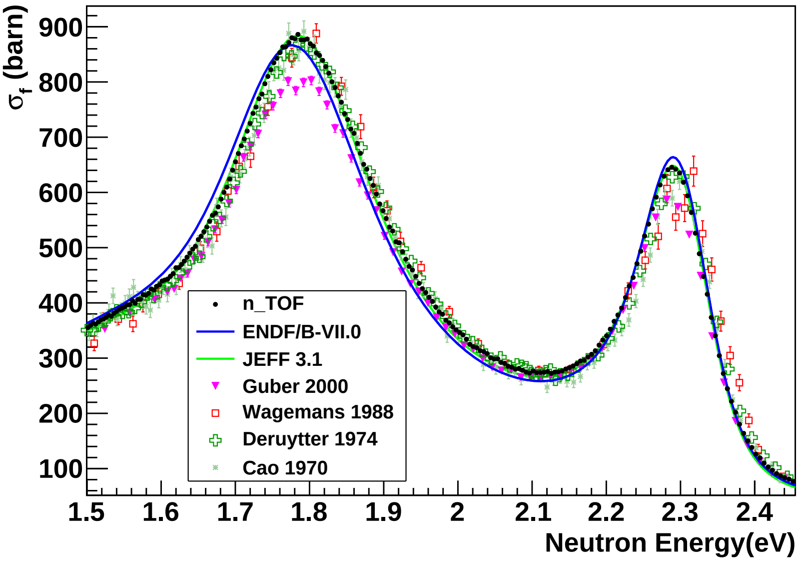

Figure 5.15 – The first two resonances in the ^{233}U(n, f) cross-section measured at n_TOF (black symbols), compared with previous results [125, 128, 130, 133] and with evaluated cross-sections [33, 34]. The lower cross-section value in the results of Guber *et al.* is most probably due to self-shielding effects, not corrected for in that experiment, although significant.

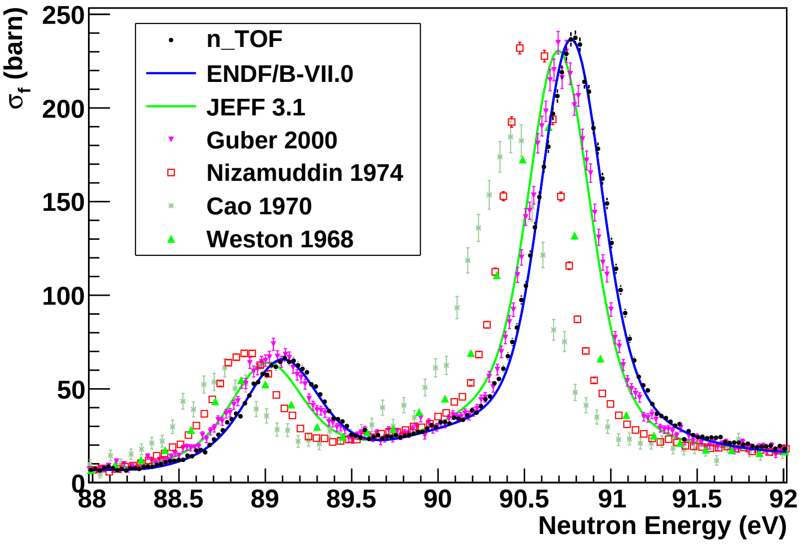

Figure 5.16 – Resonances in the ^{233}U(n, f) cross-section measured at n_TOF around 90 eV. Large discrepancies between previous data and between libraries are observed in this case. The n_TOF results confirm the evaluated data from ENDF/B-VII.0, (while in other cases a better agreement is observed with JEFF-3.1).

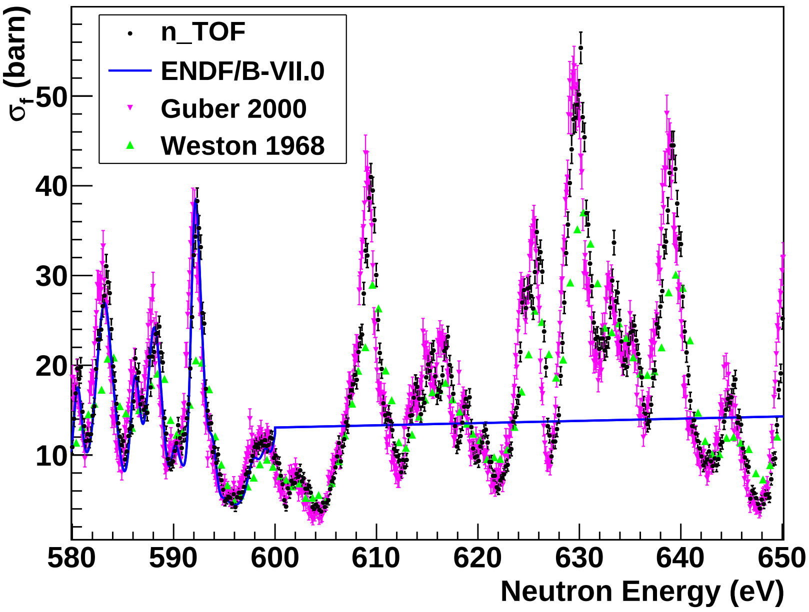

Figure 5.17 – The ^{233}U(n,f) cross-section at the current limit of the Resolved Resonance Region in the ENDF/B-VII.0 library. Resonance structures are observed at n_TOF above this limit, in agreement with recent results of Ref.[125] and compared to results of [134].

and ^{235}U(n,f) cross-section. For a consistent comparison with the n_TOF results, those data sets were multiplied by the tabulated ^{235}U(n,f) cross-section taken from ENDF/B-VII.0.

Up to approximately 200 keV, the n_TOF data are mostly consistent with previous measurements, except for a bump between 100 and 200 keV in Guber's results, not observed in present data. Above this energy, previous data do not show a unique trend. In particular, the n_TOF cross-section is in agreement with the measurements of Lisowski *et al.* [136], Meadows *et al.* [137] and Guber *et al.* [125], but higher than the measurements of Carlson *et al.* [138], Fursov *et al.* [139], and the relatively new data of Shpak *et al.* [140]. A further, important indication that can be drawn from the figure is that the tabulated cross-section in ENDF/B-VII.0 typically underestimate the n_TOF cross-section, by up to 10%.

An overview of the differences between n_TOF and existing databases is shown in Figure 5.20, in the whole neutron energy range covered by the n_TOF results. In this case, the cross-sections are reported as average over large bins, each corresponding to a decade in the logarithm of neutron energy. While at low energy, below 100 eV, the average difference between experimental and evaluated cross-section is within 2%, a much larger discrepancy, well above the systematic uncertainties of present data, of up to 10%, exist in the region between 100 eV and 100 keV, as already pointed out in Figure 5.19. An underestimate of the results in this energy region may have

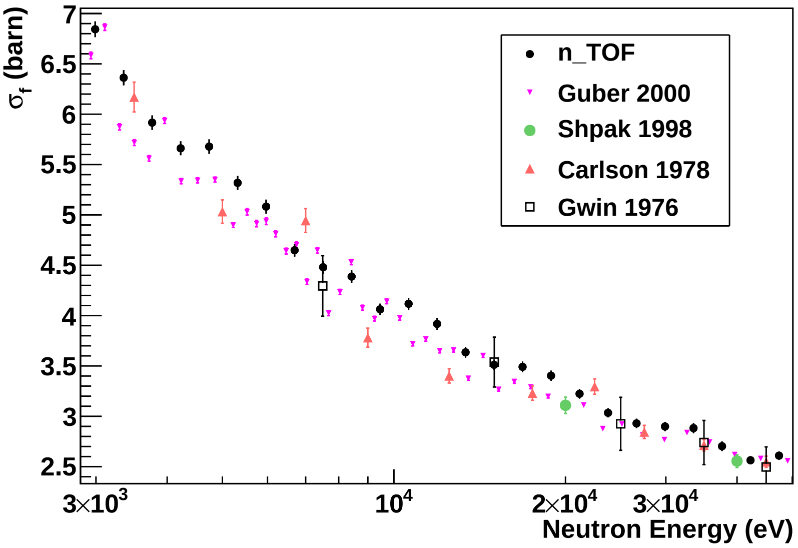

Figure 5.18 – Comparison of the ^{233}U(n, f) cross-section measured at n_TOF (black symbols) with previous results, from 3 keV up to 40 keV.

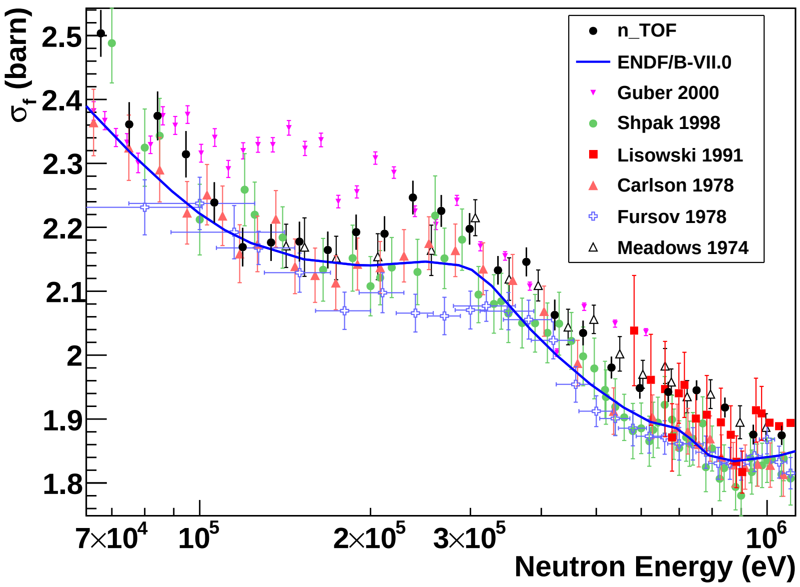

Figure 5.19 – Comparison of the ^{233}U(n, f) cross-section measured at n_TOF (black symbols), with previous results and with evaluated data from ENDF/B-VII.0 and JEFF 3.1, from 70 keV to 1 MeV. The present results confirm that current evaluations underestimate the cross-section. Data points from Ref. [125], taken from the EXFOR database, have been rebinned in this work. The bump present between 100 and 250 keV is not clearly observed in Guber's *et al.* paper [125].

some important influence on reactor calculations for the Th/U cycle, in particular for fast reactors. The n_TOF data suggest therefore that a revision of the evaluated cross-sections is needed, at least above 100 eV. This observation is also corroborated by the results of Guber *et al.*, which show a discrepancy from 7% to 10% in the energy region above 30 eV [125], relative to databases of evaluated cross-sections, while showing a close agreement with the present results.

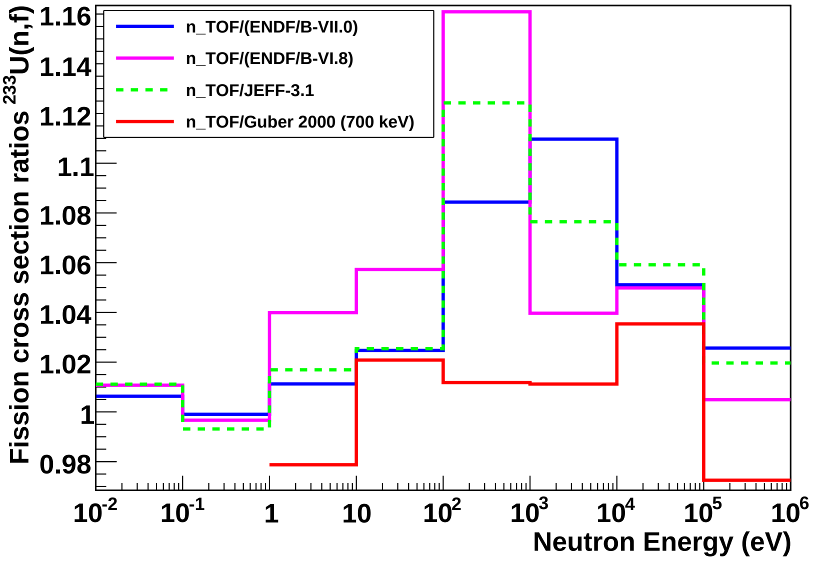

Figure 5.20 – Ratio between ^{233}U(n, f) cross-section measured at n_TOF and previous data or evaluated cross-sections. The results from thermal energy up to 1 MeV are averaged in bins corresponding to a decade in the logarithm of the neutron energy. The present results indicate that current evaluations underestimate the cross-section, by as much as 10%, between 100 eV and 10 keV, a region of interest for advanced nuclear reactor technology.

The normalization procedure is a critical issue in most of experiments, since reference samples are not measured simultaneously and different energy ranges are measured at different times with different experimental arrangements. In most measurements a different normalization procedure is used; most of the old data are directly normalized to the thermal cross-section, while others are normalized via other indirect methods (see for example, Table IV of Ref. [141]). In the measurement of Guber *et al.*, the data have been normalized to the results from Deruytter and Wagemans [141] following their suggestion, i.e. by integrating the cross-section in the 8.1 eV to 17.6 eV neutron energy range[3]. The proposed value was revised in 1988 by Wagemans *et al.* to 965.2 b·eV, which is the value used in Ref. [125].

Since the fission cross-section measurements at n_TOF have been performed under

---

[3] The reason for this choice is that only one well separated resonance is present in this energy region, so that there is no interference from neighboring resonance.

Table 5.3 – ^{233}U(n,f) cross-section integrals ($\int \sigma(n,f) \times dE$ in b·eV) and related statistical uncertainties calculated from the present results. For comparison, the integrals obtained from previous experimental results (Guber *et al.* [125], Weston *et al.* [134], Blons *et al.* [143], Deruytter *et al.* [141] and Wagemans *et al.* [128]), calculated in Ref. [125], are also reported in this table.

Energy Interval (eV)	Present Work (b·eV)	Guber *et al.*[125][a] (b·eV)	[134][b] (b·eV)	[143][b] (b·eV)	[141][b] (b·eV)	[128][b] (b·eV)
0.5 to 1.0	62.68±0.03	63.60±0.22	62.68±1.71		62.77	63.70
1.0 to 10.0	1250.63±0.31	1241.66±1.31	1234.1±8.67		1239.0	1248.2
8.1 to 17.6	976.70±0.50	965.2±1.79	964.25±8.79		964.1	965.2
17.6 to 20.0	239.24±0.30	237.99±1.04	237.55±4.49	227.7±0.5	237.0	

---

[a] In calculating averaged fission cross-sections, Guber *et al.* used the SAMMY R-matrix code in combination with the same energy bins as in Ref. [142].

[b] Data values in the present intervals are taken from Ref. [125], using the SAMMY code for averaging other experimental data.

excellent measuring conditions (very high instantaneous neutron flux, low repetition rate, low background and thin samples), the present data have been used to calculate fission integrals, extracted, together with average average fission cross-sections, by applying Eq. 5.3 and 5.4, using the same coarse energy bins as of Ref. [125, 142].

$$\text{fission integral} = \int \sigma(n,f)(E) \times dE \simeq \sum_i \sigma_i \times \Delta E_i \tag{5.3}$$

$$\text{average fission} = \int \sigma(n,f)(E) \times dE/\Delta E \simeq \sum_i \sigma_i \times \frac{\Delta E_i}{\Delta E} \tag{5.4}$$

Here σ_i is the experimental fission cross-section in the i^{th} bin of energy width ΔE_i and ΔE is the width of the energy interval over which the average is calculated.

The cross-section integrals and averages allow to easily compare present data directly with the most recent evaluation of Ref. [127], for neutron energies between 0.05 eV and 600 eV, as well as with some of the experimental data in the energy range between 0.05 eV and 2 keV. In the last case fission integrals and average cross-sections were also calculated by using SAMMY. In the choice of the binning, Ref. [125] (Guber *et al.*) was followed.

From Table 5.3, where ^{233}U(n,f) cross-section integrals are shown in selected energy ranges, it can be noticed that the present results agree with previous experimental results and with the suggested normalization integral within $\sim$1.2%, up to 20 eV neutron energy.

From Table 5.4, where comparison of ^{233}U(n,f) cross-section averages in the neutron energy interval from 0.05 eV to 2 keV are shown, it could be concluded that the present data are in good agreement - well within systematics errors - with the

Table 5.4 – ^{233}U(n, f) cross-section average ($\int \sigma(n,f) \times dE/\Delta E$ in barn) and related statistical uncertainties calculated for the present results and compared to values obtained from previous measurements (Guber *et al.* [125], Blons *et al.* [143], Weston *et al.* [134] and Wagemans *et al.* [128]) and evaluations (Leal *et al.* and ENDF/B-VI [127]), for the energy range between 0.4 eV and 2 keV.

Energy Interval (eV)	Present Work (b)	Guber *et al.*[125][a] (b)	[143][b] (b)	[134][b] (b)	[128][b] (b)	Leal *et al.*[127][c] (b)	ENDF/B-VI[d] (b)
0.05 to 0.4	201.75±0.04				201.85	202.63	
0.4 to 1.0	128.40±0.05	129.86±0.54		129.20±3.10	130.7	127.69	126.91
1.0 to 2.1	392.92±0.11	385.19±0.49		391.70±4.80	388.8	388.97	378.56
2.1 to 2.75	209.42±0.12	205.39±0.53		207.50±4.50	204.4	206.67	198.02
2.75 to 3.0	53.73±0.11	56.77±0.53		51.90±1.70	50.1	49.84	50.45
3.0 to 15.0	106.40±0.04	105.65±0.15		104.90±0.80	106.2	104.26	101.26
15.0 to 30.0	96.67±0.05	94.43±0.13	91.86±0.08	95.06±0.79		94.76	91.79
30.0 to 50.0	42.16±0.04	42.36±0.08	39.11±0.05	40.14±0.30		40.73	38.86
50.0 to 75.0	43.02±0.04	42.62±0.07	39.50±0.05	40.66±0.36		41.24	41.20
75.0 to 100.0	38.32±0.05	37.96±0.07	35.73±0.05	35.58±0.34		36.89	33.73
100.0 to 125.0	40.42±0.06	39.20±0.08	35.59±0.05	36.86±0.39		38.24	29.97
125.0 to 150.0	22.72±0.05	22.98±0.06	19.76±0.04	21.36±0.28		21.90	22.12
15.0 to 150.0	43.72±0.02	42.21±0.03	40.18±0.02	41.39±0.16			
150.0 to 200.0	23.12±0.04	22.93±0.04	19.59±0.03	21.12±0.16		20.97	21.34
200.0 to 250.0	25.17±0.04	24.58±0.05	22.37±0.04	23.07±0.20		23.02	19.87
250.0 to 300.0	24.67±0.05	24.15±0.05	21.05±0.04	22.59±0.25			
300.0 to 350.0	18.44±0.05	18.95±0.05	16.47±0.04	17.51±0.20		18.24	16.66
350.0 to 400.0	20.61±0.05	20.34±0.05	17.87±0.04	19.06±0.25			
400.0 to 450.0	11.02±0.04	10.93±0.04	9.08±0.03	9.80±0.13		11.01	13.17
450.0 to 500.0	13.60±0.05	13.64±0.05	12.28±0.04	12.70±0.15			
500.0 to 600.0	14.52±0.04	14.71±0.04	12.64±0.03	13.63±0.11		13.47	13.40
600.0 to 700.0	17.37±0.04	17.35±0.04	15.72±0.03	16.52±0.15			
700.0 to 800.0	12.86±0.04	12.91±0.04	11.32±0.03	11.89±0.12			
800.0 to 900.0	14.57±0.04	14.63±0.04	13.67±0.04	14.09±0.15			
900.0 to 1000.0	11.11±0.04	11.12±0.04	10.16±0.03	10.57±0.12			
1000.0 to 1200.0	10.55±0.03	10.84±0.03	9.48±0.02	9.72±0.09			
1200.0 to 1400.0	10.47±0.03	10.39±0.03	9.49±0.03	9.77±0.10			
1400.0 to 1600.0	9.33±0.03	9.50±0.03	8.92±0.03	9.07±0.10			
1600.0 to 1800.0	8.40±0.03	8.54±0.03	7.91±0.03	7.84±0.10			
1800.0 to 2000.0	8.77±0.04	8.70±0.03	8.21±0.03	8.14±0.11			

---

[a] In calculating averaged fission cross-sections, Guber *et al.* used the SAMMY R-matrix code in combination with the same energy bins as in Ref. [142].

[b] Data values in the present intervals are taken from Ref. [125], using the SAMMY code for averaging other experimental data.

[c] This work has been included for the ENDF/B-VII.0 ^{233}U(n, f) evaluation. The average (n, f) cross-section has been calculated with the NJOY [38] code assuming a constant flux.

[d] As calculated in Ref. [127].

latest evaluation of ENDF/B-VII.0 (and with [128]). In the low energy range, up to 30 eV, an overall good agreement is observed between the different experimental data sets and the evaluation, except for Blons *et al.* [143] and for ENDF/B-VI. Above 30 eV the n_TOF cross-sections mostly agree within systematic uncertainties with Guber's results, although with a systematic tendency of being higher that those data; in the energy bin between 15 eV to 150 eV a discrepancy between 5% to 9% is observed with previous experimental data. This trend continues up to the high energy range. In the neutron energy bin from 1.8 to 2.0 keV, n_TOF data agree with Guber's results within less that 1% while deviating up to 6% with respect to experimental data from Ref. [143] and 7% for Ref. [134].

In Table 5.5 and 5.6 n_TOF data are compared with other high energy data from Ref. [144, 143, 145, 137].

Table 5.5 – ^{233}U(n,f) cross-section average ($\int \sigma(n,f) \times dE/\Delta E$ in barn) and related statistical uncertainties calculated from n_TOF data and compared to values extracted from previous measurements (Guber *et al.* [125], Gwin *et al.* [144] and Blons *et al.* [143]) and evaluations, in the energy range between 5 keV and 200 keV.

Energy Interval (keV)	Present Work (b·eV)	Guber *et al.*[125] (b·eV)	[144][a] (b·eV)	[143][a] (b·eV)
5.0 to 10.0	4.53±0.01	4.46±0.01	4.26±0.22	4.37±0.01
10.0 to 20.0	3.60±0.01	3.43±0.01	3.31±0.19	3.53±0.01
20.0 to 30.0	3.00±0.01	2.89±0.01	2.89±0.17	2.91±0.01
30.0 to 40.0	2.78±0.01	2.64±0.01	2.66±0.16	
40.0 to 50.0	2.59±0.01	2.53±0.01	2.45±0.16	
50.0 to 60.0	2.47±0.01	2.43±0.01	2.45±0.16	
60.0 to 70.0	2.40±0.01	2.34±0.01	2.40±0.17	
70.0 to 80.0	2.38±0.01	2.27±0.01	2.35±0.18	
80.0 to 90.0	2.32±0.01	2.24±0.01	2.33±0.18	
90.0 to 100.0	2.35±0.02	2.26±0.01	2.22±0.19	
100.0 to 200.0	2.190±0.005	2.26±0.01	2.33±0.24	

---

[a] Data values in the present intervals are taken from Ref. [125].

Table 5.6 – ^{233}U(n,f) cross-section average ($\int \sigma(n,f) \times dE/\Delta E$ in barn) and related statistical uncertainties calculated for n_TOF results and for previous measurements (Guber *et al.* [125], Poenitz *et al.* [145] and Meadows *et al.* [137]) and evaluations, in the energy range between 200 keV and 700 keV.

Energy Interval (keV)	Present Work (b·eV)	Guber *et al.*[125] (b·eV)	[145][a] (b·eV)	[137][a] (b·eV)
200.0 to 300.0	2.17±0.01	2.15±0.01	2.19±0.02	2.17±0.02
300.0 to 400.0	2.15±0.01	2.06±0.01	2.17±0.03	2.14±0.01
400.0 to 500.0	2.02±0.01	1.97±0.01	1.98±0.02	2.06±0.01
500.0 to 600.0	1.95±0.01	1.95±0.01	1.93±0.02	2.01±0.01
600.0 to 700.0	1.96±0.01	1.92±0.01	1.90±0.02	1.97±0.01

---

[a] Data values in the present intervals are taken from Ref. [125].

5.4 Final remarks

The high resolution, high accuracy data obtained at n_TOF for the ^{233}U(n, f) cross-section will allow the determination of resonance parameters over a broader neutron energy range. It should be considered, however, that, as shown in Ref. [127], the average level spacing of the ^{233}U nucleus is too small to allow identification of the individual resonances in the energy range above 70 eV; therefore the observed structures are in reality aggregates of resonances (also called "pseudo" resonances). The R-matrix analysis of this data is nevertheless very useful for reliable calculations of the Doppler broadening correction and resonance self-shielding [146]. It is important to stress that accurate resonance data are fundamental to improve predictions of the Doppler reactivity coefficient of advanced reactor systems that use ^{233}U as fuel [24]. The observed differences of the fission cross-section with respect to the evaluated databases are significant especially in the epithermal range, of interest for reactors, in particular fast ones fueled with Th/U matrix. The origin of such discrepancy most probably resides in the choice of evaluators when selecting the experimental data on which to base their evaluation, as well as in adjustments of cross-section operated in order to be compatible with critical benchmarks, which rely on parameters such as the k_{eff} [127]. In the particular case of ENDF/B-VII.0, Leal *et al.* found out that for the energy range above 100 eV, a better prediction of some experimentally determined k_{eff} values required the systematic decrease of the value of the evaluated cross-sections by ~8%, away from the recent data of Guber *et al.* and towards the results of Weston *et al.* [134]. This explains why the latest evaluation in ENDF/B-VII.0 underestimates the present results, which are instead in agreement, within 2%, with the data of Guber *et al.*.

Chapter 6

Fission cross-sections on actinides

In this chapter the results of the fission cross-section of three actinides - ^{241}Am, ^{243}Am and ^{245}Cm - are reported. The measurements were performed at n_TOF with the FIC chamber, and the results have been obtained in the energy range between ≈30 meV and 1 MeV. For each isotope, the analysis procedure is first described, followed by the experimental results (and related uncertainties), and by the comparison with data from previous measurements and from evaluated libraries. As a general remark, the very high α-activity of the ^{245}Cm and ^{241}Am isotopes results in α-pile-up that makes the efficiency corrections uncertain. For this reason the present cross-sections have been normalized to previous data, with the consequence that the quality of the data, in terms of accuracy, is not as good as in the case of the ^{233}U(n, f) reaction, especially for the ^{241}Am isotope. Moreover, due to the presence of contaminants in the ^{243}Am sample, the analysis for this isotope has been limited to the threshold region, above a few hundreds of keV, which is the most important region for its interest in transmutation scenarios.

6.1 ^{241}Am(n, f) cross-section

The fission cross-section of ^{241}Am is of interest in reactor design and for the engineering studies of spent fuel reprocessing and waste management facilities. Measurements of this cross-section are difficult due to the extremely large α activity of this nuclide, as a result of its relatively short half-life ($t_{1/2} \simeq$433 yr). A large number of measurements performed in the past suffered from this difficulty or from the lack of isotopically pure samples. In addition to these complications, the fission cross-section of ^{241}Am is extremely low ($\leq$0.1 b) over the range between 1 keV to 1 MeV neutron energy. Uncertainties in the capture and particularly in fission cross-sections are the dominating factors in the overall uncertainty of the multiplicative factor k_{eff} in the case of typical minor actinide burner reactors.

6.1.1 Analysis procedure

In the present measurement, eight ^{241}Am samples were used, listed in Table 6.1. The discrimination between α-particles and fission fragments is performed by means of the amplitude distribution of the recorded signals. Fig. 6.1 shows the amplitude distributions for the ^{241}Am sample, integrated over all neutron energies (solid red histogram). For comparison, the spectrum of the reference ^{235}U sample is also shown in the figure (blue histogram). Due to the very short half-life of the ^{241}Am isotope, a significant background due to α-particles and their pile-up is present. It is therefore mandatory to apply a different threshold with respect to the one used for ^{235}U.

Table 6.1 – Samples used in the ^{241}Am(n, f) measurement. The reported mass is that of the U and Am isotopes only.

Sample	Chemical form	Mass (mg)	Areal density (10^{-7} atoms/b)	Uncertainty (%)
^{235}U	U_3O_8	15.2	7.75	1.4
^{235}U	U_3O_8	16.6	8.46	1.3
^{241}Am	AmO_2	0.234	0.1163	1.1
^{241}Am	AmO_2	0.230	0.1143	1.2
^{241}Am	AmO_2	0.280	0.1392	1.2
^{241}Am	AmO_2	0.279	0.1387	1.2
^{241}Am	AmO_2	0.304	0.1511	1.2
^{241}Am	AmO_2	0.336	0.1670	1.2
^{241}Am	AmO_2	0.321	0.1596	1.2
^{241}Am	AmO_2	0.277	0.1377	1.2

By selecting only neutrons in the energy range from 630 keV up to 1.5 MeV, therefore reducing the time-of-flight window, it is possible to construct a spectrum

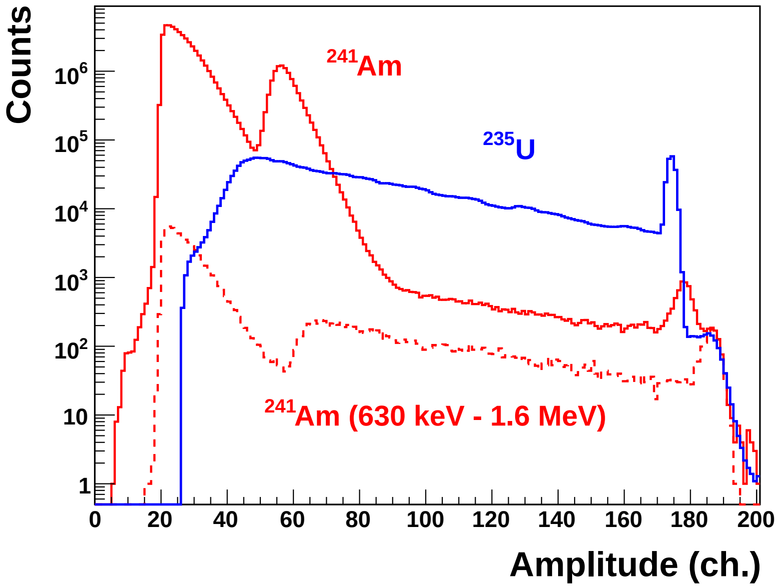

Figure 6.1 – The ^{241}Am fission fragments pulse height distribution in the whole neutron energy range (solid red histogram) and between 630 keV and 1.6 MeV (dashed red histogram). For comparison, the amplitude distribution for ^{235}U is also shown (blue histogram).

in which the pile-up is strongly reduced. The resulting pulse height distribution (red dashed histogram) is similar to that obtained from the ^{235}U case. However, for the ^{241}Am(n, f) reaction, a shift towards higher amplitudes of the fission fragment spectrum is observed. The peak at channel ∼70 could be attributed to the pile-up between α-particles and fission fragments.

In order to minimize the α-particle background, a higher threshold has to be applied. As a consequence, however, a significant fraction of fission fragments is also rejected. This has the effect of a significant reduction of the statistical precision of the data. Most importantly, the loss of efficiency caused by the higher threshold cannot be easily corrected with simulations. Therefore a normalization has to be performed, increasing the overall uncertainty of the cross-section.

The background due to α-particles and their pile-up could be estimated by means of runs without neutron beam. The results are shown in Fig. 6.2. In order to reject most of the α-particle background, while keeping a significant fraction of fission fragments, a threshold at channel 80 has been adopted. The residual background, as a function of the neutron energy reconstructed from the time of the signals, is shown in Fig. 6.3 (black dots), for the threshold at 80 ch., and in Fig. 6.4 for a lower threshold at 60 ch. As expected from a radioactive decay, the background distribution, which is constant in the time scale, follow an exponential behavior in the energy scale (linear in logarithmic units). The analysis has been performed using the higher threshold of

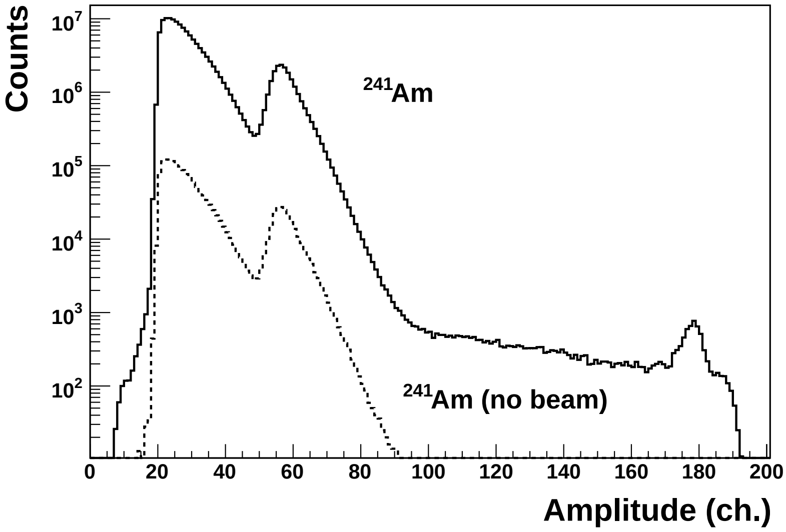

Figure 6.2 – Pulse height distribution recorded for the the ^{241}Am sample with and without the neutron beam (solid and dashed histogram, respectively).

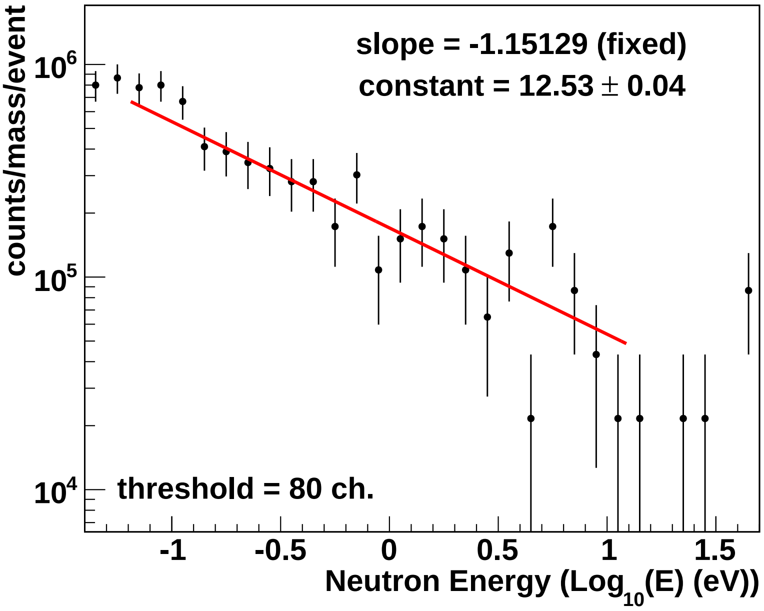

Figure 6.3 – Equivalent neutron energy distribution of the α-particle background, measured without the neutron beam, for the ^{241}Am sample (black symbols), and with an amplitude threshold at channel 80. The start of the time-of-flight measurement in the background runs was provided by a pulse generator. For convenience, the total recorded counts are divided by the mass of the sample and by the number of generated events (the equivalent of a neutron bunch). The red line represents the result of an exponential fit of the data. The slope is fixed to a value obtained by assuming a flat distribution in time-of-flight. The other parameter is used for background subtraction.

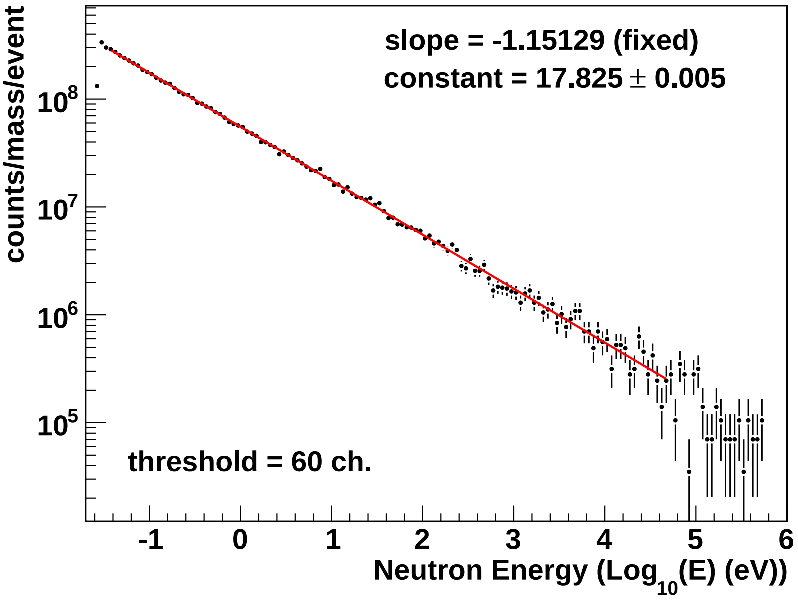

Figure 6.4 – Same as Fig. 6.3, but for a threshold on the signal amplitude at channel 60.

channel 80, since this minimizes the uncertainty due to the background subtraction. An exponential fit of the background is shown by the red line in Fig. 6.3 and Fig. 6.4. The fit was performed according to formula e^{A+Bx}, where A and B are the offset and slope, respectively, while x is the $Log(E_n)$. Since the α-particle background remains significant even with the high threshold applied, the background subtraction has a large effect (see Fig. 6.5), especially at lower energy. The slope of the α-particle background, as a consequence of the constant α-decay rate, is fixed, and equal to the value of -1.15129, derived analytically.

Before extracting the fission cross-section, a dead-time correction has been applied using Eq. 4.1. However due to the small count-rate, the correction for the ^{241}Am sample is less than 1% at all neutron energies, reaching $\sim$1.5% at 1.5 MeV. It should be considered however that the dead-time correction is still necessary for the reference ^{235}U sample.

In principle, as for the analysis of the ^{233}U(n, f) reaction seen in Chapter 5, the cross-section for a specific fission reaction could be determined relative to the ^{235}U sample without the need of further normalization. However due to the large α-particle background and the consequent uncertainty in the value of the amplitude threshold for the ^{241}Am(n, f) measurement, the extracted cross-section does not have a good accuracy and show large discrepancies with respect to previous data or evaluated cross-sections. In particular, it differs by $\sim$30% from evaluated data in the whole neutron energy range. One possible explanation for this result is the inefficiency of the chamber due to the intense α-activity of the ^{241}Am sample;

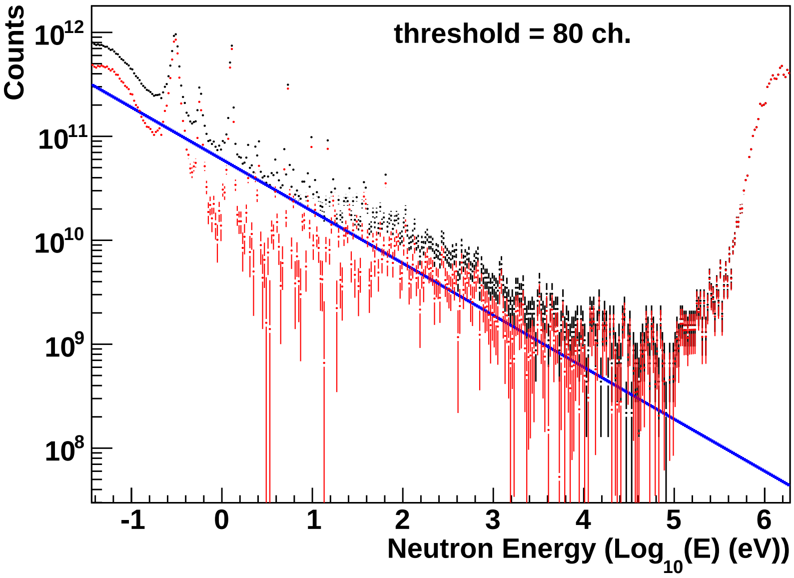

Figure 6.5 – Neutron energy distribution measured for the ^{241}Am sample and with the neutron beam, for a threshold on the signal amplitude at channel 80. The black symbols represent the total counts, while the red ones represent the distribution after subtracting the background, shown by the blue line. This was built from the fit of the data without beam (shown in Figs. 6.3 and 6.4), using the same threshold and scaling the distribution for the corresponding number of neutron bunches (or events).

significant space charge effects could in fact produce a loss of efficiency and therefore be responsible for the decrease of the fission yield. The other possibility is related to a distortion of the amplitude distribution due to the large α-particle background, with a fraction of the distribution below the threshold, not accounted for by the simulations.

Therefore, for the ^{241}Am(n, f) reaction, a normalization of the n_TOF data to previous experimental or evaluated values is required. Contrary to other cases, normalization to the thermal region is not straightforward, due to the uncertainty in the contamination of the ^{239}Pu isotope in the ^{241}Am sample. In fact, resonances not belonging to the ^{241}Am(n, f) reaction have been observed, hinting at the presence of undeclared contamination of other isotopes. Two of these resonances, at ≃7.8 eV and ≃75 eV and shown in Fig. 6.6, even with significant statistical uncertainties, allowed to conclude that a ∼0.2% contamination of ^{239}Pu is present in the ^{241}Am deposit. Normalization in another neutron energy region, where the contamination is negligible, is therefore needed.

A thorough evaluation of systematic uncertainties has not been performed as in the case of the ^{233}U(n, f) reaction analysis. In the present case, due to the large α-particle background, the most important contribution to the systematic uncertainties

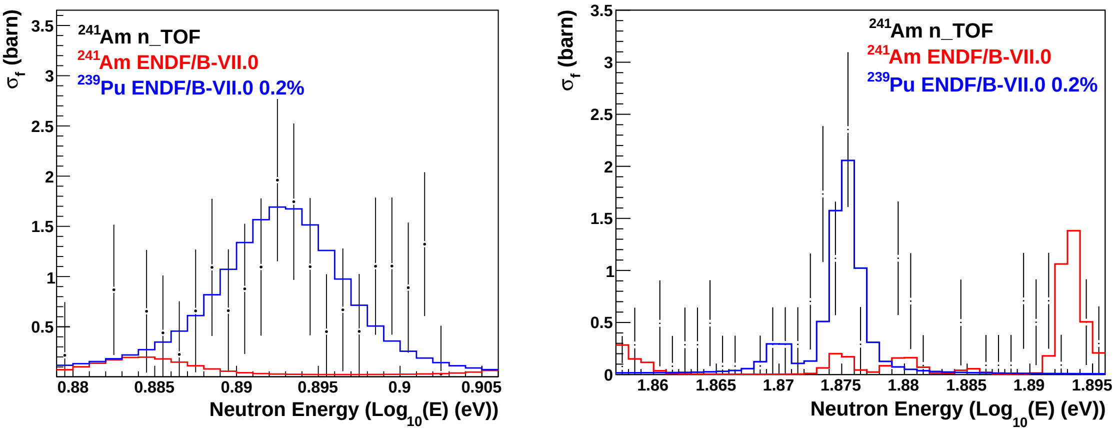

(a) (b)

Figure 6.6 – The ^{241}Am(n, f) cross-section measured at n_TOF, compared with evaluated ones. The contribution of a ^{239}Pu contamination in the sample is shown by some of its fission resonances.

is due to the background subtraction evaluated with runs without neutron beam. The offset in the fit of the background (shown in Fig. 6.3) is the only free parameter in the subtraction procedure, so that its error propagates to the extracted cross-section. The resulting uncertainty is strongly dependent on the neutron energy: in particular, close to resonance peaks, the effect of the error in the background subtraction is negligible, $\leq 1\%$, while in the resonance valleys the effect is larger and can reach up to 50%, especially where the cross-section is low. This is resulting from the fact that the background related to the α-activity is still relevant even with the high threshold employed in the analysis.

6.1.2 Comparison with evaluated libraries and previous results

The evaluated databases shows significant discrepancies between themselves in the resonance region, sometimes even by a factor of 2, as in the case of the 0.3 eV and 0.57 eV resonances (the first two resonances of the ^{241}Am(n, f) reaction). The comparison between the different evaluated cross-sections is shown in Fig. 6.7. A special case is the 1.272 eV resonance, for which the discrepancies are within 10% and are all in agreement with the measurement of Dabbs *et al.* [147], performed at ORELA in 1983. This measurement covers the neutron energy range between 0.02 eV and 20 MeV and is taken as a basis for the evaluations of the resonance region. We have therefore chosen to normalize our data to the resonance integral of Dabbs *et al.* cross-sections from 0.9 to 1.5 eV.

As already shown, resonances not belonging to the ^{241}Am(n, f) cross-section

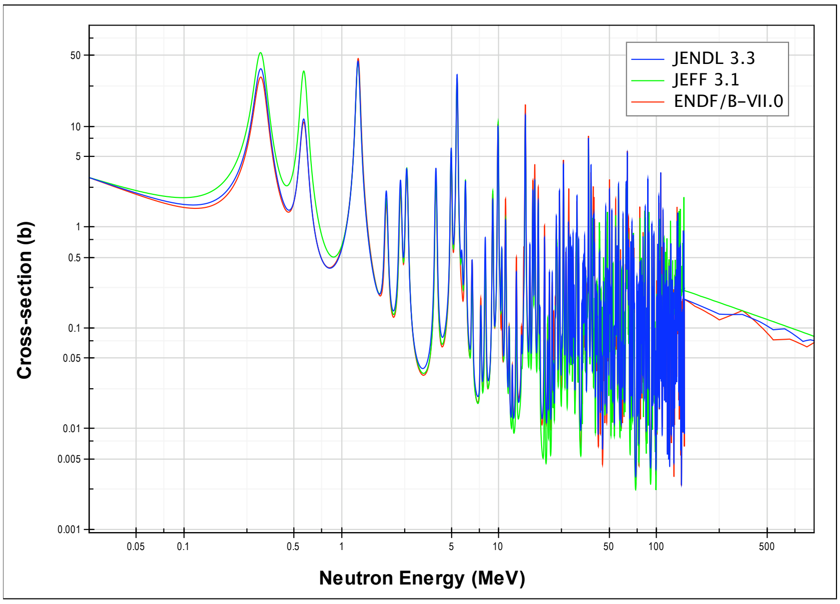

Figure 6.7 – Comparison of the ^{241}Am neutron-induced fission cross-section from the three major evaluated data libraries (ENDF/B-VII.0, JEFF-3.1 and JENDL-3.3).

hinted to the presence of an undeclared contamination of $\simeq$0.2% of ^{239}Pu. Due to the high thermal ^{239}Pu(n,f) cross-section (747.99±1.87 b according to ENDF/B-VII.0), the effect of this contaminant is significant at low energy. Fig. 6.8 shows the present data, already normalized to the 1.27 eV resonance, compared to cross-sections tabulated from the ENDF/B-VII.0 library, together with the contribution from the ^{239}Pu(n,f) reaction, estimated from ENDF/B-VII.0. It is worth noticing that, after the subtraction of the ^{239}Pu contribution, the resonance integral of the resonance of ^{241}Am(n,f) at 0.3 eV, is in agreement with the value from Dabbs *et al.* within systematic uncertainties.

The comparison between n_TOF results, evaluated databases and previous experimental results for various neutron energy ranges is shown from Fig. 6.9 to Fig. 6.16.

The region from thermal to 0.25 eV is shown in Fig. 6.9. Present data do not extend all the way down to the thermal point, but an extrapolation can be performed, as in the case of the ^{233}U(n,f) reaction. Assuming a $1/v$ behavior of the cross-section at low energy, in the energy range from 40 meV to 60 meV, a linear fit of the velocity-weighted cross-section leads to the value of 3.30±0.20 b for the thermal cross-section, in agreement with the value reported by Zhuravlev *et al.* of 3.2±0.15 b [148] and with the ENDF/B-VII.0 (and ENDF/V-VI) value of 3.15 b. Also shown in the figure is the thermal cross-section by Yamamoto *et al.* [149]. Both Zhuravlev *et al.* and Yamamoto *et al.* are, within uncertainties, in agreement with the cross-section of Dabbs *et al.*.

Above thermal energy it is evident the significant spread between different mea-

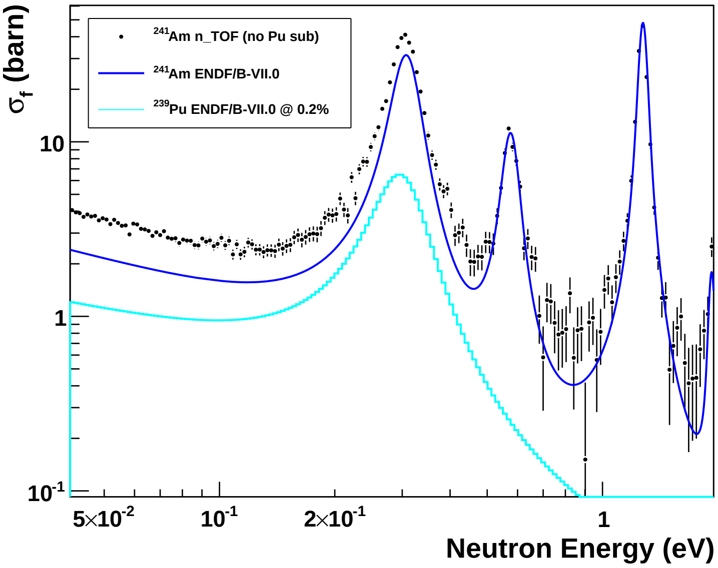

Figure 6.8 – The ^{241}Am(n, f) cross-section measured at n_TOF in the low energy region, prior to ^{239}Pu(n, f) subtraction, compared with cross-section from ENDF/B-VII.0. The present data are normalized to Dabbs *et al.* measurement [147] in the 1.27 eV resonance. The contribution of the ^{239}Pu(n, f) cross-section, for an assumed contamination of 0.2% is also shown by the light blue curve.

surements: the present cross-sections are in reasonable agreement with Gerasimov *et al.* [150] from 40 meV to 100 meV, but show a ∼30% discrepancy relative to Dabbs data. However above 100 meV the situation is inverted, and the agreement with Dabbs measurement is very good. The results for the first resonance is shown in Fig. 6.10. In that resonance, a good agreement is observed also with Bowman *et al.* [151] and Gerasimov *et al.*.

Fig. 6.11 shows the energy range in which the present results are normalized to Dabbs *et al.* results: the shape of the resonance matches almost perfectly with Dabbs's data, while discrepancies exists with Gerasimov's cross-section, due probably to the bad resolution of their experiment, as evident also at higher energies (see Fig. 6.12). A worse experimental resolution also characterizes Bowman's cross-sections, as can be noticed in Fig. 6.12 and 6.13, where the corresponding resonances appear very broad. Inadequate resolution and statistical uncertainties were in fact the main limitations of the measurement by Bowman [151].

The present results also confirm the results obtained by Dabbs in the energy region close to 15 eV (see Fig. 6.13), both in terms of resonance strength and in resonance energy. Both data sets suggest that the resonance energy in the evaluated data libraries are quite inaccurate. In particular the resonance at ∼14.63 eV is centered at an energy that differs by nearly 1% from the ENDF/B-VII.0 value.

Figure 6.17 shows the ratio of the present results for the ^{241}Am(n, f) reaction

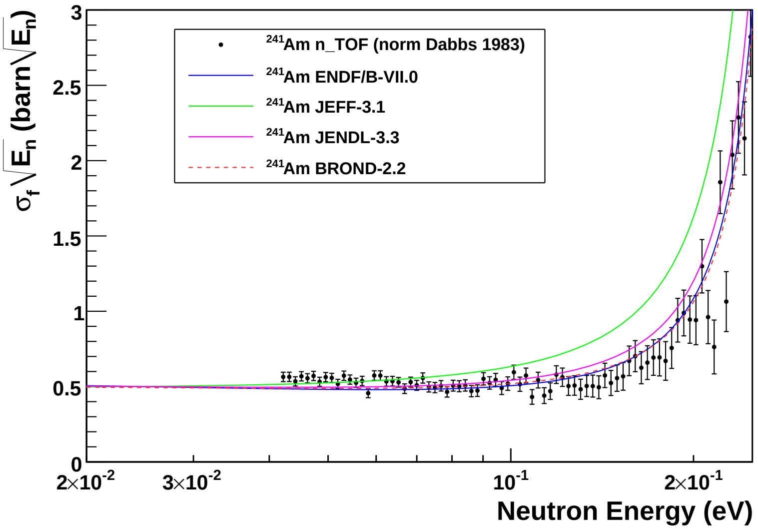

(a) Present results compared with evaluated libraries.

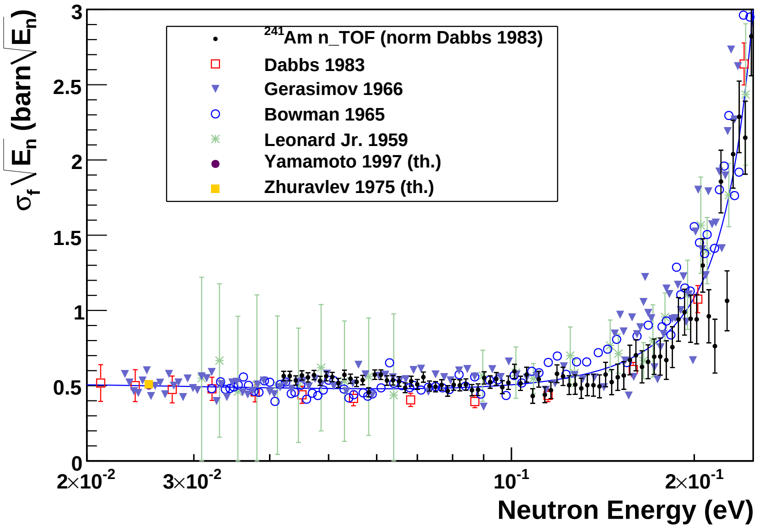

(b) Present results compared with previous measurements.

Figure 6.9 – Velocity-weighted ^{241}Am(n,f) cross-sections between 0.04 eV to 0.25 eV, compared with tabulated cross-sections and previous experimental results [147, 150, 151, 152]. Due to limitations on the time range of Flash ADCs, n_TOF data start from ~40 meV. Two previous results at thermal energy have been added for the sake of comparison (in the present graphs they cannot be distinguished, since they differ by ~2%) [149, 148].

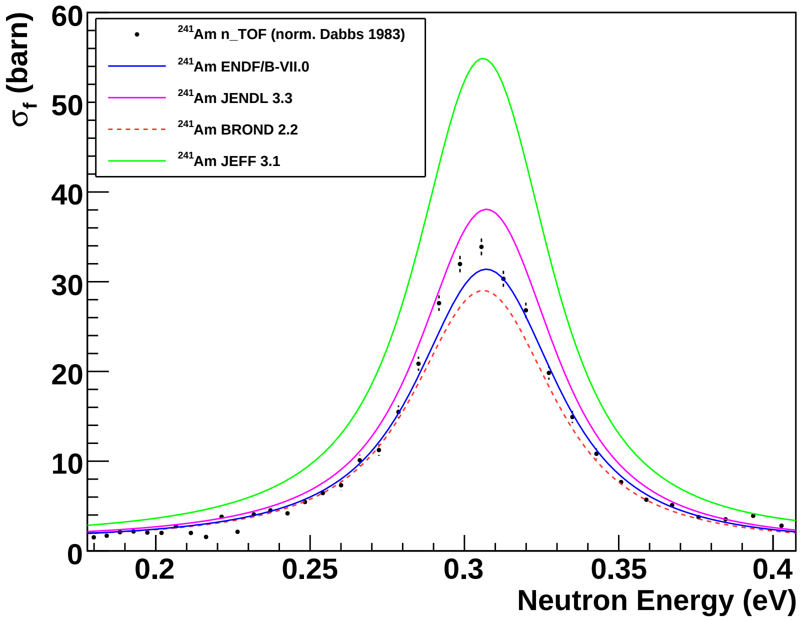

(a) Present results compared with evaluated libraries.

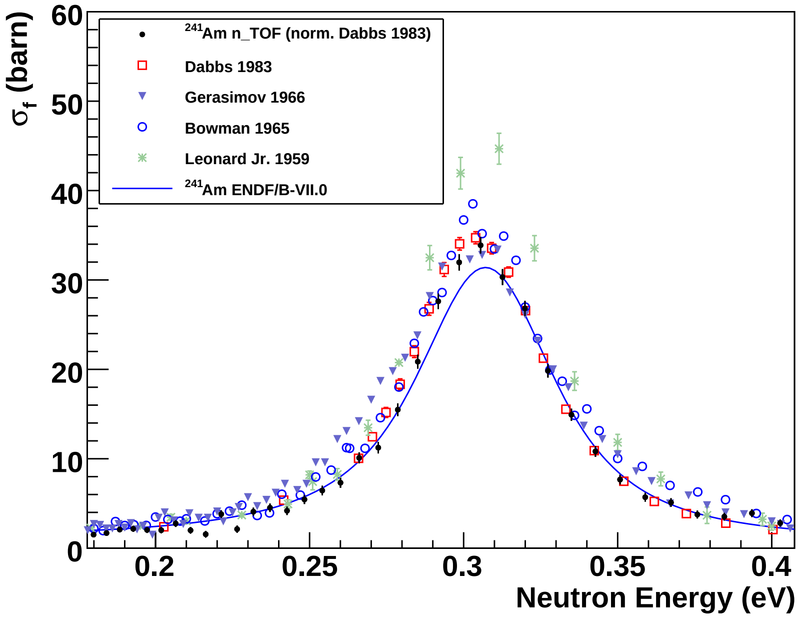

(b) Present results compared with previous measurements.

Figure 6.10 – The first resonance in the ^{241}Am(n, f) cross-section, measured at n_TOF, compared to evaluated cross-sections from major databases and previous experimental results. Significant discrepancies between different databases, up to a factor of 2, are clearly evident in the figure.

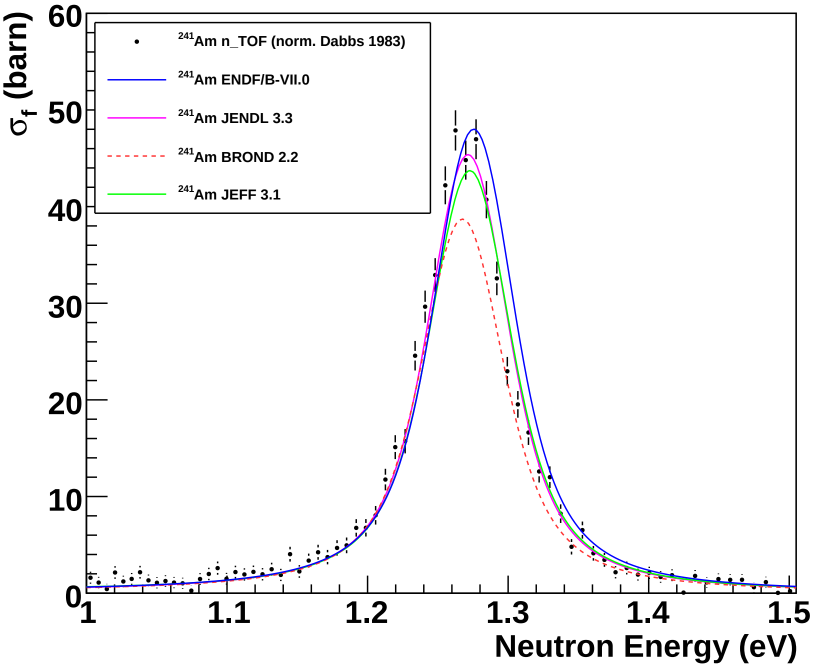

(a) Present results compared with evaluated libraries.

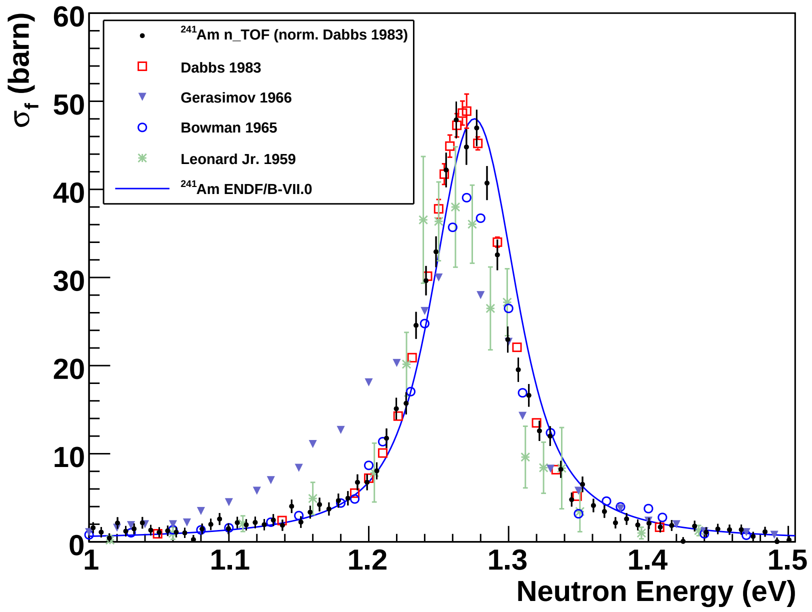

(b) Present results compared with previous measurements.

Figure 6.11 – The third, large resonance in the ^{241}Am(n, f) cross-section, between 1 eV and 1.5 eV. The present results (black symbols) are compared with the evaluated cross-sections from major databases and with previous experimental results. This is the only large resonance for which different databases agree within 10%. The n_TOF data have been normalized to the resonance integral of the Dabbs *et al.* [147] data.

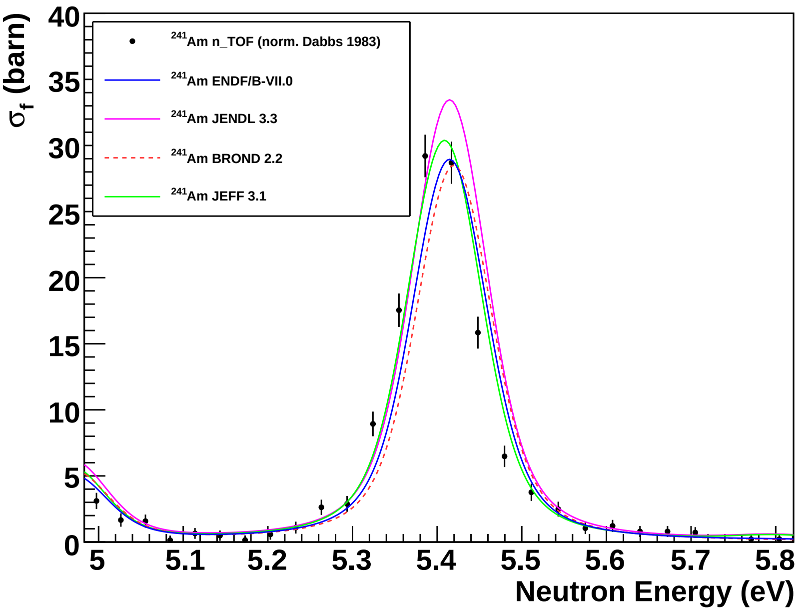

(a) Present results compared with evaluated libraries.

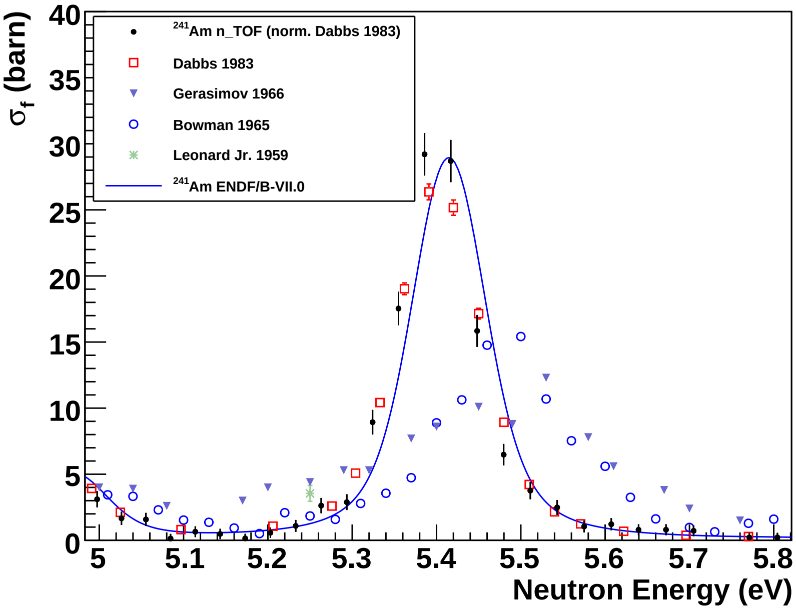

(b) Present results compared with previous measurements.

Figure 6.12 – The ^{241}Am(n, f) cross-section measured at n_TOF between 5 eV and 5.8 eV, compared with evaluated cross-sections and previous measurements.

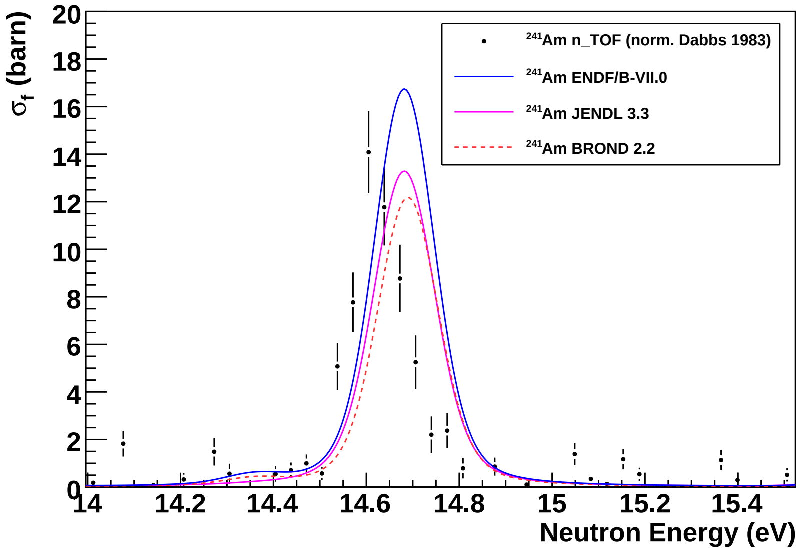

(a) Present results compared with evaluated libraries.

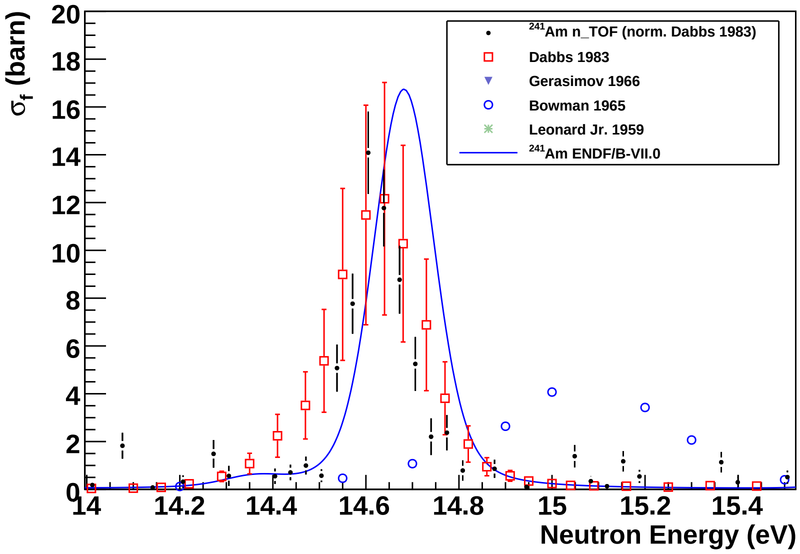

(b) Present results compared with previous measurements.

Figure 6.13 – Present results for the ^{241}Am(n, f) cross-section between 14 eV and 15.5 eV, compared with evaluations and previous results. The good resolution of the n_TOF data is evident from the 14.65 eV resonance, which shows a width narrower than in the measurement of Dabbs *et al.*.

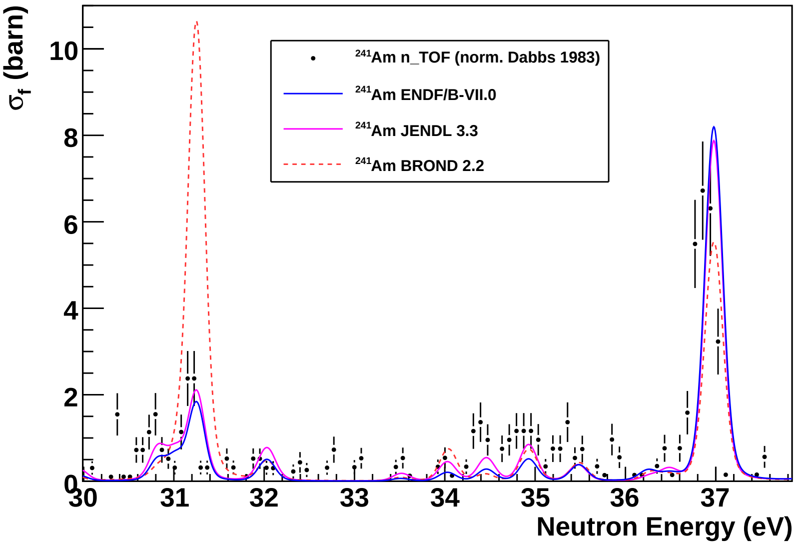

(a) Present results compared with evaluated libraries.

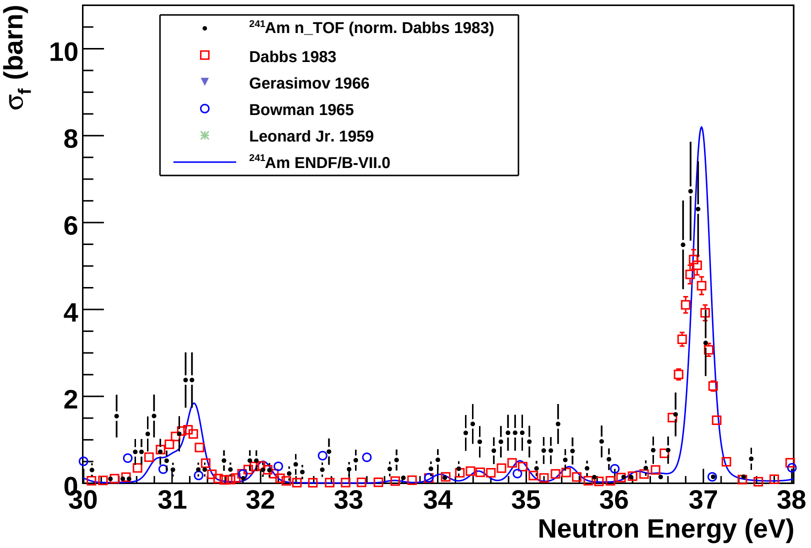

(b) Present results compared with previous measurements.

Figure 6.14 – The ^{241}Am(n, f) cross-section measured at n_TOF between 30 eV and 38 eV, compared with evaluated cross-sections and previous experimental results. The present results confirm the erroneous evaluation present in the BROND-2.2 database for the ~31 eV resonance, while in agreement with the data of Dabbs *et al.*.

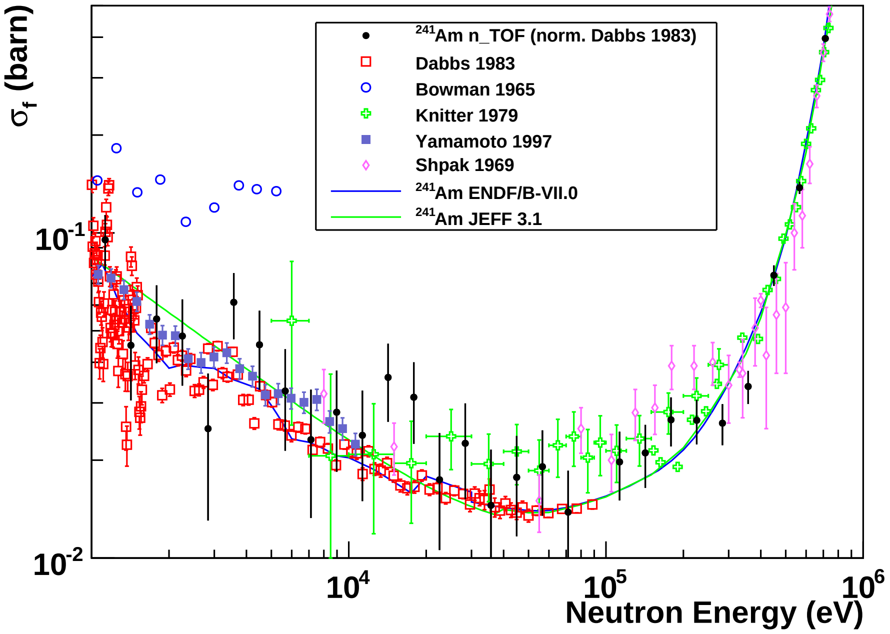

Figure 6.15 – Cross-section of the ^{241}Am(n, f) reaction, measured at n_TOF, compared with tabulated cross-sections from ENDF/B-VII.0 and JEFF-3.1 libraries, as well as with various previous results in the energy range between 1 keV and 1 MeV.

with previous measurements and with cross-sections from evaluated libraries, averaged over neutron energy decades. The present data are in agreement (within 5%) with the ENDF/B-VII.0 library (evaluated using mainly the results of Dabbs *et al.* in the resonance region) up until 100 eV. Above this limit the discrepancies with most evaluated libraries is ∼40%, with only JEFF-3.1 showing a ∼20% difference in the energy region between 100 eV and 10 keV. It is interesting to note that in the last bin, i.e. between 100 keV and 1 MeV neutron energy, the agreement between present results and all evaluated libraries is again within 5% again. An additional comparison with recent results from Yamamoto *et al.* [149] has also been performed. This measurement provided low resolution data of the ^{241}Am(n, f) cross-section in the neutron energy range from 1 eV to 10 keV. The discrepancy with n_TOF data is as large as 35% in the energy bin between 1 and 10 eV, where - however - present results are in agreement with ENDF/B-VII.0 and JENDL-3.3 by less than 5%. Above 100 eV, the data of Yamamoto *et al.* follow the libraries, and therefore are lower than n_TOF by ≈30%.

It is important to stress that the present results are still preliminary and have to be confirmed by a more refined analysis.

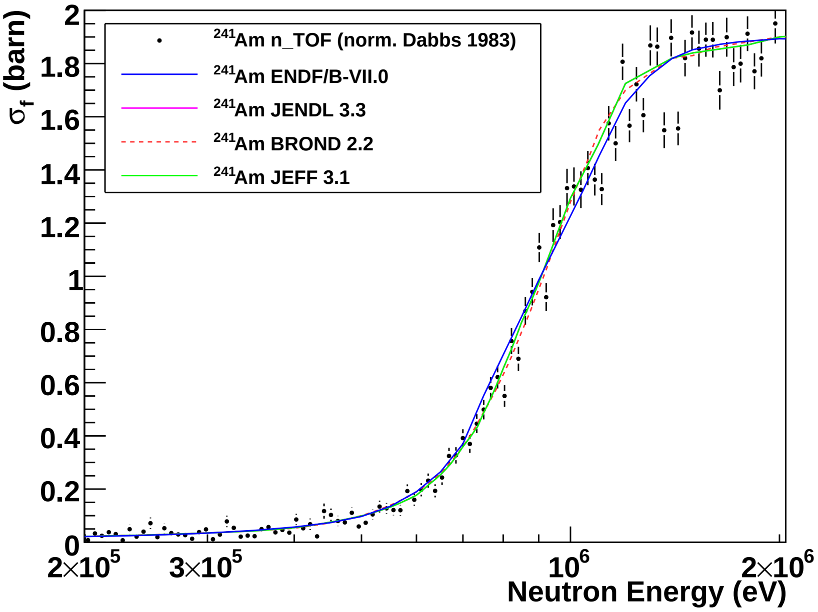

(a) Present results compared with evaluated libraries.

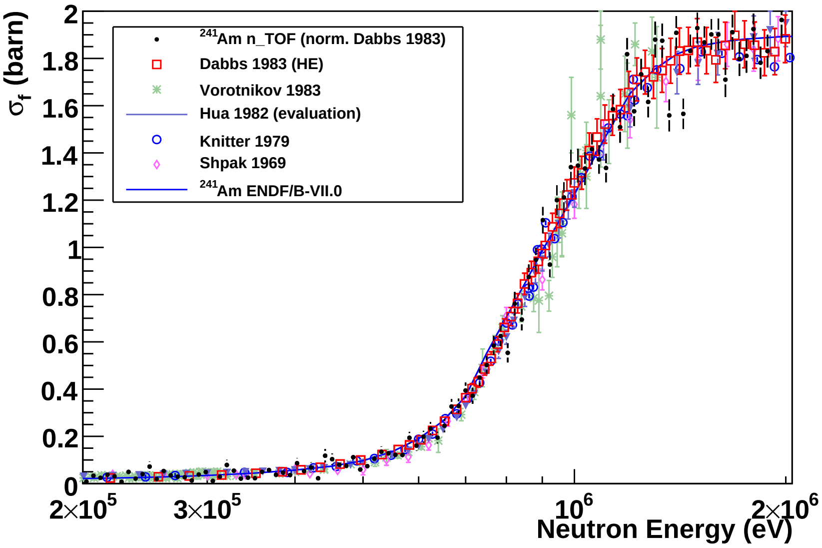

(b) Present results compared with previous measurements.

Figure 6.16 – The ^{241}Am(n, f) cross-section in the region of the fission threshold. Evaluated cross-sections and previous results are shown for comparison.

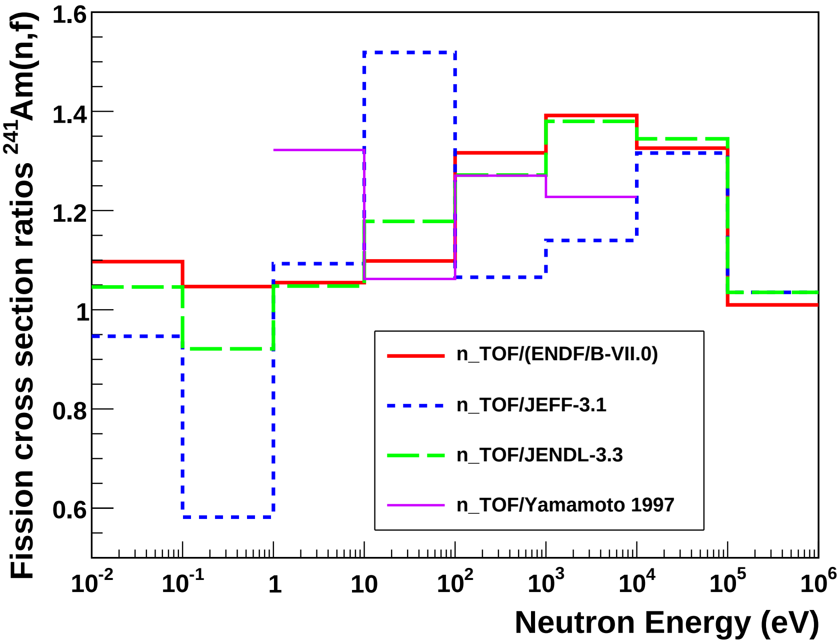

Figure 6.17 – Ratio between average ^{241}Am(n, f) cross-section determined at n_TOF, and those from evaluated libraries or previous results. The average is performed over a decade in the logarithm of neutron energy.

6.2 ^{243}Am(n, f) cross-section

^{243}Am is a minor actinide abundantly produced, together with ^{237}Np and ^{241}Am, in spent fuels of light water reactors. As already pointed out in Chapter 1, nuclear data of minor actinides are of great importance for understanding the burn-up characteristics of MOX or Pu fuels and for the design of systems for spent fuel reprocessing or radioactive waste disposal. The ^{243}Am fission cross-section is in particular fundamental for transmutation projects. It has a maximum in the resonance region, where the values goes up to about 10 barn; the cross-section steadily decreases for energies up to $\sim$0.3 MeV, where it starts to increase again, reaching $\simeq$1.5 barn in the MeV region. Due to its short half-life ($t_{1/2}$=7370 y) and consequently high α-activity, not many experimental measurements exists for this isotope. Of the few measurements available, Wagemans *et al.* have reported the thermal fission cross-section measured with a neutron guide at the Institut Laue-Langevin (ILL) [153], while Knitter *et al.* have measured the ^{243}Am(n, f) cross-section using a 7 MV Van de Graaf accelerator and an electron linear accelerator (GELINA) as pulsed neutron sources [154]. Seeger *et al.* have reported data obtained by the neutron time-of-flight method using the very high flux from a nuclear explosion [155]. Nevertheless data available up to now are scarce and of doubtful quality, especially in the thermal and resonance neutron energy regions. In the EXFOR database, no data are present from ∼100 meV up to 50 eV except for the recent data by Kobayashi *et al.* [156], which however are characterized by a very low resolution. Even if fission resonance parameters can be obtained from measurements of total cross-section [156, 157], the predictions are not accurate enough for the minor actinides: as a result, discrepancies between evaluated libraries, as shown in Fig. 6.18, are large in the whole energy range, in particular where experimental data are missing, thus demonstrating that current evaluated cross-sections are not very reliable, in particular for the applications to advanced nuclear technologies.

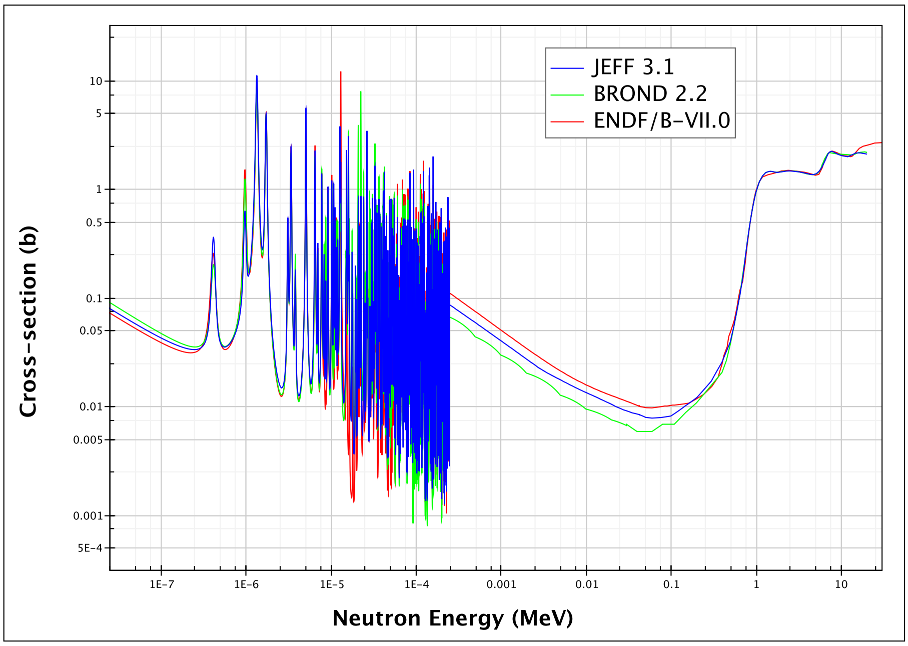

Figure 6.18 – The ^{243}Am(n, f) cross-section from the most recent evaluated data files: ENDF/B-VII.0, JEFF-3.1 and BROND-2.2. For this isotope, the data contained in JEFF-3.1 are taken from JENDL-3.3, apart for small changes described in the text.

Another problem that complicates the analysis of the ^{243}Am(n, f) reaction is the presence of contamination in the sample. In a ^{243}Am deposit, a growth of ^{239}Pu contamination naturally occurs due to the following decay process:

$$^{243}\mathrm{Am} \xrightarrow[7370y]{\alpha} {}^{239}\mathrm{Np} \xrightarrow[2.355d]{\beta-} {}^{239}\mathrm{Pu} \xrightarrow[24110y]{\alpha} {}^{235}\mathrm{U} \tag{6.1}$$

As a consequence of the much larger ^{239}Pu(n_{th}, f) cross-section (747.99±1.87 b according to the ENDF/V-VII.0 evaluated database, as opposed to the ≃74 mb of the ^{243}Am(n_{th}, f) cross-section), the ^{239}Pu contamination results in an important contribution to the measured fission counting rate. Fig. 6.19 shows the Pu in-growth as a function of time after the Am-Pu separation (assuming 100% efficiency).

From this figure it is clear that 1 yr after separation, the ^{239}Pu contamination

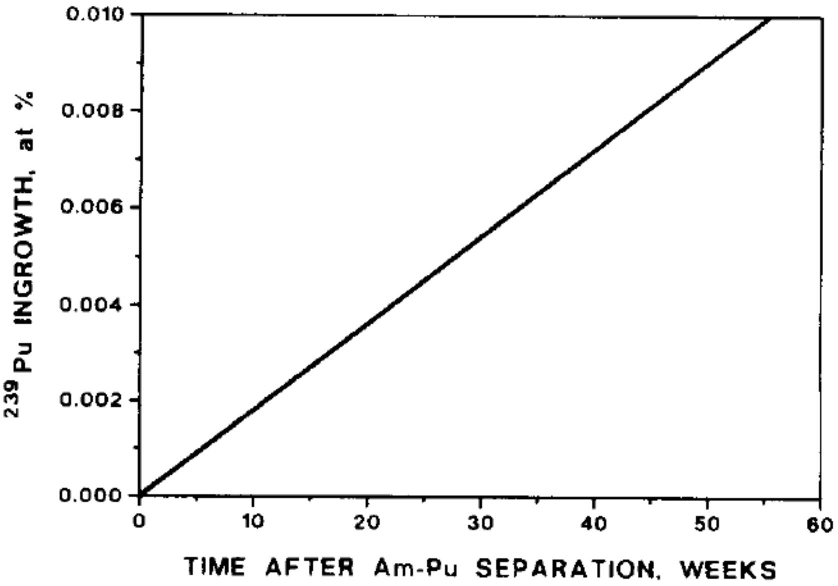

Figure 6.19 – Increase of ^{239}Pu contamination in the ^{243}Am sample as a function of time elapsed after the Am-Pu separation. Figure taken from Ref. [158].

contributes with up to ~70 mb to the measured fission cross-section. For the samples used in the n_TOF measurement, there is no information concerning the production date, and therefore no knowledge of the ^{239}Pu contamination fraction. However, it can be estimated that a significant contribution from this isotope is present in the results at low energies.

6.2.1 Analysis procedure

Eight ^{243}Am samples were used (listed in Table 6.2) in the n_TOF measurements.

Table 6.2 – Samples used in the ^{243}Am(n, f) measurement. The reported mass is that of the U and Am isotopes only.

Sample	Chemical form	Mass (mg)	Areal density (10^{-7} atoms/b)	Uncertainty (%)
^{235}U	U_3O_8	15.2	7.75	1.4
^{235}U	U_3O_8	16.6	8.46	1.3
^{243}Am	AmO_2	0.556	0.2741	1.1
^{243}Am	AmO_2	0.585	0.2884	1.3
^{243}Am	AmO_2	0.613	0.3022	1.3
^{243}Am	AmO_2	0.631	0.3111	1.3
^{243}Am	AmO_2	0.537	0.2648	1.2
^{243}Am	AmO_2	0.558	0.2751	1.2
^{243}Am	AmO_2	0.595	0.2933	1.3
^{243}Am	AmO_2	0.710	0.3500	1.2

As for other actinides, the discrimination of fission fragments from the electronic noise and α-particles is performed via a threshold set on the amplitude distribution of recorded signals (reconstructed through the appropriate routine). As for the ^{241}Am, the presence of a significant background of α-particles and their pile-up (see Fig. 6.20) makes necessary to apply a high threshold in order to minimize the background contribution. By selecting only high energy neutrons, i.e. with energy between 630 keV and 1.5 MeV, which corresponds to a smaller time-of-flight window, it is possible to reduce the pile-up component. The resulting pulse height distribution, shown by the dashed curve in Fig. 6.20, is similar to the one obtained for the ^{235}U case.

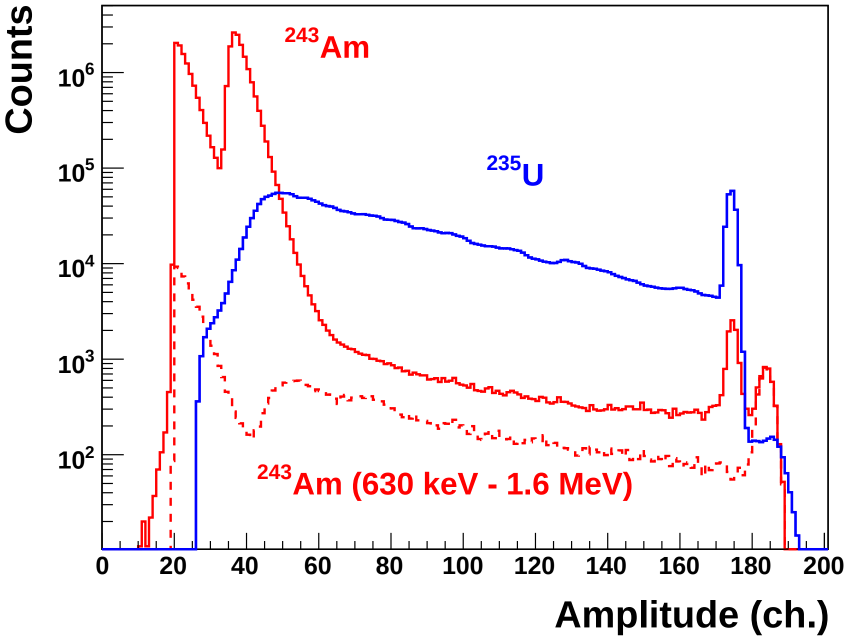

Figure 6.20 – Comparison of the fission fragments pulse height distribution for the ^{243}Am sample, in the whole neutron energy range from thermal to 1 MeV (solid red histogram), and in the energy range between 630 keV and 1.6 MeV (dashed red histogram). For comparison, the distribution for the ^{235}U sample is shown (blue histogram).

Therefore, an analysis similar to ^{235}U can be done by considering only the high energy neutrons and applying the same threshold of the ^{243}Am sample. An attempt was nevertheless made in the whole energy region, with the aim of extracting some information at least for the largest resonances.

The contribution of the residual background due to α-particles and α-pile-up was estimated by analyzing the data acquired without the neutron beam, shown in Fig. 6.21 by the dashed histogram. In order to minimize the α-particle background while rejecting the smallest fraction of fission fragments, a threshold at FADC channel 60 of the digitizer was adopted.

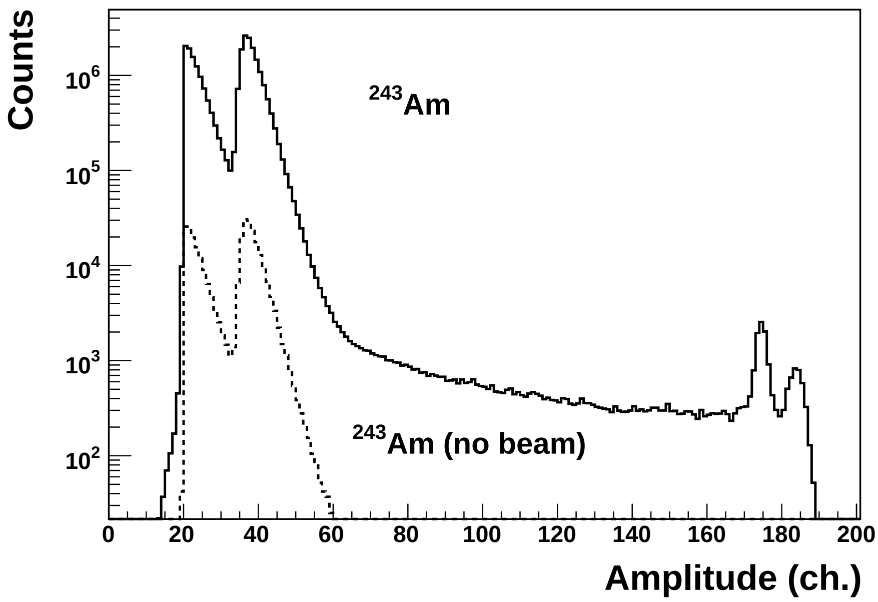

Figure 6.21 – The pulse height distribution of signals recorded for the ^{243}Am sample in measurements with and without the neutron beam (solid and dashed histogram respectively).

The residual background as a function of neutron energy, for this threshold, is shown in Fig. 6.22 by the black dots. In order to determine the residual background to be subtracted from the neutron energy distribution measured with the beam, an exponential fit, according to formula e^{A+Bx}, was performed. The result of the fit is shown in Fig. 6.22 by the red line. The slope of the α-particles background, assuming a constant α-decay rate during the acquisition, is fixed to -1.15129.

Since the residual background for the chosen threshold is almost negligible, the neutron energy distribution after background subtraction is not much different from the original histogram, as shown in Fig. 6.23.

As in previous cases, in order to extract the fission cross-sections, different corrections have to be applied.

An efficiency correction is needed due to the different thicknesses of the ^{243}Am and reference ^{235}U deposits, and to the different amplitude threshold used in the analysis. Figure 6.24 shows the comparison between the experimental pulse height distribution (calculated in the neutron energy range between 630 keV and 1.5 MeV) and the simulated FF energy distribution, scaled to match the experimental distribution. The efficiency correction, calculated for the threshold at channel 60, is of the order of $\sim$18%.

At low neutron energies, cross-sections cannot be easily extracted, due to the presence of contaminants in the sample, which masks the very low cross-section of

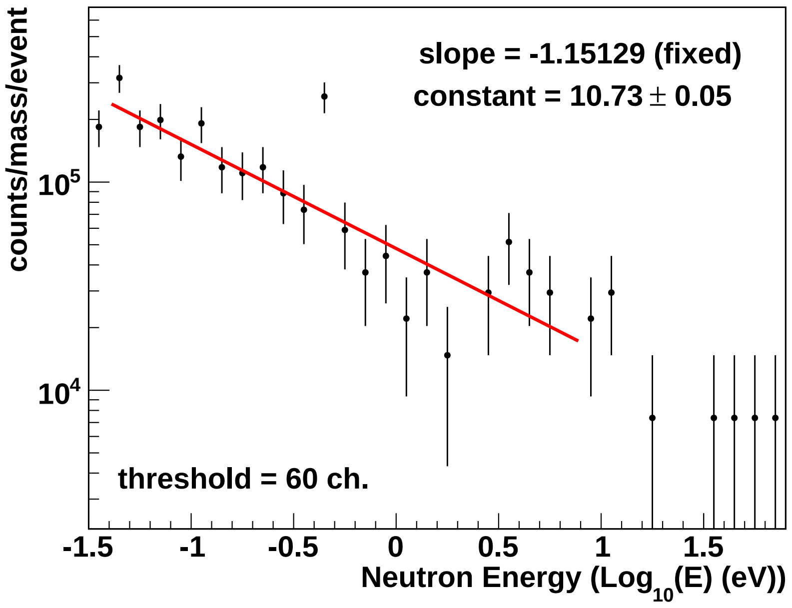

Figure 6.22 – Evaluated neutron energy distribution of the α-particle background, measured without the neutron beam for the ^{243}Am samples (black symbols). The red line represents the result of an exponential fit of the data.

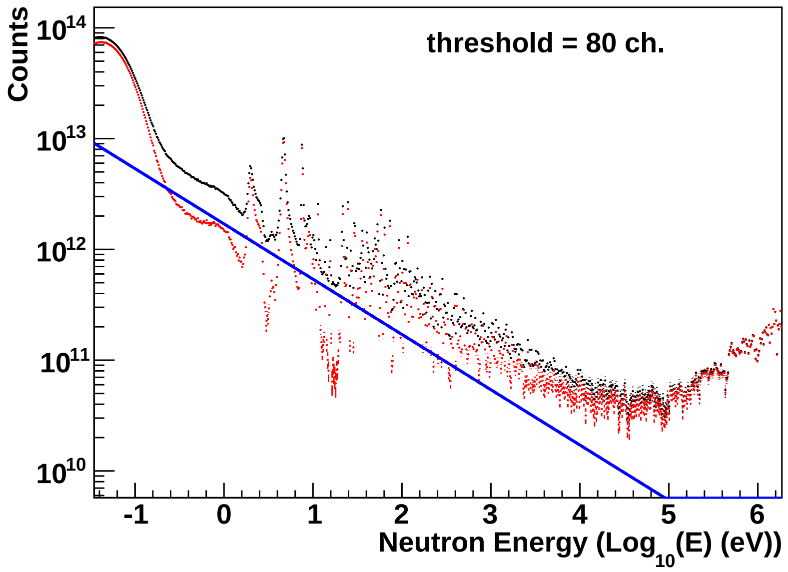

Figure 6.23 – Distribution of counts as a function of the neutron energy, recorded in the ^{243}Am(n, f) reaction, for a threshold on the signal's amplitude at channel 60. The black symbols represent the total counts, while the red ones are obtained after subtraction of α-particle background (shown by the blue line). To this purpose, a function is used, obtained from the fit shown in figure 6.22 for the same threshold. The contribution of the α-particle background is significantly smaller than in the case of the ^{241}Am sample.

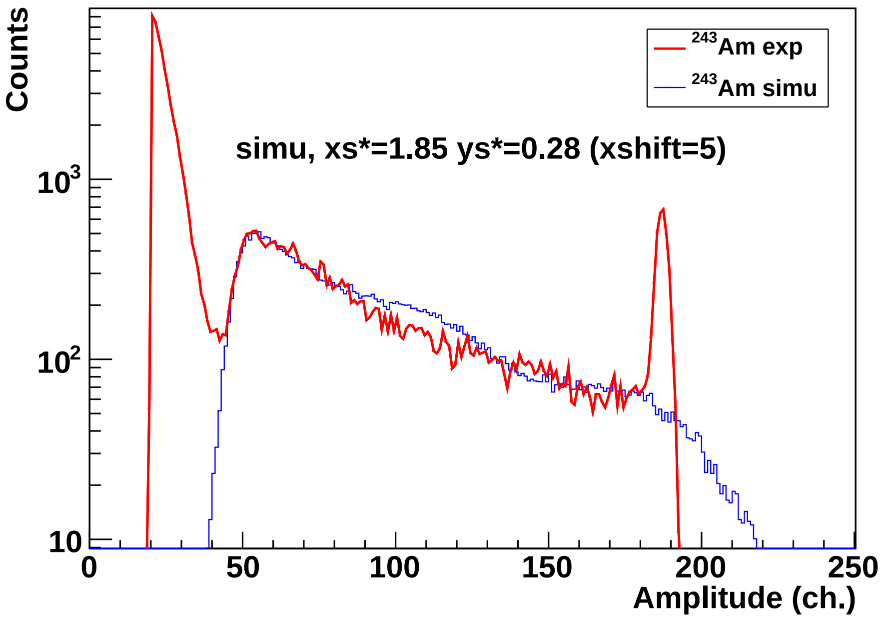

Figure 6.24 – Pulse height distribution measured for signals from the $^{243}\mathrm{Am}(n, f)$ reaction in the neutron energy range between 630 keV and 1.6 MeV (red histogram), compared with the results of the simulated fission fragments energy loss in the gas cell of the FIC1 detector. The simulation results are scaled both the X and Y axis, in order to match the shape of the experimental distribution. The peak close to 180 ch. in the experimental data is due to the end of range in the FADC.

the ^{243}Am(n,f) reaction ($\simeq$74 mb [153]). A known contamination of ^{241}Am, of 2.5%, is declared for the employed samples. This is still far too low to account for the observed fission rate, shown in Fig. 6.25. As mentioned before, another contaminant expected in the sample (although not declared), is ^{239}Pu, produced as a consequence of the α-decay of ^{243}Am. Although the amount of ^{239}Pu is not known, it certainly contributes significantly to the measured fission yield. In fact, even assuming a build-up time as low as 60 weeks, the count-rate due to Pu is of the same order of magnitude of the one expected for the ^{243}Am(n,f) reaction. Finally, another possible contaminant is ^{242m}Am, whose fission reaction has a very high cross-section, with a value at thermal energy of 6950±280 b [153]). This isotope is produced via the ^{241}Am$(n,\gamma)^{242}$Am reaction and destroyed via fission, with an estimated equilibrium value of a few parts per million. Due to its long lifetime ($t_{1/2}$ $\sim$141 y), it may be also present from the beginning in the sample material. A contamination of $\sim 10^{-4}$ of ^{242m}Am could contribute to a significant fraction of the observed fission yield in the low energy region, as evident in Fig. 6.25.

6.2.2 Comparison with evaluated libraries and previous results

While at low energies reliable results on the ^{243}Am(n,f) cross-section cannot be extracted due to contamination issues, above $\sim$300 keV the data are not significantly affected by the effects of impurities. At high energy, in fact, all Am and Pu isotopes have similar fission cross-section, so that contaminations $\leq$1% do not contribute to the measured fission yield. The only sizable contribution comes from the ^{241}Am(n,f) reaction, which has to be subtracted from the measured fission yield.

A comparison between previous experimental results, reported in Fig. 6.27, shows a striking feature: the fission cross-section are grouped in two distinct clusters, separated by nearly 15% difference. The most recent experimental data set is by Laptev *et al.* [159] which extends up to 200 MeV neutron energy. The extracted cross-section lies in the higher cluster together with the data by Behrens and Browne [160]. The latest evaluations[1], such as ENDF/B-VII.0, follow the lower cluster, and in particular the data by Knitter and Budtz-Jørgensen [154]. As shown in Fig. 6.26 and 6.27, the present results agree very well with the lower data group and therefore with the tabulated cross-section in ENDF/B-VII.0 and JENDL-3.3. Recent "quasi-absolute" results by Aïche *et al.* [161] also confirm the lower cross-section group, in agreement with this work. It is interesting to note that - as shown in Ref. [162] - the two groups seem to differ, in this energy range, only by a normalization factor.

---

[1] The ENDF/B-VII.0 evaluation is the same as ENDF/B-VI.8 while JEFF-3.1 is a carry over from the JENDL-3.3 library.

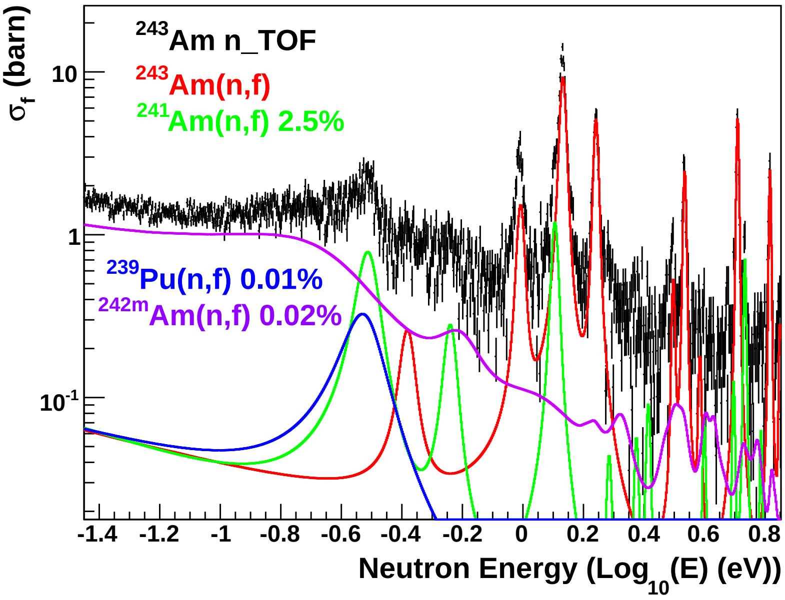

(a) Energy region between 0.035 eV and 7 eV.

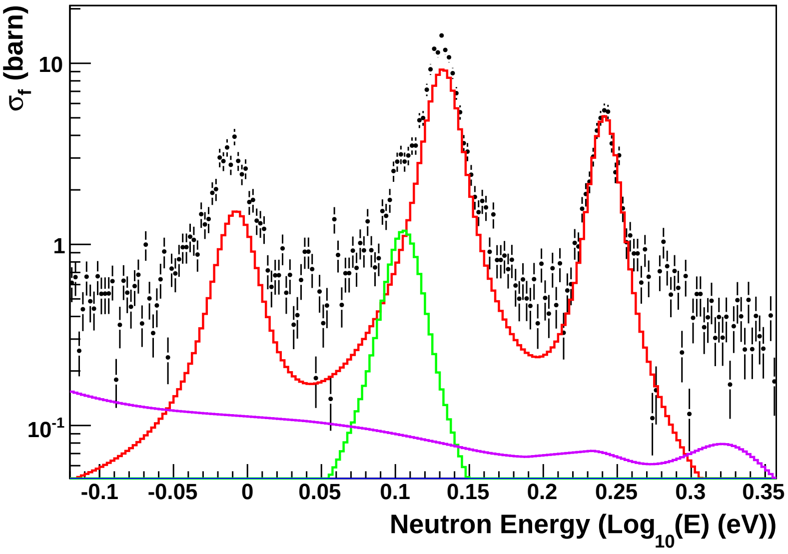

(b) Close-up view of the three resonances between 0.8 eV and 2.2 eV. The color codes are the same as those of the upper panel.

Figure 6.25 – ^{243}Am(n,f) cross-section in the low energy region compared with evaluated data from the ENDF/B-VII.0 library. The contribution coming from the ^{241}Am(n,f) reaction is calculated from the known 2.5% contamination of the ^{241}Am isotope in the ^{243}Am sample. The 0.01% contamination of ^{239}Pu is estimated assuming that the measurement took place 60 weeks after the Am-Pu separation. The 0.02% fraction of ^{242m}Am is instead guessed from the assumption that the observed experimental cross-section at low energy is mostly due to this contamination.

It should be underlined, finally, that surrogate data by Younes *et al.*[2] [163] lie even lower than all other direct experimental data. However, as suggested in Ref. [162], since those results are obtained from the surrogate reaction ^{244}Pu(^{3}He,tf), larger systematic errors affect the reported cross-section, due to difficulties of obtaining the ^{244}Pu sample.

In Ref. [154] the data are compared also with results obtained in integral (reactor) measurements: the conclusion is that averaged cross-sections calculated with the ZEBRA reactor spectrum ([154] and references therein) are in agreement with the lower cluster of cross-sections. On the contrary, Rochman *et al.*, have recently shown, based on EMPIRE calculations [164, 165] that, by using systematics of fission barrier heights, the predicted cross-section would lie within the higher cluster. The new n_TOF results could help in ruling out one of these two possibilities.

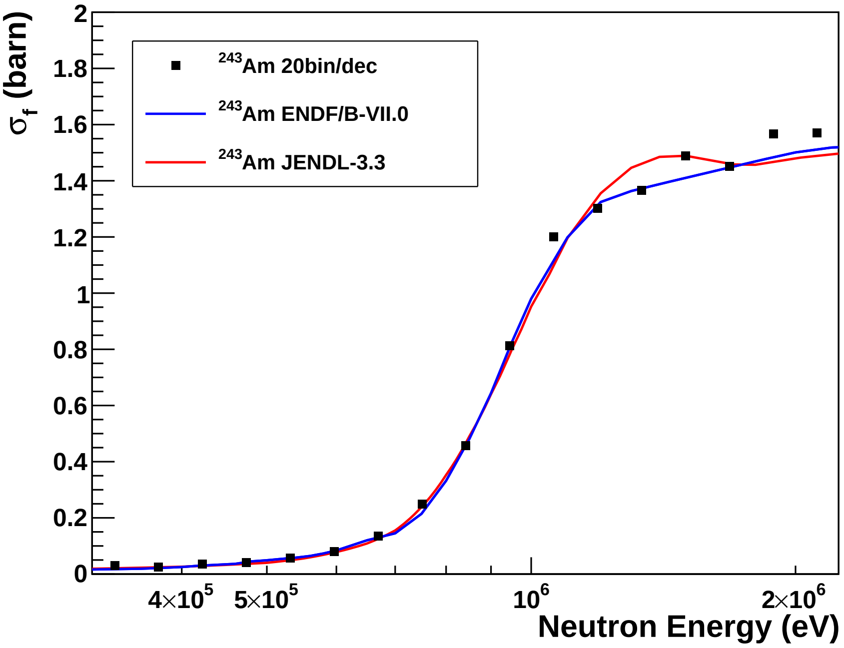

Figure 6.26 – Cross-section of the ^{243}Am(n, f) reaction, measured at n_TOF, compared with evaluated data from major libraries. In the ENDF/B-VII.0 database no changes have been made for this isotope relative to the older ENDF/B-VI.8 file, as suggested in [162], while the same evaluated cross-sections are contained in JEFF-3.1 and JENDL-3.3. Statistical errors are included in the n_TOF results, but they are smaller than the symbols.

---

[2] Not present as of now in the EXFOR database.

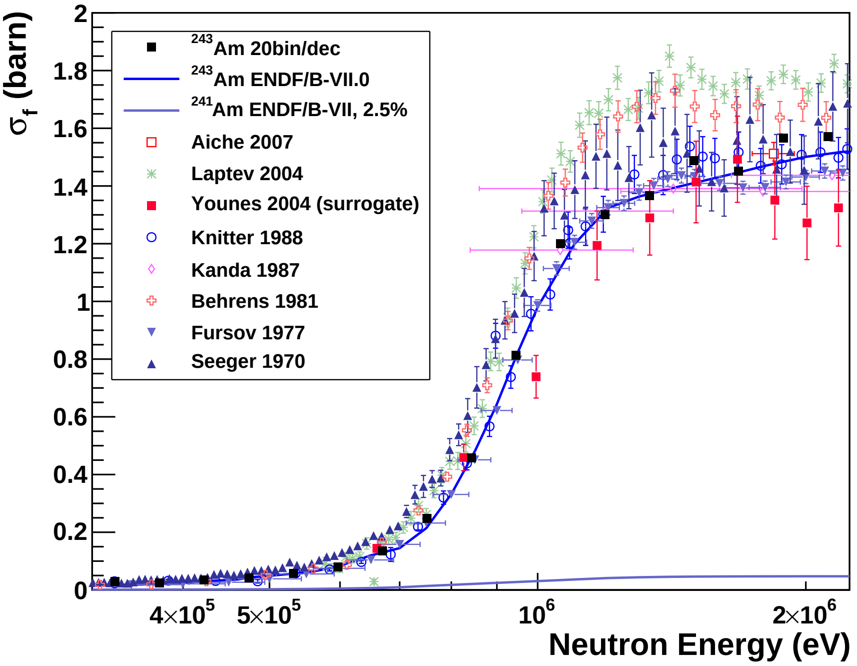

Figure 6.27 – The ^{243}Am(n, f) cross-section from the present work, compared to previous experimental results. A detailed discussions on the various measurements can be found in the text. The measurements seems to be grouped in two separate clusters, differing by ∼0.2 b from each other. The present results agree with the lower group. Recent data from Aıche *et al.* are also included (one point only, since the measurement extends only from 1.8 MeV up to ≃7 MeV). Statistical errors are included in the present results, but they are smaller than the symbols.

6.3 ^{245}Cm(n, f) cross-section

As pointed out in Chapter 1, accurate cross-sections of neutron-induced reactions are required for many of the transplutonium isotopes in order to predict the concentration of heavy actinides in reactor fuel elements, as well as for calculating transmutation rates in advanced nuclear systems. The location of ^{245}Cm in the production chain makes the knowledge of its cross-section particularly important. The path to heavier curium isotopes, such as ^{246}Cm, is in fact affected by the fission and capture cross-sections of ^{245}Cm and on their dependence on the neutron energy. Furthermore, the possibility to burn ^{245}Cm, a long lived minor actinide, relies mostly on fission reactions. Cross-sections for this isotope are therefore fundamental for the feasibility studies and eventually the design of advanced systems (such as Generation-IV systems) that could be used to burn this isotope. At present, the fission cross-section is known with a very large uncertainty, around ~50%, whereas sensitivity analysis of some new reactor systems indicate that an accuracy better than 10% is required.

6.3.1 Analysis procedure

Four ^{245}Cm samples were used (listed in Table 6.3) in the n_TOF measurements.

Table 6.3 – Samples used in the ^{245}Cm(n, f) measurement. The reported mass is that of the U and Cm isotopes only.

Sample	Chemical form	Mass (mg)	Areal density (10^{-7} atoms/b)	Uncertainty (%)
^{235}U	U_3O_8	15.2	7.75	1.4
^{235}U	U_3O_8	16.6	8.46	1.3
^{245}Cm	CmO_2	0.367	0.179	1.3
^{245}Cm	CmO_2	0.538	0.263	1.2
^{245}Cm	CmO_2	0.407	0.199	1.3
^{245}Cm	CmO_2	0.399	0.195	1.3

As for all other actinides, the analysis of the ^{245}Cm(n, f) reaction is more complex than that of the ^{233}U(n, f) reaction. In particular, the discrimination of fission fragments from α-particles is not straightforward, due to the very high radioactivity of the samples, which results in the presence of a high pile-up between α-particles and between α-particles and fission fragments. This is clearly observed in Fig. 6.28, where the comparison between the pulse height distribution for ^{245}Cm and ^{235}U is shown. Contrary to ^{235}U(n, f) reaction, the amplitude distribution for the ^{245}Cm(n, f) reaction, integrated over all neutron energies, shows two peaks related to the α-particles

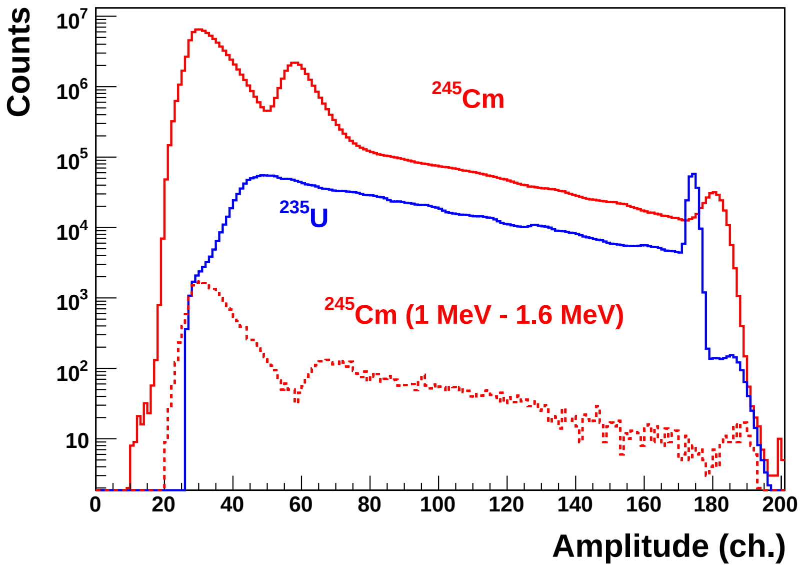

Figure 6.28 – The fission fragments pulse height distribution measured in the ^{245}Cm(n, f) reaction, in the whole neutron energy range (red solid histogram), and in the energy range between 1 MeV and 1.6 MeV (dashed histogram). For comparison, the amplitude distribution measured with the ^{235}U sample is also shown (blue histogram).

background, which hide the expected fission fragments peak. By selecting events in the neutron energy range between 1 MeV and 1.6 MeV, corresponding to a very small window in neutron time-of-flight, it is possible to reduce the α-particle background and especially the pile-up contribution. As a result, a pulse height distribution similar to the one obtained in the ^{235}U(n, f) case is observed, although a shift of the distribution to higher amplitudes can be clearly noticed. The peak at channel $\simeq$70 could be attributed to the pile-up between α-particles and fission fragments.

It is clear from Fig. 6.28 that a very high threshold has to be applied in the analysis of the ^{245}Cm(n, f) reaction in order to reduce the α-particle component. Furthermore, the large background prevents from accurately determining the fraction of FF rejected below the threshold. Although a large suppression of the α-particle background is achieved by means of a high threshold, a significant residual background still survives and has to be subtracted.

The contribution of the α-particle background could be estimated from the data acquired without the neutron beam, shown in Fig. 6.29. In addition to the α-particle background, in this case an additional component is also observed; the amplitude distribution is similar to that of FFs, and is due to spontaneous fission of ^{244}Cm. This isotope has an half-life of 18.10 y, and a spontaneous fission branching ratio of 1.37×10^{-4}%, so that its fission decay rate is much higher compared to that of ^{245}Cm, which has an half-life of 8500 y and a spontaneous fission branching ratio of

6.1×10^{-7}%. The ^{245}Cm sample contains a contamination of ^{244}Cm, measured through α-particle pulse-height analysis (see Fig. 3.10 in Chapter 3), of 6.6%, consistent with the spontaneous fission rate determined at n_TOF. It is important to note that this isotope does not contribute to the results of the ^{245}Cm(n, f) reaction, since its cross-section is much lower than that of ^{245}Cm.

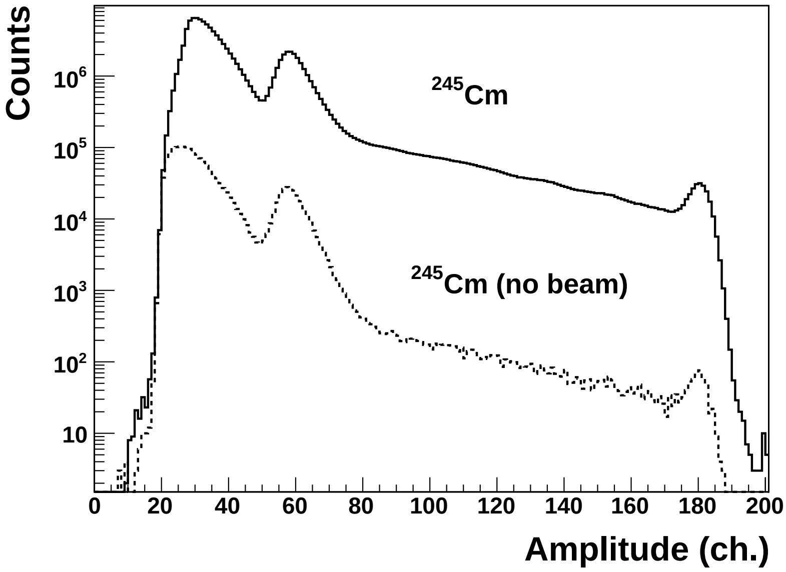

Figure 6.29 – Comparison of the pulse height distribution measured for the ^{245}Cm sample with and without the neutron beam. The presence of fission fragments signals related to the spontaneous fission of the ^{244}Cm impurity is evident in the histogram without the neutron beam.

In order to reduce the α-particles background and to maximize the number of fission fragments included in the data analysis, a threshold at FADC channel 80 has been adopted. The residual background in the neutron energy spectrum for this threshold is shown in Fig. 6.30. The black symbols represent the measured background. An exponential fit, according to formula e^{A+Bx}, where A and B are the offset and slope, respectively, has been performed (see blue line in Fig. 6.30), in order to determine this contribution. As in previous cases, the slope of the α-particle background is fixed to -1.15129. The result of the fit is then subtracted from the spectrum measured with the neutron beam. This is shown in Fig. 6.31, where the red histogram represent the fission counts after subtraction of the residual background (blue line).

After background subtraction, different corrections where applied in order to extract the fission cross-section.

A dead-time correction has been introduced, as for ^{233}U analysis, using Eq. 4.1. However due to the small counting-rate, the correction is less than 1% in the whole

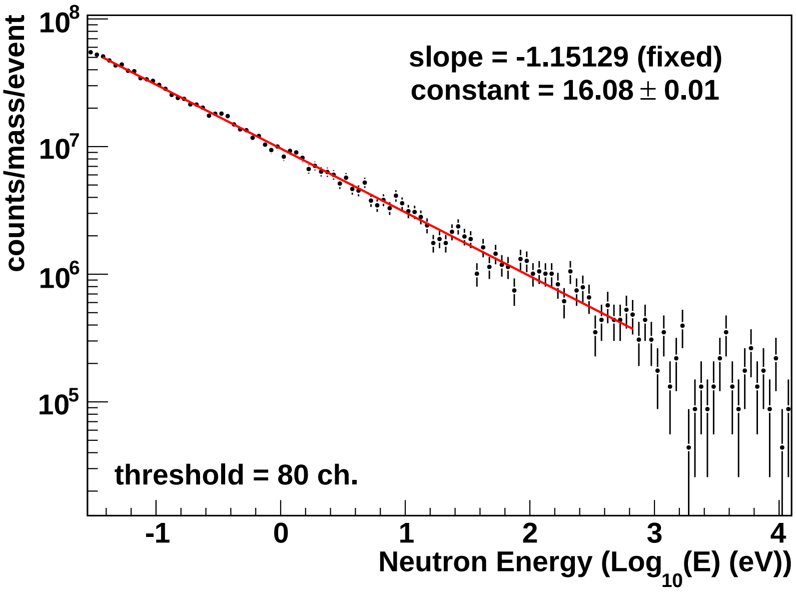

Figure 6.30 – Counts related to the α-particle background from the ^{245}Cm sample, as a function of the neutron energy (reconstructed from the time information), and for a threshold on the signals amplitude at channel 80 (black symbols). The red line represents the result of an exponential fit of the data.

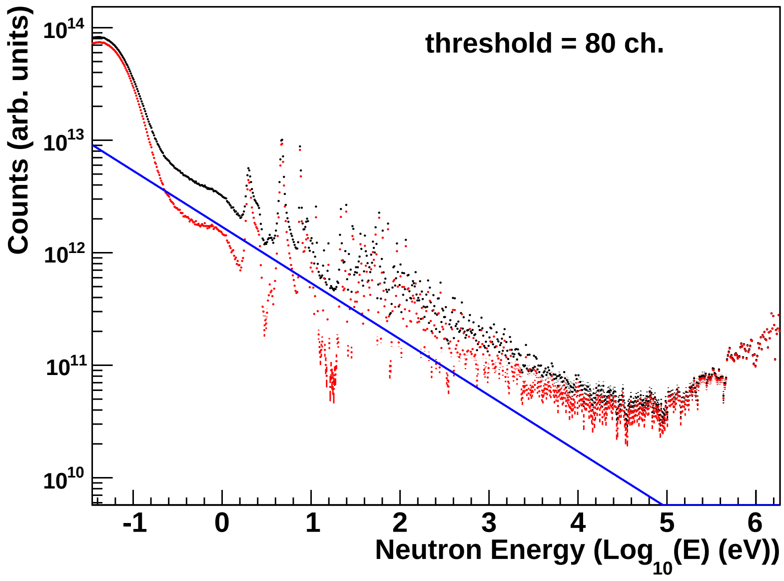

Figure 6.31 – Counts recorded in the ^{245}Cm(n, f) reaction, as a function of the neutron energy. The black symbols show the total counts, while the red ones those obtained after subtracting the α-particle background shown by the blue line. The function used in the subtraction is obtained by scaling the fit shown in the previous figure, by the number of neutron bunches in the measurement.

neutron energy range, reaching up to 1.5% at 1.5 MeV. It should be considered however that the dead-time correction is still necessary for the reference ^{235}U sample.

In principle, as it has been done for the ^{233}U case, the use of the flux extracted from the ^{235}U sample makes possible to determine the isotope cross-section without the need of further normalization. However, due to the large α-particle background and the consequent uncertainty in the value of the amplitude threshold for the ^{245}Cm(n,f) measurement, the results obtained are not very accurate in absolute value and show a large discrepancy with respect to previous data or evaluated cross-sections. In particular, the resulting cross-section are $\sim$50% lower than the evaluated libraries at low energy. The reason for such discrepancy is not clear. One explanation could be the inefficiency of the chamber due to the very high α-activity; in this case space charge effects could produce a loss of efficiency and therefore lead to a decrease of the fission yield. Another possible explanation could be related to the distortion of the amplitude distribution due to the large α-particle background, with a fraction of the distribution lost below the threshold. Due to the complex shape of the pulse height distribution, it is therefore not possible to perform accurate simulations to estimate the efficiency for the different amplitude thresholds used in the analysis of the ^{245}Cm(n,f) and ^{235}U(n,f) reactions.

In order to improve the accuracy of the present data, a normalization to previous results at thermal energy has been performed. For the ^{245}Cm(n,f) reaction, several measurements have been reported at thermal energy (see Fig. 6.32 and references therein). The present data were normalized to the value adopted in ENDF/B-VII.0, which is in agreement with the thermal value of Browne *et al.* [166], Diamond *et al.* [167] and Zhuravlev *et al.* [148] within 1σ. The ENDF/B-VII.0 data seems to have been evaluated only considering Browne *et al.* data, since other thermal measurement, Gavrilov *et al.* [168], Benjamin *et al.* [169] and Halperin *et al.* [170], in agreement between themselves within 2σ, are not in agreement with the results by Browne *et al.*. The last data has been extracted from a time-of-flight measurement, while most of the other ones are thermal reactor measurements.

Contrary to what done in the case of the ^{233}U(n,f) reaction, for ^{245}Cm(n,f) it is not straightforward to perform an extrapolation of the measured cross-sections at thermal energy since, as pointed out in the paper of Browne *et al.* [166] and confirmed in these data (see Fig. 6.35), the cross-section does not follows the $1/v$ behavior between 0.03 eV and 1 eV. For this reason, the normalization was performed at the neutron energy of 31.6 meV, which is approximately the lower limit of the energy range of the present data.

A complete evaluation of systematic uncertainties has not been performed as in the case of the ^{233}U(n,f) reaction. In the present case, due to the large α-particle

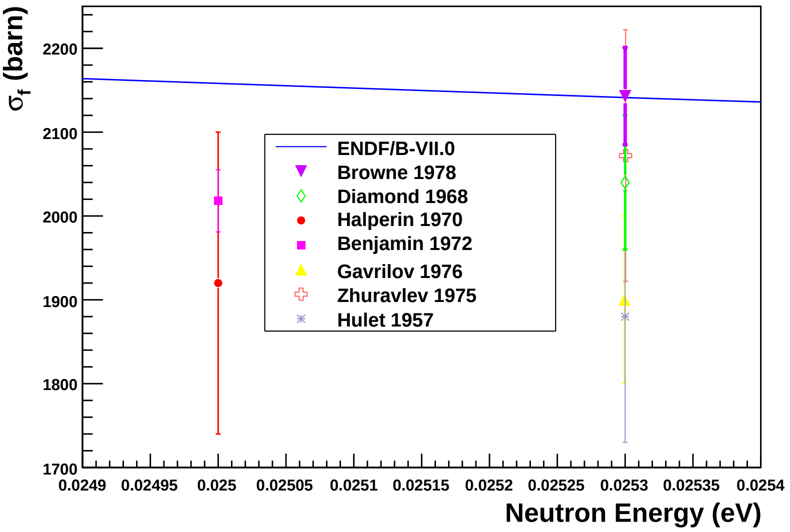

Figure 6.32 – Comparison of the ^{245}Cm(n, f) cross-section, in the thermal neutron energy region, between evaluated cross-sections of the ENDF/B-VII.0 library and previous experimental results [166, 167, 148, 169, 168, 170, 171].

background, the most significant contribution to the systematic uncertainties is due to the background subtraction (evaluated from the runs without neutron beam). The uncertainty is estimated by propagating the error in the free parameter of the fit. As expected the uncertainty depends strongly on the neutron energy: in particular, as shown in Fig. 6.33, close to the resonance peaks the effect of the background is negligible ($\leq$1%), while, as expected, in the resonance valleys the effect is greater and can reach up to 15%.

6.3.2 Comparison with evaluated libraries and previous results

Fig. 6.34 shows the n_TOF ^{245}Cm(n, f) results from nearly 30 meV up to 1 MeV, compared with the ENDF/B-VII.0 library and with previous experimental measurement. As for the ^{233}U case, this is the first time the entire energy range is covered in a single measurement. The currently known resonance parameters for ^{245}Cm are based on fission cross-section data measured from 0.01 eV up to 35 eV by Browne *et al.* [166] and, at higher energies, by Moore *et al.* [172], as described in Ref. [173]. For this isotope the evaluated cross-section in ENDF/B-VII.0 (as well as JEFF-3.1) is essentially a replica of those contained in the JENDL-3.3 database. Such evaluation is mainly based, apart for some differences in the unresolved and fast neutron region, on the work of Maslov [173]. This has been performed by using a Single-Level Breit-Wigner parametrization, so that interference effects between different levels are not accounted for. As pointed out in the paper by Browne *et al.*, this prevents the eval-

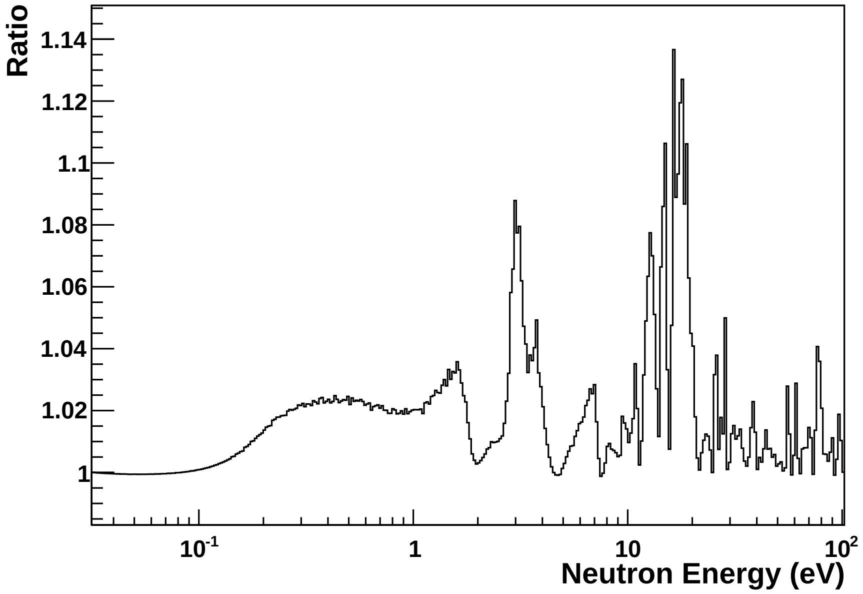

Figure 6.33 – Ratio of the ^{245}Cm(n, f) cross-section obtained using two different values of the constant parameter in the fit of the background (16.07 and 16.09). This ratio provides an indication of the systematic uncertainty associated with the background subtraction.

uated libraries from reproducing the valleys between resonances in the ^{245}Cm(n, f) cross-section, which present marked interference effects.

Fig. 6.35 shows the velocity-weighted n_TOF ^{245}Cm(n, f) data in the energy range from ∼35 meV to 10 eV separately compared with evaluated libraries (Fig. 6.35(a)) and with previous experimental data (Fig. 6.35(b)). Fig. 6.35(a) shows a comparison with ENDF/B-VII.0 and JEFF-3.0 which are essentially a replica of the evaluation performed in JENDL-3.3. Most of the features of the present results are already in the latest evaluation, although the strength and position of the main resonances are slightly different. Fig. 6.35(b) shows the comparison of the n_TOF results with previous measurements: the agreement is fairly good below 2 eV with discrepancies lower than ∼4% with Browne's data and ∼15% with White's results in the region below 0.2 eV. Above 1 eV the present data are in almost perfect agreement with White's data: the dips at 1.6 eV, 3 eV and 3.8 eV observed in Browne's and White's data, but not in the evaluation (since they are probably due to interferences effects), are also confirmed by the present work, together with the "resonance-like" structure at ≃3.45 eV. As shown in Fig. 6.36(a), this structure is not very clear in Browne's results, but evident in White's data. The present cross-sections agree also with White's data in showing an asymmetric shape of the resonance that is not reproduced by evaluations, together with a "shoulder-like" structure on the right side of the peaks for the first three most prominent resonances. It is interesting to note that the present

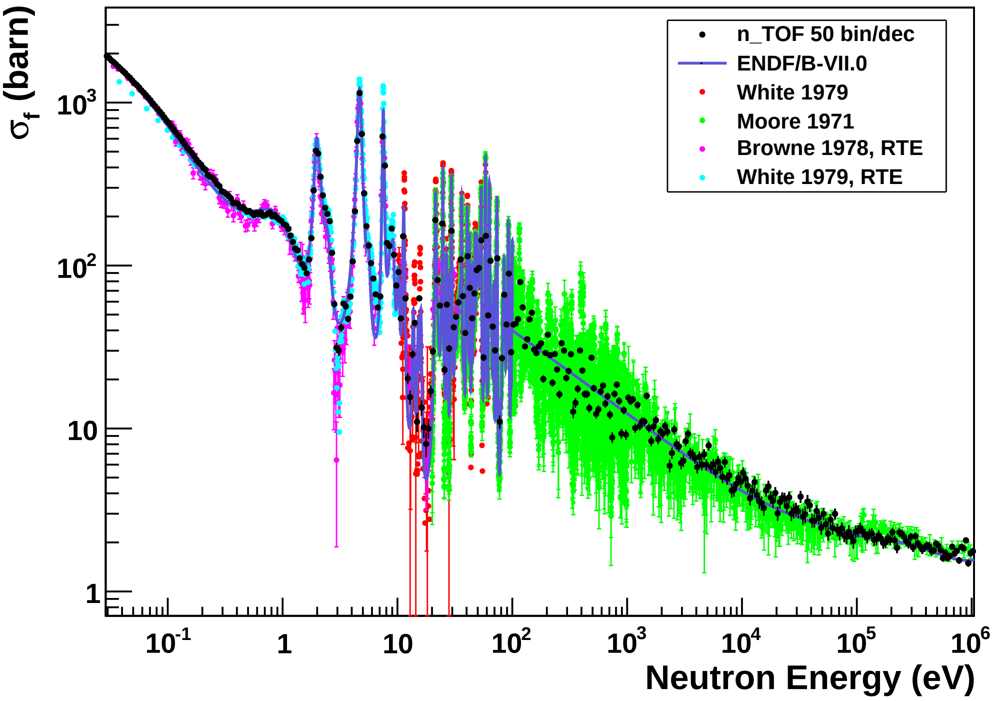

Figure 6.34 – The cross-section of the ^{245}Cm(n, f) reaction measured at n_TOF in the full energy range, compared with data from the ENDF/B-VII.0 library and from previous measurements.

results for the 4.7 eV resonance are in agreement within statistical uncertainties with ENDF/B-VII.0 and 5% higher than Browne's results, while approximately 13% lower than White's one. The situation is different for the 7.54 eV resonance, where present results and White cross-sections are $\simeq$30% higher than ENDF/B-VII.0 (and therefore relative to Browne's data), as can be clearly seen in Fig. 6.36(b).

Similar considerations regarding the discrepancies between different evaluated libraries and with experimental results can be made for the region between 9 and 17 eV, shown in Fig. 6.37. In particular, in the energy range between 15 and 17 eV, JENDL-3.3 (and therefore ENDF/B-VII.0) shows two resonances at $\simeq$15.2 and 16 eV; it is interesting to note that in previous versions of the evaluated libraries (e.g. JEFF-3.0) only one resonance was considered, centered slightly above 16 eV, while the doublet was most probably introduced in the latest evaluations. The present data clearly show the existence of a single resonance at $\simeq$15.5 eV, therefore shifted by 0.5 eV with respect to the old evaluation. This observation is also supported by the results of White *et al.* [174], which show a single resonance centered at $\simeq$15.7 eV (see Fig. 6.37(b)).

Fig. 6.38 shows the data in the energy range between 50 and 200 eV, compared with evaluated data and previous experimental results. As already mentioned [173]

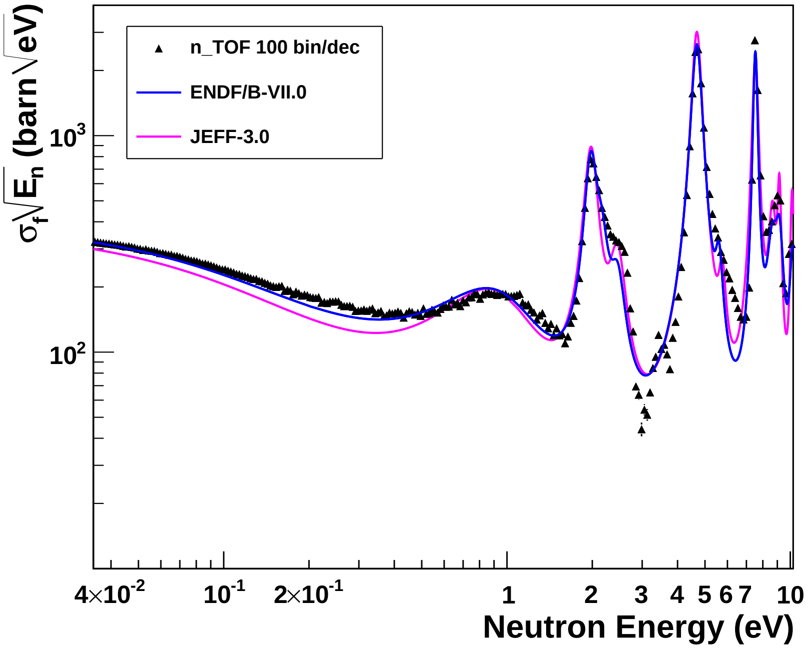

(a) Present results compared with evaluated libraries.

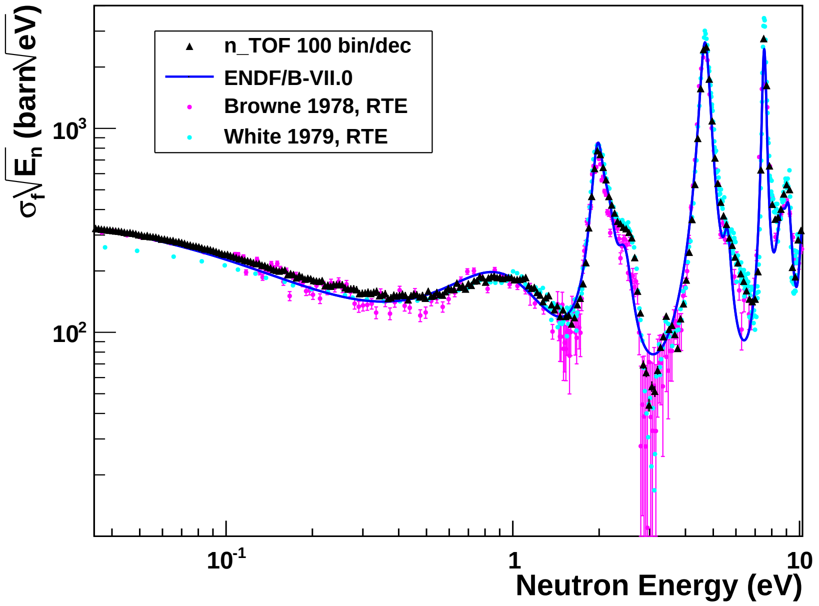

(b) Present results compared with previous measurements.

Figure 6.35 – Velocity-weighted n_TOF ^{245}Cm(n, f) cross-section in the energy range from ~35 meV to 10 eV. The results are normalized - as described in the text - to the ENDF/B-VII.0 value at 32 meV. The valleys observed around 1.5 eV and 3 eV cannot be reproduced by the single-level Breit-Wigner formalism used in the evaluations, but only via a multi-level fission analysis (not performed in this work). As claimed in Ref. [166], the fluctuations in the data by Browne *et al.* data at ~0.25 eV could be due to the resonances in the ^{241}Pu(n, f) cross-section, which is a daughter of the ^{245}Cm α-decay and is therefore present as contamination in the sample.

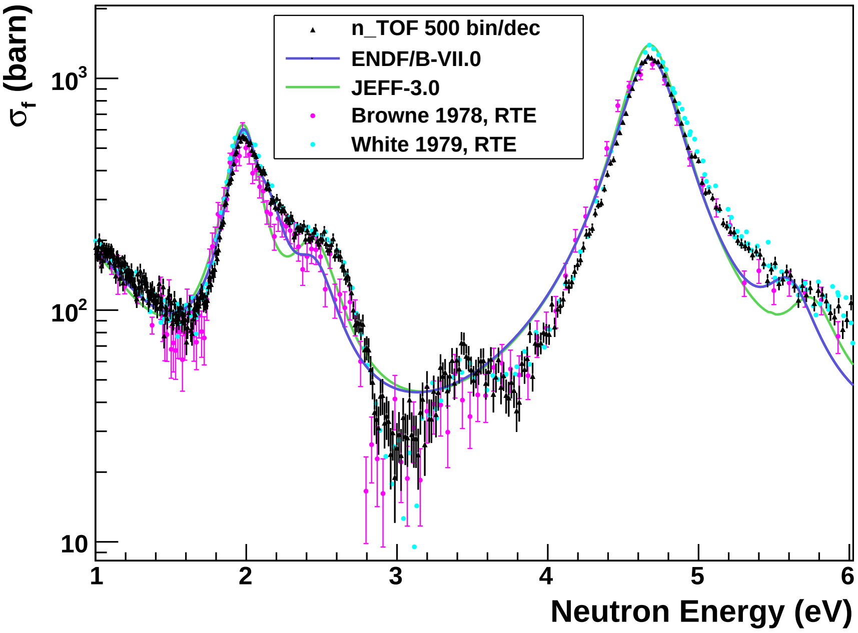

(a) ^{245}Cm(n, f) data in the neutron energy range between 1 and 6 eV.

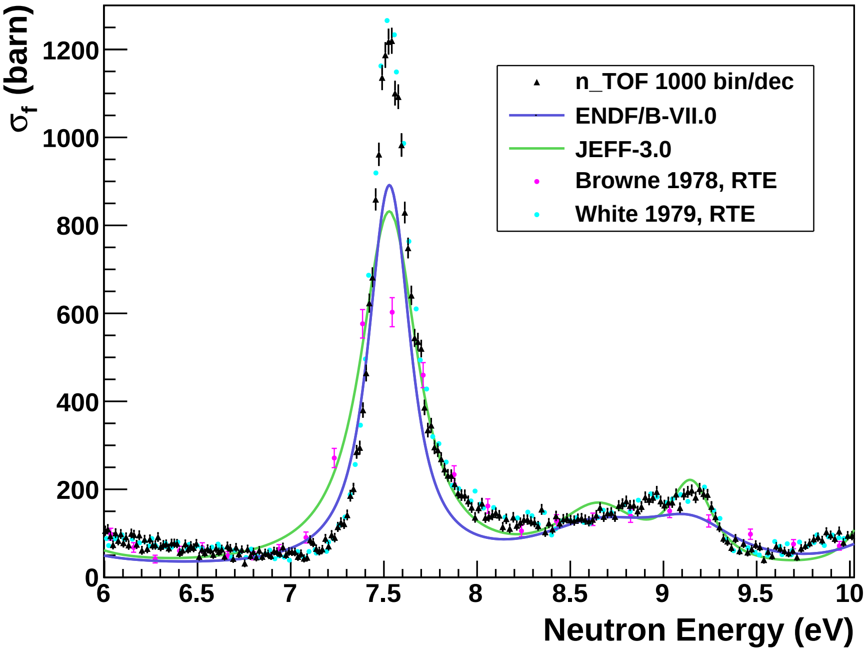

(b) ^{245}Cm(n, f) data in the neutron energy range between 6 and 10 eV.

Figure 6.36 – The first three resonances in the ^{245}Cm(n, f) cross-section, compared with evaluated data and with the results of previous measurements. Data from the JEFF-3.0 library show sizable differences with respect to ENDF/B-VII.0.

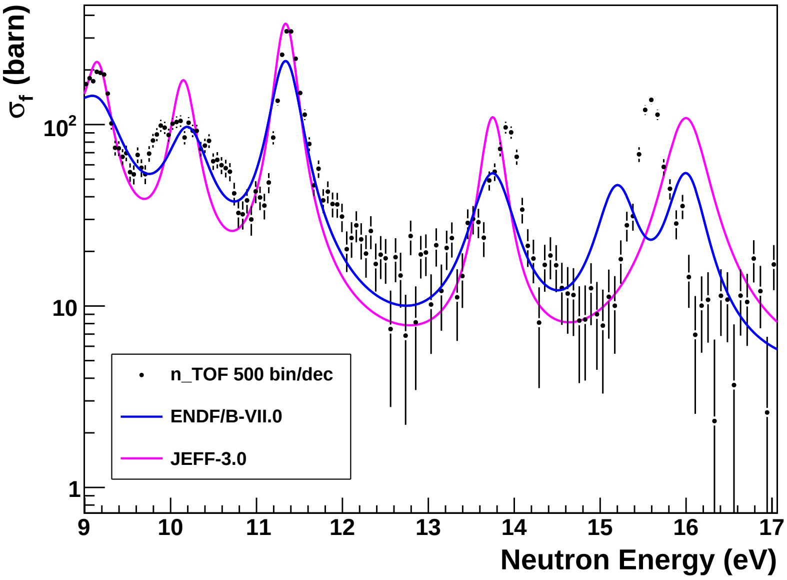

(a) Present results compared with evaluated libraries.

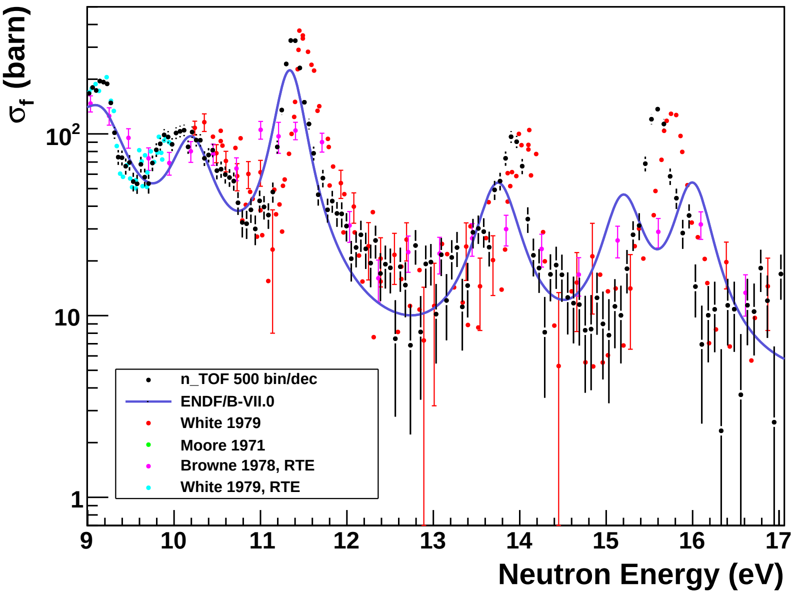

(b) Present results compared with previous measurements.

Figure 6.37 – The ^{245}Cm(n, f) cross-section from the present analysis, in the energy range between 9 eV and 17 eV. A comparison with evaluated libraries and previous experimental measurements is reported.

the JEFF-3.0 (JENDL-3.2) evaluation stops at 60 eV, while ENDF/B-VII.0 contains also the informations from the Maslov's evaluation [173]. The data by Moore *et al.*, employed for the evaluation above 20 eV, are also shown. This was up to now the measurement with the highest resolution above 10 eV, carried out in 1969 using a nuclear explosion as the neutron source. One of the advantages of nuclear explosions is the high reaction rate, consequence of the very high flux of $\sim 10^{31}$n/s, many orders of magnitude higher than possible at n_TOF or other existing neutron facilities. The extremely high flux makes very attractive the use of nuclear explosions for measurements of highly radioactive materials, since it allows to minimize sample-related background and target masses. A discussion of the use of underground nuclear explosions as neutron sources can be found in Ref. [175].

Even if the statistical uncertainties of the present work are higher than for Moore's data, is it evident from Fig. 6.38 (starting from 100 eV) and from Fig. 6.39, that n_TOF data are characterized by a higher resolution in the epithermal range.

The ratio between preliminary results for the ^{245}Cm(n, f) reaction and evaluated or experimental data - averaged over neutron energy decades - is shown in Fig. 6.40.

The n_TOF data are systematically higher by ≈10% relative to ENDF-B/VI.8 (and ENDF-B/VII.0) for low neutron energies (E_n ≤10 eV), and by 10-15% for higher energies. A similar discrepancy is also observed with respect to Moore's data. It should be remarked, however, that the observed discrepancy can be considered well within the systematic uncertainties of the current analysis. A more refined analysis is therefore needed before drawing a definite conclusion on the fission cross-section for this isotope.

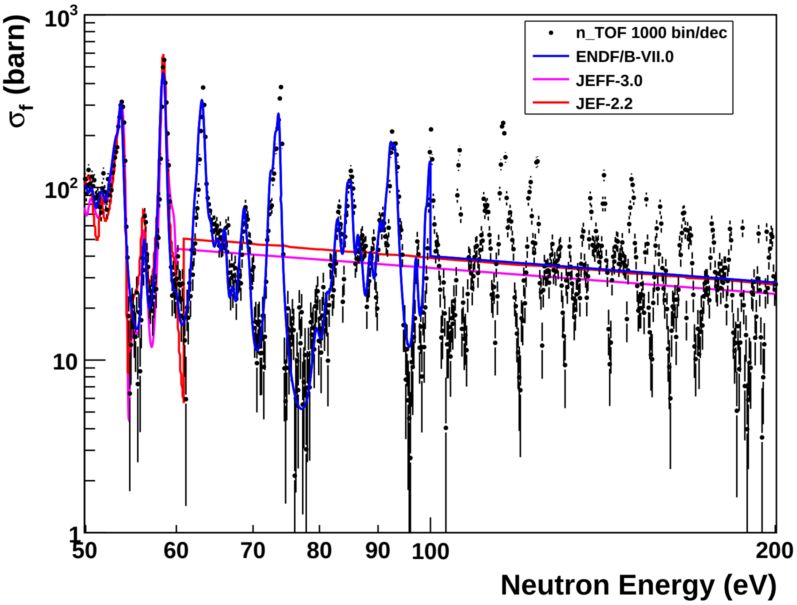

(a) Present results compared with evaluated libraries.

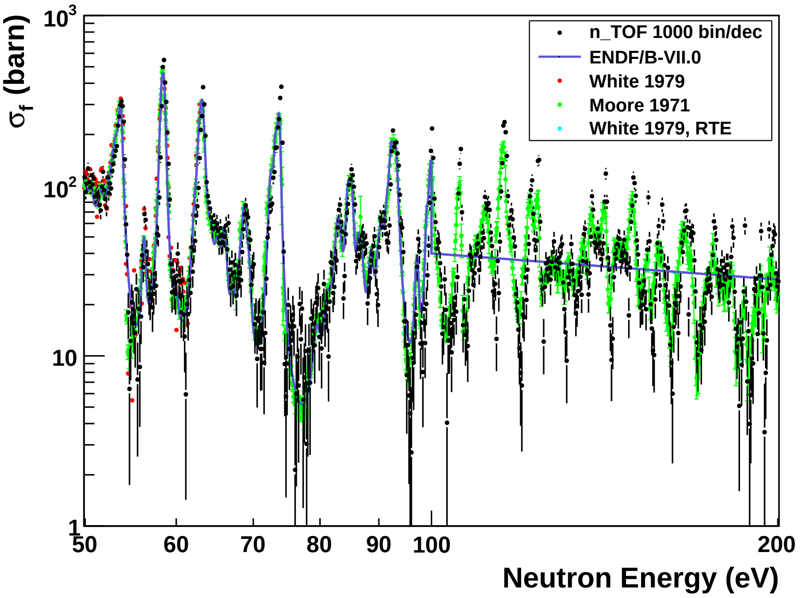

(b) Present results compared with previous measurements.

Figure 6.38 – The cross-section of the ^{245}Cm(n, f) reaction in the energy range between 50 eV and 200 eV compared with evaluated data from major libraries libraries and with previous experimental results.

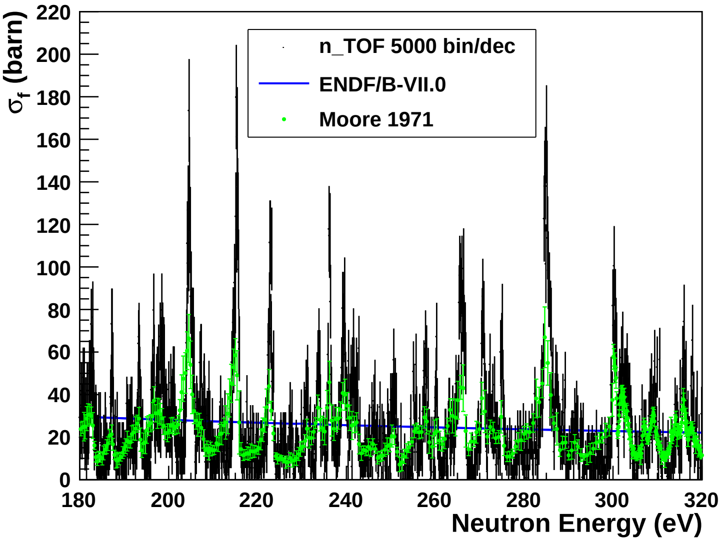

Figure 6.39 – The ^{245}Cm(n, f) cross-section measured at n_TOF in the energy range between 180 eV and 320 eV compared with data by Moore *et al.* [172]. The superior energy resolution of the n_TOF data is evident.

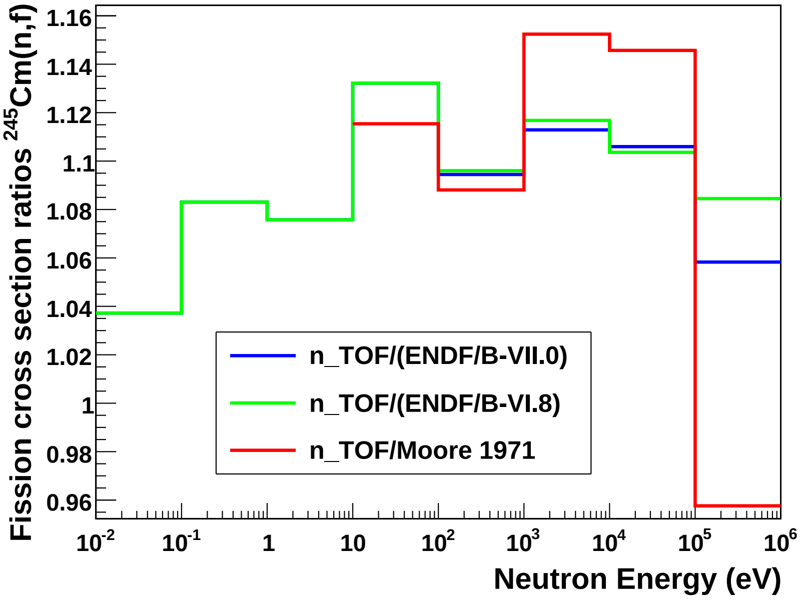

Figure 6.40 – Ratio between the n_TOF cross-section and previous data or evaluations. The cross-section from near thermal energy up to 1 MeV are averaged over the decades in the logarithm of the neutron energy.

Conclusions

The increase in the world's population and improvements in the life standards for a larger number of people is leading to a steady increase in the world's energy needs. Fossil fuels, which now represent the biggest source of energy production worldwide, may in a relatively short term become unable to fulfill the energy request, since their availability is predicted to reach a peak in a few years from now and, more importantly, the emission of CO_2 associated with their use is the main reason of the greenhouse effect and consequent climatic changes. New energy supplies have therefore to be developed, to meet in a sustainable way the future energy needs. In the longer term, natural renewable sources (like solar, wind, tides, etc.), as well as nuclear fusion may become a valid alternative to fossil fuels. In the short and medium term, however, humanity may still have to rely on nuclear energy from fission. At present, nuclear power accounts for 6% of the total energy consumption in the world, and about 15% of electricity production. It is possible that the share of nuclear energy may increase in the next few years, in particular due to new reactors coming into operation in developing countries.

At present, two issues affect the sustainable use of nuclear fission for energy production. On the longer term, the availability of uranium (at low prices) may become a limiting factor to the use of current generation reactors. The second, and more important issue, even in the short term, is the problem of nuclear waste treatment and storage, in particular the high-level radioactive waste that require geological depositories. A significant fraction of the high-level nuclear waste is constituted by minor actinides, in particular neptunium, americium and curium, built up as a result of multiple neutron captures and radioactive decays in current nuclear reactors. A possible solution to the problem of nuclear waste disposal could come from transmutation, via neutron-induced fission of transuranic elements in subcritical systems, such as an Accelerator Driven System (ADS), or in critical systems, such as future Gen-IV (fast) nuclear reactors. The possibility to incinerate nuclear waste, together with a more efficient use of the uranium resources, are the main advantages of the new generation reactors currently being developed. R&D is also being conducted on the use of lighter fuel cycles, such as the Th/U Fuel Cycle, interesting for the lower production of minor actinides, relative to current reactors based on the U/Pu cycle, for non-proliferation issues and for the relatively good availability of thorium.

In order to reduce calculation uncertainties in the design and operation of new generation reactors, high precision data on neutron-induced fission cross-sections are required for several transuranic elements, from thermal energy to several tens of MeV. In particular, a pressing need exists for new measurements of neutron-induced fission cross-section for ^{233}U, the main fissile isotope in the Th/U fuel cycle. Similarly, new and accurate data on fission cross-sections are needed for many Pu, Am and Cm isotopes, for which available data are scarce or show large discrepancies. As an example, sensitivities studies indicate that required accuracies ^{245}Cm(n,f) cross-section are of the order of $\sim$10%, far lower than presently available. Similarly, present uncertainties on fission cross-section for Am reflect in a large uncertainty in the ^{241}Am and ^{243}Am at the end of the reactor irradiation cycle, thus complicating the spent fuel management.

With the aim of improving the accuracy of current databases, the n_TOF Collaboration has performed measurements of neutron-induced fission cross-sections for ^{233}U, ^{241}Am, ^{243}Am, and ^{245}Cm, as well as for the fission standards ^{235}U and ^{238}U. The measurements, performed at the innovative neutron facility n_TOF at CERN, have allowed to collect data from thermal energy to several tens of MeV, with the full energy covered in a single measurement. Together with the wide energy range, the n_TOF facility is characterized by a very high instantaneous neutron flux (1.5×10^7 n/pulse at the measuring station with the 8 cm diameter collimator employed in fission measurements), which makes it particularly suited for measurements of radioactive targets. Other characteristics of the facility are the wide energy range, the low duty cycle (repetition rate of 0.4 Hz), the very high resolution in energy (1.1×10^{-3} at 30 keV) and a very low ambient background. All these characteristics allow the n_TOF facility to be well suited for measurements of high quality neutron cross-sections.

The subject of the present thesis is the determination of neutron-induced fission cross-sections of ^{233}U, important in the context of future Th/U fuel cycle, as well as of several actinides, ^{245}Cm, ^{241}Am and ^{243}Am, relevant for transmutation purposes and for the design of Gen-IV nuclear reactors.

The detection apparatus used in measurements is a Fast Ionization Chamber (FIC) constituted by a stack of several cells, for the simultaneous measurement of up to

16 samples. The detector's signals were acquired with a state-of-the-art acquisition system based on Flash Analog to Digital Converters (FADC) modules, which allow to minimize dead-time and pile-up problems, particularly important due to the high instantaneous flux of the n_TOF neutron beam.

The neutron-induced fission cross-sections for ^{233}U and minor actinides have been determined relative to the ^{235}U(n, f) cross-section reaction, measured simultaneously and with the same experimental setup. Since this cross-section is considered as a standard at thermal energy and between 0.15 eV and 200 MeV, there is no need of further normalization, provided that the detection efficiency for each sample is correctly taken into account. In this work, detailed simulations of the detector response have been performed, in order to determine the efficiency for the different samples, as well as the attenuation of the neutron beam in the fission chamber.

The FIC signals were analyzed off-line in order to determine the most relevant informations, in particular the signal amplitude and the neutron time-of-flight. The residual background was determined from the analysis of runs without neutron beam and subtracted from the measured fission yield. For the time-to-energy conversion, the resonances of the ^{235}U(n, f) reaction below 600 eV were used. The background related to scattered neutrons, measured by means of a ^{235}U sample mounted outside the neutron beam, was found to be negligible. The very low level of the overall background in the extracted cross-section is demonstrated by the data of the ^{235}U(n, f) reaction, which show resonance valleys comparable, or in some cases even below, evaluated data.

The ^{233}U(n, f) cross-section has been determined at n_TOF from $\simeq$30 meV to 1 MeV neutron energy, a range covered for the first time in a single measurement. On average, the present results show good agreement with previous data and evaluations from thermal neutron energy to 100 eV, although some differences are observed for the energy and strength of individual resonances. Important advantages for the present data are the high accuracy of the cross-section (systematic uncertainties slightly above 3%), the wide energy range covered and the high resolution in neutron energy, which allows to extend the R-matrix analysis of the cross-section to higher energies. Above 1 keV, the present results indicate that the evaluated cross-section in major libraries is underestimated by as much as 12% in certain energy ranges. This finding is confirmed also by another measurement performed at n_TOF with a different experimental setup. On the basis of these results, a revision of the evaluations in that energy region is called for.

Preliminary results have also been obtained for the minor actinides, ^{241}Am, ^{243}Am and ^{245}Cm, important for reliable design of ADS and Gen-IV reactors. Especially in the case of the ^{241}Am and ^{245}Cm, the significant pile-up between α-particles and between fission fragments and α-particles, makes difficult to evaluate the detection efficiency related to the threshold on the signal amplitude.

The $^{241}\mathrm{Am}(n, f)$ cross-section tabulated in evaluated databases shows significant discrepancies between themselves in the resonance region. For convenience, the present data have been normalized to the 1.27 eV resonance of Dabbs *et al.* results. The agreement with Dabbs *et al.* cross-section is pretty good in the resonance region, while significant differences exist with evaluated databases and previous experimental data, all characterized by a worse energy resolution.

The $^{243}\mathrm{Am}(n, f)$ reaction has been studied only in the region above the fission threshold (approximately 300 keV), due to a large contamination of other isotopes which contributes significantly to the cross-section in the low energy region. The present results agree with evaluations in the threshold region, and disagree with a series of measurements that reported a higher cross-section. This results could be used to solve a longstanding issue related to the discrepancies between various measurements of about 15%.

Finally, the present $^{245}\mathrm{Cm}(n, f)$ cross-section, normalized to the ENDF/B-VII.0 cross section at 31.6 meV, shows several differences relative to evaluated data in the resonance region, especially in the strength of some resonances. For the first three resonances, the present results show a cross-section in the right tail $\simeq$25% higher with respect to tabulated cross-sections from major libraries, while in agreement with previous measurements.

The preliminary results for the three minor actinides demonstrate the high quality of the data that can be obtained at n_TOF even for these very radioactive isotopes. However, a more refined analysis is still needed in order to determine the cross-section for ^{241}Am and ^{245}Cm with the accuracy required for energy applications.

In conclusion, the present thesis represents a step forward in addressing the issue of new data needed towards the development of innovative reactor systems for energy production and nuclear waste transmutation.

Appendix A

Range of fission fragments in the various components of the Fast Ionization Chamber

The efficiency of the Fast Ionization Chamber depends primarily on the range of fission fragments in the sample deposits. Furthermore, it is important to know under which conditions the fission fragments are completely stopped inside the gas cell and, finally, if there is the possibiliy that some of them could punch through the Al electrodes and produce a signal in a contiguous gas cell, giving rise to a cross-talk and being counted twice.

In order to evaluate the range of FFs in the various components of the fission chamber, as a function of their mass and kinetic energy, the SRIM-2008 code [176] was used. The code is well suited for calculations of the energy loss of heavy ions in materials, and it is based on a quantum mechanical treatment of ion-atom collisions. Figure A.1 shows the range of a Sr ion inside a deposit of U_3O_8. The energy of the ion is considered up to the maximum expected in a fission reaction. The thickness of the deposit used in the present measurement is indicated by the horizontal line. The calculations indicate that fragments emitted perpendicular to the sample deposit, or at smaller angles relative to the normal of the plane, are not stopped inside the deposit (even for a reduced kinetic energy), as expected.

The range in the gas cell (at a pressure close to 1 atm), is shown for two fission fragments in Figure A.2. The horizontal line represents the width of the individual gas cells in the FIC1 and FIC2 detectors used in the present measurement. The results of the SRIM calcuations show clearly that heavy ions release only a small fraction of their energy inside the chamber. Although their masses are quite different, this fraction is approximately the same for the two considered fission fragments (Br and

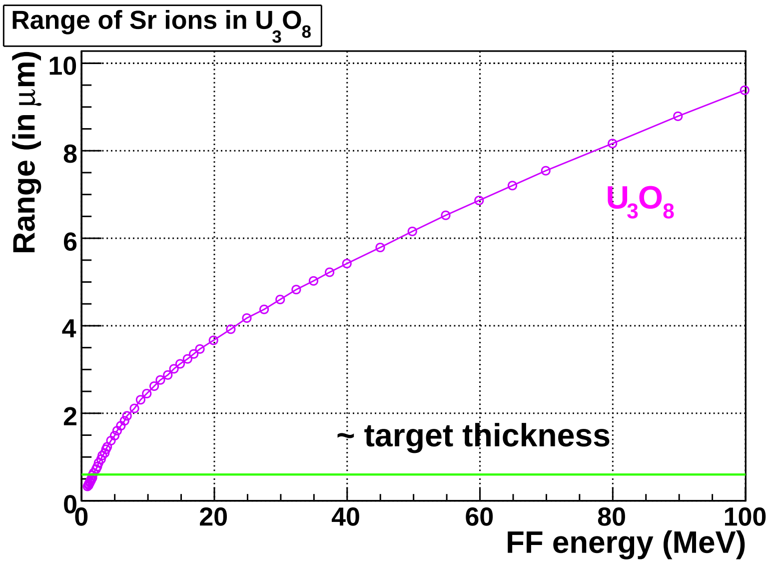

Figure A.1 – Range of Sr ions as a function of their kinetic energy in U_3O_8, as calculated with the SRIM-2008 code [176].

Sr), thus explaining the absence of a two-peak structure in the spectrum of signal amplitude obtained with FIC1 and FIC2. The structure would appear instead for a larger gap width (such as 20 mm, the case of FIC0), since in that case FFs would release in the gas a much larger fraction of their total kinetic energy, or would be even stopped in the gas.

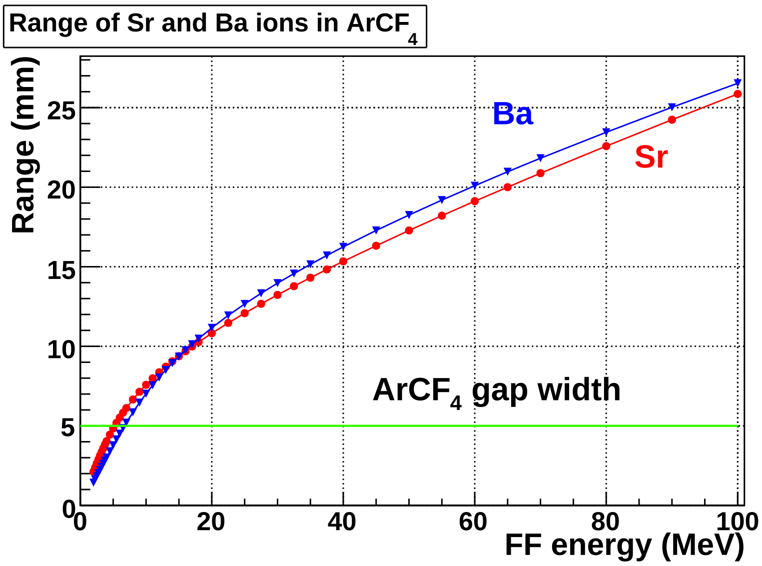

Figure A.2 – Range of Sr and Ba ions as a function of their kinetic energy in $ArCF_4$ at the pressure of 720 mbar, as calculated with the SRIM-2008 code [176].

Finally, SRIM calculations for the range of FFs in the Al electrodes are shown in Figure A.3. The horizontal line represent the thickness of the electrodes used in the FIC chambers. From the calculations it turns out that the possibility that fission fragments cross the gap between two contiguous gas cells is excluded, since, at all energies typical of a fission reaction, the FFs are stopped inside the electrode. Even if some fission fragments with higher energy cross the aluminum electrode, their residual energy would be very small, thus falling below the threshold used in the analysis routine.

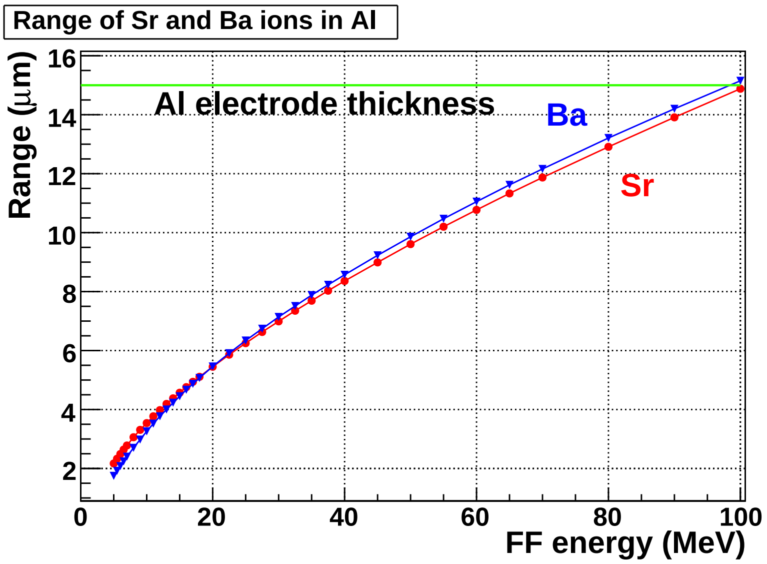

Figure A.3 – Range of Sr and Ba ions as a function of their kinetic energy in Al, as calculated with the SRIM-2008 code [176].

Appendix B

Units of the neutron flux

For historical reasons, the neutron flux at various time-of-flight facilities is often represented in the so-called *lethargy* units. The lethargy is a convenient variable in treating neutron slowing down, and it is defined as:

$$u = ln\left(\frac{E_0}{E}\right)$$

Here E_0 is a defined neutron energy, which is different for different applications[1]. It is found that for any given scattering material the average logarithmic energy loss per collision independent of the energy, as it is equal to the lethargy defined before. In other words, in collisions with specified target nuclei, a neutron always loses, on the average, the same fraction of the energy it had before collision. It is worth noticing that a gain in lethargy is a loss in energy.

For a moderated neutron source, as in the n_TOF case, the advantage of representing the flux in lethargy units (i.e. in the natural logarithm of the energy) resides in the fact that in this case the obtained distribution is flat (or isolethargic); at n_TOF the flux has an isolethargic behavior from 0.2 eV up to 300 keV. When necessary, the flux in energy units can be easily determined from the isolethargic flux, starting from the relations between the infinitesimal energy interval dE, $d\ln(E)$ and $d\log(E)$.

Since:

$$\ln E = \ln(10^{\log E}) \qquad \text{or} \qquad \ln E = \ln 10 \times \log E$$

and

$$d\ln E = \frac{dE}{E}$$

one obtains that

$$d\log E = \frac{d\ln E}{\ln 10} = \frac{dE}{E} \times \ln 10$$

---

[1] As an example, 10 MeV for reactor applications.

From the last relation, it is straightforward to obtain the following, assuming that dn is the number of neutrons per energy interval:

$$\frac{dn}{d\log E} = \frac{dn}{d\ln E} \times \ln 10 = \frac{dn}{dE} \times E \times \ln 10$$

In other words, it is then possible to go from the number of neutrons per energy interval $\left(\frac{dn}{dE}\right)$ to the number of neutron per lethargy unit $\left(\frac{dn}{d\ln E}\right)$ by multiplying the first quantity by the energy value E, while the number of neutron per energy decade $\left(\frac{dn}{d\log E}\right)$, is obtained by multiplying $\left(\frac{dn}{d\ln E}\right)$ by a constant equal to $\ln 10$.

Appendix C

Pulse shape routine

The first step in the analysis of the fission data consists in the reconstruction of signals produced in the FIC detectors and recorded with the Flash-ADC. This step is fundamental in order to extract informations on the signal amplitude and on the neutron time-of-flight. To this end, a detailed pulse shape analysis can be performed. In the present work, a simpler and more time-efficient solution has been adopted, based on a C++ class already present in the ROOT library [89]. The method relies on the use of the advanced Spectra Processing Function class TSpectrum, developed by M. Morháč and repackaged as a C++ class by R. Brun, which allows to perform one-dimensional background estimation, smoothing, deconvolution and peak searching on input data. In order to describe the performance of the routine, some examples of FIC raw data, to which the routine has been applied, are here shown. For each neutron bunch, a large number of digitized signals are stored on tape. In Fig. C.1 an example of the 80 ms "movie" for a single neutron bunch in FIC1 is presented. A close-up view of a selected time window, with clear fission fragment signals, is shown in Fig. C.2.

The baseline estimation function allows to separate the low frequency component from the peaks, and to take into account the variation of the baseline as a function of time (which could affect the fission fragments detection efficiency if not properly considered). The methods is based on the Sensitive Nonlinear Iterative Peak clipping algorithm, described in Ref. [90]. Assuming that the raw data are stored in the vector $v(i)$, the routine calculates iteratively the vectors $v_1(i)$, $v_2(i)$ up to $v_m(i)$, where the index m refers to the iteration number. The new value of the i^{th} element of the vector in the p^{th} iteration step $v_p(i)$ is obtained by taking the average of the values $v_{p-1}(i-p), v_{p-1}(i+p)$ and comparing it with the value $v_{p-1}(i)$, both of them belonging to the previous iteration step. The new $v_p(i)$ value is then given by the minimum of

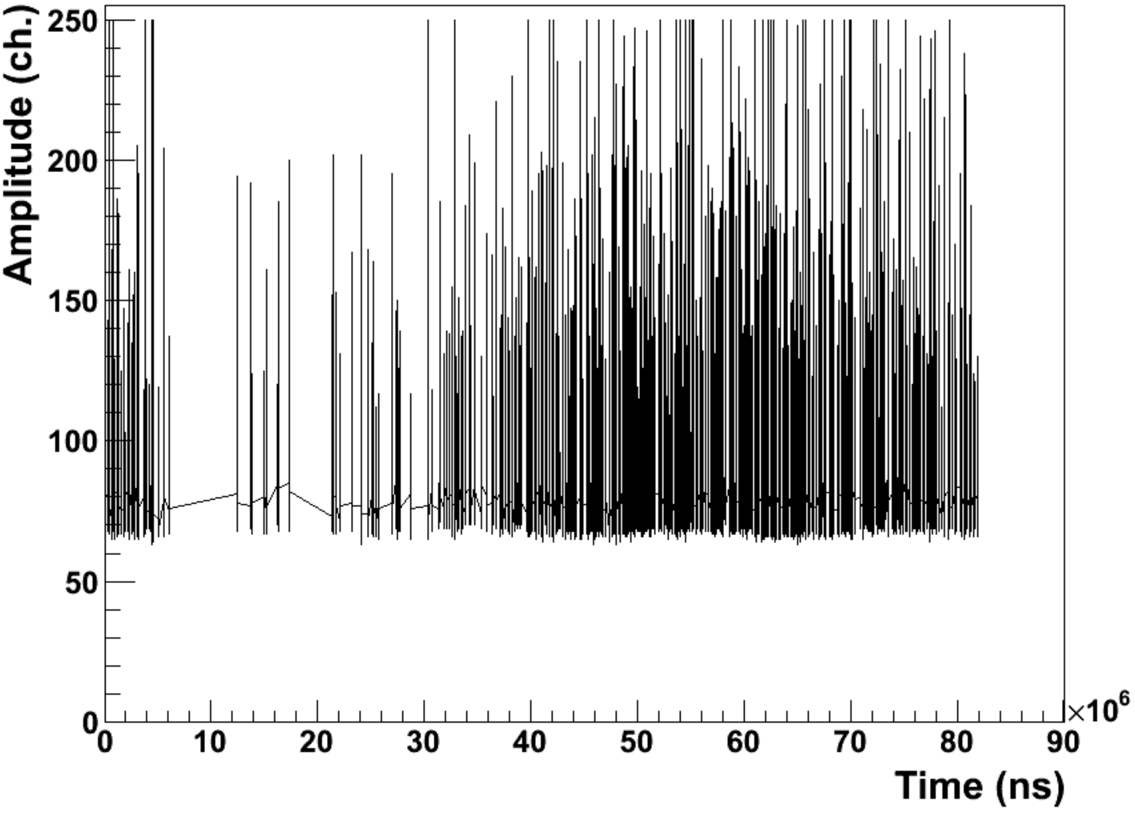

Figure C.1 – Full raw data "movie" for a single neutron bunch in FIC1, for a ^{235}U sample. The line connecting different clusters of data is an artifact of the plotting procedure.

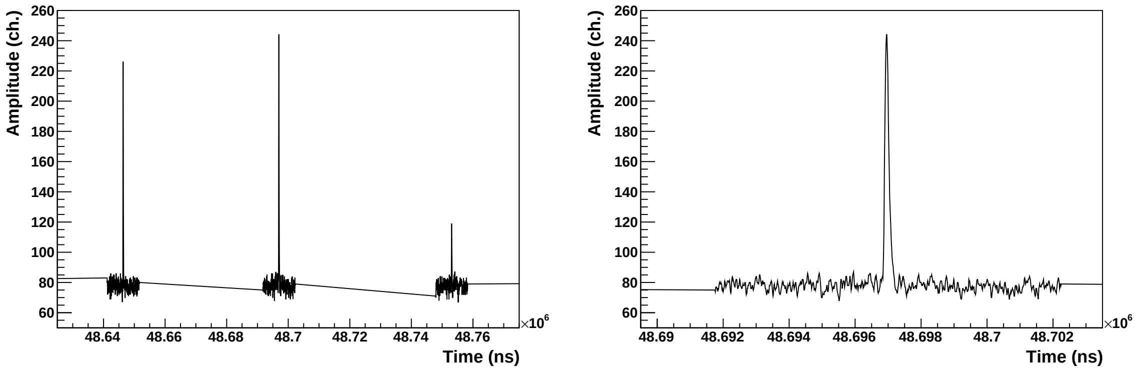

(a)

(b)

Figure C.2 – Same as Fig. C.1, but in a restricted time window.

these two values:

$$v_p(i) = min\left(v_{p-1}(i), \left(\frac{v_{p-1}(i+p) + v_{p-1}(i-p)}{2}\right)\right)$$

The resulting baseline spectrum obtained in this way is then subtracted from the original histogram, in order to obtain pure signals without any offset. In the present work a number of iteration steps equal to 50 has been adopted; this has been determined as the optimal value that allows to take into account slow variations of the baseline, while excluding local oscillations.

The peak-searching routine allows to determine the position and amplitude of peaks in a spectrum, in the presence of a background and statistical fluctuations (i.e. noise). The algorithm is based on the comparison between the smoothed second derivatives of the signals and its standard deviation, as described in Ref. [92, 177, 93]. The method assumes that near the maximum the signal is convex, so that its second derivative is negative, with a minimum around the maximum of the peak; additionally the value of the second derivative at the peak position must be significantly different from its standard deviation in order to initiate the peak-searching procedure.

As input, the user has to introduce the value of the standard deviation (σ) of the searched peaks. After determining the peak position, the routine compares the value of the peak (i.e. the signal amplitude) to the average between the signal values at $\pm 3\sigma$ from the peak position. If the peak value is greater than a predefined threshold, the peak position and value are retained as the amplitude and time of the signal. Otherwise the peak is ignored. In the present case the σ has been chosen by trial and error so to optimize the selection of fission fragments. The chosen value corresponds to 100 ns, which, with good approximation, represent the width of fission fragments signals.

The routine is applied on a compressed raw data spectrum, i.e. without the gaps between signals caused by the zero-suppression algorithm in the Data Acquisition System. This minimizes the number of elements in the vector corresponding to a single neutron bunch (since the "movie" is 80 ms long, with a sampling rate of 10 ns, this would result in a vector of 8×10^6 elements), and therefore reduces the time needed for data processing. The graphs showing the outcome of the peak and background searching appear as a continuous "movie" without the same gaps observed in Figg. C.1 and C.2.

The identification of the γ-flash position t_γ is made on the first saturated signal of a neutron bunch, as observed in Fig. C.3. In this case, the selection criterion is much simpler, due to the rapid rise and long saturation time interval, and is based only on the crossing of a high threshold (in this case around FADC channel 100).

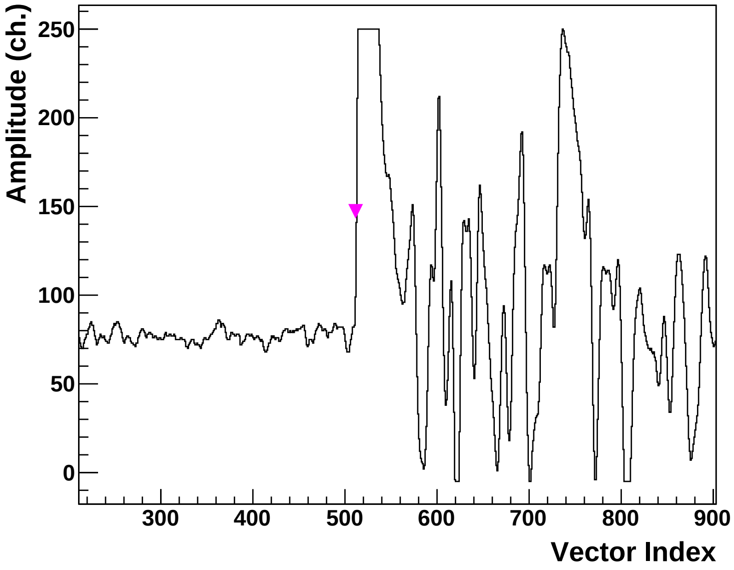

Figure C.3 – Raw data representing the γ-flash signal with identification of the t_γ position (shown by the purple marker).

As for the baseline determination, an example of the results obtained for the ^{233}U and ^{241}Am sample, for a selected time interval, is shown in Fig. C.4 as a red line. The different signal-to-α-background condition for the two cases is evident in the figure. Since the rate of signals due to fission fragments from the ^{241}Am sample is small (due to the small mass used), while the α activity is high, the number of signals due to α-particles is overwhelming with respect to fission fragment signals.

The peak searching routine acting on a baseline-subtracted spectrum for the ^{233}U sample is shown in Fig. C.5: the threshold on the signal's amplitude in the identification routine is set around FADC channel 20, corresponding to a value where only α-particle are present. As can be seen in the figure, all peaks below this value are not identified. A close-up view of fission fragments signal is shown in Fig. C.5(b).

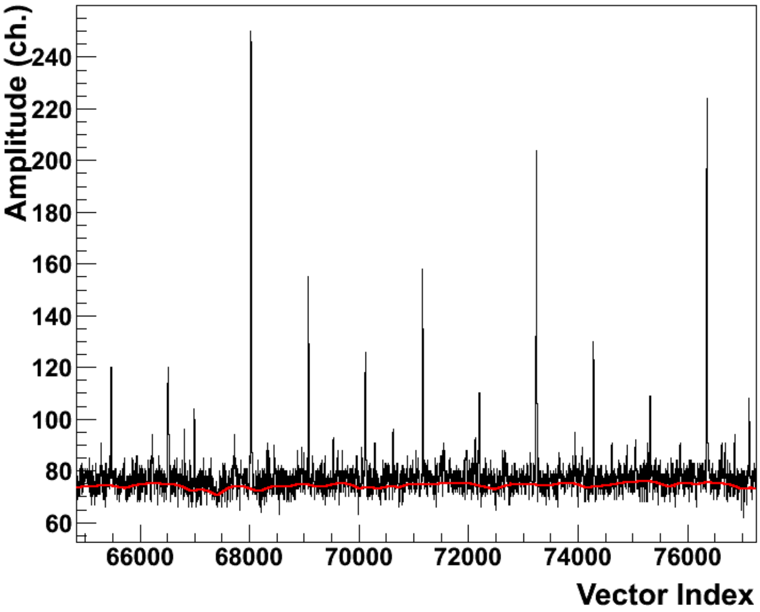

(a) ^{233}U sample.

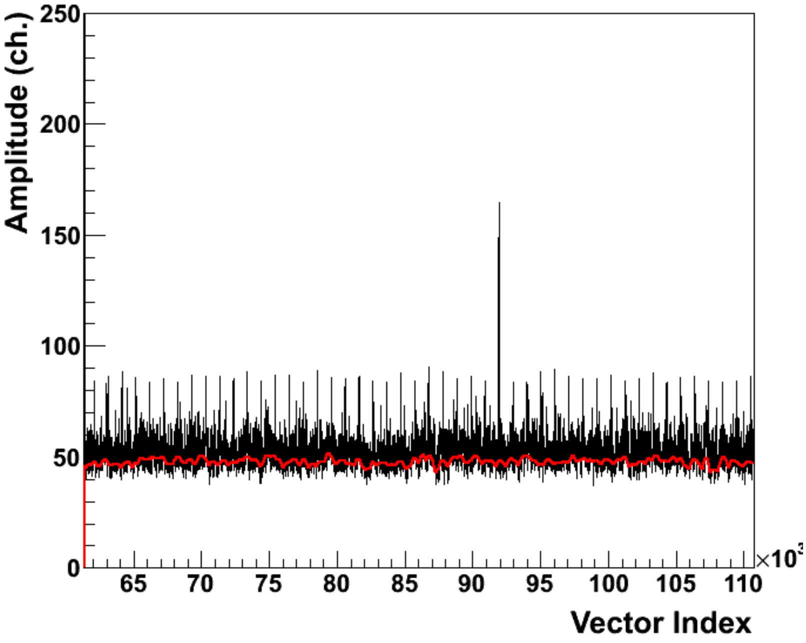

(b) ^{241}Am sample.

Figure C.4 – Raw data (shown sequentially) for a selected time interval of a neutron bunch, for a ^{235}U (C.4(a)) and a ^{241}Am (C.4(b)) sample. The baseline determined by the analysis routine is also shown. The small number of fission fragments relative to α particles for the ^{241}Am sample is evident.

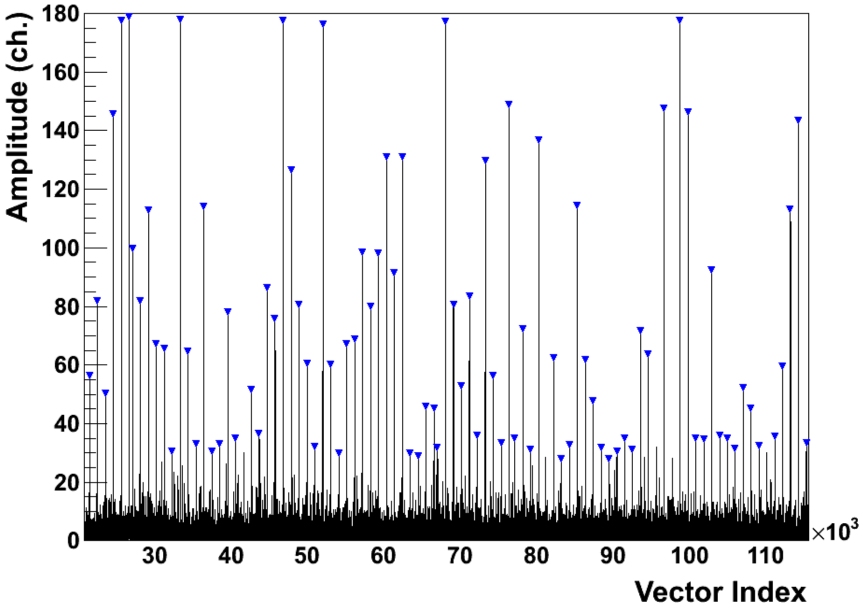

(a)

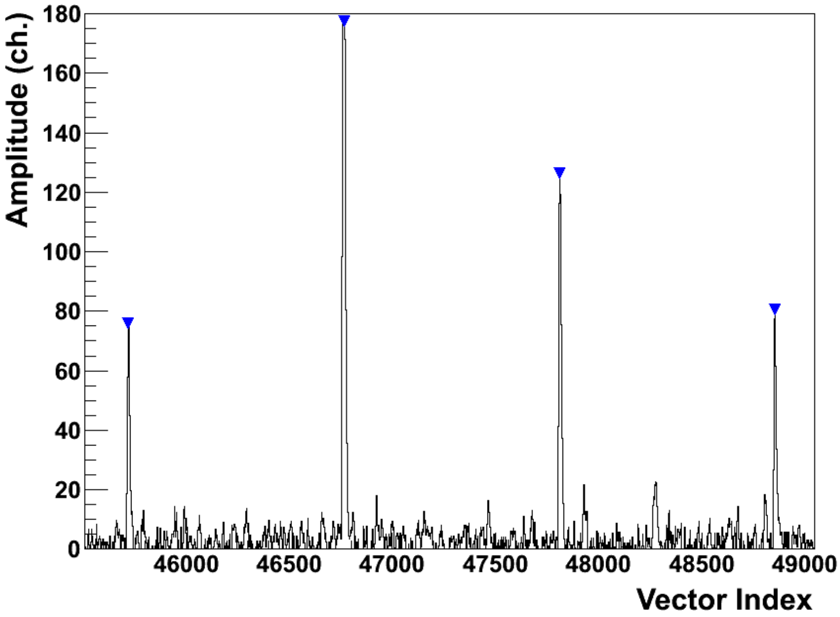

(b)

Figure C.5 – Raw data (shown sequentially) for a selected time interval of a neutron bunch, after the original baseline subtraction. The positions and amplitudes of each individual signal, as determined by the analysis routine, is also shown.

List of Figures

List of Tables

Bibliography

[1] IAEA (International Atomic Energy Agency), Power Reactor Information System (PRIS), `http://www.iaea.org/programmes/a2/`.

[2] H. NIFENECKER, O. MEPLAN AND S. DAVID. *Accelerator Driven Subcritical Reactors* (Institute of Physics Publishing, 2003).

[3] COMMISARIAT À L'ÉNERGIE ATOMIQUE (CEA). *Mémento sur l'Énergie, Edition 2007* (CEA, 2007).

[4] INTERNATIONAL ENERGY AGENCY. *Key World Energy Statistics* (International Energy Agency (IEA), 2007 edition).

[5] US DEPARTMENT OF ENERGY NUCLEAR ENERGY RESEARCH ADVISORY COMMITTEE AND GENERATION IV INTERNATIONAL FORUM . *Technology Roadmap for Generation IV Nuclear Energy Systems* (US DOE, 2002).

[6] INTERNATIONAL ENERGY AGENCY. *Renewables in Global Energy Supply* (International Energy Agency (IEA), 2007 edition).

[7] NUCLEAR ENERGY AGENCY (NEA). *Risks and Benefits of Nuclear Energy* (NEA-OECD, 2007).

[8] UK ENERGY RESEARCH CENTRE (UKERC). *The Costs and Impacts of Intermittency:An assessment of the evidence on the costs and impacts of intermittent generation on the British electricity network.* (UKERC, 2006).

[9] NUCLEAR ENERGY AGENCY (NEA). *Accelerator Driven Systems (ADS) and Fast Reactors (FR) in Advanced Nuclear Fuel Cycles* (NEA-OECD, 2002).

[10] NUCLEAR ENERGY AGENCY (NEA). *Actinide and Fission Product Partitioning and Transmutation, Status and Assessment Report* (NEA-OECD, 1999).

[11] G. ALIBERTI, G. PALMIOTTI, M. SALVATORES, T. K. KIM, T. A. TAIWO, M. ANITESCU, I. KODELI, E. SARTORI, J. C. BOSQ, J. TOMMASI. Nuclear Data Sensitivity, uncertainty and target accuracy assessment for future nuclear systems. *Ann. Nucl. En.*, **33**, (2006) 700–733.

[12] G. ALIBERTI, G. PALMIOTTI, M. SALVATORES AND C. G. STENBERG. Impact of Nuclear Data Uncertainties on Transmutation of Actinides in Accelerator-Driven Assemblies. *Nucl. Sci. Eng.*, **146**, (2004) 13–50.

[13] M. DAHLFORS, Y. KADI, A. HERRERA-MARTÍNEZ. *Ann. Nucl. En.*, **34**, (2007) 824–835.

[14] JOHN R. LAMARSH, ANTHONY J. BARATTA. *Introduction to Nuclear Engineering* (Prentice Hall, 2001, Third Edition).

[15] DAVID BODANSKY. *Nuclear Energy, Principles, Practices, and Prospects* (Springer, 2nd edition, 2004).

[16] WESTON M. STACEY. *Nuclear Reactor Physics* (Wiley Interscience, 2001).

[17] J. CARSON MARK. Reactor-Grade Plutonium's Explosive Properties. *Technical report*, Nuclear Control Institute (NCI), 1990.

[18] NUCLEAR REGULATORY COMMISSION (NRC). NRC Regulations Title 10, Code of Federal Regulations. United States.

[19] T. MUKAIYAMA. Motivation and Programs for Trasmutation of Nuclear Waste. Otto Hahn Summer School 2002 Lectures, CEA - Cadarache, France, 2002.

[20] IAEA, NUCLEAR FUEL CYCLE AND MATERIAL SECTION. Thorium Fuel Cycle - Potential Benefits and challenges - IAEA-TECDOC-1450. *Technical report*, IAEA, International Atomic Energy Agency, 2005.

[21] THE N_TOF COLLABORATION. Measurements of Fission Cross Sections for the Isotopes relevant to the Thorium Fuel Cycle, 2001. CERN-INTC-2001-025.

[22] V. JAGANNATHAN AND U. PAL. *Energy Conversion and Management*, **47**, (2006) 2781–2793.

[23] OKAN H. ZABUNOGLU, TAHIR AKBAS. *Nucl. Eng. Des.*, **213**, (2003) 77–86.

[24] S. GANESAN. A review of the current status of nuclear data for major and minor isotopes of thorium fuel cycle. *International Topical Meeting on Advances in Reactor Physics and Mathematics and Computation into the Next Millennium, Pittsburgh, Pennsylvania, USA.* (2000).

[25] NATIONAL RESEARCH COUNCIL. *Nuclear Wastes, Technologies for Separations and Transmutation, Report of the Committee on Separations Technology and Trasmutation Systems* (National Academy Press, Washington, DC, USA, 1996).

[26] B. PFEIFFER AND K. KRATZ. *Prog. Nucl. En.*, **41**, (2002) 39.

[27] ANSALDO NUCLEARE. Energy Amplifier Demonstration Facility reference configuration: Summary Report - EA-B0.000-1-200, Rev.0. *Technical report*, Ansaldo Nucleare, 1999.

[28] `http://nuclear.energy.gov/genIV/neGenIV1.html`.

[29] Operating Experience With Nuclear Power Stations in Member States in 2007. *Technical report*, IAEA - International Atomic Energy Agency, 2007.

[30] VICTORIA MCLANE. EXFOR Basics, A Short Guide to the Nuclear Reaction Data Exchange Format. *Technical report*, International Atomic Energy Agency, 2005. `http://www-nds.iaea.org/exfor/exfor00.htm`.

[31] EMPIRE 2.19 Nuclear Reaction Model Code - `http://www.nndc.bnl.gov/empire219/`.

[32] TALYS Nuclear Reaction Code - `http://www.talys.eu/`.

[33] M. B. CHADWICK, P. OBLOŽINSKÝ, M. HERMAN *et al.* ENDF/B-VII.0: Next Generation Evaluated Nuclear Data Library for Nuclear Science and Technology. *Nucl. Data Sheets*, **107**(12), (2006) 2931–3118.

[34] ARJAN KONING, ROBIN FORREST, MARK KELLET, ROBERT MILLS, HANS HENRIKSSON, YOLANDA RUGAMA. JEFF-3.1 Nuclear Data Library. 2006. ISBN 92-64-02314-3.

[35] KEIICHI SHIBATA, TOSHIHIKO KAWANO, TSUNEO NAKAGAWA, OSAMU IWAMOTO, JUN-ICHI KATAKURA, TOKIO FUKAHORI, SATOSHI CHIBA, AKIRA HASEGAWA, TORU MURATA, HIROYUKI MATSUNOBU, TAKAAKI OHSAWA, YUTAKA NAKAJIMA, TADASHI YOSHIDA, ATSUSHI ZUKERAN, MASAYOSHI KAWAI, MAMORU BABA, MAKOTO ISHIKAWA, TETSUO ASAMI, TAKASHI WATANABE, YUKINOBU WATANABE, MASAYUKI IGASHIRA, NOBUHIRO YAMAMURO, HIDEO KITAZAWA, NAOKI YAMANO AND HIDEKI TAKANO. Japanese Evaluated Nuclear Data Library Version 3 Revision-3: JENDL-3.3. *Journal of Nuclear Science and Technology*, **39**(11), (2002) 1125–1136.

[36] A.I.Blokhin et al. Current Status of Russian Evaluated Neutron Data Libraries. *Conf. on Nucl. Data for Sci. and Technol., Gatlinburg, Tennessee, USA*, page 695 (1994).

[37] M. Herman. ENDF-6 Formats Manual. *Technical Report BNL-NCS-44945-05-Rev.*, Brookhaven National Laboratory, 2005.

[38] Los Alamos National Laboratory. The NJOY Nuclear Data Processing System, Version 91. *Technical report*, 1994.

[39] NEA. Present Status of Minor Actinide Data - NEA/WPEC-8. *Technical report*, OECD/NEA, 1999.

[40] ENDF/B-VII.0 library descriptive comments.

[41] INDC International Nuclear Data Committee. Summary Report of the Consultants' Meeting on Assessment of Nuclear Data Needs for Thorium and other Advanced Cycles - INDC(NDS)-408. *Technical report*, IAEA, 1999.

[42] Adonai Herrera-Martínez. *Transmutation of Nuclear Waste in Accelerator-Driven Systems*. Ph.D. thesis, Department of Engineering, University of Cambridge, 2004.

[43] INDC International Nuclear Data Committee. EVALUATED NUCLEAR DATA FOR TH-U FUEL CYCLE - INDC(NDS)-494. *Technical report*, IAEA, 2006.

[44] B. D. Kuzminov, V. N. Manokhin. STATUS OF NUCLEAR DATA FOR THE THORIUM FUEL CYCLE. *Technical report*, Institute of Physics and Power Engineering, Obninsk, 1998.

[45] `http://www.cern.ch`.

[46] Commisariat à l'Énergie Atomique (CEA). *CLEFS CEA - N.46. Technical report*, 2002.

[47] A. J. Cole et al. *Phys. Rev. C*, **36**, (1987) 1484 – 1488.

[48] Y. Kadi and J. P. Revol. Design of Accelerator-Driven System for the Destruction of Nuclear Waste. *Accelerator-Driven Systems for Energy Production and Waste Incineration: Physics, Design and Related Nuclear Data* (2002).

[49] U. Abbondanno *et al. n_TOF Performance Report, CERN/INTC-O-011, INTC-2002-037*, 2002.

[50] C. Carrapiço, S. Andriamonjie, E. Berthoumieux and F. Gunsing. Proposal for an air-cooled tungsten spallation target for the n_TOF facility at CERN. *Technical report*, Commisariat à l'Énergie Atomique (CEA), 2006.

[51] D. Nio et al. *J. Nucl. Mat.*, **343**, (2005) 163–168.

[52] N. Takenaka et al. *J. Nucl. Mat.*, **343**, (2005) 169–177.

[53] D. Cano-Ott et al. Evaluation of the status of the irradiated n_TOF spallation target. n_TOF Collaboration Meeting, Bari, Italy, 2007.

[54] The n_TOF Collaboration. Proposal: European Collaboration For High-Resolution Measurements of Neutron Cross-Sections between 1 eV and 250 MeV. *Technical report*, CERN/SPSC 99-8, 1999.

[55] C. Borcea et al. *Nucl. Instr. and Meth. A*, **513**, (2003) 524–537.

[56] The n_TOF Collaboration. Study of the Background in the Measuring Station at the n_TOF Facility at CERN: Sources and Solutions. *Technical report*, CERN/INTC 2001-038, 2001.

[57] A. Fassó, A. Ferrari, J. Ranft, and P. R. Sala. FLUKA: a multi-particle transport code. *Technical report*, CERN-2005-10 (2005), INFN/TC_05/11, SLAC-R-773, 2005.

[58] F. Carminati et al. TARC General purpose Monte Carlo. *Technical report*, CERN/LHC/EET 96-011, 1996.

[59] Y. Kadi. The EA-MC Monte Carlo Code Package. *Proceedings of the Fifth International Meeting on Simulating Accelerator Radiation Environment - SARE5: Models and Codes for Spallation Neutron Sources* (2000).

[60] MCNPX Version 2.5.0 User's Manual, LA-CP-05-0369, April 2005.

[61] A. Ferrari et al. FLUKA for CNGS. 6th International Workshop on Neutrino Beams and Instrumentation.

[62] J. Pancin et al. *Nucl. Instr. and Meth. A*, **524**, (2004) 102–114.

[63] I. Savvidis et al. *Radiation Measurements*, **42**, (2007) 1492–1498.

[64] H. Arnould et al. *Phys. Lett. B*, **458**.

[65] D. Rochman et al. *Nucl. Instr. and Meth. A*, **550**, (2005) 397–413.

[66] C. Coceva, M. Frisoni, M. Magnani, A. Mengoni. *Nucl. Instr. and Meth. A*, **489**, (2002) 346–356.

[67] A. Ferrari, C. Rubbia and V. Vlachoudis. A Comprehensive Study of the n_TOF Background. *Technical report*, SL-EET Note 2001-036, 2001.

[68] N. M. Larson. Updated Users' Guide for SAMMY: Multilevel R-matrix Fits to Neutron Data Using Bayes' Equations. *Technical report*, ORNL/TM-9179/7, Oak Ridge National Laboratory, Oak Ridge, TN, USA - ENDF-364/R1, 2006.

[69] P. Koehler. Nuclear Facilities and Instrumentation. Presentation at the Nuclear Physics and Related Computational Science R&D for Advanced Fuel Cycles Workshop, August 10-12, 2006, Bethesda, Maryland.

[70] Walid Dridi. *Mesure de la section efficace de capture neutronique de l'^{234}U à n_TOF au CERN pour les réacteurs nucléaires de Génération IV*. Ph.D. thesis, Universite d'Evry Val D'Essonne, Ecole Doctorale Sitevry, 2006.

[71] A. Borella et al. Advances in neutron-induced resonance reaction cross section studies at GELINA. *Conf. on Nucl. Data for Sci. and Technol., Nice, France*, page 547 (2007).

[72] Y. Danon. Cross Section Measurements and Analysis at Rensselaer, 2005. Report at the CSEWG meeting 2005.

[73] Con Beausang, Michael Dunn and Bob Haight. Nuclear Data Measurement Facilities for Supporting Advanced Fuel Cycle Basic Science Research Needs. Presentation at the Nuclear Physics and Related Computational Science R&D for Advanced Fuel Cycles Workshop, August 10-12, 2006, Bethesda, Maryland.

[74] M. G. Holloway and C. P. Baker. Note on the origin of the term "barn". *Technical Report 523*, Los Alamos Research Report, LAMS 523, 1947.

[75] Frank Gunsing. Neutron Resonance Spectroscopy. *Technical report*, DAPNIA-05-345, CEA, 2005.

[76] `http://www-nds.iaea.org/standards/Data/endf-6-format/std-092_U_235.endf`.

[77] `http://www-nds.iaea.org/standards/Data/endf-6-format/std-092_U_238.endf`.

[78] Kenneth S. Krane. *Introductory Nuclear Physics* (John Wiley & Sons, 1988).

[79] ANTHONY FODERARO. *The Elements of Neutron Interaction Theory* (The MIT Press, 1971).

[80] U. ABBONDANNO ET AL. *Nucl. Instr. and Meth. A*, **538**, (2005) 692–702.

[81] `http://www.acqiris.com/`.

[82] *CERN Advanced STORage manager website*, `http://www.cern.ch/castor`.

[83] *Central Data Recording website*, `http://www.cern.ch/cdr`.

[84] M. CALVIANI *et al. Nucl. Instr. and Meth. A*, **594**, (2008) 220–227.

[85] L. V. DRAPCHINSKY *et al. Nucl. Instr. and Meth. A*, **438**, (1999) 116–118.

[86] L. V. DRAPCHINSKY *et al. Nucl. Instr. and Meth. A*, **303**, (1991) 19–23.

[87] J. W. BEHRENS. *Nucl. Instr. and Meth.*, **200**, (1982) 67–70.

[88] V. KETLEROV *et al.* Preliminary Results of (n,f) Measurements at CERN n_TOF with FIC0 and FIC1 Detectors, 2004. n_TOF Winter School, Flachau.

[89] ROOT, An Object-Oriented Data Analysis Framework. `http://root.cern.ch`.

[90] C. G. RYAN *et al. Nucl. Instr. and Meth. B*, **34**, (1988) 396.

[91] C. V. HAMPTON *et al. Nucl. Instr. and Meth. A*, **353**, (1994) 280.

[92] M. A. MARISCOTTI *et al. Nucl. Instr. and Meth.*, **50**, (1967) 309.

[93] M. MORHÁČ *et al. Nucl. Instr. and Meth. A*, **443**, (2000) 108.

[94] N. COLONNA ET AL. *in preparation*.

[95] A. FERRARI AND P. SALA. The FLUKA radiation transport code and its use for space problems, 2000. Presentation at the 1^{st} International Workshop on Space Radiation Research.

[96] G. D. ADEEV *et al. Technical report*, Preprint INR 861/93, 1993.

[97] STEPHEN S. FRIEDLAND. *Phys. Rev.*, **84**, (1951) 75–77.

[98] G. LORUSSO *et al. Nucl. Instr. and Meth. A*, **532**, (2004) 622–630.

[99] G. F. KNOLL. *Radiation Detection and Measurements, 2nd edition* (Wiley, New York, 1989).

[100] G. AERTS *et al.* (THE N_TOF COLLABORATION). *Phys. Rev. C*, **73**, (2006) 054610.

[101] S. MARRONE *et al.* *Nucl. Instr.and Meth. A*, **517**, (2004) 389.

[102] N_TOF Beam Profile FLUKA utility: `http://pceet075.cern.ch/Tools/Profile/profile.r`.

[103] F. D. BROOKS *et al.* A.E.R.E Harwell Reports, No.1670.

[104] M. G. CAO *et al.* *Journ. Nucl. En.*, **22**, (1968) 211.

[105] A. J. DERUYTTER AND C. WAGEMANS. *Journ. Nucl. En.*, **25**, (1971) 264.

[106] R. GWIN *et al.*. *Nucl. Sci. Eng.*, **88**, (1984) 37.

[107] K. G. IGNATEV *et al.*. *Atomnaya Energiya*, **16**, (1964) 110. Issue 2.

[108] M. S. MOORE. *Phys. Rev. C*, **18**, (1978) 1328.

[109] C. WAGEMANS *et al.* *Conf. on Nucl. Data for Sci. and Technol.*, page 91 (Mito, Japan, 1988).

[110] C. WAGEMANS *et al.* *Conf. on Nucl. Data for Sci. and Technol.*, page 961 (Knoxville, USA, 1979).

[111] C. D. BOWMAN *et al.* *Neutron Cross-Section Techn. Conf.*, page 1004 (Washington, USA, 1966).

[112] VAN SHI-DI *et al.* *Atomnaya Energiya*, **19**, (1965) 43. Issue 1.

[113] F. J. SHORE *et al.* *Physical Review*, **112**, (1958) 191.

[114] G. DE SAUSSURE *et al.* *Nuclear Data For Reactors Conf.*, page 233 (Paris, France, 1966).

[115] G. AUDOUIN *et al.* (THE N_TOF COLLABORATION). Neutron-induced fission cross sections measurements at n_TOF. *Conf. on Nucl. Data for Sci. and Technol.*, page 421 (Nice, France, 2007).

[116] L. TASSAN-GOT *et al.* (in preparation).

[117] O. A. SHCHERBAKOV *et al.* Neutron induced fission of ^{233}U, ^{238}U, ^{232}Th, ^{239}Pu, ^{237}Np, ^{nat}Pb and ^{209}Bi relative to ^{235}U in the energy range $1-200$ MeV. *Interaction of Neutrons with Nuclei*, page 288 (2001).

[118] P. W. LISOWSKI *et al.* Fission cross sections ratios for ^{233,234,236}U relative to ^{235}U from 0.5 to 400 MeV. *Conf. on Nucl. Data for Sci. and Technol.*, page 732 (1991).

[119] J. W. BEHRENS AND G. W. CARLSON. *Nucl. Sci. Eng.*, **63**, (1977) 250.

[120] R. NOLTE *et al.* Measurement of ^{235}U, ^{238}U, ^{209}Bi and ^{nat}Pb fission cross sections using quasimonoenergetic neutrons with energies from 30 to 150 MeV. *Conf. on Nucl. Data for Sci. and Technol.* (Tsukuba, Japan). J. Nucl. Sci. Technol. Suppl. 2 (2002) 311314.

[121] R. NOLTE *et al.* Cross Sections for Neutron-Induced Fission of ^{235}U, ^{238}U, ^{209}Bi, and ^{nat}Pb in the Energy Range from 33 to 200 MeV Measured Relative to n-p Scattering. *Nucl. Sci. Eng.*, **156**, (2007) 197–210.

[122] J. W. MEADOWS AND C. BUDTZ-JORGENSEN. The fission fragment angular distributions and total kinetic energies for 235-U(n,f) from .18 to 8.83 MeV. *Conf. on Nucl. Data for Sci. and Technol.*, page 740 (Antwerp, Belgium, 1982).

[123] D. L. SHPAK *et al.* Angular anisotropy of fragments from U-233 fission induced by 0.02 - 6.38 MeV neutrons. *Yadernaya Fizika*, **61**, (1998) 1436.

[124] JEFF-3.1 library descriptive comments.

[125] K. H. GUBER *et al.* *Nucl. Sci. Eng.*, **135**, (2000) 141.

[126] K. H. GUBER *et al.* *Nucl. Sci. Eng.*, **139**, (2001) 111–117.

[127] L. C. LEAL, H. DERRIEN, J. A. HARVEY, K. H. GUBER, N. M. LARSON AND R. R. SPENCER. R-Matrix Resonance Analysis and Statistical Properties of the Resonance Parameters of 233U in the Neutron Energy Range from Thermal to 600 eV. *Technical Report ORNL/TM-2000/372*, Oak Ridge National Laboratory, 2001.

[128] C. WAGEMANS *et al.* Subthermal Fission Cross-Section Measurements for 233U, 235U and 239Pu. *Conf. on Nucl. Data for Sci. and Technol.*, page 91 (Mito, Japan, 1988).

[129] L. W. WESTON *et al.* *Nucl. Sci. Eng.*, **42**, (1970) 143.

[130] A. J. DERUYTTER AND C. WAGEMANS. *Nucl. Sci. Eng.*, **54**, (1974) 423.

[131] V. A. PSHENICHNYJ *et al.* *Yaderno-Fizicheskie Issledovaniya Reports*, **21**, (1976) 29.

[132] M. S. MOORE, M. G. MILLER AND O. D. SIMPSON. *Phys. Rev.*, **118**, (1960) 714.

[133] M. G. CAO *et al.* *Journal of Nuclear Energy*, **24**, (1970) 111.

[134] L. W. WESTON *et al.* *Nucl. Sci. Eng.*, **34**, (1968) 1.

[135] S. NIZAMUDDIN AND J. BLONS. *Nucl. Sci. Eng.*, **54**, (1974) 116.

[136] P. W. LISOWSKI *et al.* Fission cross sections ratios for 233, 234, 236U relative to 235U from 0.5 to 400 MeV. *Conf. on Nucl. Data for Sci. and Technol.*, page 732 (Juelich, Germany, 1991).

[137] J. W. MEADOWS. *Nucl. Sci. Eng.*, **54**, (1974) 317.

[138] G. W. CARLSON AND J. W. BEHRENS. *Nucl. Sci. Eng.*, **66**, (1978) 205.

[139] B. I. FURSOV, V. M. KUPRIJANOV AND G. N. SMIRENKING. *Atomnaya Energiya*, **44**, (1978) 236.

[140] D. L. SHPAK. *Physics of Atomic Nuclei*, **61**, (1998) 1333.

[141] A. J. DERUYTTER, C. WAGEMANS. *Nucl. Sci. Eng.*, **54**, (1974) 423.

[142] H. DERRIEN. *J. Nucl. Sci. Technol.*, **31**, (1994) 379.

[143] J. BLONS. *Nucl. Sci. Eng.*, **51**, (1973) 130.

[144] R. GWIN *et al.* *Nucl. Sci. Eng.*, **59**, (1976) 79.

[145] W. P. POENITZ. Absolute Measurement of the ^{233}U(n,f) Cross Section Between 0.13 and 8 MeV. (ANL/NDH-36).

[146] F. B. GUIMARAES, L. C. LEAL, H. DERRIEN AND N. M. LARSON. Test of "Pseudo" Resonance Representation in the keV Range for 235U for Self-Shielding Parameters Calculation, 2000.

[147] J. W. T. DABBS, C. H. JOHNSON AND C. E. BEMIS JR. *Nucl. Sci. Eng.*, **83**, (1983) 22–36.

[148] K. D. ZHURAVLEV, N. I. KROSHKIN AND A. P. CHETVERIKOV. *Atomnaya Energiya*, **39**, (1975) 285.

[149] S. YAMAMOTO, K. KOBAYASHI, M. MIYOSHI, I. KIMURA, I. KANNO, N. SHINOHARA AND Y. FUJITA. Fission cross-section measurements of 241Am between 0.1eV and 10 keV with lead slowing-down spectrometer and at Thermal Energy. *Nucl. Sci. Eng.*, **126**, (1997) 201.

[150] V. F. GERASIMOV. *Yadernaya Fizika*, **4**, (1966) 985.

[151] C. D. BOWMAN, M. S. COOPS, G. F. AUCHAMPAUGH, S. C. FULTZ. Subthreshold neutron-induced fission cross section of Am241. *Phys. Rev.*, **137**, (1965) B326.

[152] B. R. LEONARD JR AND E. J. SEPPI. Subthreshold Fission - Np237 and Am241. *Bulletin of the Am. Phys. Soc.*, **4**, (1959) 31.

[153] C. WAGEMANS *et al. Nucl. Sci. Eng.*, **101**, (1989) 201.

[154] H.-H. KNITTER AND C. BUDTZ-JØRGENSEN. *Nucl. Sci. Eng.*, **99**, (1988) 1.

[155] P. A. SEEGER. *Technical Report 4420 (138)*, Los Alamos Scientific Lab. Reports, 1970.

[156] K. KOBAYASHI, T. KAI, S. YAMAMOTO, H.-J. CHO, Y. FUJITA, I. KIMURA AND N. SHINOARA. *Journ. for. Nucl. Sci. and Tech.*, **36**, (1999) 20–28.

[157] Y. KIKUCHI. *Technical Report JAERI-M-82-096*, Japan Atomic Energy Research Institute, 1982.

[158] H. MAST, R. EYKENS, J. PAUWELS AND C. WAGEMANS. 243Am Targets for Nuclear Fission Experiments: Requirements and Realisation. *Nucl. Instr. and Meth. A*, **282**, (1989) 107–109.

[159] A. LAPTEV *et al.* Neutron-Induced Fission Cross Sections of 240-Pu, 243-Am, and Nat-W in the Energy Range 1-200 MeV. *Conf. on Nucl. Data for Sci. and Technol.*, page 865 (Santa Fe, USA, 2004).

[160] J. W. BEHRENS AND J. C. BROWNE. Measurement of the Neutron-Induced Fission Cross Sections of Americium-241 and Americium-243 Relative to Uranium-235 from 0.2 to 30 MeV. *Nucl. Sci. Eng.*, **77**, (1981) 444.

[161] M. AÏCHE *et al.* Quasi-absolute neutron-induced fission cross section of 243Am. *Conf. on Nucl. Data for Sci. and Technol.*, page 186 (Nice, France, 2007).

[162] P. TALOU, T. KAWANO AND P. G. YOUNG. Improved Evaluations of Neutron-Induced Reactions on Americium Isotopes. *Nucl. Sci. Eng.*, **155**, (2007) 84–95.

[163] W. YOUNES, H. C. BRITT AND J. A. BECKER. Estimated (n,f) Cross Sections for Np-236,236m,237,238,Pu-237,237m, and Am-240,241,242,242m,243,244,244m Isotopes. *Technical Report UCRL-TR-201913*, Lawrence Livermore National Laboratory, 2004.

[164] D. ROCHMAN, M. HERMAN, P. OBLOŽINSKÝ AND M. SIN. *Nucl. Sci. Eng.*, **154**, (2006) 280–293.

[165] D. ROCHMAN, M. HERMAN, P. OBLOŽINSKÝ. Modeling and Fission Cross Sections for Americium. *Technical Report BNL-74667-2005*, Brookhaven National Laboratory, 2005.

[166] C. BROWNE *et al.* *Nucl. Sci. Eng.*, **65**, (1978) 166.

[167] H. DIAMOND *et al.* *Journal of Inorganic and Nuclear Chemistry*, **30**, (1968) 2553.

[168] V. D. GAVRILOV *et al.* *Atomnaya Energiya*, **41**, (1975) 185.

[169] R. W. BENJAMIN *et al.* *Nucl. Sci. Eng.*, **41**, (1972) 203.

[170] J. HALPERIN, J. H. OLIVER AND R. W. STOUGHTON. The fission thermal-neutron cross section and resonance integral of 245Cm, 247Cm, and 249Cf. *Technical Report ORNL-4581,37,197009*, ORNL - Oak Ridge National Laboratory, 1979.

[171] E. K. HULET *et al.* *Phys. Rev. C*, **107**, (1957) 1294.

[172] M. S. MOORE *et al.* *Phys. Rev. C*, **3**, (1971) 1656.

[173] V. M. MASLOV *et al.* EVALUATION OF NEUTRON DATA FOR CURIUM-245. *Technical Report INDC-BLR-003*, 1995.

[174] R. M. WHITE *et al.* Fission cross sections of 245Cm from 1e-3 to 1e-4 eV. *Conf. on Nucl. Data for Sci. and Technol.*, page 496 (Knoxville, USA, 1979).

[175] B. C. DIVEN. Nuclear Explosions as a Nuclear Physics Tool. *Annu. Rev. Nucl. Sci.*, **20**, 79–104.

[176] JAMES F. ZIEGLER. The Stopping and Range of Ions in Matter, SRIM-2008, 2008. `http://www.srim.org`.

[177] Z. K. SILAGADZE. A new algorithm for automatic photopeak searches. *Nucl. Instr. and Meth. A*, **376**, (1996) 451.

Acknowledgments

This work has been made possible by the almost daily help of Nicola Colonna, who guided me in the context of neutron research and in particular of neutron-induced fission reactions during the course of these three years. He taught me the importance of working with dedication and patience, trying always to overcome the difficulties, that were not always related to analysis and technical issues, and to focus the work in the right direction, adjusting the natural proclivity of the author to diverge. This experience has been useful also for my everyday experience of life. During this period I took advantage of his experience in neutron physics, detectors and electronics to acquire knowledge and a work method that I didn't had before. His careful reading and correction of the present thesis has also allowed to improve the readability and fluency of this manuscript. The residual errors and typos are only due to myself. My frequent visits to Bari have also allowed me to discover and live this nice city and its surroundings.

Many thanks also to my Supervisor, Giovanna Montagnoli, who believed in my work and that gave many useful suggestions during these three years.

Thanks also to Pierfrancesco Mastinu for hosting me at LNL, for the help provided during the Ph.D. and for the comments and advices on this manuscript.

I have also to thank several n_TOF Collaboration members, for the help and the good environment created during many analysis meetings and "social" activities. Paolo Cennini is worth mentioning for the always warm welcoming at CERN, for the time he spent replying to my questions and for sharing his vast experience in experimental and technical methods. I'm grateful to Vasilis Vlachoudis for many analysis suggestions during these years, especially for the part related to FLUKA simulations and for the hints given at the beginning of this work. A special thanks also to Franz Käppeler for his continuous encouragements and for his punctual and very fast corrections and suggestions. I'm also indebted to the scientific support and to the friendly environment established with Frank Gunsing and Eric Berthoumieux;

I hope it could continue also in the future. During these years Alberto Mengoni provided many scientific advices that proved to be decisive for the advancing of this work, especially for the ^{233}U(n, f) analysis. Other members of the Collaboration are also worth of a warm thank: Laurent Tassan-Got, Daniel Cano-Ott, Carlos Paradela, Carlos Guerrero, Samuel Andriamonje and Ralf Plag, for their reception and kindliness. Thanks also to Francesco Cerutti for the hospitality during many CERN visits and for the help provided with FLUKA.

During my visit at Dubna, Russia, I've had the pleasure to meet and discuss with Walter Furman and Andrei Goverdovski. Their great experience in neutron-induced fission reactions has helped me in carrying out this work. I'm especially indebted to Dr. Furman, for his kindness and hospitality at the Frank Laboratory for Neutron Physics (and for the nice tours of JINR facilities - including the reactor building of IBR-2 - and of Dubna amenities). Most of fission analysis would have not been possible without the technical informations that - directly or indirectly - Vladimir Ketlerov provided me. During the last months of this work I've also had the opportunity to enjoy with him a "class-A experience" at ISOLDE facilities, and to prepare the restart of the FIC fission setup at n_TOF.

I wish also to thank all the members of the Italian n_TOF Collaboration, especially Pino, Gianni, Paolo, Javier, Kaori, Francesca and Cristian, with whom I enjoyed many abroad transfers and nice meetings all over Europe and Italy.

A special thank also to the Ph.D. secretary of the Physics Department in Padova, Cristina Mazzucco, for her continuous help and for the always smiling welcome in her office.

At last but not at least, I wish to thank all the other friends and colleagues with whom I shared these three years in both difficulties and good times (I would proceed strictly in alphabetic order...) : Antonio, Carlo, Lucia, Marco, Marina, Paola, Sandra and Silvia.